University of Southampton

Faculty of Engineering and Physical Sciences

School of Electronics and Computer Science

Improved Current Rating Methods of Subsea HVAC Cable Systems for Renewable Energy Applications

by

Dimitrios Chatzipetros

Thesis for the degree of Doctor of Philosophy

October 2019

University of Southampton

Abstract

Faculty of Engineering and Physical Sciences
School of Electronics and Computer Science

Thesis for the degree of
Doctor of Philosophy

Improved Current Rating Methods of Subsea HVAC Cable Systems for Renewable Energy Applications

by

Dimitrios Chatzipetros

The number and size of renewable projects, such as Offshore Wind Farms (OWFs), has been rapidly growing during the last years, mainly due to the increasingly great environmental concerns. The submarine cables used to transmit the power generated offshore to the mainland are crucial for the entire project's economic viability. Although cables are manufactured in rather cost-efficient ways and delivered in reasonable timelines thanks to the progress made in insulating material technology, they are presently subjected to a hard compromise: fixed costs are pushed to go down as much as possible, but at the same time the chance of failures is required to be minimised. The golden ratio in this difficult problem can certainly be sought to optimising the cable design.

Three-core (3C), HVAC cables are presently the most cost-effective technical solution for offshore power transmission. They are also expected to be so in the future, at least regarding the interconnection of OWFs located in reasonable distance from shore. To optimise the cable design, the current carrying capacity of the cable, often called as "ampacity", needs to be determined as accurately as possible. Due to electromagnetic induction, additional induced losses are generated inside the cable, which are dissipated in the form of heat from the cable to its surroundings. In order to investigate any likely optimisation margins, the way these losses are generated needs to be clearly understood. In parallel, the heat paths that enable the dissipation of heat inside the cable must be in depth considered. The existing calculation methods allow for such an analysis and cover, in theory, the larger cable sizes required in modern OWFs. However, empirically derived approximations are often used in these methods instead of rigorously extracted, mathematical solutions and sometimes refer to cable types different from the modern submarine cables. Furthermore, the physical models implied usually rely on simplifying assumptions that are expected to work sufficiently for smaller cables sizes,

but need to be benchmarked in larger sizes. Thus, the existing calculation methods have to be reviewed and improved, where necessary.

In order to allow for a quantitative analysis around the accuracy of the presently used methods, models representing more realistically the physical phenomena involved are developed. In 3C cables, the 2-D nature of heat transfer cannot be omitted, due to the physical proximity between the power cores. Traditional methods imply 1-D, radial analysis, which is in principle incapable of capturing the heat transfer occurring in the angular direction. Comparisons between the existing, traditional methods and the models developed demonstrate that this effect can be significant in larger cables.

A submarine cable often encounters various conditions, which in some cases may be thermally adverse, forming the so-called “hotspots”. Cables armoured with non-magnetic steel wires are preferred in these points, due to lower induced losses. To avoid any unnecessary increase in conductor size and, thus, any economic impact such an increase would have, an optimum design is sought for. For this purpose, numerical models capable of representing the AC phenomena involved are developed. These are benchmarked against the existing analytical methods and the thermal gain obtained from the more realistic loss generation is assessed.

Cables being armoured with magnetic steel wires are typically preferred in the main subsea section, due to techno-economic reasons. The cable geometry in this case influences the physical model to a great extent. Unfortunately, this is not considered by the traditional methods of calculating the losses, due to its inherent complexity. By applying 3-D electromagnetic analysis, it is possible to study the effect of the cable geometry on the induced losses. Hence, it becomes feasible to evaluate the accuracy level afforded by the traditional methods and, thus, anticipate the potential for design optimisation and further cost reduction.

University of Southampton

Περίληψη

Faculty of Engineering and Physical Sciences
School of Electronics and Computer Science
Thesis for the degree of
Doctor of Philosophy

Βελτιωμένες Μέθοδοι Υπολογισμού Ρεύματος Υποθαλάσσιων Καλωδιακών Συστημάτων Εναλλασσομένου Ρεύματος Υψηλής Τάσης για Εφαρμογές Ανανεώσιμων Πηγών Ενέργειας

by
Dimitrios Chatzipetros

Το πλήθος και το μέγεθος των έργων Ανανεώσιμων Πηγών Ενέργειας (ΑΠΕ), όπως είναι τα Υπεράκτια Αιολικά Πάρκα (Α/Π), αυξάνει ταχύτατα τα τελευταία χρόνια, κυρίως εξαιτίας των ολοένα και περισσότερο έντονων περιβαλλοντικών ανησυχιών. Τα Υποβρύχια (Υ/Β) καλώδια ισχύος που απαιτούνται για την μεταφορά της παραγόμενης ισχύος από τις υπεράκτιες Ανεμογεννήτριες (Α/Γ) στην ξηρά αποτελούν έναν κρίσιμο παράγοντα για την βιωσιμότητα των έργων αυτών. Σήμερα, έχει επιτευχθεί σημαντική μείωση τόσο στο κόστος παραγωγής όσο και στα χρονοδιαγράμματα παράδοσης των καλωδίων, χάρη στην πρόοδο που έχει συντελεστεί στην τεχνολογία των μονωτικών υλικών. Ωστόσο, τα Υ/Β καλώδια υπόκεινται σε έναν δύσκολο συμβιβασμό: τα πάγια κόστη πιέζονται ολοένα και χαμηλότερα, ενώ την ίδια στιγμή απαιτείται ελαχιστοποίηση ενδεχόμενων σφαλμάτων και αύξηση της αξιοπιστίας του συστήματος μεταφοράς. Η χρυσή τομή σε αυτό το δύσκολο πρόβλημα εντοπίζεται στην σχεδιαστική βελτιστοποίηση του καλωδίου.

Τα τριπολικά καλώδια Εναλασσομένου Ρεύματος Υψηλής Τάσης (ΕΡΥΤ) αποτελούν σήμερα την πιο αποδοτική, οικονομικά, λύση για την μεταφορά της ισχύος σε υπεράκτια Α/Π. Η ζήτησή τους αναμένεται σημαντική και στο άμεσο μέλλον, τουλάχιστον όσον αφορά στις διασυνδέσεις υπεράκτιων Α/Π που βρίσκονται εγκατεστημένα σε σχετικά μικρή απόσταση απ' την ξηρά. Απαραίτητη προϋπόθεση για την βελτιστοποίηση του σχεδιασμού είναι ο κατά το δυνατόν ακριβέστερος υπολογισμός της μεταφορικής ικανότητας του καλωδίου. Λόγω του φαινομένου της ηλεκτρομαγνητικής επαγωγής, πρόσθετες επαγόμενες απώλειες ισχύος παράγονται στο καλώδιο, οι οποίες στην συνέχεια διαχέονται, με την μορφή θερμότητας, στον περιβάλλοντα χώρο. Για να διερευνηθούν τυχόν περιθώρια σχεδιαστικής βελτιστοποίησης, θα πρέπει να κατανοηθεί σε βάθος ο τρόπος με τον οποίον αυτές οι απώλειες παράγονται και

διαχέονται. Οι υπάρχουσες μέθοδοι υπολογισμού επιτρέπουν μια τέτοια ανάλυση και θεωρητικά καλύπτουν τα μεγαλύτερα καλώδια που χρησιμοποιούνται στα σύγχρονα υπεράκτια Α/Π. Ωστόσο, σε αυτές τις μεθόδους γίνεται συχνά χρήση προσεγγιστικών μαθηματικών σχέσεων, οι οποίες έχουν προκύψει με τρόπο εμπειρικό αντί για τις αυστηρά μαθηματικές λύσεις των αντίστοιχων φυσικών προβλημάτων· συχνά, οι σχέσεις αυτές αναφέρονται σε τύπους καλωδίων που χρησιμοποιήθηκαν στο παρελθόν και διαφέρουν σημαντικά απ' τα σύγχρονα Υ/Β καλώδια. Περαιτέρω, τα θεωρούμενα φυσικά μοντέλα συνήθως βασίζονται σε απλοποιητικές παραδοχές, οι οποίες αναμένεται, μεν, να δίνουν ικανοποιητικά αποτελέσματα σε μικρότερες διατομές, χρήζουν, δε, προσεκτικής διερεύνησης όσον αφορά στην υιοθέτησή τους σε μεγαλύτερα μεγέθη. Είναι, επομένως, αναγκαίο να μελετηθούν οι υπάρχουσες μέθοδοι υπολογισμού ρεύματος και να αναθεωρηθούν στα σημεία που απαιτείται.

Για την ποσοτική αξιολόγηση της ακρίβειας των επί του παρόντος χρησιμοποιούμενων μεθόδων, φυσικά μοντέλα που αναπαριστούν με περισσότερο ρεαλιστικό τρόπο τα εμπλεκόμενα φαινόμενα αναπτύσσονται στην παρούσα εργασία. Στα τριπολικά καλώδια ισχύος, η διδιάστατη φύση της μεταφοράς θερμότητας δεν μπορεί να αγνοηθεί, λόγω της γειτνίασης μεταξύ των πόλων. Οι συμβατικές μέθοδοι υπολογισμού υιοθετούν μονοδιάστατη, ακτινική ανάλυση, η οποία καταρχήν αδυνατεί να λάβει υπόψιν την γωνιακή συνιστώσα της θερμικής ροής. Οι συγκρίσεις που γίνονται μεταξύ των μοντέλων που αναπτύσσονται και των παραδοσιακών μεθόδων υπολογισμού αναδεικνύουν ότι μια τέτοια απλοποίηση μπορεί να έχει σημαντική επίδραση στα μεγαλύτερα καλώδια.

Ένα Υ/Β καλώδιο είναι, συνήθως, εκτεθειμένο σε ποικίλες συνθήκες εγκατάστασης, οι οποίες συχνά μπορεί να είναι θερμικά δυσμενείς. Καλώδια οπλισμένα με σύρματα μη μαγνητικού χάλυβα προτιμώνται σε αυτά τα σημεία της διαδρομής, λόγω των μειωμένων επαγόμενων απωλειών. Επομένως, είναι αναγκαία η σχεδιαστική βελτιστοποίηση των καλωδίων αυτών, έτσι ώστε να αποφευχθεί μια περιττή αύξηση του, συχνά χάλκινου, αγωγού, με ό,τι οικονομική επίπτωση μια τέτοια αύξηση θα συνεπαγόταν. Για το σκοπό αυτό, αριθμητικά μοντέλα, ικανά να αναπαραστήσουν τα εμπλεκόμενα επαγωγικά φαινόμενα, όπως είναι το επιδερμικό φαινόμενο και τα φαινόμενα γειτνίασης, αναπτύσσονται στην παρούσα εργασία. Γίνεται συγκριτική αξιολόγηση με τις υπάρχουσες, αναλυτικές μεθόδους και εκτιμάται το θερμικό κέρδος που απορρέει απ' τις ρεαλιστικότερες απώλειες ισχύος.

Καλώδια οπλισμένα με σύρματα μαγνητικού χάλυβα προτιμώνται, κατά κανόνα, στο κυρίως τμήμα της υποθαλάσσιας διαδρομής για τεχνοοικονομικούς λόγους. Στην περίπτωση αυτή, η τριδιάστατη γεωμετρία του καλωδίου δεν μπορεί να αγνοηθεί από το θεωρούμενο φυσικό μοντέλο. Λόγω της εγγενούς πολυπλοκότητας μιας τέτοιας θεώρησης, οι συμβατικές μέθοδοι την αγνοούν. Εφαρμόζοντας τριδιάστατη ηλεκτρομαγνητική ανάλυση, μέσω της Μεθόδου των

Πεπερασμένων Στοιχείων, είναι εφικτό να μελετηθεί η επίδραση της γεωμετρίας στις επαγόμενες απώλειες ισχύος. Ως εκ τούτου, καθίσταται δυνατή η αξιολόγηση του βαθμού ακρίβειας που παρέχεται από τις παραδοσιακές μεθόδους υπολογισμού και, συνεπώς, η σχεδιαστική βελτιστοποίηση και η περαιτέρω μείωση του κόστους.

Table of Contents

Table of Tables

Table of Tables

Table of Figures

Table of Figures

Table of Figures

List of Accompanying Materials

Digital Object Identifier: https://doi.org/10.5258/SOTON/D1328

Research Thesis: Declaration of Authorship

Print name:	Dimitrios Chatzipetros

Title of thesis:	Improved Current Rating Methods of Subsea HVAC Cable Systems for Renewable Energy Applications

I, Dimitrios Chatzipetros, declare that this thesis and the work presented in it are my own and has been generated by me as the result of my own original research.

I confirm that:

1. This work was done wholly or mainly while in candidature for a research degree at this University;
2. Where any part of this thesis has previously been submitted for a degree or any other qualification at this University or any other institution, this has been clearly stated;
3. Where I have consulted the published work of others, this is always clearly attributed;
4. Where I have quoted from the work of others, the source is always given. With the exception of such quotations, this thesis is entirely my own work;
5. I have acknowledged all main sources of help;
6. Where the thesis is based on work done by myself jointly with others, I have made clear exactly what was done by others and what I have contributed myself;
7. Parts of this work have been published as:

    - Chatzipetros, D., Pilgrim, J.A. (2018) “Induced Losses in Non-Magnetically Armoured HVAC Windfarm Export Cables” IEEE International Conference on High Voltage Engineering and Application, 10-13 September 2018, Athens, Greece.
    - Chatzipetros, D., Pilgrim, J.A. (2018) “Review of the Accuracy of Single Core Equivalent Thermal Model for Offshore Wind Farm Cables” IEEE Transactions on Power Delivery, vol. 33, no. 4, pp 1913-1921.
    - Chatzipetros, D., Pilgrim, J.A. (2019) “Impact of Proximity Effects on Sheath Losses in Trefoil Cable Arrangements” IEEE Transactions on Power Delivery, Early Access.

Signature:		Date:	

Acknowledgements

I would like to acknowledge the support of a number of people who have provided assistance in a wide variety of fields over the course of my PhD. Firstly, I would like to acknowledge CABLEL® Hellenic Cables S.A. Company for funding the vast majority of the work contained within this thesis. Particularly, I would like to express my sincere gratitude to the Head of Hellenic Cables R&D and Engineering Dpt., Mr. George Georgallis, and the Head of Hellenic Cables Engineering Dpt., Dr. Konstantinos Tastavridis for the opportunity and trust they offered me.

I am grateful to my colleagues here, in the Electrical Power Engineering (EPE) Group of the University of Southampton, who have been so useful, supportive and encouraging during my efforts in this PhD. Particular mention should go to my supervisor, Dr. James A. Pilgrim, whose feedback has been always helpful and guidelines have proved determinant since the beginning of my PhD, in February 2016.

Although moving out so many times and some people left the EPE Group during these years, I cannot forget the support provided by Dr. Richard D. Chippendale in my initial modelling steps and the useful discussions with Dr. Kevin F. Goddard upon my scientific concerns.

Back to Hellenic Cables, particular and a lot of acknowledgements should go to my colleague and friend Dr. Andreas I. Chrysochos, who has always been helpful, encouraging and supportive, both scientifically and morally.

Last but not least I would like to say a huge 'thank you' to all my colleagues at the Hellenic Cables Engineering Dpt. for their support, patience and ideas offered throughout these years.

Finally, I wish to acknowledge the overwhelming support of my parents, Nikolaos Chatzipetros and Evdokia Karapati-Chatzipetrou, as well as my brother Emmanouil Chatzipetros, throughout not only the good, but also the not-so-good times, over the course of my time at the University of Southampton.

Symbols[1] and Abbreviations

a	Radius of a circular shaped ring representing the return path (m)
A	Area (m^2)
A_{sr}	Effective radiation area (m^2)
$\vec{A}$	Magnetic vector potential (Wb/m)
$\overrightarrow{A_z}$	z-component of the magnetic vector potential (Wb/m)
AC	Alternating Current
bei	Kelvin function
ber	Kelvin function
B_{norm}	Normal to a boundary $\vec{B}$ component (T)
B_{tang}	Tangential to a boundary $\vec{B}$ component (T)
$\vec{B}$	Magnetic flux density (T)
$\overrightarrow{B_{\mathrm{A}}}$	Total magnetic flux vector in a steel wire (T)
$\overrightarrow{B_x}$	Transversal to a steel wire magnetic flux component vector (T)
$\overrightarrow{B_y}$	Longitudinal to a steel wire magnetic flux component vector (T)
BC	Boundary condition
c	Distance between the conductor axis and the cable centre (m)
C	Electrical pul capacitance (F/m)
C_A	Coefficient used to calculate $\lambda''_{1_{\mathrm{Jack}}}$ (dimensionless)
$C_A{}'$	Coefficient used to calculate $\lambda''_{1_{\mathrm{Jack}}}$ (dimensionless)
C_{p}	Specific heat capacity at constant pressure (J/(kgK))
C_1	Constant of integration (dimensionless)
C_2	Constant of integration (dimensionless)
$\mathbf{C}$	Capacitance matrix (F/m)
CP	Crossing pitch
CT	Current Transformer
CPU	Central Processing Unit
CFD	Computational Fluid Dynamics

[1] SI units are referred in this section, although units different from SI may be referred to this work.

Symbols and Abbreviations

d	Sheath mean diameter (m)
d_{c}	Conductor diameter (m)
d_{core}	Power core diameter (m)
d_{f}	Diameter of a steel wire (m)
$d_{\mathrm{f},i}$	Radial coordinate of fictitious filament *i* (m)
$d_{\mathrm{ph},i}$	Radial coordinate of physical filament *i* (m)
d_{A}	Armour mean diameter (m)
d_{under}	Inner diameter of a non-metallic layer (m)
dr	Infinitesimal radius (m)
$d\vec{S}$	Infinitesimal surface (m^2)
D	Density (kg/m^3)
D_{ii}	Self-geometric mean distance of filament (subconductor) *i* (m)
D_{ij}	Geometric mean distance between 2 filaments (subconductors) *i, j* (m)
D_{j}	Outer diameter over the jacket (m)
D_{s}	Outer diameter over the sheath (m)
DE	Drive End
DC	Direct Current
DsOF	Degrees of freedom
$\vec{D}$	Electric displacement field (C/m^2)
e_{EMTP}	Relative difference between EMTP and Js – FEM method (%)
e_{FM}	Relative difference between FM and Js – FEM method (%)
$e_{\mathrm{FE,FM}}$	Relative difference between FE and FM models (%)
$e^{\mathrm{IEC}}_{\mathrm{AVG\_SPB}}$	Average of the relative differences $\left(\lambda''_{1,\mathrm{IEC}} - \lambda''_{1,\mathrm{FEA}}\right)/\lambda''_{1,\mathrm{FEA}}$ (%)
$e^{\mathrm{IEC}}_{\mathrm{AVG\_SB}}$	Average of the relative differences $\left(\lambda_{1,\mathrm{IEC}} - \lambda_{1,\mathrm{FEA}}\right)/\lambda_{1,\mathrm{FEA}}$ (%)
$e^{\mathrm{New}}_{\mathrm{AVG\_SPB}}$	Average of the relative differences $\left(\lambda''_{1,\mathrm{New}} - \lambda''_{1,\mathrm{FEA}}\right)/\lambda''_{1,\mathrm{FEA}}$ (%)
$e^{\mathrm{New}}_{\mathrm{AVG\_SB}}$	Average of the relative differences $\left(\lambda_{1,\mathrm{New}} - \lambda_{1,\mathrm{FEA}}\right)/\lambda_{1,\mathrm{FEA}}$ (%)
$\vec{E}$	Electric field (V/m)
emf	Electromotive force
EE	Earth End
EPR	Ethylene Propylene Rubber
EHV	Extra High Voltage

EMTP	Electromagnetic Transients Program
EPRI	Electric Power Research Institute
f	System frequency (Hz)
ff_k	Factor used to correct the DC resistance of a stranded conductor *k*, accounting for the air-gaps between strands. Often called as 'Fill-factor' (dimensionless)
FE	Finite Element
FEA	Finite Element Analysis
FEM	Finite Element Method
FM	Filament Method
g_{S}	Coefficient used in calculating $\lambda''_{1,\mathrm{IEC}}$ (dimensionless)
G	Geometric factor (dimensionless)
G_{FEA}	Geometric factor computed by Finite Element Analysis (dimensionless)
G_{SL}	Geometric factor proposed for SL-Type cables (dimensionless)
G_{Cu}	Geometric factor proposed for Copper foiled cables (dimensionless)
G_{Al}	Geometric factor proposed for Aluminium foiled cables (dimensionless)
G	Conductance matrix (S/m)
$\vec{H}$	Magnetic field intensity (H/m)
HV	High Voltage
HDD	Horizontal Directional Drilling
HVAC	High Voltage Alternating Current
HVDC	High Voltage Direct Current
I	Current vector (A)
$\mathbf{I}_{\mathrm{FM}}$	Current filament vector (A)
I_{C}	Conductor current (A)
I_{FEA}	I_{S} computed by FEA (A)
I_{IEC}	I_{S} calculated by the IEC 60287-1-1 method (A)
I_i	Current of filament (subconductor) *i* (A)
I_{S}	Sheath current (A)
IEC	International Electrotechnical Committee
IEEE	Institute of Electrical and Electronics Engineers
J	Surface current density (A/m^2)
J_{nu} (A/m^2)	Non-uniform current density in conductors (skin/ proximity effects considered)

J_{u} (A/m²)	Uniform current density in conductors (no skin/ proximity effects considered)
J_{o}	Bessel function of the first kind and zero order
J_1	Bessel function of the first kind and first order
$\overrightarrow{J_z}$	Total current density vector composed of $\overrightarrow{J_{ez}}$ and $\overrightarrow{J_{sz}}$ (A/m²)
$\overrightarrow{J_{ez}}$	Eddy current density vector (A/m²)
$\overrightarrow{J_{sz}}$	Source current density vector (A/m²)
k	Thermal conductivity (W/(Km))
k_{p}	Factor used in calculating x_{p} (proximity effect)
k_{s}	Factor used in calculating x_{s} (skin effect)
$k_{\mathrm{fb\_eqvl}}$	Equivalent thermal conductivity of fillers and bedding material (W/(Km))
L	Depth of burial of the cable (m)
$\mathbf{L}$	Inductance matrix (H/m)
$\mathbf{L}_{\mathrm{FM}}$	Inductance filament matrix (H/m)
L_{ii}	Self-inductance pul of filament (subconductor) *i* (H/m)
L_{ij}	Mutual inductance pul between filaments (subconductors) *i* and *j* (H/m)
L_{C}	Cable length (m)
$L_{ii,\mathrm{ext}}$	External inductance pul of a generic conductor *i* (H/m)
$L_{ii,\mathrm{int}}$	Internal inductance pul of a generic conductor *i* (H/m)
$L_{ij,\mathrm{int}}$	Internal mutual inductance pul of two generic conductors *i*, *j* (H/m)
$L_{ij,\mathrm{ext}}$	External mutual inductance pul of two generic conductors *i*, *j* (H/m)
LCM	Least common multiple
LDPE	Low-Density Polyethylene
m	Frequency to resistance ratio (dimensionless)
MV	Medium Voltage
MoI	Method of Images
MVAC	Medium Voltage Alternating Current
MoM-SO	Moments-Surface Operator
$\hat{n}$	Unit vector normal to surface
n_{A}	Number of steel wires
NM & SC	Non-Magnetic &Super Conductive
N/A	Not applicable

OWF	Offshore Wind Farm
OHVS	Offshore High Voltage Substation
p_{A}	Armour pitch (m)
p_{C}	Power core pitch (m)
p_{ij}	Coefficients used to calculate the RF polynomial formulae, where *i,j* may be 0, 1, 2 or 3 (dimensionless)
P_{tot}	Total pul active power losses measured in the 3C cable (W/m)
pul	Per unit length
PE	Polyethylene
PP	Polypropylene
PoS	Principle of Superposition
PVC	Polyvinyl Chloride
q_r	Heat power flux per unit area (W/m^2)
$\dot{q}$	Heat power generation per unit volume of the medium (W/m^3)
Q	Heat power flow (W)
r	Radius from the cable centre (m)
r_i	Radius of filament (subconductor) *i* (m)
r_C	Conductor radius (m)
r_{A}	Armour mean radius (m)
$r_{\mathrm{A,in}}$	Armour inner radius (m)
$r_{\mathrm{A,out}}$	Armour outer radius (m)
$r_{\mathrm{J,out}}$	Power core outer radius (m)
$r_{\mathrm{S,in}}$	Sheath inner radius (m)
$r_{\mathrm{S,out}}$	Sheath outer radius (m)
$r_{\mathrm{P,in}}$	Pipe inner radius (m)
$\mathbf{R}$	Resistance matrix (Ω/m)
$\mathbf{R}_{\mathrm{FM}}$	Resistance filament matrix (Ω/m)
R_i	DC resistance pul of filament (subconductor) *i* (Ω/m)
R_{A}	Armour AC pul resistance (Ω/m)
R_{AC}	Conductor AC pul resistance (Ω/m)
R_{DC}	Conductor DC pul resistance (Ω/m)
R_{FEA}	R_{S} computed by FEA (Ω/m)

R_{IEC}	R_{S} calculated by the IEC 60287-1-1 method (Ω/m)
R_{S}	Sheath pul resistance (Ω/m)
R_{Si_int}	Variable internal resistance connected in series with sheath *i*, where *i* equal to 1, 2 or 3, to simulate SPB and SB (Ω)
Re	Reynolds number (dimensionless)
RF_{SB}	RF for SB case (dimensionless)
RF_{SPB}	RF for SPB case (dimensionless)
RF_{lin}	RF derived for linear approximation (dimensionless)
RF_{3rd}	RF derived for 3rd order polynomial approximation (dimensionless)
RF	Reductive Factor
RAM	Random access memory
s	Axial distance between conductors (m)
S_k	Cross-sectional area of conductor *k* (m^2)
S_{tot}	Total complex power losses measured in the 3C cable (VA)
SA	Separate Aluminium
SB	Solid Bonding
SL	Separate Lead
SM & NC	Super Magnetic & Non-Conductive
SPB	Single-Point Bonding
SSE	Sum of Squares of Error
SCETM	Single-Core Equivalent Thermal Model
t	Time (s)
t_i	Thickness of the *i*-th layer (m)
$t_{\mathrm{eq\_fb}}$	Equivalent thickness representing the fillers and bedding domain (m)
t_{j}	Thickness of the jacket (m)
$t_{\mathrm{A\_eqvl}}$	Thickness of an equivalent tubular armour (m)
t_{S}	Thickness of the sheath (m)
t_{P}	Thickness of the pipe (m)
$t_{\mathrm{j\_ar}}$	Thickness of material between the outer surface of jackets and the inner surface of armour (m)
$t_{\mathrm{s\_ar}}$	Thickness of material between the outer surface of sheaths and the inner surface of armour (m)
T_i	Thermal resistance of the *i*-th non-metallic layer pul (Km/W)

T_1	Thermal resistance of insulation pul (Km/W)
T_{2j}	Thermal resistance of jacket pul (Km/W)
T_2	Thermal resistance of fillers and bedding pul (Km/W)
$T_{2,FEA}$	Thermal resistance of fillers and bedding pul computed by Finite Element Analysis (Km/W)
T_3	Thermal resistance of serving pul (Km/W)
T_4	External thermal resistance pul (Km/W)
TB	Technical Brochure
$tan\delta$	Tangent of the dielectric loss angle
U_0	Phase-to-ground voltage (V)
V_{i_DE}	Phase-to-ground voltage phasor measured at DE, where *i* is phase a, b or c (V)
V_{i_EE}	Phase-to-ground voltage phasor measured at EE, where *i* is phase a, b or c (V)
$\mathbf{V}$	Voltage drop vector (V/m)
$\mathbf{V}_{FM}$	Voltage drop filament vector (V/m)
W_A	Armour pul loss (W/m)
W_C	Conductor pul loss (W/m)
W_D	Dielectric pul loss (W/m)
W_S	Sheath pul loss (W/m)
W_{tot}	Total pul cable losses (W/m)
WG	Working Group
WTG	Wind Turbine Generator
x_s	Argument of a Bessel function used to calculated skin effect
x_p	Argument of a Bessel function used to calculated proximity effect
X	Thickness of material between sheaths and armour as a fraction of the outer diameter of the sheath (dimensionless)
X_S	Sheath pul reactance (Ω/m)
X_{sc}	Geometrical parameter representing the net distance between the inner surface of sheath and the outer surface of conductor in a sheathed core (m)
X_{touch}	Thickness of material between touching power cores (jacketed or unjacketed) and armour as a fraction of the outer diameter of the power core (dimensionless)
X_{non_touch}	Thickness of material between non-touching unjacketed power cores and armour as a fraction of the outer diameter of the sheath (dimensionless)
XLPE	Cross-linked Polyethylene
XSA	Conductor cross-sectional area (mm^2)

y_{p}	Proximity effect factor (dimensionless)
y_{s}	Skin effect factor (dimensionless)
$\mathbf{Y}$	Full admittance matrix (S/m)
$\mathbf{Z}$	Full impedance matrix (Ω/m)
$\mathbf{Z_0}$	External impedance matrix (Ω/m)
$\mathbf{Z_i}$	Internal impedance matrix (Ω/m)
$\mathbf{Z}_{\mathrm{p}}$	Pipe internal impedance matrix (Ω/m)
$\mathbf{Z}_{\mathrm{c}}$	Connection impedance matrix between pipe inner and outer surfaces (Ω/m)
$\mathbf{Z_{i\_pt}}$	Pipe-type cable internal impedance matrix (Ω/m)
$\mathbf{Z}_{\mathrm{FM}}$	Impedance filament matrix (Ω/m)
$\mathbf{Z^{red}}$	Impedance reduced matrix (Ω/m)
ΑΠΕ	Ανανεώσιμες Πηγές Ενέργειας
Α/Γ	Ανεμογεννήτρια
Α/Π	Αιολικό Πάρκο
β	Thermal expansion coefficient (1/K)
β_{CA}	Angle calculated to account for a shorter helical path through the armour (rad)
β_1	Coefficient used in calculating $\lambda''_{1,\mathrm{IEC}}$ and $\lambda''_{1_{\mathrm{Jack}}}$
γ	Ratio of the inner to the outer radius of a generic hollow conductor (dimensionless)
δ_{P}	Skin depth of pipe (m)
Δ_1	Coefficient used in calculating $\lambda''_{1,\mathrm{IEC}}$ (dimensionless)
Δ_2	Coefficient used in calculating $\lambda''_{1,\mathrm{IEC}}$ (dimensionless)
ΔV_i	Voltage drop along filament (subconductor) i (V/m)
$\Delta\theta$	Conductor temperature rise above local ambient (K)
$\Delta\theta_{\mathrm{f}}$	Temperature drop across filler (K)
$\Delta\theta_{\mathrm{j\_ar}}$	Temperature drop between jackets and armour (K)
ε	Emissivity (dimensionless)
ΕΡΥΤ	Εναλλασσόμενο Ρεύμα Υψηλής Τάσης
θ	Temperature (°C)
θ_{A}	Armour temperature (°C)
θ_{amb}	Local ambient temperature (°C)
θ_{C}	Conductor temperature (°C)

θ_e Cable surface temperature (°C)

θ_J Jacket temperature (°C)

θ_S Sheath temperature (°C)

θ_{soil} Remote soil temperature (°C)

λ_0 Coefficient used in calculating $\lambda''_{1,IEC}$ (dimensionless)

λ_1 Sheath total losses factor (dimensionless)

$\lambda_{1,FEA}$ λ_1 factor computed with FEA (dimensionless)

$\lambda_{1,IEC}$ λ_1 factor according to the IEC 60287-1-1 Standard (dimensionless)

$\lambda_{1,New}$ New (corrected) λ_1 factor based on the analysis adopted in Chapter 5 (dimensionless)

λ'_1 Sheath circulating current loss factor (dimensionless)

$\lambda'_{1,FEA}$ λ'_1 factor computed with FEA (dimensionless)

$\lambda'_{1,IEC}$ λ'_1 factor according to the IEC 60287-1-1 Standard (dimensionless)

$\lambda'_{1,test}$ λ'_1 factor measured (dimensionless)

λ''_1 Sheath eddy current loss factor (dimensionless)

$\lambda''_{1\,1st}$ λ''_1 factor due to external conductor currents - 1st order (dimensionless)

$\lambda''_{1,FEA}$ λ''_1 factor computed with FEA (dimensionless)

$\lambda''_{1,IEC}$ λ''_1 factor according to the IEC 60287-1-1 Standard (dimensionless)

$\lambda''_{1_{Jack}}$ λ''_1 factor calculated through the analytical method suggested by Jackson [1] (dimensionless)

$\lambda''_{1,New}$ New (corrected) λ''_1 factor based on the analysis adopted in Chapter 5 (dimensionless)

$\lambda''_{1,test}$ λ''_1 factor measured (dimensionless)

$\lambda_{i,ext}$ External flux linkage pul of a generic conductor *i* (Wb/m)

$\lambda_{i,ext}^{avg}$ Spatial average of $\lambda_{i,ext}$ (Wb/m)

λ_2 Armour loss factor (dimensionless)

$\lambda_{2,IEC}$ λ_2 factor according to the IEC 60287-1-1 Standard (dimensionless)

μ_0 Vacuum magnetic permeability ($4\pi \cdot 10^{-7}$H/m)

$\boldsymbol{\mu_e}$ Complex relative, longitudinal magnetic permeability (dimensionless)

μ_p Relative magnetic permeability of pipe (dimensionless)

μ_r Relative magnetic permeability (dimensionless)

$\mu_{r,A}$ Relative magnetic permeability of armour (dimensionless)

$\boldsymbol{\mu_{r,A}}$ Complex relative magnetic permeability of armour (dimensionless)

$\boldsymbol{\mu_{r,A\_eqvl}}$ Complex relative magnetic permeability of an equivalent tubular armour (dimensionless)

$\mu_{r,P}$ Relative magnetic permeability of pipe (dimensionless)

$\mu_{r,S}$ Relative magnetic permeability of sheath (dimensionless)

$\boldsymbol{\mu_{L}}$ Complex relative longitudinal magnetic permeability, translated to the tubular geometry (dimensionless)

μ_S Magnetic permeability of sheath (H/m)

$\boldsymbol{\mu_{T}}$ Complex relative tranverse magnetic permeability, translated to the tubular geometry (dimensionless)

ρ_i Thermal resistivity of the *i*-th material (Km/W), (Chapters 2, 3: *i* can be 1, 2j or 3)

ρ_i Electrical resistivity of the *i*-th filament (subconductor) (Ωm), (Chapters 4, 5: *i* can be whatever integer number from 1 to *n*, where *n* the total number of filaments)

ρ_{air} Thermal resistivity of air (Km/W)

$\rho_{Al\_90°C}$ Aluminium electrical resistivity at 90°C implied by the IEC 60287-1-1 Standard (Ωm)

ρ_C Conductor electrical resistivity (Ωm)

$\rho_{Cu\_20°C}$ Copper electrical resistivity at 20°C suggested by the IEC 60287-1-1 Standard (Ωm)

ρ_S Sheath electrical resistivity (Ωm)

ρ_{fb} Thermal resistivity of fillers and bedding material (Km/W)

ρ_t Thermal resistivity of core insulation (Km/W)

σ Electrical conductivity (S/m)

σ_{A_eqvl} Electrical conductivity of an equivalent tubular armour (S/m)

σ_B Stephan-Boltzman constant ($5.67 \cdot 10^{-8}$ W/(m^{2}K^4))

σ_P Electrical conductivity of pipe (S/m)

Υ/Β Υποβρύχιο

$\varphi_{f,i}$ Angular coordinate of fictitious filament *i* (rad)

$\varphi_{ph,i}$ Angular coordinate of physical filament *i* (rad)

Φ Electric scalar potential (V)

ω Angular frequency (rad/s)

1C Single-core

1-D One dimensional

2-D Two dimensional

2.5-D	Two and a half dimensional
3C	Three-core
3-D	Three dimensional

This work is dedicated to my grandfather 'Smanolis', who was passionate about studying and educating and his soul will be certainly somewhere, wherever this is, happy and proud of me; not only for this step-forward, but mostly for my hard efforts until I reach up to it.

Η εργασία αυτή αφιερώνεται στον πάππο μου τον Σμανώλη, ο οποίος είχε πάθος για τα γράμματα και την μόρφωση και σίγουρα η ψυχή του θα 'ναι κάπου, όπου κι αν είν' αυτό, δροσισμένη και περήφανη· όχι μόνο για το σκαλοπάτι καθεαυτό, παρά για τον Ανήφορό μου ώσπου ν' ανέβω σε αυτό.

«Φοιτητές είναι οι έγγο-

νοί μου και θαρρώ πως φέγγω

Εθάρρου πως μου δώκανε

Το φως μου όντε μου το 'πανε»

Chapter 1 Introduction

The rapid evolution of human civilisation over the last 1 and ½ century has been achieved to a great extent thanks to the electrification of most aspects in domestic and industrial activities. Although the basic principles based on which that electricity is transmitted still remain unchanged, significant changes have taken place regarding the components of the transmission system: power cables are increasingly used, not only in shorter distances inside urban, densely-populated areas, but also in longer distances, so as to interlink different countries, often being separated by the sea.

Owing to the global warming, reported since about 1950 [2], electric power generation in more environmentally friendly ways had to be achieved. Hence, technologies such as renewable energy sources have presently been matured and already contributed towards a lower carbon energy footprint. Amongst others, onshore wind farms appeared as a quite cost-effective way of generating electricity in considerable amounts. Due to the increasingly higher power demands, larger and more powerful wind turbines had to be used, thus leading to the development of enormous wind farms which had to be installed far away from urban areas. Placing these wind farms offshore seemed to be a quite attractive solution. In such a case the interconnection between generation points and the mainland network is obviously feasible only through submarine cable systems.

1.1 Offshore Wind Farms (OWFs) and Submarine Cables

1.1.1 OWFs

The wind is a free, clean, and inexhaustible energy source. It has served humankind well for many centuries by propelling ships and driving wind turbines to grind grain and pump water. Denmark was the first country to use wind for generation of electricity, by using a wind turbine of 23 m diameter in 1890 [3].

Although offshore technology has existed for several decades, offshore wind power has substantially been developed as an alternative or supplement to onshore wind during the last 15 years. Many of the obstacles inherent to onshore wind farms can be effectively tackled by offshore farms. Firstly, wind speeds over the ocean are typically much higher and steadier than those prevailing in the mainland. Hence, higher utilisation and more stable operation is achieved when wind farms are extended to deeper waters and far from shore [4]. Another important reason that makes the offshore solution more attractive is the public dislike and reaction regarding wind turbines installed in their landscapes. Wind turbines are often viewed

as repulsive by the residents of nearby regions and there may often be considerable public pressure that must be overcome when constructing such facilities. On the contrary, deep-water offshore solutions give access to large areas with less sensitivity to noise, visual impacts and size. However, the cost of developing and operating an offshore wind farm is many times higher than onshore due to large water depths and harsh offshore environments [5].

Thanks to the technological development and the relevant cost reduction, the installed offshore wind power capacity has been considerably increased over last ten years: as shown in Figure 1.1, starting from about 1.5% out of the total wind power (onshore and offshore) in 2008, it has become almost 10% in 2018 [6]. An increase up to about 20% is foreseen by 2030 considering the central scenario, varying between 18% and 23% in terms of the low and high scenarios, respectively [7].

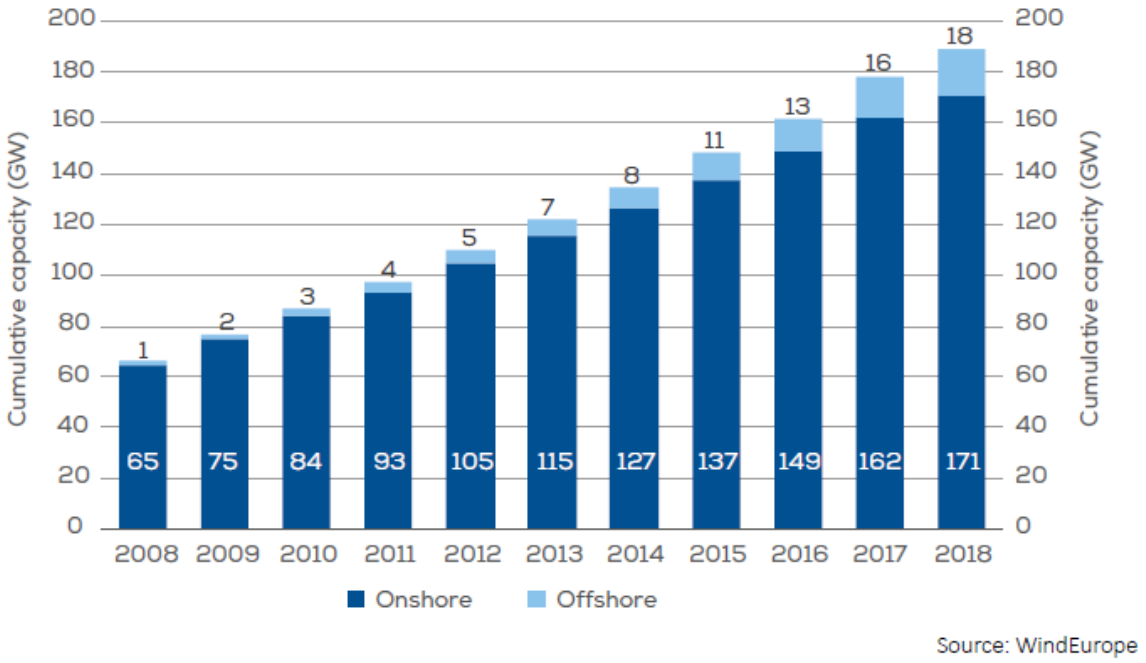

FIGURE 1.1: Cumulative Onshore and Offshore Wind Installations in Europe [6].

The percentage of the total capital expenditure pertaining to the grid interconnection of an OWF to the mainland varies between 10-20%, of which a considerable part relates to the manufacturing and installation of the necessary submarine cables ([8], [9]). In order to meet the increased power transfer demands, larger submarine cable sizes and higher voltage levels are currently being considered, as implied by the 2000 mm^2 conductor size of a 275 kV cable in [10]. Hence, the overall build cost of OWFs is boosted to significantly higher levels and submarine cables become one of the key factors concerning their economic viability.

1.1.2 Submarine Cables: Brief Historical Review

Submarine power cables have been around for more than a century, but their major uses have shifted through the decades. Initially, submarine power cables were used to supply isolated offshore facilities such as lighthouses, infirmary ships, etc. Later, they tended to supply near-shore islands, replacing island-stationed, often-inefficient power generation such as diesel generators. One of the earliest subsea island-to-mainland interconnections was that of the archipelago of the North Frisian Islands in Northern Germany by a grid of 20 kV submarine cables which started in 1944. Furthermore, the interconnection of autonomous power grids for the sake of better stability and resource utilisation has been pursued since 1960. These grids usually consist of various power plants, more or less environmentally friendly, while they very often differ with each other in terms of nominal frequency and/or voltage level [11].

Early submarine cables were composed of insulating materials similar to land cables. Oil-filled cables had been installed in significant lengths in several subsea projects. However, their manufacturing process was quite complicated, while feeding stations were necessary in order to keep the oil pressure at fairly high levels. Perhaps the most important negative point is their doubtful environmental behaviour, with outpouring of oil in case of a submarine cable damage. Mass impregnated paper and Ethylene propylene rubber (EPR) have also been used as insulation materials in submarine cables. The former has been today abandoned to a large extent other than for HVDC applications, owing to its complexity in manufacturing process, while both technologies are limited to MVAC applications, because of the high dielectric losses generated [11].

Cross-linked polyethylene (XLPE) has been used for subsea applications since 1973. The long molecular chains of low-density polyethylene (LDPE) are cross-linked, shaping a 3-D network which is irreversible and prevents the polymer from melting at elevated temperatures: although thermoplastic polyethylene (PE) softens and eventually melts at 80-110°C, depending on the density, XLPE remains stable at far higher temperatures. Instead of melting, it is destroyed by pyrolysis above 300°C.

Early XLPE insulated cables were prone to electrical breakdown owing to the development of water trees in the insulation layer: under the combined influence of water, electric field and impurities, water-treeing could be initiated. However, these early XLPE cables were manufactured by applying steam-induced cross-linking, while the extrusion of the semiconductive layers and the main insulation had often been in subsequent phases, thus facilitating the ingress of water and dirt into the insulation. Once the triple extrusion process along with dry curing became feasible, the quality and breakdown voltage of XLPE technology has been dramatically improved (since 1980s) [11].

XLPE insulated cables are today qualified for very high voltages. Thanks to their ease of manufacturing and installation and the mature XLPE insulation systems with good electrical properties, they constitute the most popular choice for subsea projects, leaving little space for other insulation solutions [11]. It must be referred that some, alternative to XLPE, polymeric insulation solutions have been recently developed by certain cable manufacturers, such as High Performance Thermoplastic Elastomers, showing good electrical properties and an overall promising performance [12].

1.1.3 Submarine Cables: Use in OWFs

The rapid evolution of OWFs, as presented in section 1.1.1, would not be feasible without an in parallel development of the submarine cables which are necessary to interconnect the Wind Turbine Generators (WTGs) one another, as well as the entire OWF to the mainland. The so called "in-field" or "inter-array" cables are used to collect the power from the individual offshore WTGs or connect these with an offshore HVAC substation [11]. They were initially three-phase medium-voltage cables (10-36 kV) with polymeric insulation, while due to the use of WTGs of up to 10 MW or even more in recent years, the increased power transfer demands are commonly covered by 66 kV inter-array cables in order to further reduce the transmission losses [13].

Since OWFs usually consist of many turbines, a large output power is generated offshore. A high voltage connection to the mainland becomes apparently more economic, especially for OWFs located in longer distances from shore. Three-phase cables with operating voltage higher than 100 kV serve most often as export cables for distances exceeding 30 km [11]. Today a further increase in voltage is attempted, reaching up to 275 kV for OWF applications [10].

Typical export cables are shown in Figure 1.2. It is of great importance to ensure in both array and export cables that their insulation system is kept watertight enough throughout the entire life time of the cable. The most efficient way to achieve this, which is preferred in export cables, is by providing separate lead (SL) sheaths above the insulation system (dry design). Because of that, 3C submarine cables are also known as SL-Type cables, although other sheath materials, such as Copper or Aluminium, are not ruled out.

In these large and remote OWFs, the individual WTGs are connected to an offshore platform, which includes an offshore HV substation (OHVS) carrying a step-up transformer. From the OHVS, one or more submarine power cable (export cables) carry the power to shore. The transmission of the offshore generated power to the mainland may also be through HVDC cables. However, the erection of converter stations both offshore and onshore is required in this case, thus significantly increasing the total link cost. A drawing showing an indicative

network of submarine cables interconnecting an OWF to the mainland is illustrated in Figure 1.3.

FIGURE 1.2: 3x630 mm² 150 kV Cu Conductor with Solid Fillers (on the left) and 3x1800 mm² 220 kV Al Conductor with Extruded Fillers (on the right) Export Submarine Cables.

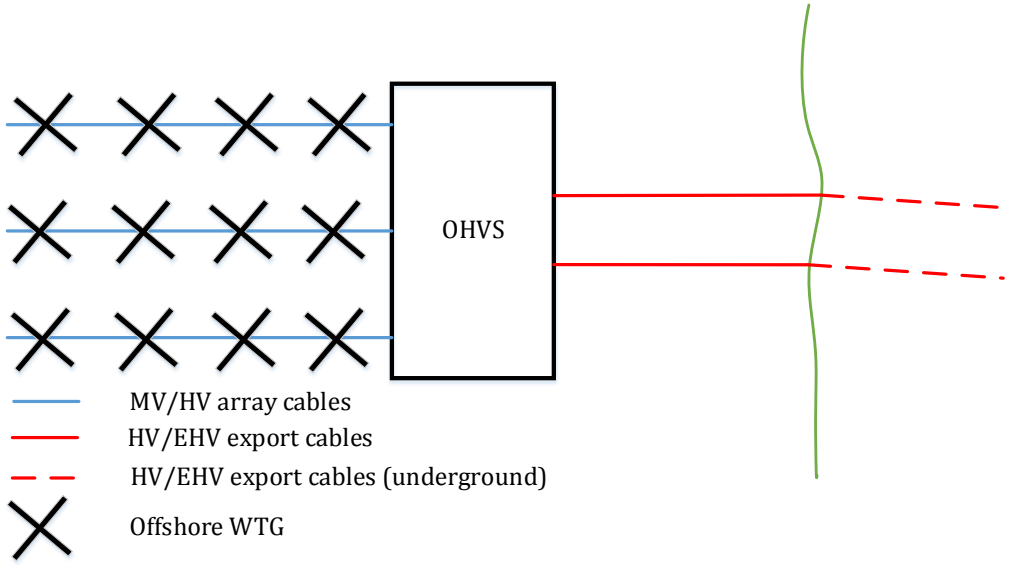

FIGURE 1.3: Indicative Drawing Showing Array Cables, OHVS and Connection to Shore via Two Export (High or Extra High Voltage, i.e. HV or EHV, Respectively) Cables [13].

An export cable may experience different installation conditions along the whole subsea route, i.e. from the OHVS up to the transition joint bay where the underground section typically begins. Although a thermally more favourable environment is expected in the main seabed section (due to the permanent presence of water), more adverse conditions are often met in

the landfall section, i.e. close to the beach, or close to the OHVS, where the export cables are upraised through J-tubes, being exposed to air conditions. Concerning the latter, only few meters of the entire cable length are employed within the J-tube: hence, the use of a separate, thermally more efficient cable, wouldn't be a reasonable choice. Regarding the former, one of the most acknowledged techniques to cross the beach zone is through Horizontal Directional Drilling (HDD). Despite HDD installations offering many advantages, such as the avoidance of sensitive, touristic beach crossings and the minimal environmental footprint, the increased depth of laying leads to worse cooling conditions for the cable. HDD sections are often fairly long: several hundreds of meters or even a few km in some cases are often required. Thus, it is more preferable to have a cable generating in total lower losses. Installing cables with non-magnetic armour is an increasingly common practice which is adopted in many projects to reduce the unwanted magnetic losses of the cable in HDD sections [11].

1.1.4 Current Rating

The thermoelectrical performance of the cable has to be considered carefully in the design of a cable system. The cable must fulfil several design requirements, amongst which two of the most important are the capability of dielectric material to withstand to a certain voltage gradient and the maximum permissible current carrying capacity. Although the former can be satisfactorily tested inside the high voltage laboratories, the latter is in general not tested or experimentally validated. Working Group B1.35 constituted by Cigré Study Committee B1 has provided a rather comprehensive and complete definition for current rating and it is reproduced herein verbatim: "*The topic of cable rating (or "cable current rating", "ampere capacity" or "ampacity") refers to the amount of current (in Ampères) a cable system can transmit without exceeding design limitations of the cable system at any position along the circuit.*" [14].

The main design limitation for AC cables is the maximum permissible operating temperature of the cable, typically defined by the maximum conductor temperature. This temperature limit has to be set such that the thermal degradation is not significant over the life of the cable, and to ensure that the mechanical properties of the insulation system are sufficient for the stresses imposed on it. XLPE has dominated for at least 30 years as the most cost efficient and reliable insulating material: the corresponding temperature limit is 90°C for the vast majority of cables. It is noted that insulating materials capable of operating under normal conditions at temperatures in excess of 100°C are being investigated [15].

The calculation of current rating requires the solution of a heat transfer problem: due to the losses generated inside an SL-Type cable, the conductor temperature will always be in an elevated temperature compared with local ambient. The rating calculation must assess the balance between heat generation inside the cable system and the transfer of this heat through

the cable components and away from it into its surroundings, determining the load at which the temperature limit on the cable might be exceeded [15].

The generation of losses within the cable constitutes a low-frequency electromagnetic problem that has to be considered in conjunction with heat transfer. In HVAC cables losses are generated not only due to the current carried by the conductor: owing to the alternated magnetic field induced by the currents flowing in the conductors, ohmic and potentially hysteresis (in cases that magnetic material is used for the armour) losses are also induced in the metallic parts of the cable. These extra heat losses along with the loss generated in the dielectric further contribute to the temperature rise of the conductor.

As it becomes apparent, achieving a higher current rating for given installation conditions can lead to an optimum cable design, thus a more cost-effective cable system. This becomes in its turn feasible by treating the two main components of current rating, namely the thermal and electromagnetic models, as accurately as possible. Although several simplifications had to be adopted in the past in order to implement current rating through hand calculations, powerful computers, implementing modern numerical techniques, such as Finite Element Method (FEM), can be used today to produce more accurate results. Hence, any likely margins of optimisation can be revealed and exploited, thus potentially contributing to the viability of modern OWFs.

1.2 Research Motivation

Three-core (3C) HVAC submarine cables constitute an essential part of OWF projects, which have grown rapidly in recent years as reported in [6]. No major technology change is expected in the basic components of these cables and they are likely to remain in use for some considerable time. Their current rating presently relies on methods that had initially been developed for cable geometries similar but not identical to modern submarine cables: the SL-Type, currently adopted by the IEC 60287-2-1 Standard [16], ignores certain components inherent to the modern cable design, such as the polymeric jacket applied over each core or different material besides lead in metallic sheaths. These new features substantially differentiate the thermal behaviour of the cable, leading to possible compromise in the accuracy of current rating calculations. Furthermore, larger cables are now necessary in order to meet the higher power demands required by the increasingly larger OWFs. Although the existing Standard methods are expected to be accurate enough for modest cable sizes and theoretically cover larger designs, their accuracy may become questionable when pushing the dimensions towards the extreme design limits. This is particularly true where validation tests were done several decades ago on very different cables to those in use today. For these reasons, a critical review of the existing thermal model of the cable interior is necessary.

The cost of a cable circuit is partly determined by the conductor size and is often crucial for the viability of OWF projects. To optimise the cable size, an accurate calculation of losses is required. Although magnetically armoured cables are usually used for the longest part of a subsea link, one of the possible thermal bottlenecks is usually at the point where the cable approaches the mainland, as discussed in Section 1.1.2. Non-magnetic armour is often employed in that section, due to lower induced losses. Although loss models with magnetic armour have already been extensively examined ([17], [18]), less work has been done for cables with non-magnetic armour. A key issue being raised is the size of modern OWF cables. The existing calculations make several simplifying assumptions when assessing induced losses, for instance that the current distribution in conductors is uniform when calculating sheath losses. These assumptions may be accurate enough for smaller and modest conductor sizes. However, they may not hold true when significantly larger conductor sizes are utilised. Hence, the origins of the existing formulation need to be investigated, while its applicability has to be checked in cables with larger conductor sizes.

As widely known in both the scientific and industry communities, cable losses are currently overestimated by the IEC 60287-1-1 Standard [16] for magnetically armoured cables in common use by windfarms. Since magnetic steel is considerably cheaper than non-magnetic alloys and due to its ease in manufacturing process, further design optimisation and cost reduction can be achieved if more realistic losses are predicted. By making the export cables more competitive, the overall cost of subsea interconnections can be further reduced, thus improving the viability of projects, such as OWFs. For this reason the Cigré B1 Study Committee has recently constituted WG B1.64 which deals with this issue. Although several models are already available ([17], [18], [19]) and suggest in general reduced armour loss, it still remains controversial to what extent the presence of the armour affects the conductor and sheath losses. The present IEC 60287-1-1 Standard suggests in certain cases empirical factors which are believed to be questionable when applied in SL-Type cables. The problem of calculating accurately cable losses becomes even more complex, since 3-D effects are present due to the twisted armour wires. The existing theoretical methods accounting for skin and proximity effects and allowing, in theory, for the physical representation of the armour, have to be carefully reviewed.

1.3 Contribution of this Thesis

In responding to the research motivation presented in Section 1.2, this thesis makes two significant contributions to the state of the art in the area of current rating in 3C HVAC submarine cables. Firstly, the Single-Core Equivalent Thermal Model (SCETM), currently used and adopted by the IEC 60287-2-1 Standard for the cable thermal representation, turns out to

provide insufficient accuracy in some cases: the results presented show that it may underestimate conductor temperature when larger cable sizes are considered. The existing SCETM is being improved in the present thesis taking into account of the modern cable geometry, as demonstrated in Chapter 3. This is achieved by applying powerful computational techniques, such as Finite Element Analysis (FEA), while a new analytical formulation is suggested, calculating more accurately the thermal resistance between power cores and the armour, namely T_2. By adopting this, improved, and more realistic SCETM, cable designing becomes more precise, while the derived temperatures now lie on the safe side. Besides the benefits afforded to the cable designer, deeper insight is given in the industry and scientific communities and a direction for updating the present Standard version is provided: the suggested SCETM is suitable for adoption by the current IEC 60287-2-1 Standard and improves its accuracy.

The second key contribution of this thesis is the improved loss formulae with respect to the electromagnetic model currently adopted by the IEC 60287-1-1 Standard for 3C HVAC submarine cables when non-magnetic armour is used. AC phenomena that are present in power frequency and expected to affect losses, such as skin and proximity effects, are simulated. Modern numerical methods having an analytical background, such as Filament Method (FM), are employed for this purpose, after being first thoroughly validated. It is found that the current distribution in phase conductors affects the losses induced in the metallic sheaths of the cable, particularly when larger conductor sizes are utilised. Reduced sheath losses are suggested by the methods used, thus potentially allowing engineers to optimise the cable design and further reduce its cost. Hence, the larger cables which are necessary to cover the increased power transfer demands of modern OWFs (as cited in section 1.1.1) can become even more competitive, thus contributing to the viability of the corresponding offshore projects. Although the techniques used in the present thesis are more accurate than the existing, traditional methods, they wouldn't be suitable for Standardisation purposes, because of their inherent complexity. For this reason, reductive, analytical factors, which may be easily multiplied with the existing IEC factors and provide more accurate results, are suggested in Chapter 5.

Besides the above two contributions, cable losses are investigated when magnetic armour is used, focusing on conductor and sheath losses. The potential extension of the existing numerical methods, such as Filament Method (FM), so as to account for the presence of magnetic entities is initially considered in Chapter 6. The existing FM formulation appears to have certain fundamental limitations and turns out to be insufficient to represent magnetic materials, despite having been used in the past for similar cables ([20], [21]). The Method of Images (MoI) is examined and the replacement of the magnetic armour by fictitious filaments is considered. Although MoI has been successfully applied in the past for pipe-type cables [22],

it proves to be inapplicable to SL-Type, wire armoured cable. Models employing 3-D Finite Element Method (FEM) are eventually developed and the effect of several design factors, such as the armour geometry and magnetic permeability, on conductor and sheath losses is quantified. The use of empirical factors presently suggested by international committees, such as the IEC or Cigré, is evaluated. Valuable modelling advice is provided, while the analytical models ([18], [17]) presently discussed by the Cigré WG B1.64 for potential use in the forthcoming Technical Brochure are benchmarked against the developed 3-D FE models.

The above contributions offer a significant step forward in the state of the art for 3C HVAC submarine cable rating calculations, while simultaneously providing useful and informative guidance on critical modelling aspects. Taken together, they will be of great value to both the cable and offshore industries in building and optimising the offshore grid of the future.

1.4 Thesis Structure

This Chapter provides the necessary outline about the role of 3C HVAC submarine cables used to interconnect OWFs to the mainland. It becomes clear that optimising the cable design is a prerequisite for the economic viability of OWF projects. The current-carrying capacity of the cable is the key-factor for this purpose: any likely overestimation in the ampacity potentially increases the total fixed costs, can make the cable installation under the sea rather difficult and technically challenging and renders the entire project less cost-effective; on the other hand, any likely underestimation in the ampacity potentially leads to excessive ageing of the cable asset and increases the possibility of premature failure, leading to the early repair of an expensive asset. It must be noted that repair costs in sections of a submarine cable link are often comparable to the cost required to replace the entire cable with a new one [11]. Given the capital constrained environment in which manufacturers and operators exist and act, obviously none of the above scenarios is desirable. The remainder of this thesis intends to address these concerns and looks for a golden ratio, such that the viability of subsea link projects is ensured with no compromise in reliability.

The necessary theoretical background is presented in separate Chapters to ensure a clear focus to each chapter. As noted in section 1.1.4, one part of the ampacity model is the heat transfer from the cable to its surroundings. A comprehensive review of the literature is undertaken and a summary of the key-findings is presented in Chapter 2, making focus on the cable interior and the Single-Core Equivalent Thermal Model (SCETM) presently used. The origins of the existing methods are traced and their potential use to modern submarine cables is considered.

Chapter 3 introduces an in-depth analysis of the existing formulation about the thermal resistance between the power cores and the armour, namely T_2. The existing T_2 formulation is

initially validated against FE models adopting equivalent assumptions for the thermal properties of the sheaths. Significant discrepancies between the 2-D FE models and the existing T_2 formula are noticed as soon as more realistic assumptions are adopted, particularly increasing the core diameter. The key-design factors affecting T_2 are identified and a parametric analysis is made, intending to suggest an improving T_2 formula. The thermal impact of the modified SCETM is then assessed. Useful guidelines are given at the end of the Chapter around the modelling of extruded fillers, which are increasingly used in modern cables.

The second part of the ampacity model, i.e. the electromagnetic model used to calculate the generated losses, is the main objective of the following Chapters. A thorough literature review is undertaken in Chapter 4, paying attention to the assumptions adopted by the existing methods. Possible weak points are identified for cables with both non-magnetic and magnetic armour. Alternative methods, already presented in the literature, are examined for potential use in loss calculation. The main principles of Filament Method (FM) are presented, including a critique on several aspects of the existing versions.

Chapter 5 presents numerical methods for the analysis of cables employing non-magnetic armour, which are often used in thermally unfavourable environments. Since the armour loss itself is expected to be fairly low, the focus shifts to sheath losses: the results obtained demonstrate that the existing calculation methods may overestimate significantly the losses induced in the sheaths, especially for larger cable sizes. By using FEM and FM models, a parametric analysis is made and the key-design factors affecting sheath losses are identified. Appropriate Reductive Factors, improving the existing methods accuracy, are finally suggested for Standardisation purposes.

Cables being armoured with magnetic wires are the main object of Chapter 6, focusing on conductor and sheath losses. The potential extension of the existing FM formulation, in order for this to account for the presence of magnetic entities is initially discussed. The main principles of the Method of Images (MoI) are also presented, emphasising on its applicability to SL-Type cables. Both methods seem to be insufficient to include the effect of the magnetic armour, thus ruling out their use for loss calculation. In the last part of this Chapter, 3-D FE models are developed, highlighting some crucial modelling aspects and parameters. Comparisons against existing analytical methods are made and interesting conclusions are deduced. The final Chapter summarises the work done, highlights the benefits gained from it and recommends areas meriting further research around the several topics discussed.

Chapter 2 Current Rating for 3C Submarine Cables: Present Practice

The necessity of estimating the current-carrying capacity of electrical systems in order to improve their safety and reliability has motivated numerous research efforts for the establishment of standardised thermal computation methods since the advent of electricity in the late 19th and the early 20th centuries. The works published by Forbes [23] and Kennelly ([24],[25]) are of the earliest ones and treat the problem of current rating in a semi-empirical way, including theoretical calculations and experimental measurements. Although the analogy between the flow of electric current and the flow of heat had been well known long before 1957, Neher & McGrath put effectively all of the ampacity principles into a single, comprehensive paper, which also formed the basis for modern ampacity standards [26].

This chapter seeks to identify the key issues related to the thermal model currently used for 3C submarine cables for Steady-State conditions. The origins of the existing thermal model are investigated, while its potential applicability to modern submarine cables is considered. Although the representation of cable surroundings is also briefly discussed, focus is made on the cable interior.

2.1 Heat Sources in Submarine Cables

In conventional thermal models, cables are treated as sources of heat, which has to be dissipated firstly through the inherent cable components and eventually through the direct surroundings to the infinite environment. Depending on cable construction and installation conditions, there may be a number of sources generating heat losses inside the cable. In general, there are two types of losses generated in the cable interior: current-dependent losses and voltage-dependent losses.

In terms of submarine applications, the vast majority of High Voltage Alternating Current (HVAC) cables intended to interconnect Offshore Wind Farms (OWFs) with the mainland consist of three cores laid up in an assembly that is covered by an armour layer. A typical submarine cable geometry is illustrated in Figure 2.1. Due to the separate Lead (SL) sheath mostly used in export cables, this cable is also referred to as SL-Type.

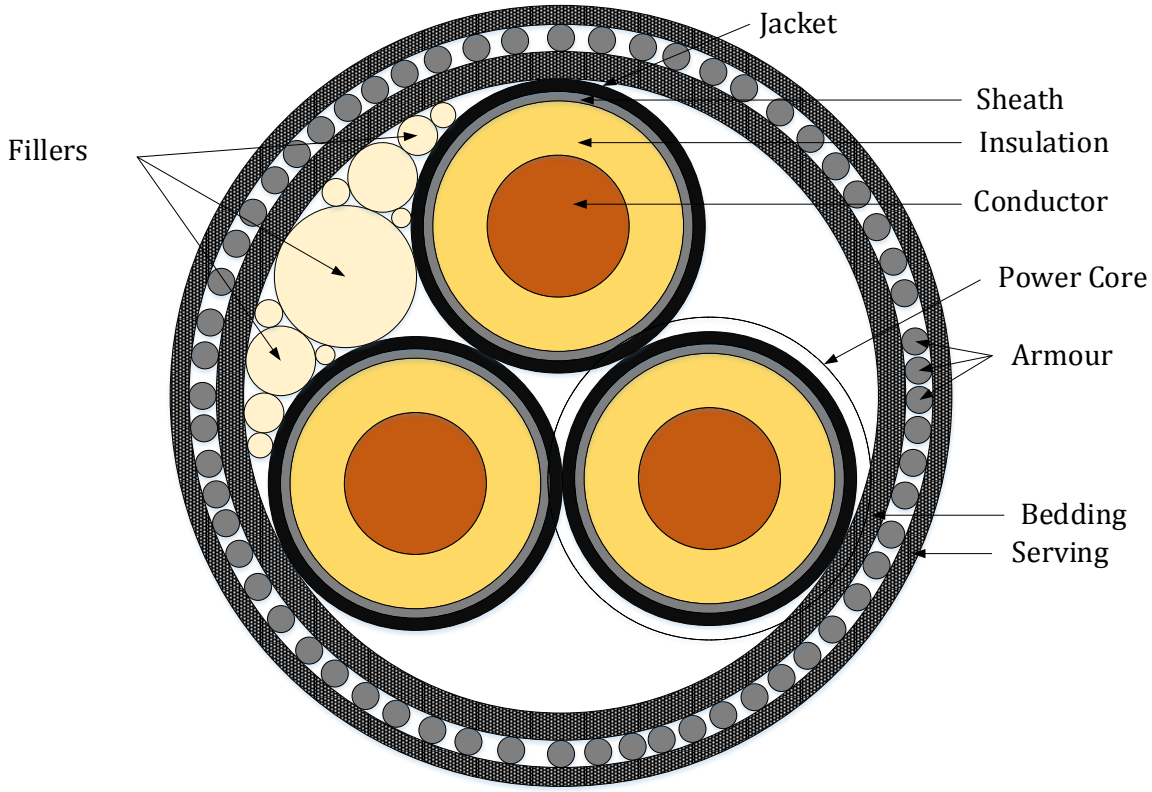

FIGURE 2.1: 'Typical' Modern HVAC 3C Submarine (SL-Type) Cable Geometry.

Each core consists of its conductor, insulation, metallic sheath or screen[2] and non-metallic jacket. Either solid or extruded fillers are applied in the interstices between cores, in order to give a round shape in the entire three-core assembly. Extruded fillers include explicit gaps filled with air or water, depending on the point of the cable route. Although solid fillers usually consist of polypropylene ropes and some tiny gaps might theoretically exist, they are well compacted in practice. Bedding and serving layers, consisting in most cases of polypropylene yarns, are then concentrically applied.

Current-dependent losses refer to the heat generated in metallic cable components; namely, the conductor, sheath or screen and armour. Perhaps the most significant of the electrical losses is the Joule loss which occurs due to the electrical resistance of the conductor, namely W_C (W/m). The conductor resistance leads to a reduction in electron energy as current flows in it, with this energy being dissipated as heat. The magnitude of W_C is easily defined using the following formula:

$$W_C = {I_C}^2 R_{AC} \tag{2.1}$$

[2] Metallic screen usually refers to a construction consisting of one or more tapes, or a braid, or a concentric layer of wires or a combination of wires and tape(s), mostly helically applied. On the other hand, metallic sheath typically refers to a continuous layer which constitutes a reasonably tight-fitting seamless tube [100].

where I_C is conductor current (A) and R_{AC} is conductor AC resistance (Ω/m). R_{AC} depends on conductor DC resistance, R_{DC}, at operating temperature (Ω/m), as well as skin and proximity effects inevitably occurring in power frequency. Except for pipe-type cables, the following formula is suggested by IEC 60287-1-1 [16] for any other cable type, including SL-Type:

$$R_{AC} = R_{DC}(1 + y_s + y_p) \tag{2.2}$$

where y_s and y_p is the skin and proximity effect factor, respectively. Appropriate calculation procedures pertaining to y_s and y_p, which take into account of a lot of different factors (conductor material, detailed structure), are referred to [16], while more details are presented in Chapter 4, since the present chapter focuses on the thermal model adopted by IEC.

The second set of current dependent losses is metallic sheath or screen loss, W_S (W/m), which occurs through circulating currents being induced in the metallic cable sheath, and through eddy current losses owing to the skin and proximity effects. These losses are defined according to the formula presented below:

$$W_S = \lambda_1 W_C \tag{2.3}$$

where λ_1 is the so called sheath loss factor that represents the proportion of the metallic sheath or screen losses with reference to the conductor losses. λ_1" and λ_1' refer to the eddy and circulating current loss factor, respectively, while it is $\lambda_1 = \lambda_1" + \lambda_1'$. λ_1" is considered negligible by the current IEC Standard for solid bonding systems, such as the case of submarine cable systems. Regarding the circulating current loss factor, this is calculated based on the formula:

$$\lambda_1' = \frac{R_S}{R_{AC}} \frac{1}{1 + \left(\frac{R_S}{X_S}\right)^2} \tag{2.4}$$

where R_S is the resistance of sheath per unit length (pul) of cable (Ω/m) and X_S is the reactance pul of sheath (Ω/m), i.e.:

$$X_S = 2\omega 10^{-7} \ln\left(\frac{2s}{d}\right) \tag{2.5}$$

where ω is the angular frequency of the current waveform (rad/s), s is the distance between conductor axes (mm) and d is the mean diameter of sheath (mm). It must be noted that (2.4) is to be multiplied by a factor 1.5 when the armour is made of ferromagnetic material, thus accounting for its magnetic effect on λ_1'.

The third part of current dependent losses is the armour loss, W_A (W/m), which occurs through likely circulating currents being induced in the metallic armour, and through eddy current losses owing to the skin and proximity effects. Moreover, in the case of armour made from

ferromagnetic material, hysteresis losses are also generated and must be included in current rating calculations. The relevant formula is presented below:

$$W_{\mathrm{A}} = 3\lambda_2 W_{\mathrm{C}} \tag{2.6}$$

where λ_2 is the so-called armour loss factor that represents the per core proportion of the armour loss with reference to the total conductor losses. The current IEC Standard version suggests the following formula for the armour loss factor when SL-Type cables are considered with magnetic armour:

$$\lambda_2 = 1.23\frac{R_{\mathrm{A}}}{R_{\mathrm{AC}}}\left(\frac{2c}{d_{\mathrm{A}}}\right)^2 \frac{1}{\left(\frac{2.77R_A \cdot 10^6}{\omega}\right)^2 + 1}\left(1 - \frac{R_{\mathrm{AC}}}{R_{\mathrm{S}}}\lambda_1'\right) \tag{2.7}$$

where R_{A} is the AC resistance of the armour (Ω/m) at operating temperature, c is the distance between the axis of a conductor and the cable centre (mm), d_{A} is the mean diameter of armour (mm). It should be noted that λ_2 calculated per (2.7) is referred to many, recently published works ([18], [17], [27]) as overestimating the armour losses.

Conductor resistance, R_{AC}, λ_1 and λ_2 factors are considered as suggested by IEC 60287-1-1 [16] in the context of the present Chapter, since its objective is limited to the thermal aspect of ampacity. Although certain of them may not be realistic enough, such as the overestimated λ_2 factor, no difference is expected because of that when studying the thermal model of an SL-Type cable. In other words, whatever the losses are, these are to be dissipated through the same heat paths, i.e. the cable interior and its surroundings. Discussion in more detail around the induced losses generated inside the cable is made later on, starting from Chapter 4.

Finally, heat is generated due to the fact that in reality no electrical insulator is perfect and a leakage current always takes place through the insulation layer. Therefore, the cable core acts as a cylindrical capacitor with a capacitance C (F/m) and a finite resistance R (Ωm). This kind of losses is strongly dependent on voltage, and can be defined by the following formula.

$$W_{\mathrm{D}} = \omega C U_o^2 tan\delta \tag{2.8}$$

where W_{D} is the dielectric loss (W/m), U_0 is the phase-to-ground voltage applied (V) and tanδ represents the tangent of the dielectric loss angle.

2.2 Heat Transfer in Submarine Cables: IEC 60287

The way heat is dissipated, firstly through the cable interior and then through the direct surroundings, forms a heat transfer problem, quite complex in reality. Thanks to the resemblance of Fourier's Law with Ohm's Law, conductive heat transfer can be represented by

a thermal circuit with lumped parameters under certain circumstances. This thermal circuit along with the relevant ampacity equation for SL-Type cables with jacketed cores are first presented in this section. Then, emphasis is given on the representation of the cable interior and the corresponding thermal resistances. Thanks to the cylindrical geometry of most of the cable components, 1-D analysis may be adopted, i.e. assuming that temperature gradients exist only in the radial direction. This can be directly applicable to insulation, jacket and serving layers. However, strictly analytical solutions to heat transfer equations are not available when treating non-cylindrical geometries, such as the fillers applied in between the power cores. In this case, semi-empirical formulae are adopted by the IEC Standard. Finally, the formulae used to represent the cable surroundings are briefly presented at the end of this section for the sake of completeness.

2.2.1 Cable Ampacity and Thermal Circuit for SL-Type Cables

The sources of heat inside the cable are briefly presented in section 2.1. Assuming that all the metallic parts are isothermal volumes, the only thermal impedance to this heat comes from the non-metallic parts of the cable, as well as its surroundings. Each lumped, thermal resistance is considered between two temperature nodes: the thermal resistance of insulation, T_1 (Km/W), is defined between conductor and sheath temperatures, i.e. θ_C and θ_S (°C), the thermal resistance of jacket, T_{2j} (Km/W), between sheath and jacket temperatures, i.e. θ_S and θ_J (°C), the thermal resistance of fillers and bedding, T_2 (Km/W), between jacket and armour temperatures, i.e. θ_J and θ_A (°C), the thermal resistance of serving, T_3 (Km/W), between armour and cable surface temperatures, i.e. θ_A and θ_e (°C), and, finally, the thermal resistance of soil (the so called "external thermal resistance"), T_4 (Km/W), is confined between cable surface and local ambient temperatures, i.e. θ_e and θ_{amb} (°C). This thermal network is illustrated in Figure 2.2, assuming Steady-State conditions (no heat storage happens). From θ_C up to θ_J all heat sources and thermal resistances are multiplied and divided by 3, respectively, due to the Single-Core representation. The heat sources are introduced as the thermal analogues of current sources in an electrical circuit. W_C, W_S and W_A are located at the corresponding temperature nodes, while W_D is assumed to be injected in the middle of T_1.

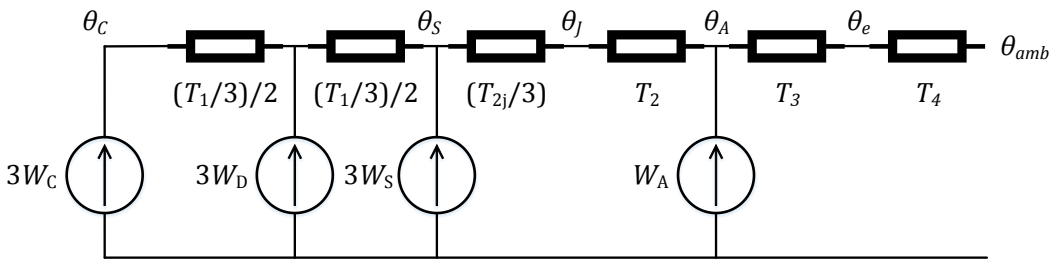

FIGURE 2.2: An Illustration of the Thermal Circuit Representing the SCETM Implied by IEC 60287.

The fundamental formula currently used by IEC 60287-1-1 [16] to calculate the permissible current rating in SL-Type cables is adopted by Anders in [28], though properly modified so as to account for the thermal resistance of jacket over each core. This is used in the present thesis, is consistent with the thermal circuit shown in Figure 2.2 and presented in (2.9).

$$I = \left[\frac{\Delta\theta - W_{\mathrm{D}}\left[0.5T_1 + T_{2\mathrm{j}} + n(T_2 + T_3 + T_4)\right]}{R_{\mathrm{AC}}T_1 + nR_{\mathrm{AC}}(1+\lambda_1)\left((T_{2\mathrm{j}}/n) + T_2\right) + nR_{\mathrm{AC}}(1+\lambda_1+\lambda_2)(T_3+T_4)} \right]^{0.5} \tag{2.9}$$

where $\Delta\theta = \theta_{\mathrm{C}} - \theta_{\mathrm{amb}}$ is the conductor temperature rise above local ambient (K), n is the number of load carrying conductors in the cable (n = 3 for 3C cables). $T_{2\mathrm{j}}$ is separately defined in the above analysis: this practice is also adopted by Anders [28] and suggested by the draft Technical Brochure (TB) prepared by the Cigré WG B1.56 [29], [30]. However, some other, recently published works, such as that by Ramirez [31], suggest that the thermal resistance of jackets is merged with T_2, which should be now defined between θ_{S} and θ_{A}. In such a case, a uniform material between sheaths and armour is assumed and $T_{2\mathrm{j}}$ is nulled in (2.9).

2.2.2 Cylindrical Geometries in Cable Interior

The generic Heat Diffusion Equation expressed in cylindrical coordinates is:

$$\frac{1}{r}\frac{\partial}{\partial r}\left(kr\frac{\partial\theta}{\partial r}\right) + \frac{1}{r^2}\frac{\partial}{\partial\varphi}\left(k\frac{\partial\theta}{\partial\varphi}\right) + \frac{\partial}{\partial z}\left(k\frac{\partial\theta}{\partial z}\right) + \dot{q} = DC_{\mathrm{p}}\frac{\partial\theta}{\partial t} \tag{2.10}$$

where k is the thermal conductivity (W/(Km)) of the medium (which is in general spatially dependent), $\theta(r,\varphi,z)$ is the temperature at point (r,φ,z), $\dot{q}$ is the rate at which energy is generated per unit volume of the medium (W/m^3), D and C_{p} is the density (kg/m^3) and the specific heat (J/(kg·K)) of the medium, respectively. What (2.10) actually implies is an expression of the Energy Conservation Principle, i.e. that at any point in the medium the net rate of energy transfer by conduction into a unit volume plus the volumetric rate of thermal energy generation must equal the rate of change of thermal energy stored within the volume. For Steady-State conditions, assuming no heat generation and accounting for the radial direction only, (2.10) becomes:

$$\frac{1}{r}\frac{d}{dr}\left(kr\frac{d\theta}{dr}\right) = 0 \tag{2.11}$$

where the partial derivative has been replaced by the ordinary derivative. According to Fourier's Law:

$$q_r = -k\frac{d\theta}{dr} \tag{2.12}$$

where q_r is the radial heat flux, i.e. the heat transfer rate in the r direction per unit area perpendicular to the direction of transfer (W/m^2). Assuming a cylindrical ring as that illustrated in Figure 2.3, (which might be the insulation layer of a power core), the area perpendicular to the direction of transfer (m^2) is $A = 2\pi r L_C$, where L_C is the length of the cylinder (m). The temperature distribution inside the ring area may be determined by solving (2.11) and applying appropriate boundary conditions. Assuming a uniform material, thus constant thermal conductivity k (which is the case in the insulation layer), (2.11) may be integrated twice to obtain the general solution:

$$\theta(r) = C_1 \ln(r) + C_2 \tag{2.13}$$

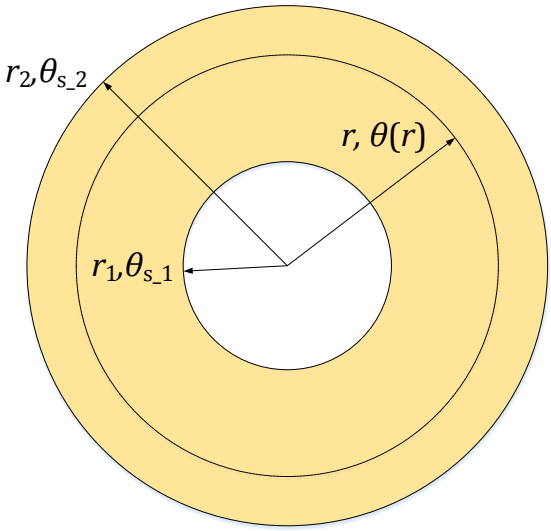

FIGURE 2.3: An Indicative Cylindrical Ring Representing the Insulation Layer of a Power Core.

The constants of integration C_1, C_2 may be obtained by exploiting the corresponding boundary conditions, i.e. $\theta(r_1) = \theta_{s\_1}$ and $\theta(r_2) = \theta_{s\_2}$. Applying these to (2.13) a system of order 2 x 2 occurs. Solving for C_1, C_2 and substituting into (2.13), (2.14) is deduced.

$$\theta(r) = \frac{\theta_{s\_1} - \theta_{s\_2}}{\ln\left(\frac{r_1}{r_2}\right)} \ln\left(\frac{r}{r_2}\right) + \theta_{s\_2} \tag{2.14}$$

Using (2.14) back into Fourier's Law, i.e. (2.12), this becomes as in (2.15).

$$q_r = \frac{Q}{2\pi r L_C} = -k\frac{d\theta}{dr} = k\frac{\theta_{s_1} - \theta_{s_2}}{\ln\left(\frac{r_2}{r_1}\right)} \cdot \frac{1}{r} \Longrightarrow \frac{\theta_{s_1} - \theta_{s_2}}{Q} = \frac{\ln\left(\frac{r_2}{r_1}\right)}{2\pi L_C \cdot k} \tag{2.15}$$

where Q is the heat power (W) conducted across the ring thickness. The term on the left side at the last equation of (2.15) expresses an impedance to heat flow (K/W) and may be considered equivalent to the way an electrical resistor impedes current flow (temperature is

the thermal analogue of electric potential, while heat flow is the thermal analogue of electric current) [32].

IEC 60287-2-1 [33] takes advantage of this cylindrical geometry and a SCETM is suggested to represent most of the non-metallic layers involved in an SL-Type cable. By multiplying by L_C both sides of the last equation of (2.15), the relevant thermal resistance per unit length (pul) of the cable (Km/W) may be defined as suggested by [33] and shown in (2.16).

$$T_i = \frac{\rho_i}{2\pi} \ln\left(1 + \frac{2t_i}{d_{\text{under}}}\right) \tag{2.16}$$

where ρ_i is the reciprocal of thermal conductivity k, namely the thermal resistivity of the i-th material (Km/W), $t_i = r_2 - r_1$ is the thickness of the i-th layer (mm) and $d_{\text{under}} = 2r_1$ the diameter beneath it (mm). As discussed in section 2.2.1, index i can be 1, 2j or 3, depending on the cylindrical layer considered (insulation, jacket or serving, respectively).

Although the thermal resistance of the metallic parts is not equal to zero, the corresponding temperature rise because of their impedance to radial heat flow is assumed so low, that they are usually neglected in rating calculations. Indeed, owing to their small thickness and the assumption that heat flow is radially dissipated, i.e. that θ_{s_1} and θ_{s_2} in Figure 2.3 are isotherms, no significant thermal resistance is expected. However, the thermal profile inside the three-core cable is not actually radial, due to the close physical proximity of power cores. In other words, the thermal field induced by each power core is expected to be distorted by those from the neighbouring ones and vice versa; hence, the Principle of Superposition is not anymore applicable and, as a result, θ_{s_1} and θ_{s_2} in Figure 2.3 are not isotherms in reality. Moreover, it seems a bit strange that similar cable geometries are treated in a different way by IEC 60287-2-1: correction factors are adopted for T_1, T_3 thermal resistances for three single-core cables in touching trefoil formation. Anders states that these factors are used to account for the circumferential heat conduction taking place when three cores are touching each other [34].

2.2.3 Non-Cylindrical Geometries in Cable Interior

The problem of evaluating the thermal resistance of non-cylindrical geometries, such as that of fillers and bedding inside a 3C submarine cable, is not so straightforward, due to the absence of rigorous analytical formulae.

Most of the works published date back to the early 1900's and deal with similar but not identical geometries to those of modern submarine cables. Belted cables, which consist of three conductors being filled with paper insulation and enclosed by a common sheath (Figure 2.4), were of high interest in those years. Due to the absence of separate Lead sheaths over each core, the entire domain from the conductors up to the inner surface of the common sheath is

represented by a single thermal resistance, namely insulation thermal resistance, T_1. This is justified by the quite similar thermal properties of the individual domains: core insulation, filler and belt layers were composed of paper-based materials, which have a thermal resistivity of around 6 Km/W according to IEC 60287-2-1 [33]. The general method for calculating T_1 calculation is of the form:

$$T_1 = \frac{\rho_t}{2\pi} G \tag{2.17}$$

where ρ_t is the thermal resistivity of core insulation, fillers and belt (Km/W) and G a geometric factor, graphically derived.

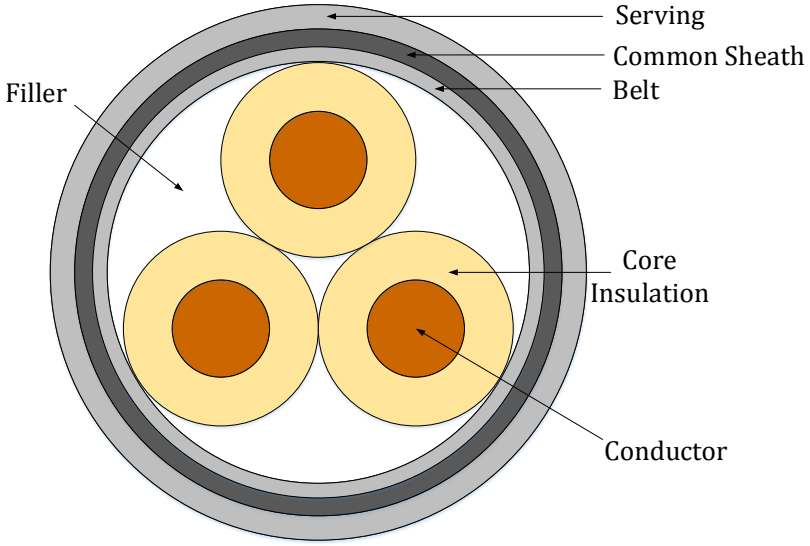

FIGURE 2.4: Indicative Geometry for Belted Cables.

Several methods intended to evaluate G in semi-empirical ways are reported in the literature. One of the earliest works is that by Mie [35] in 1905: due to mathematical difficulties arising in the case of the original geometry (Figure 2.4), Mie replaced the actual conductors by auxiliary, deformed geometries that could represent more realistically the distribution of the isothermal contours inside the cable. A theoretical formula for G was derived based on this deformed geometry. Several years later, in 1923, Simons reviews in [36] all the previously existing formulae around G: Mie formula appears to provide the most sensible results amongst others, such as Russell's theoretical formulas [37], and also stands quite close to the experimental data provided by Atkinson [38]. Simons suggests another semi-empirical formula, which appears to improve that previously proposed by Mie, by correcting the relevant errors due to the deformed geometry assumed.

Since the advent of polymeric insulated cores, the thermal properties of core insulation and fillers have been substantially different: polypropylene, having a thermal resistivity similar to that of paper (6 Km/W is suggested in IEC 60287-2-1 [33]) is often used in fillers, whereas

XLPE with 3.5 Km/W according to [33] is used for core insulation. IEC 60287-2-1 has adopted an approximating formula published by Anders [39] to account for the different material thermal properties, which is derived based on Finite Element Method (FEM).

In order to provide a uniform electric field around the power cores, individual metallic screens were added later over each core. Screening reduces the thermal resistance of a cable by providing additional heat paths along the screening material of high thermal conductivity, in parallel with the path through the dielectric. A *screening factor* is additionally used by IEC 60287-2-1 in (2.17) for this purpose. Anders suggests an even more accurate semi-empirical formula in his work [40], again based on FEM simulations, while assuming the metallic screens are isotherms.

Although many works have been published regarding T_1 calculation in 3C belted cables, as discussed above, considerably less publications exist in terms of T_2 calculation for 3C SL-Type cables. The T_2 formula currently used by IEC 60287-2-1 [33] is:

$$T_2 = \frac{\rho_{\text{fb}}}{6\pi} G \tag{2.18}$$

where ρ_{fb} is the thermal resistivity of fillers and bedding domains (Km/W) (assuming they are made of the same material), while a graph for G is provided by IEC 60287-2-1 and shown in Figure 2.5. In the case of non-touching sheaths, equal thicknesses of material between sheaths and between sheaths and armour are assumed. In both cases, variable X expresses the thickness of material between sheaths and armour as a fraction of the outer diameter of the sheath. Analytical equations are also given by IEC 60287-2-1 [33] to fit the relevant curves, depending on X.

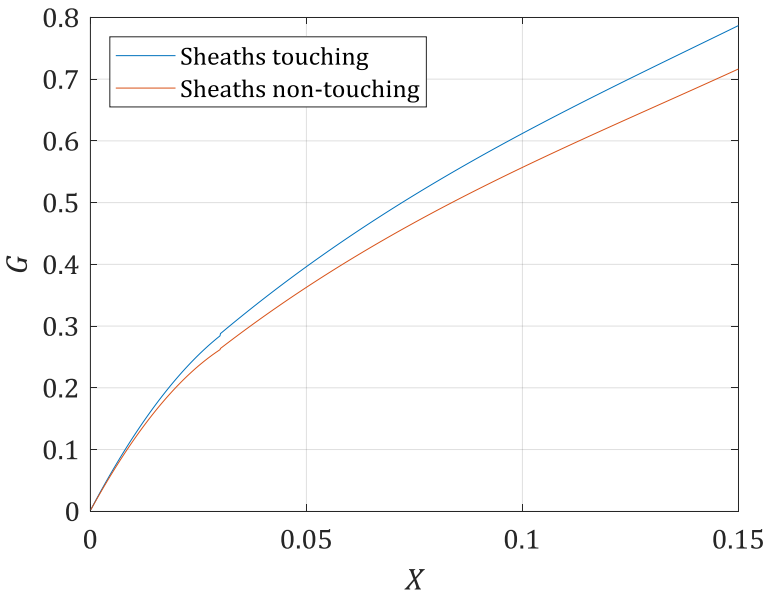

FIGURE 2.5: Geometric Factor G for T_2 Calculation (2.18) According to IEC 60287-2-1 [33].

Unfortunately, no reference is made by IEC 60287-2-1 to SL-Type cables with jacketed cores. Two different interpretations of the G curves shown in Figure 2.5 can be made for SL-Type cables with jacketed cores. The lower curve (sheaths non-touching) could be, at first glance, considered applicable. T_2 represents in this case the domain between sheaths and armour, assuming that both of them are isotherms. In this case, jacket resistance, T_{2j} should be nulled in (2.9), since the thermal resistance of jacket is now included in T_2. However, jackets are normally made of material with different thermal properties compared with the filler. Adopting another perspective, the upper curve (sheaths touching) could also be used, by extending the isothermal assumption over the outer surface of jackets (thus 'jacket touching'). In that case, T_{2j} remains non-zero and is calculated according to (2.16). Depending on the interpretation made, different definitions in terms of X can be given, as described by (2.19) and (2.20).

$$X_{\text{touch}} = \frac{t_{\text{j\_ar}}}{D_{\text{j}}} \tag{2.19}$$

$$X_{\text{non\_touch}} = \frac{t_{\text{j\_ar}} + t_{\text{j}}}{D_{\text{s}}} \tag{2.20}$$

where X_{touch}, $X_{\text{non\_touch}}$ refers to the upper, lower curve, respectively, (Figure 2.5), $t_{\text{j\_ar}}$ is the thickness of material between the external surface of jackets and the internal surface of armour (mm), t_{j} is the jacket thickness (mm), D_{s} and D_{j} are the outer diameters over the sheath and jacket (mm), respectively. These definitions become even clearer by considering the geometry illustrated in Figure 2.6.

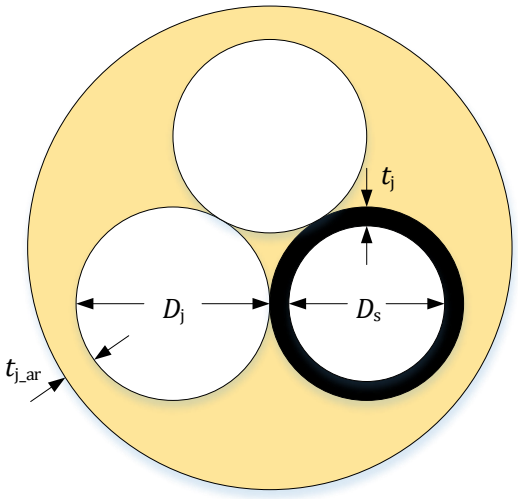

FIGURE 2.6: A Typical Three-Core Geometry where D_{j}, $t_{\text{j\_ar}}$ and D_{s} , t_{j} Are Depicted.

The geometrical method used to define G in (2.18) dates back to 1923 and was developed by Wedmore in Appendix IV of a report presented by Melsom [41]. As in the work published by Simons, Mie's and Russell's theoretical formulae are also reviewed in [41]: they appear to give

results significantly diverging from experimental values (relative errors 7 - 29%), although Mie's formula provide relatively slightly better results. Wedmore adopts Russel's formula, because of its greater simplicity, and introduces a geometrical method in order to correct the errors observed between theoretical and experimental values. Hence, relative errors not exceeding 3% are finally reported in [41].

The problem of defining the thermal resistance of non-cylindrical geometries in 3C geometries was undoubtedly complicated in the first two decades of 1900. Earlier researchers, such as Mie and Russel, had to calculate and draw the exact distribution of isothermal contours and heat flow lines so as to obtain some representation of the actual thermal field. Hence, several simplifying assumptions were necessary and inevitable, which at the same time introduced some considerable amount of error. Later researchers, such as Simons and Wedmore, attempted to correct this error by means of semi-empirical methods, such as Wedmore's geometrical method. These improved methods are reported to provide good results against experimental works when benchmarked for the cables considered in those years: belted cables with a geometry similar to that shown in Figure 2.4 are implied. They consisted of common sheath, enclosing three unscreened phase conductors. In such a case, the thermal resistance of the dielectric is more uniformly distributed around the three phase conductors. However, these methods are likely to lack in accuracy if applied to modern 3C submarine cables: the introduction of separate lead sheaths over each core is expected to induce a different, less uniform thermal field inside the cable.

In modern SL-Type cables the thickness t_{j_ar} does not typically vary immensely and is kept relatively small, since the main purpose of the bedding is to prevent the armour from causing any mechanical damage on the power cores. At the same time, D_j may vary considerably, especially now that larger export cables are needed to cover the higher power demands of OWFs. Thus, X_{touch} gets smaller and so does T_2, based on Figure 2.5 and (2.18), although t_{j_ar} might be kept nearly constant in such as case. This may look strange at first glance: let's assume two cables with the same thickness t_{j_ar} and $D_{j,2} > D_{j,1}$, as illustrated in Figure 2.7. At the same time, a constant $\Delta\theta = \theta_J - \theta_A$ is considered on the boundaries of the relevant T_2. $T_{2,2}$ will be lower than $T_{2,1}$, although t_{j_ar} is kept unchanged.

The smallest part of T_2 is mainly concentrated around the areas between the power cores and the bedding, closer to the outer edge of the power cores. These areas, illustrated with the blue smaller ellipses in Figure 2.7, contribute more to the total T_2, since higher temperature gradients are expected across them: thus, the relevant local heat flow and thermal resistance, Q_{Short_Path} and $T_{2\_Short\_Path}$, will be higher and lower, respectively. On the other side, less heat will pass via the bigger blue elliptical domains shown in Figure 2.7, because they are relatively thicker and, as a result, lower temperature gradients will be present there: thus the relevant

local heat flow and thermal resistance, $Q_{\text{Long\_Path}}$ and $T_{2\_\text{Long\_Path}}$, will be lower and higher, respectively. The total T_2 may be considered equal to the parallel combination of $T_{2\_\text{Short\_Path}}$ and $T_{2\_\text{Long\_Path}}$ and this will be obviously lower than the lowest term, i.e. $T_{2\_\text{Short\_Path}}$. However, by increasing D_j, $T_{2\_\text{Short\_Path}}$ becomes even lower: although t_{j_ar} remains unchanged, more heat paths of nearly equal lengths are in parallel added, because of the increased core circumference. Thus, the total T_2 eventually decreases and the concept behind Figure 2.5 and (2.18) makes sense.

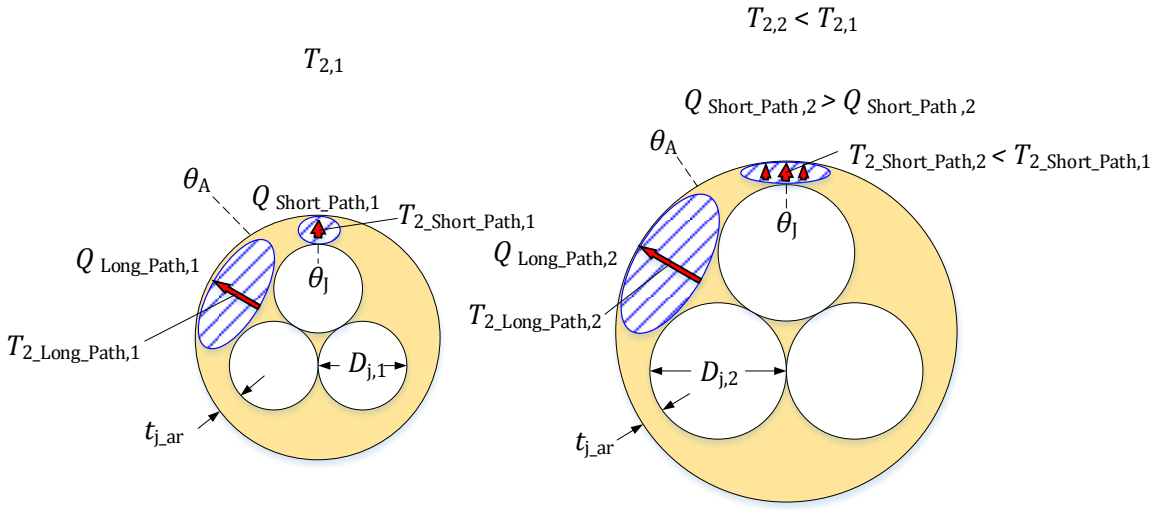

FIGURE 2.7: Two Cases Under Consideration Having Different D_j, though Equal t_{j_ar}.

The assumption made to compare these two cases is that a constant $\Delta\theta = \theta_J - \theta_A$ is considered, i.e. that θ_J, θ_A are constant and that the temperature distribution is uniform along the circumference of each core. This is in reality not true: higher temperature values are expected towards the cable centre and lower at the outer edges of the cores, where the cable is better cooled. In particular, even more non-uniform distributions are expected in larger cables with increased D_j. $T_{2\_\text{Long\_Path}}$ has a minor contribution when the cores are considered isothermal, since the same, constant $\Delta\theta$ is applied on its ends, as that applied on $T_{2\_\text{Short\_Path}}$. However, $T_{2\_\text{Long\_Path}}$ is expected to come more into play when non-uniform temperature distribution is considered above the cores, thus making the heat dissipation through the entire filler and bedding domain even worse and the curves shown in Figure 2.5 potentially optimistic. In the above analysis (2.19) and the upper curve in Figure 2.5 are considered, i.e. the isothermal assumption is extended over the outer surface of jackets (jacket touching). It is noted that similar results would occur if (2.20) and the lower curve in Figure 2.5 were considered. In both cases, the finite thermal conductivity of the sheaths makes them non-isothermal, thus leading to non-uniform thermal profiles along them, which are also reflected in the surface over the cores.

Proceeding with the origins of (2.18) and its relation to belted cables, a single thermal resistivity was employed to represent their dielectric, which included both the core insulation and filler material. Modern 3C submarine cables very often involve fillers with different thermal properties in comparison with core insulation, or the jacket over the sheath. Cable geometries including Copper screened cores are closer to that of an SL-Type cable and these are analysed by Anders [40], as already cited. However, the assumption of the isothermal Copper screen surfaces adopted in [40] may be questionable in SL-Type: Lead has a thermal conductivity one order of magnitude lower than Copper. Furthermore, the thickness of these screens can be even 10 times lower than that of Lead sheaths. This is a geometrical parameter expected to affect the circumferential heat transfer along the sheaths. For these two reasons, the formulae referred to [40] cannot be applicable to SL-Type cables.

More recently, Ramirez suggests in [31] empirically derived (based on FE models) G_{FEA} formulae that could be used to replace the existing G in (2.18) in order to account for the presence of the jacket above each core in SL-Type cables. Although Ramirez addresses the issue of different material properties between jackets and fillers, the metallic sheaths are still treated as isotherms in [31]. A relative error of 2% in terms of conductor temperature is cited because of that, *based on extensive validation cases*. Although 2% looks at first glance a fairly low relative difference, this might be critical if translated in an absolute difference of a few °C, which could occur in practice in certain extreme cases: for instance, if 89.9°C is theoretically calculated instead of 92.1°C in reality expected. Moreover, the thermal resistances of the cable interior have a minor effect on conductor temperature when the cable is buried and T_4 is considerable, but become of major importance when the cable is installed in air conditions, e.g. in J-tubes, or laid unburied on the seabed: in such cases T_4 becomes substantially lower and some change in T_2 has stronger impact on conductor temperature. Unfortunately, no additional information is provided by Ramirez about how representative this 2% is with reference to specific installation conditions.

2.2.4 Cable Surroundings

The current carrying capacity of cables depends to a large extent on the thermal resistance of the medium surrounding the cable. For cables buried underground, this resistance accounts for more than 70% of the temperature rise of the conductor. The so called "*external thermal resistance*" or T_4 in (2.9) depends on several parameters, such as the thermal characteristics of the soil, the diameter of the cable, the depth of laying and on the thermal field induced by adjacent cables [34].

In order to derive an analytical formula for T_4 certain simplifying assumptions are necessary. The thermal resistivity of soil is considered unaffected by the temperature and assumed to be

uniform throughout the entire ground domain. Since the soil is a semi-infinite medium bounded by the ground surface where other media exist (air or water), another assumption needs to be made, that is, the ground surface is an isotherm. Kennelly, who was the first researcher adopting such an assumption in [25], assumes that the heat flowing upwards from the buried cable is entirely dissipated at ground surface due to the combination of radiation and convection mechanisms. Hence, the external thermal resistance for an isolated, buried cable is defined as per (2.21).

$$T_4 = \frac{\rho_s}{2\pi} \ln\left(u + \sqrt{u^2 - 1}\right) \tag{2.21}$$

where ρ_s is the thermal resistivity of soil (Km/W), u = $(2L/D_e)$, where L is the depth of laying (m) and D_e the cable outer diameter (m). Eq. (2.21) is also adopted by IEC 60287-2-1 [33], where the case of group of buried cables is also covered.

The assumption of an isothermal ground surface is recognised as strictly not true even by Kennelly in his work [25]. As discussed by Swaffield in [42], where IEC against more realistic assumptions are compared, significant error is introduced when using the IEC formula in cases that underground cables are buried shallower than 0.9 m. More conservative ratings by 3.4% occur when convective heat transfer with still air is assumed at 0.9 m, while this percentage becomes 12.2% for even shallower cables. Although the isothermal assumption for ground surface is correctly considered questionable by Swaffield for shallow buried underground cables, it is not expected to be so in submarine cable installations. Indeed, even considering still water above the seafloor, a convective heat transfer coefficient of two orders of magnitude higher than that cited by Swaffield for still air may be found in the literature [43]. Moreover, strong water currents are expected in OWFs when the submarine cables reach their maximum load, thus further increasing the convective heat transfer coefficient.

Submarine cable projects often include sections where the cable is deeply installed, such as at the point where it approaches the mainland. Furthermore, even in cable sections of shallower depths, the cable surroundings are often enhanced with filling materials of higher thermal conductivity in order to improve the heat dissipation from the cable. In all these cases multilayer structures actually exist instead of a uniform soil and the assumption of a single thermal resistivity obviously does not hold true. The present practice is to assume the soil layer having the highest thermal resistivity value to extend throughout the entire domain, thus leading to very conservative ratings which are not at all representative. Various methods have been proposed to calculate the effective thermal resistance of the surrounding soil. Certain analytical methods, such as those suggested by [44] and [45], are based on the multiple reflections of heat sources and their images. Their main advantage is the ease of use, since they are usually formed as closed mathematical expressions. Their main drawback is their limited

applicability to simple cases of multilayer soil and thermal backfills of simplified geometries. Some other numerical methods, such as [46] and [47], are based on the technique of conformal transformation with the use of finite differences. These methods are applicable to any geometry of multilayer or backfilled soil, although involve high numerical and programming complexity. Since the present thesis is mainly confined to the study of cable interior, the reader is referred to the above cited references for further research.

2.3 Summary

This chapter has made an overview of the existing cable rating Standards as applicable to 3C submarine cables. The Single-Core Equivalent Thermal Model (SCETM) implied by the current IEC 60287 version has been presented, making focus on the representation of cable interior. Certain key points are identified: it is not very clear in the existing SCETM how the jacket over each power core should be represented, whereas the T_2 calculation seems to be rather questionable as it is. A thorough literature review indicates that the existing formulae pertaining to non-cylindrical geometries, such as that of fillers and bedding domain, date back to the first two decades of 1900s and refer to essentially different cable types and geometries. Some of the inherent assumptions which might restrict the applicability of SCETM to modern submarine cables have been highlighted, with the assumption that metallic sheaths can be treated as isotherms being the most important. For cables consisting of smaller cores, such as those considered by the previous researchers, the assumption of isothermal sheaths would not be unreasonable. However, as the modern 3C submarine cables get larger, so do the power cores; hence, such an assumption may be questionable, particularly if combined with the relatively poor, compared to other metals, thermal conductivity of Lead sheaths. The next chapter introduces an in depth review of the existing SCETM as adopted by the current Standard version. Finite Element Method (FEM) is used to reveal the weak points of SCETM, while the key parameters driving the divergence between the IEC 60287-2-1 method and FEM are identified.

Chapter 3 Improved Thermal Model of the Cable Interior

The literature review presented in Chapter 2 demonstrates certain gaps in the existing thermal model adopted by IEC 60287 for submarine cables. In particular, the way the existing model represents the cable interior seems rather questionable when considering modern cable geometries, mainly because its origins date back to the early 1900's and intended to describe the thermal field in quite different cable types; hence, the simplifications that had to be adopted for those cables are likely to have a stronger impact on modern submarine cables.

One of the main objectives of this Chapter is first to review the existing thermal model implied by the IEC 60287-2-1 Standard [33]; its applicability to modern submarine cables is assessed, making focus on the thermal resistance between jackets and armour, namely T_2; the extent to which the assumptions made hold true is investigated, while the key design factors rendering these assumptions unrealistic are identified. Modern, Finite Element (FE) techniques are employed for this purpose. Although FE modelling is today considered a very accurate approach for studying conductive heat transfer in complex geometries, such as that of an SL-Type cable, it is not suitable for Standardisation purposes. The second aim of this Chapter is to derive an improved, readily usable analytical formula for T_2, which could be adoptable by the IEC 60287-2-1 Standard. Although empirically derived, it is still called analytical in the context of the present Chapter in order to distinguish it from the FE techniques. The material presented in this chapter is largely based on the paper "Review of the Accuracy of Single Core Equivalent Thermal Model (SCETM) for Offshore Wind Farm (OWF) Cables" already published by the author in IEEE Transactions on Power Delivery [48].

3.1 Introduction

Three-core (3C) HVAC submarine cables are currently treated as "SL-Type (Separate Lead) and armoured cables" by the IEC 60287 Standard ([16],[33]) where a Single Core Equivalent Thermal Model (SCETM) is described. Although "SA-type" (Separate Aluminium) is also referred to in IEC 60287-2-1 [33], no actual distinction is made for different screen materials. Today, thin Copper or Aluminium foils are widely used for modern array cables. Several simplifying assumptions are used by the existing SCETM, such as the sheaths being considered isothermal, as pointed out in Chapter 2. Certain components inherent to the modern cable design, such as the jacketing layer above each metallic sheath, or the extruded (profile) fillers being widely used in modern cables, are not explicitly treated by IEC 60287-2-1.

The chapter's structure is organised as follows: the necessary theoretical background is provided in section 3.2; then, starting from the SCETM currently used by the IEC 60287 Standard (section 3.3.1) more realistic conditions seen in the cable are considered (sections 3.3.2 and 3.3.3). Finally, the questionable issue of extruded profile fillers including air and water gaps is evaluated and recommendations are given on how this should be modelled.

3.2 SCETM Adopted by the IEC 60287 Standard

The IEC 60287-2-1 Standard [33] takes advantage of the circular geometry of most of the components involved in the 3C structure and a SCETM is suggested to represent the cable, provided that 1-D (radial) heat transfer is assumed. As discussed in Chapter 2, section 2.2.2, this in its turn holds true on the condition that the boundaries which enclose the several circular domains (insulation, jacket and serving) and define the corresponding thermal resistances are isothermal. The relevant formula calculating the thermal resistance of each circular, non-metallic layer has been already presented in Chapter 2, section 2.2.2 and is also shown in (3.1) for convenience.

$$T_i = \frac{\rho_i}{2\pi} \ln\left(1 + \frac{2t_i}{d_{\text{under}}}\right) \tag{3.1}$$

where ρ_i is the thermal resistivity of the i-th material (Km/W), t_i is the thickness of the i-th layer (mm), d_{under} the diameter beneath it (mm) and index i may be 1, 2j or 3, depending on the layer. The thermal resistance of the fillers, which are used to make the assembly of cores as round as possible, and the bedding above them are together represented by thermal resistance T_2. This is calculated by using a geometric factor G whose origins are investigated in section 2.2.3. The relevant formula is also shown in (3.2) for convenience.

$$T_2 = \frac{\rho_{\text{fb}}}{6\pi} G \tag{3.2}$$

where ρ_{fb} is the thermal resistivity of the material of fillers and bedding (Km/W), while a graph showing two G-curves is provided by IEC 60287-2-1 [33] as illustrated in Figure 3.1. Analytical equations are also given by [33] to fit the relevant curves, depending on the ratio of the thickness of material between sheaths and armour to the outer diameter of the sheath, denoted by [33] as variable X. Since no reference is made by [33] to the modern design of SL-Type cables with jacketed cores, either of the two curves could be potentially applicable, depending on how the jacket is treated, as already discussed in section 2.2.3. In case that the upper curve is used, touching jackets are implied instead of touching sheaths and the jacket resistance, $T_{2\text{j}}$, is separately calculated based on (3.1). The two possible X definitions are also presented in (3.3) and (3.4).

$$X_{\text{touch}} = \frac{t_{\text{j\_ar}}}{D_{\text{j}}} \tag{3.3}$$

$$X_{\text{non\_touch}} = \frac{t_{\text{j\_ar}} + t_{\text{j}}}{D_{\text{s}}} \tag{3.4}$$

where X_{touch}, $X_{\text{non\_touch}}$ refers to the upper, lower curve, respectively, $t_{\text{j\_ar}}$ is the thickness of material between the external surface of jackets and the inner surface of the armour (mm), t_{j} is the jacket thickness (mm), D_{s} and D_{j} are the outer diameters over the sheath and jacket (mm), respectively. These definitions become even clearer by considering the geometry illustrated in Figure 3.2. It must be noted that t_{j} is assumed to be equal to $t_{\text{j\_ar}}$ by IEC 60287-2-1. It is, however, fairly possible to have jackets of different thickness than the armour bedding in reality.

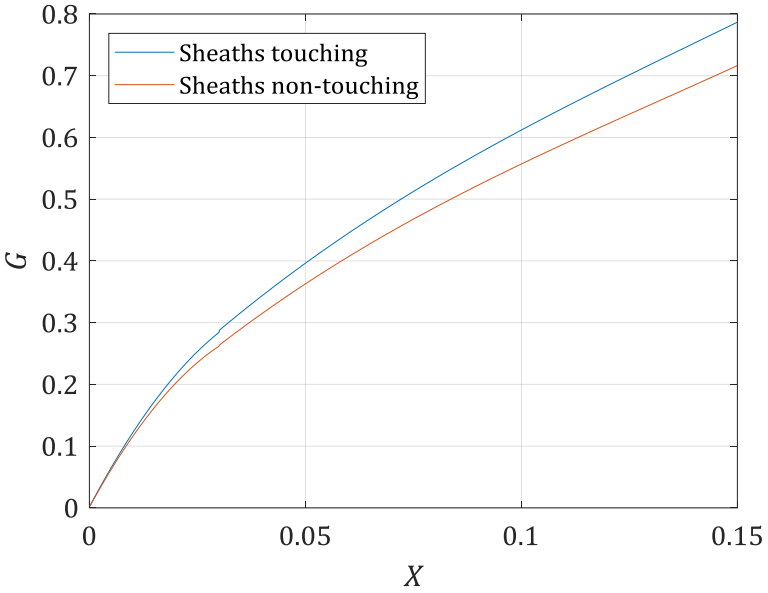

FIGURE 3.1: Geometric Factor G for T_2 Calculation by (3.2) According to IEC 60287-2-1 [33].

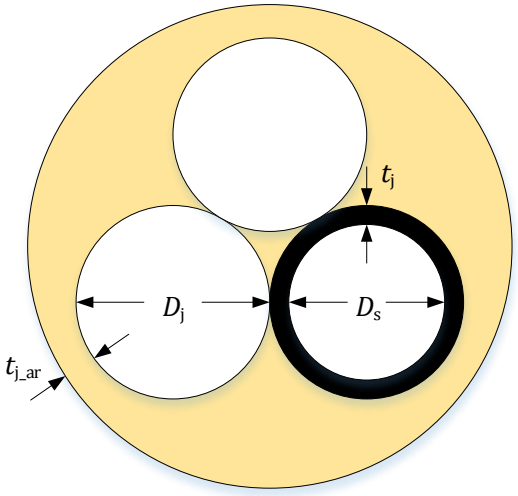

FIGURE 3.2: A Typical 3C Geometry where D_{j}, $t_{\text{j\_ar}}$ and D_{s} , t_{j} Are Depicted.

Depending on the interpretation adopted and the curve selected, substantially different X values may occur, thus potentially causing confusion between engineers. The difference between X_{touch} and $X_{\text{non\_touch}}$ becomes even clearer from the chart shown in Figure 3.3 which shows the correlation for various t_j and for D_j ranging from 40 mm to 120 mm. X_{touch} is adopted in the IEC calculations of the present Chapter (touching jackets). Hence, the thermal resistance of jacket, namely T_{2j}, remains non-zero in the ampacity calculation,(2.9), while T_2 involves the domain extending from the outer surface of power cores up to the inner surface of the armour.

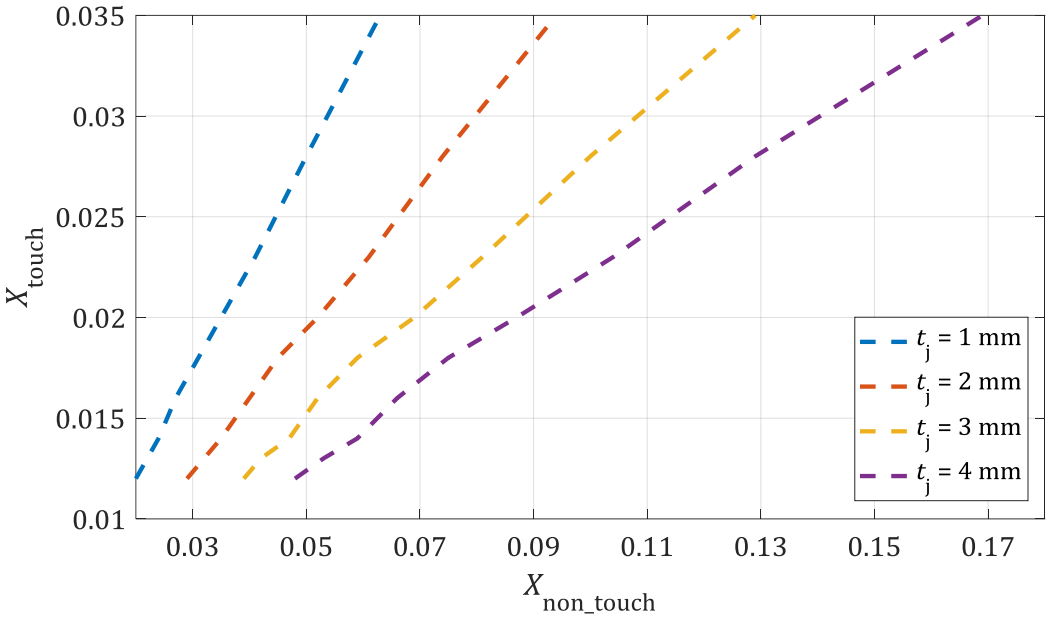

FIGURE 3.3: Relation between X_{touch} and $X_{\text{non\_touch}}$ Variables.

Irrespective of the selection of X, the assumption of isothermal surfaces (either on the sheath or on the outer surface of the jacket) is implied by the existing SCETM, which considers only radial heat transfer within the cable. Although the selection of $X_{\text{non\_touch}}$ and thus the assumption that sheaths are isotherms might be more realistic compared to assuming the outer surfaces of jackets as isotherms (due to the former's higher thermal conductivity), such a selection means that T_{2j} is nulled in (2.9). In this case, materials of different thermal properties, namely jackets, fillers and bedding, would be necessary to be represented by a single thermal resistivity. Although fillers and bedding are likely to be composed of the same material from the thermal viewpoint (polypropylene has a thermal resistivity of 6 Km/W according to [33]), modern cables involve jackets of semiconductive polyethylene, with a thermal resistivity of 2.5 Km/W.

Besides the thermal representation of different materials, the assumption of a radial heat field implied by the existing SCETM is not fully valid in the case of SL-Type cables. Owing to the close physical proximity between the cable cores, the Principle of Superposition is not applicable, since the thermal field of each core strongly affects that of the other two: hence, the assumption of isothermal surfaces, even for metallic sheaths, becomes questionable. This is not considered

in the work [40] published by Anders, where a cable geometry similar to that of an SL-Type cable is analysed by considering metallic screens as isotherms. The metallic sheaths are treated as isotherms even in the more recent work published by Ramirez [31], who deals with SL-Type cables with jacketed cores. One extra indication that renders the assumption for isothermal sheaths rather controversial is that similar cable geometries are treated in a different way by IEC 60287-2-1 [33]: correction factors are adopted for T_1, T_3 thermal resistances for three single-core cables in touching trefoil formation. Anders states that these factors are used to account for the circumferential heat conduction taking place when three cores are touching each other [34].

The existing SCETM is reviewed in the following section through Finite Element Analysis (FEA), by implementing the following step-by-step approach: first the assumptions for 1-D heat transfer used in the IEC 60287 Standard are adopted in FEA to validate the existing SCETM; then, the actual 2-D thermal problem is analysed by means of FEA, though considering isothermal metallic sheaths; eventually, non-isothermal sheaths are considered and the difference against the isothermal assumption is highlighted and commented.

3.3 Finite Element Analysis: Methodology Developed

3.3.1 Verification of the Existing SCETM

Finite Element (FE) models are treated by some researchers as black-box approaches that do not allow for deeper physical insight. It is important to validate the FE model used in the present chapter against an existing analytical model, such as that proposed by IEC 60287-2-1. In order to make the FE model comparable with that suggested by IEC, the thermal model as actually considered by the latter is developed using FEA. To consider the 1-D (radial) thermal field implied by the SCETM, T_2 is represented by an annulus of equivalent thickness, namely $t_{\text{eq\_fb}}$, as depicted in (3.5). This formula occurs by equating the left side of (3.2) with the right side of (3.1), $d_{\text{under}} = D_{\text{j}}$, $\rho_i = \rho_{\text{fb}}$, $t_{\text{i}} = t_{\text{eq\_fb}}$ and solving (3.1) for t_{i}.

$$t_{\text{eq\_fb}} = \frac{D_{\text{j}}}{2}\left(e^{\frac{2\pi T_2}{\rho_{\text{fb}}}} - 1\right) \tag{3.5}$$

The armour annulus is represented as a thick layer of zero thermal resistance to keep the diameter under the serving constant, thus leaving T_3 unchanged. An indicative geometry can be seen in Figure 3.4. To avoid any issues related to the depth of laying, T_4 is set to zero, hence $\Delta\theta$ in the ampacity equation (2.9) denotes the temperature rise of the conductor above the cable surface. The same current is injected in both FE and IEC models and temperature is recorded. As shown in Table 3.1, the difference between IEC and FEA does not exceed 0.002%

in terms of the temperature calculated in all metallic components. This implies that the temperature drops between the various layers within the examined geometry are correspondingly equal, thus verifying that the two models are equivalent.

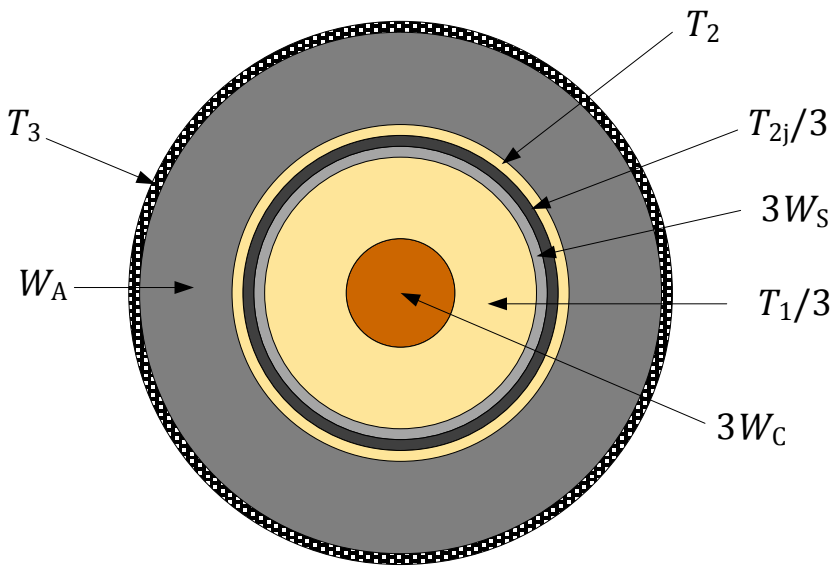

FIGURE 3.4: The SCETM Implied by IEC 60287-2-1 as Imported in the FE Model.

TABLE 3.1: Temperature Results for SCETM as Implemented by FEA and IEC Calculations.

Geometric Entity	Temperature Recorded (°C)		Difference (%)
	FEA	IEC	
Conductor	89.999	90.000	0.001
Sheath	45.006	45.007	0.002
Armour	23.600	23.600	0.000

3.3.2 Sheaths as Isotherms – Verification of Eq. (3.2)

As soon as the FE model is verified against the existing analytical 1-D model, the introduction of the actual 2-D geometry follows as the next step in the methodology adopted. The aim of this section is to verify (3.2), which is currently used by IEC 60287-2-1, using the FE model and adopting identical to IEC assumptions, as possible.

Two cases are examined in the present section with regard to the jacket over each core, which are also covered by the existing IEC 60287-2-1 Standard version [33]. First, unjacketed cores with touching sheaths are assumed. In this case t_j equals to zero, t_{j_ar} and D_j are replaced by the thickness between sheaths and armour, i.e. t_{s_ar}, and D_s, respectively, and $X_{touch} \equiv X_{non\_touch}$. The thermal effects coming from the surrounding media are not of interest and T_4 is set equal to zero for the sake of simplicity. The metallic layers are assumed as isothermal volumes by

assigning extremely large thermal conductivity values to the corresponding geometrical entities. Additionally, the thermal properties of the bedding and filler regions are considered to match, as implied by IEC. Hence, by injecting an arbitrary amount of current-dependent losses in power cores and considering the temperatures induced, the thermal resistance of the filler is obtained from the FEA model, as (3.6) indicates.

$$T_{2,\mathrm{FEA}} = \frac{\theta_\mathrm{S} - \theta_\mathrm{A}}{3(W_\mathrm{C} + W_\mathrm{S})} = \frac{\theta_\mathrm{S} - \theta_\mathrm{A}}{3W_\mathrm{C}(1 + \lambda_1)} \tag{3.6}$$

where W_C and W_S is the power loss injected in the conductor and sheath, respectively (W/m), λ_1 is the sheath loss factor, θ_S and θ_A is the temperature of the sheath and armour, respectively (°C). It should be noted that either of λ_1, λ_2, where λ_2 is the armour loss factor, can be considered equal to zero and are not expected to have any impact on $T_{2,\mathrm{FEA}}$ results. Some indicative cases with non-zero λ_1, λ_2 confirmed what was expected, because the thermal resistance is in reality geometrically defined and does not depend on the heat flow dissipated, on the condition that materials with temperature independent thermal conductivity are involved. Although some temperature dependency is expected in the thermal conductivity of cable polymeric compounds, this is such weak that permits us to consider negligible [49].

Then, by solving (3.2) for G_FEA and varying X_touch, the curve in Figure 3.5 is obtained. It should be noted that varying both $t_\mathrm{s\_ar}$ and D_s does not change the G_FEA curve in Figure 3.5, as expected. In other words, the same G_FEA value occurs whatever the combination of $t_\mathrm{s\_ar}$, D_s is, on the condition that the ratio X_touch is kept unchanged. Assuming for instance an increased $t_\mathrm{s\_ar}$, heat encounters locally higher thermal resistance because of the increased $t_\mathrm{s\_ar}$, but at the same time proportionally better heat dissipation occurs from the increased core surface close to the armour bedding, because of the increase in D_s, thus keeping $T_{2,\mathrm{FEA}}$ unchanged.

The second case under consideration is that with jacketed cores, making assumptions identical to those adopted by the IEC 60287-2-1 Standard for non-touching sheaths: the jacket is of thickness equal to the bedding, i.e. $t_\mathrm{j\_ar} = t_\mathrm{j}$, and its material is the same as that for the fillers and bedding domain. G_FEA are also extracted for non-touching sheaths and illustrated in Figure 3.5. Eq. (3.4) is used to define $X_\mathrm{non\_touch}$ and by means of (3.2) G_FEA is derived considering $T_{2,\mathrm{FEA}}$ as computed by (3.6). Extremely large thermal conductivity values are again assigned to the metallic components, so as to make them isothermal. For comparison purposes, Figure 3.5 includes also the IEC curves.

As can be noticed from Figure 3.5, G_FEA curves with touching and non-touching sheaths coincide one another, a fact that contradicts with what IEC 60287-2-1 suggests. Additionally, G_FEA stands between the two IEC curves, except for the extremely low X region where slightly higher G_FEA values appear. This relative difference, which does not in total exceed 10%, is defined as

"*geometrical error*" in the context of the present section. This differs from the "*thermal error*" defined later, in section 3.3.3. It must be noted that the geometrical method considered by Wedmore (in Appendix IV of the report published by Melsom) in 1923 [41] did not consider individual metallic sheaths over each core; hence, the lines of heat-flow would have a different distribution compared with those derived from an SL-Type geometry. Also, the thickness between conductors and the common sheath was not so incomparable compared to the diameter of the conductor and, thus, such low X values as those depicted in Figure 3.5 were not so possible in those cables.

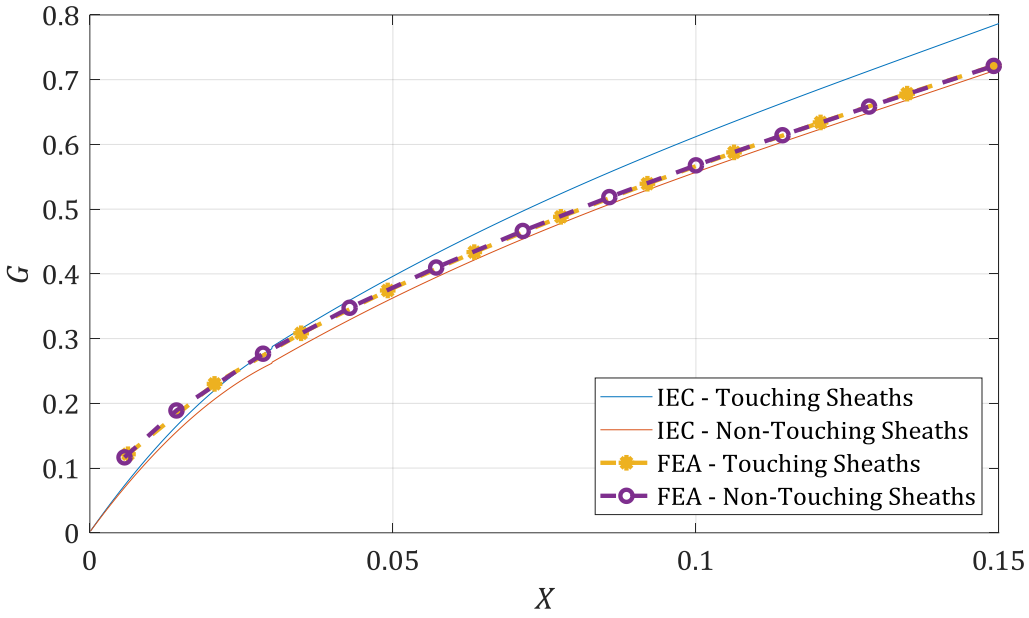

FIGURE 3.5: G Curve Derived from FEA – Isothermal Sheaths Assumed, Considering Unjacketed and Jacketed Power Cores ($t_j = t_{j\_ar}$).

3.3.3 Sheaths as Non - Isotherms

The aim of this section is to compare the G curves extracted from FEA with those from the IEC 60287-2-1 Standard [33] under more realistic conditions imposed by the 2-D heat conduction; for this purpose, the Lead sheaths are no longer treated as isothermal volumes; instead, typical book values are assigned in terms of the thermal conductivity of Lead. Since a temperature distribution along the sheath circumference now occurs in place of a fixed, single value, the average value is applied to obtain an as representative as possible estimation of temperature. This is used for θ_S in (3.6). Touching power cores with no jacket are assumed in this section to simplify the analysis: hence, (3.3) is used for X_{touch}. The volumes of conductors and armour are still treated as isotherms, while a Lead sheath of 2.0 mm thickness is assumed. The relevant curve is depicted in Figure 3.6 along with the IEC curves.

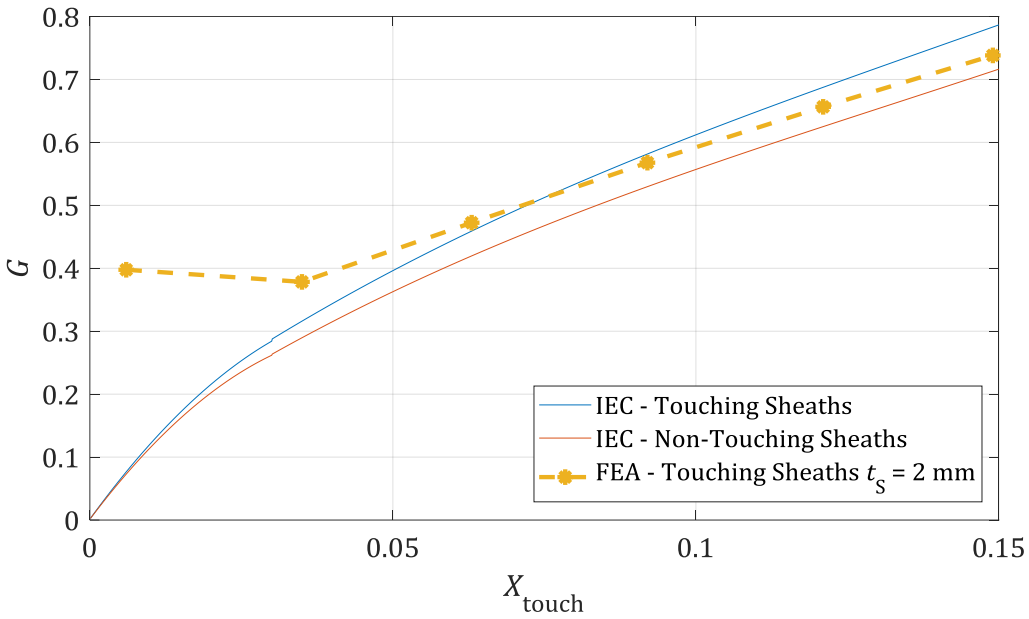

FIGURE 3.6: G Curve Derived from FEA – Non-Isothermal Sheaths Assumed, Considering Unjacketed Power Cores.

As may be readily noticed from Figure 3.6, significant divergence occurs between G_{FEA} and G_{IEC} values when the Lead sheaths are treated as non-isothermal. This "*thermal error*" seems to be significantly larger than the geometrical one: relative differences over 50% can be noticed, especially for lower X_{touch} values. It should be noted that the domain of lower X_{touch} values is quite possible in practice, since it relates to larger D_s compared with t_{s_ar}, where the latter would typically be less than 5 mm but the former could reach up to 100 mm.

Furthermore, the larger G_{FEA} values for lower X_{touch} reveal a rather weak point of the existing SCETM: significant 2-D (circumferential) heat conduction is expected to take place due to the close arrangement of the phase cores and, consequently, the Principle of Superposition becomes inapplicable. The peripheral thermal resistance of the Lead sheath is responsible for the large divergence with the IEC curves. Considerably lower discrepancy can be observed for higher X_{touch} values, namely lower D_s with respect to the same Lead sheath thickness. In other words, the thicker the Lead sheath is (or equally the shorter the sheath circumference), the less the divergence between G_{IEC} and G_{FEA} occurs.

In conclusion, the *geometrical error* should not be treated regardless of the *thermal* one, since the latter appears to be more severe. The simultaneous treatment of both errors is suggested in the present study. The following section shows the procedure followed to approach this issue through FEA. Analytical G formulations are subsequently derived, depending on the screen type of the cable.

3.4 Suggested Correction of the Existing SCETM

An indication about the difference expected between the existing SCETM and a more realistic 2-D FE model is presented in section 3.3: G factor, as derived from both models, is employed in order to represent and demonstrate this difference. By taking advantage of the FEA, a new formulation is proposed in this section which is easily adoptable by the existing SCETM and expected to improve its accuracy. The circumferential thermal resistance of the metallic sheath is of great importance, as shown in section 3.3. For this reason, sheath thickness, t_S, is considered as a variable parameter, with different materials being examined.

The Lead sheath of a typical submarine export cable falls within the range 2 – 5 mm. On the contrary, typical array cables very often comprise Copper (Cu) or Aluminium (Al) laminated tapes of thickness 0.15 – 0.3 mm as metallic foil screening. The analysis presented in this section explicitly considers jacketed cores, as typically used in modern OWF cables. The 'touching' assumption is extended over the jackets and (3.3) is used to define X_{touch}. Because of the temperature distribution noticed along their outer surface, the average temperature, namely θ_J, above it is calculated and obtained through FEA. This replaces θ_S in (3.6) and $T_{2,\text{FEA}}$ is calculated as per (3.7), while the volumes of both the conductors and armour are treated as isotherms. Then, the corresponding G_{FEA} factor is calculated by assuming $T_2 = T_{2,\text{FEA}}$ in (3.2) and solving it for G_{FEA}.

$$T_{2,\text{FEA}} = \frac{\theta_J - \theta_A}{3W_C(1+\lambda_1)} \tag{3.7}$$

3.4.1 Mesh Strategy

Before proceeding with the analysis presented in sections 3.4.2 - 3.4.4, it is important to look into the effect the mesh quality has on G_{FEA} values. A finer and a coarser mesh are considered in this section, which are illustrated in Figure 3.7 for an indicative filler case. Attention is paid to ensuring sufficiently dense mesh in the regions where high local temperature gradients are expected, namely regions II in Figure 3.7. However, it is important to verify that any decrease in the mesh of region I (Figure 3.7) has insignificant impacts on the accuracy obtained. A very fine mesh, shown on the left of Figure 3.7, is initially considered. A coarser mesh is subsequently tried, where region I is composed of substantially less elements, as depicted on the right of Figure 3.7. The corresponding results of these mesh checks are shown in Table 3.2, with those referred to "finer" being considered as reference values. Two extreme cases with regard to both t_S and D_j (thus X_{touch}) are considered.

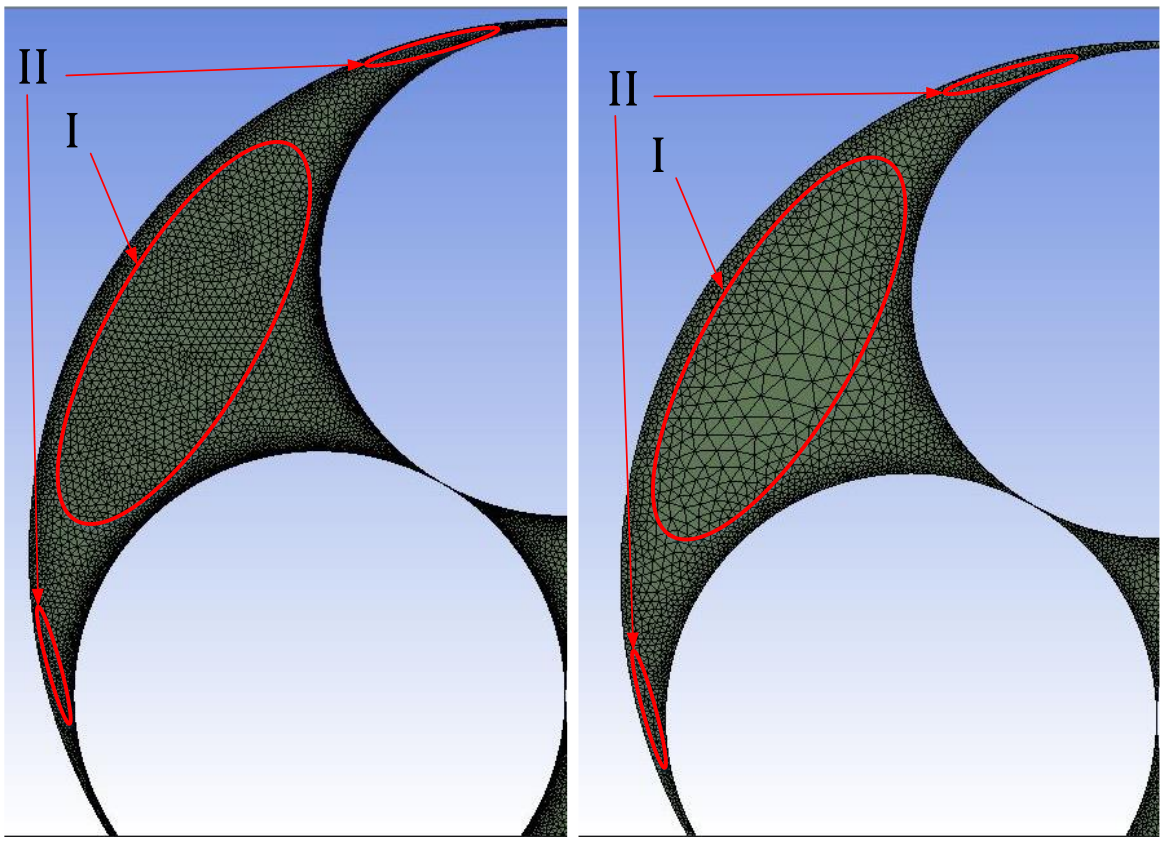

FIGURE 3.7: Finer (on the Left) and Coarser (on the Right) Filler Mesh.

TABLE 3.2: Mesh Sensitivity Analysis – Extreme Cases.

Case (mm)		X_{touch}	Mesh Density (Elements/ mm²)	G_{finer}	Mesh Density (Elements/ mm²)	$G_{coarser}$	Mesh Change (%)	G Change (%)
D_j	t_S							
152	1	0.0132	0.9566	0.439389	0.4364	0.442394	-54.4	0.68
	5	0.0132	0.9587	0.282920	0.4365	0.283913	-54.5	0.35
32	1	0.0625	9.189	0.518380	4.490	0.518878	-51.1	0.1
	5	0.0625	9.247	0.474044	4.511	0.474269	-51.2	0.05

A slight impact, not exceeding 0.68%, is shown in Table 3.2 when decreasing the mesh by about 55%. Besides the finer mesh of region I, this small difference may be attributed to the higher number of edge elements above the power cores in the finer mesh. Hence, a better estimation of the numerical integration required to calculate the average θ_j is obtained and thus a more accurate $T_{2,FEA}$ results, based on (3.7). In conclusion, the coarser mesh is computationally more efficient and accurate enough and this is employed in the parametric analysis presented in section 3.4.2.

3.4.2 Proposed *G* Curve for SL-Type Cables

To take advantage of the computational power and high level accuracy afforded by FEA, a parametric analysis is done in this section, where the core diameter, D_j, as well as the thickness of the sheath, t_S, are varied within reasonable ranges. The corresponding G_{FEA} curves are derived in each case. As soon as the average θ_j and the total heat flow $Q = 3W_C(1+\lambda_1)$ are obtained, (3.7) is solved for $T_{2,FEA}$ and then by substituting $T_2 = T_{2,FEA}$ in (3.2) and solving it for G_{FEA}, the corresponding (G_{FEA}, X_{touch}) points occur. To simplify the analysis, a jacket thickness (t_j) equal to 1 mm, as well as a thickness between jackets and armour (t_{j_ar}) equal to 2 mm are considered for all the cases studied. The impact of making these assumptions is separately considered in section 3.4.3.

For each sheath thickness, the value of D_j is varied every 10 mm in the range 32 - 152 mm to obtain the most representative fitted curve. Values of D_j out of this range are not expected for the vast majority of OWF cables. Linear fitted curves of the form $G_{SL} = aX_{touch}+b$ are proposed, as illustrated in Figure 3.8. A least square regression is employed to find the optimum line best fitting the (G_{FEA}, X_{touch}) data. The Sum of Squares of Error (SSE), as well as the R-square are shown in Table 3.3 for each sheath thickness value. The two G curves as considered by IEC 60287-2-1 are also shown in the same chart for comparison purposes, while focus is made on the area of interest.

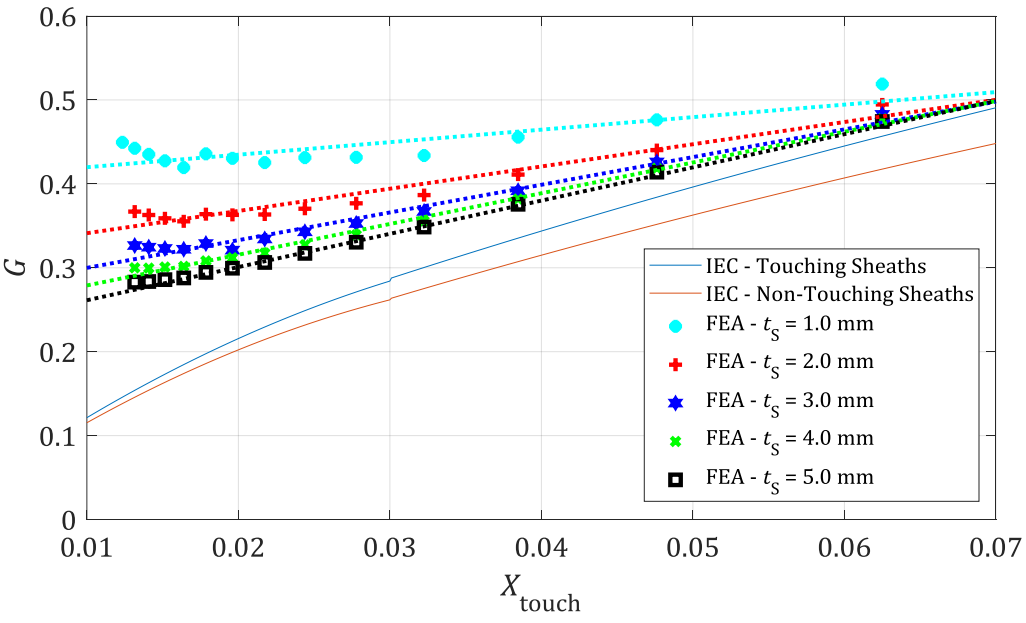

FIGURE 3.8: Derivation of G_{FEA} Curves Against Thickness of Sheath (SL-Type Cables).

As it becomes apparent from Table 3.3, R-square tends fast to 1 when increasing t_s: values well above 90% are shown for most of the sheath thicknesses examined, apart from t_S = 1 mm. For that case, a 3rd polynomial curve fitting would give SSE = $3.7596 \cdot 10^{-4}$ and R-square = 0.9573.

Although not perfect, the linear approximation affords the necessary simplicity to proceed with the analysis. All G_{FEA} curves are above G_{IEC}, thus implying that the existing SCETM represents the filler in a more optimistic way, because of treating the metallic sheaths as isotherms. The proposed curves for thicker sheaths are apparently closer to the IEC values, especially for smaller D_j (higher X_{touch}) values, since the circumferential thermal resistance of the Lead sheath decreases, thus becoming more isothermal.

TABLE 3.3: Evaluation of the Goodness of the Linear Curve Fitting, $G = aX_{touch}+b$, for each t_S Value.

t_s (mm)	SSE	R-square
1	0.0025	0.7127
2	0.0012	0.9410
3	$7.4032 \cdot 10^{-4}$	0.9745
4	$2.6552 \cdot 10^{-4}$	0.9926
5	$1.4364 \cdot 10^{-4}$	0.9965

Having the a and b terms of each line $G_{SL} = f(X_{touch})$, polynomial relations of 3rd order are used to match the corresponding (a, t_S), (b, t_S) points, where t_S is the thickness of the sheath. The regression achieved for terms a and b has SSE equal to $6.1 \cdot 10^{-4}$ and $2.4 \cdot 10^{-6}$, respectively, while the R-square values are nearly equal to 1 (0.9998 and 0.9999 for a and b, respectively). The following formula correlating both t_s and X_{touch} variables is found:

$$G(X_{\text{touch}}, t_S)_{SL} = \left(a_3 t_S^3 + a_2 t_S^2 + a_1 t_S + a_0\right) X_{\text{touch}} + \left(b_3 t_S^3 + b_2 t_S^2 + b_1 t_S + b_0\right) \qquad (3.8)$$

where $a_3 = 0.0368$, $a_2 = -0.4749$, $a_1 = 2.3253$, $a_0 = -0.3956$, $b_3 = -0.0032$, $b_2 = 0.0404$, $b_1 = -0.189$, $b_0 = 0.5567$.

3.4.3 Review of the Assumptions Made

As mentioned in section 3.4.2, fixed values of t_j and t_{j_ar} are used for the derivation of (3.8) for the sake of simplicity. In terms of the former (t_j), jacketing layers have a thermal conductivity about two orders of magnitude lower than Lead sheaths, thus preventing large amounts of heat from dissipating circumferentially around them: thus, the assumption of keeping t_j constant when deriving (3.8) seems to be reasonable. However, it is important to review the assumptions made in the parametric analysis done and carry out additional checks to assess any likely effect t_j has on the G_{SL} curves obtained from (3.8). For this purpose, t_j values from 1 mm up to 4 mm are examined, keeping t_{j_ar} constant and equal to 2 mm and varying t_S. The

increase in t_S is added outwards with respect to the core centre, thus leading to higher D_j and lower X_{touch}. Since t_j further contributes to the increase in D_j, even lower X_{touch} values occur when increasing t_j. The G_{SL} values derived from (3.8), G_{SL}, are compared against G_{FEA}, while G_{IEC} values are also compared against G_{FEA} in order to have a comparative estimation of the improvement achieved. In both cases G_{FEA} is considered as a reference. The corresponding results are shown in Table 3.4.

TABLE 3.4: Evaluation of (3.8) when Varying t_j for Several t_S Values.

t_S (mm)	t_j (mm)	D_j (mm)	X_{touch}	G_{SL}	$\frac{G_{SL}-G_{FEA}}{G_{FEA}}100\%$	$\frac{G_{IEC}-G_{FEA}}{G_{FEA}}100\%$
1	1	52	0.0385	0.462	1.39	-26.36
2		82	0.0244	0.379	2.34	-32.77
3		142	0.0141	0.313	-3.56	-49.73
1	2	54	0.0370	0.46	-1.44	-29.89
2		84	0.0238	0.378	-0.85	-35.62
3		144	0.0139	0.313	-5.77	-51.46
1	3	56	0.0357	0.458	-3.88	-32.85
2		86	0.0233	0.376	-3.91	-38.38
3		146	0.0137	0.312	-8.22	-53.15
1	4	58	0.0345	0.456	-6.09	-35.50
2		88	0.0227	0.375	-6.38	-40.91
3		148	0.0135	0.311	-10.44	-54.70
Average (%)					4.52	40.11

Better results occur in general when using (3.8) in comparison with the existing SCETM: this may be confirmed when comparing the average values between the 6th and the 7th columns in Table 3.4. For t_j equal to 1 mm, the higher divergence noticed between G_{SL} and G_{FEA} (up to -3.56%) when increasing t_S is attributed to the higher regression levels observed for lower X_{touch} values in Figure 3.8. In other words, the linear curve fitting selected for the sake of simplicity in section 3.4.2, presents higher fitting errors as X_{touch} decreases, since the actual trend of (G_{FEA}, X_{touch}) points diverges more from the linear behaviour assumed in lower X_{touch}. For t_j larger than 1 mm, a more intense effect is noticed, thus implying that t_j has some effect on the accuracy of (3.8). For the thickest jacket tested, the relative difference with FEA does not exceed 10.44%, as can be seen from Table 3.4. This percentage compares to divergences of

up to 55% between G_{FEA} and G_{IEC}. Therefore, (3.8) still generates results that are more accurate compared to the existing SCETM, considering FE model as a reference. It must be noted that jackets as thick as 4 mm are seldom met in practice in 3C export cables and are tested here merely for evaluation purposes.

Although the assumption of 2 mm for t_{j_ar} is arbitrary, it is fairly representative of the typical thickness of a single layer of yarn bedding. Beddings of up to t_{j_ar} = 4 mm are tested in the present section, assuming t_j constant and equal to 1 mm. Hence, D_j is determined by t_s only, while higher X_{touch} values occur increasing t_{j_ar}. The corresponding results are shown in Table 3.5.

TABLE 3.5: Evaluation of (3.8) when Varying t_{j_ar} for Several t_S Values.

t_S (mm)	t_{j_ar} (mm)	D_j (mm)	X_{touch}	G_{SL}	$\frac{G_{SL}-G_{FEA}}{G_{FEA}}100\%$	$\frac{G_{IEC}-G_{FEA}}{G_{FEA}}100\%$
1	1	52	0.0192	0.434	34.1	-35.4
2		82	0.0122	0.347	11.71	-53.53
3		142	0.0070	0.29	1.89	-69.04
1	2	52	0.0385	0.462	1.39	-26.36
2		82	0.0244	0.379	2.34	-32.77
3		142	0.0141	0.313	-3.56	-49.73
1	3	52	0.0577	0.491	1.09	-10.61
2		82	0.0366	0.412	-2.63	-23.19
3		142	0.0211	0.337	-6.02	-37.41
1	4	52	0.0769	0.52	-6.23	-6.14
2		82	0.0488	0.444	-5.85	-17.28
3		142	0.0282	0.36	-7.86	-29.94
				Average (%)	7.06	32.62

Better results occur in general when using (3.8) in comparison with the existing SCETM: this may be confirmed when comparing the average values between the 6th and the 7th columns in Table 3.5. When getting to lower t_{j_ar} than that assumed constant in section 3.4.2, remarkable divergences between G_{SL} and G_{FEA} are seen, especially for higher X_{touch} values. Indeed, the relative difference between G_{SL} and G_{FEA} appears to be comparable with that between G_{SL} and G_{IEC} for X_{touch} = 0.0192, though having the opposite trend: G_{SL} is rather conservative, while G_{IEC}

is quite optimistic with reference to G_{FEA}. It must be noted that this extreme value is mainly responsible for the relatively high average of 7.06%: this falls to 4.60% if that value is excluded, while the corresponding average for G_{IEC} is much less affected, i.e. turns from 32.62% into 32.36%. G_{SL} appears more consistent for the rest of the tests performed, being in most cases notably closer to G_{FEA} than G_{IEC}. An exemption is noticed when t_{j_ar} = 4 mm and X_{touch} = 0.0769: in this case G_{SL} appears slightly worse than G_{IEC}. However, the relative difference of both is kept fairly low with reference to G_{FEA}. A difference in T_2 of 6% is expected to have a thermal impact of few Amps on the current rating of buried cables, since T_4 prevails in such a case.

A general trend is noted from the results shown in Table 3.5: by decreasing t_{j_ar}, the existing SCETM diverges increasingly more from the more realistic thermal profile implied by the FE solution and the approximating, fitted curve. On the contrary, the divergence between FEA – IEC appears to be lower by increasing t_{j_ar}: this can be explained by the fact that SL-Type cables with thicker bedding resemble more to the belted cables for which the G_{IEC} curves were derived by Wedmore in 1923 [41]. Those cables consisted of a common sheath and the thermal resistance of the dielectric and fillers was more evenly distributed between the three conductors and the common sheath.

3.4.4 Proposed *G* Curve for Metallic Foil Screened Cables

Wind farm array cables are often screened by Cu or Al laminated tapes to reduce their weight and cost. Applying the same methodology as presented in section 3.4.2, new G curves, G_{Cu} and G_{Al}, are found for foil screened cables. The foil thickness is expected to vary much less compared with the SL-Type case, typically in the range 0.15 - 0.3 mm. A foil of 0.2 mm is assumed to extract G_{Cu} and G_{Al} curves in this section. These are seen in Figure 3.9, along with (G_{FEA},X_{touch}) points for the extreme cases of SL-Type for comparison. D_j is considered to vary in the range 30 - 100 mm, since array cables have smaller conductor size and insulation thickness. It must be noted that cables of up to 132 kV, which are not impossible and could be available in the future as array cables for further loss reduction, are included in the aforementioned D_j range.

G_{Cu} and G_{Al} curves stand between (G_{FEA},X_{touch}) points for Lead sheath with 1.0 mm and 5.0 mm thickness. G_{Cu} is closer to the G_{IEC} curves. This may be attributed to the higher thermal conductivity of Cu in comparison with Lead, in spite of the much smaller thickness of the metallic foil. In other words, the better conductivity of Cu (almost one order of magnitude higher than Lead) makes the relevant curve closer to the isothermal one, whereas the slightly worse conductivity of Al (almost half of Cu) results in higher G_{Al} values.

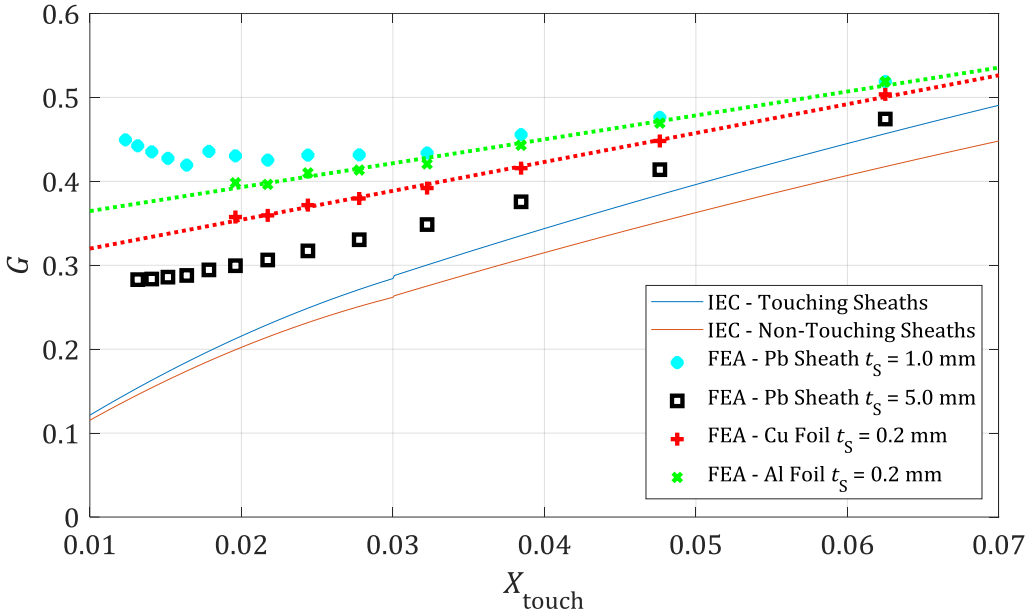

FIGURE 3.9: Derivation of G Curves Against Material of Metallic Foil (Foil-Screened Cables).

Having assumed constant thickness for the metallic foil, an equation depending only on X_{touch} is found. The relevant formulae for Copper and Aluminium are shown in (3.9) and (3.10), respectively [3]. Linear curve fitting is chosen again with very low SSE values ($6.4200 \cdot 10^{-5}$ and $1.5483 \cdot 10^{-4}$ for Cu and Al, respectively), while R-square is fairly close to 1 (0.9964 and 0.9875 for Cu and Al, respectively).

$$G(X_{\text{touch}})_{Cu} = 3.443X_{\text{touch}} + 0.2854 \tag{3.9}$$

$$G(X_{\text{touch}})_{Al} = 2.849X_{\text{touch}} + 0.3361 \tag{3.10}$$

3.5 Effect on Cable Temperature

New curves for the geometric factor are suggested in section 3.4 to represent in a more realistic way the thermal resistance of fillers and bedding, namely T_2, and improve the accuracy of the existing SCETM. As shown in Figure 3.8 and Figure 3.9, the G values extracted by FEA tend quite close to those suggested by IEC for large X_{touch} values. Nevertheless, by decreasing X_{touch} much higher discrepancies are noticed, especially if this reduction is due to increased D_j and simultaneously reduced t_s. An extreme difference of about 200% is observed for the thinnest Lead sheath. This is of particular importance, since it implies that the existing IEC Standard represents smaller OWF cables sufficiently, but not so larger export cable sizes. This could be

[3] These formulae slightly diverge from those suggested in the published paper of the author [48]. The reason for this is that a slightly wider X_{touch} range is considered in the present Chapter in order to consider larger array cables which are likely to be used in the future.

also justified by the fact that an SL-Type cable with a relatively higher X_{touch} (i.e. thick bedding or equally small core diameter) looks closer to the cable geometry treated by Wedmore in [41].

In order to check for the applicability and the degree of improvement afforded by the G_{SL}, G_{Cu} and G_{Al} formulae suggested by (3.8), (3.9) and (3.10), respectively, FE models with buried submarine cables under 'typical' installation conditions are compared against the existing SCETM. It should be noted that the filler is assumed to be of the same material as the armour bedding for the sake of simplicity. Although this is not always the case, the armour bedding mostly consists of Polypropylene (PP) yarns, while PP ropes are often used as a filler material in OWF cables. Finally, the issue of extruded (profile) fillers is reviewed in the present section, making focus on the extent to which they could be treated as though they were solid.

3.5.1 Finite Element Models: Modelling Strategy

FE models have been used by many researchers [42] for the rating of cables and are potentially more representative and accurate than the conventional IEC analytical methods ([16], [33]). In this section a de-coupled steady-state thermal response of the cable is considered, accounting for the thermal losses prescribed by the IEC 60287-1-1 Standard [16]. The IEC armour loss is chosen despite recent publications ([19], [18]) indicating that this might be an over estimation of the thermal armour loss, since the present Chapter focuses on the thermal model of the cable.

The 2-D geometry of the entire model as imported in the FEA tool is illustrated in Figure 3.10, with the cable being located at a distance from the upper boundary equal to the depth of burial (1 m). Isothermal (Dirichlet) boundary conditions are applied on the top and bottom sides of the rectangle, while adiabatic (thermal insulating) conditions are considered on the vertical boundaries, i.e. no heat flux passes through them. The model dimensions must be carefully selected, in order to represent with sufficient accuracy the semi-infinite soil. A rectangular domain of 10 m width and 5 m height is suggested by a Technical Report prepared by IEC, which gives recommendations for current rating calculations using FEM (TR 62095 [50]). A similar approach is followed by Swaffield in [42], who assumes a rectangular region of 20 m width and 7 m height, while a sensitivity analysis is proposed by Kocar in [51] in order to find an optimum position where the boundary conditions do not have any further significant influence on the thermal profile close to the cable. A sensitivity analysis is done in the present section and found that the effect of the position of boundaries is lower than 0.1% when the width and height of the soil domain is set over 100 m and 60 m, respectively. A soil domain of the same size is also employed by Catmull in the FE model used in [52].

An isotherm of 15°C, which represents the seabed temperature, is applied on the upper boundary, as shown in Figure 3.10. A yearly temperature variation of ±6°C in terms of seabed surface is suggested by Worzyk [11]; however, a constant value is adopted in the present

section, since steady-state analysis is performed. The bottom boundary essentially represents the temperature of the remote soil which is expected constant throughout the year. The mean observed equilibrium temperature for the UK at a depth of 100 m is close to 12°C according to a British Geological Survey [53] published in 2011. A value of 12°C is also suggested by Swaffield [42] and Lewin [54] and this is also adopted in the present section. The soil is considered uniform with thermal resistivity ρ = 0.7 Km/W. Concerning, finally, the modelling of the cable itself, the semiconductive layers over and below the main insulation of each core are considered to be of the same thermal resistivity as that of the insulation. Hence, the IEC and FE models become as comparable as possible, since the former assumes a single, uniform thermal layer for the entire annulus between conductor and sheath.

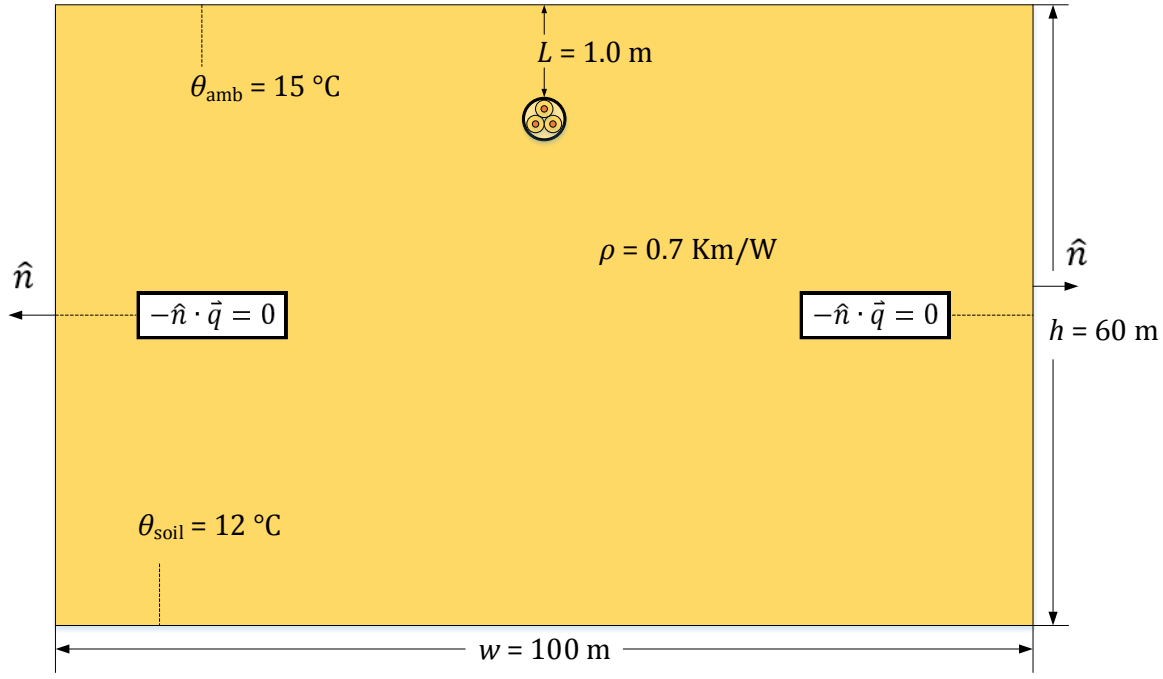

FIGURE 3.10: Model Geometry Showing Boundary Conditions (BCs) and Dimensions - 'Typical' Installation Conditions.

3.5.2 Cables with Solid Fillers

Assuming the 'typical' installation conditions briefly shown in Figure 3.10, FE models are employed, while the existing and the modified SCETM, i.e. that accounting for G_{IEC} and G_{SL}, respectively, are considered. The temperature of conductor is obtained in each case, considering the following procedure: cable ampacity is initially calculated through the existing SCETM assuming 90°C in the conductor; the same current is then applied into the FE model and the corresponding temperature values are obtained, being illustrated in the 4th column of Table 3.6. The difference between them and the existing SCETM (where 90°C is implied) is noted in Table 3.6 as *Initial Difference*, taking the FEA value as a reference. Subsequently, the G_{SL} formula as described by (3.8) is used and the modified SCETM temperature values are

taken, considering the same ampacity (5th column of Table 3.6). The difference between the modified SCETM and FEA is also noted as *Final Difference* in Table 3.6, taking the FEA value as a reference.

Three different Lead sheath thicknesses are tested, while cables of various sizes and, thus, X_{touch} values are modelled. The three X_{touch} values tested may be considered as matching to actual export cable sizes at 66 kV, 150 kV and 220 kV, respectively, with lower X_{touch} values corresponding to higher voltage levels. Indeed, larger conductors and thicker insulations and jackets are in general expected in export cables of higher voltages, so as to transmit the increased power demands; thus, increasing the voltage level, cable designs with higher D_j and, thus, lower X_{touch} are typically used in practice. D_j varies from 43 mm up to about 122 mm, keeping t_{j_ar} = const. = 1.4 mm in the present analysis. Therefore, the applicability of the proposed G_{SL} formula can be widely checked.

TABLE 3.6: Comparison of Results Obtained by FEA & Modified SCETM – SL-Type Cables.

Export Cable Design	X_{touch} (t_{j_ar}/D_j)	Lead sheath thickness, t_s (mm)	FEA (°C)	Modified SCETM (°C)	Initial Difference (°C)	Final Difference (°C)
220 kV	0.012 (1.4/122)	1.5	97.7	98.8	-7.7	1.1
		2.5	96.6	97.1	-6.6	0.5
		3.5	95.5	96.3	-5.5	0.8
150 kV	0.016 (1.4/88)	1.5	96.9	97.6	-6.9	0.7
		2.5	95.8	95.8	-5.8	0.0
		3.5	94.4	95.0	-4.4	0.6
66 kV	0.033 (1.4/43)	1.5	93.6	94.7	-3.6	1.1
		2.5	91.9	93.3	-1.9	1.3
		3.5	91.0	92.6	-1.0	1.6

The results shown in Table 3.6 clearly imply that the present SCETM underestimates the temperature, in some cases by about 7-8°C. In particular, the thinner the Lead sheath and simultaneously the larger its circumference (thus decreasing X_{touch}), the higher the divergence reported in relation to the FEA results. Better agreement between the values derived by the modified SCETM and the FEA can be noticed in most of the cases. An exception may be observed in the last case, where the *Final Difference* seems to be larger in absolute values than the *Initial* one. However, this case represents a rather non-typical cable design: small OWF cables (thus

increasing X_{touch}) do not generally have such a thick Lead sheath. On the contrary, thicker sheaths are not unusual in larger export cables. It is also noteworthy that the existing SCETM appears to be optimistic for modern cables, whereas the suggested modification appears to yield results on the safe side. This is implied by the negative sign of the values being in the *Initial Difference* column, while positive values are depicted in the *Final Difference*.

Similarly good agreement between the modified SCETM and FEA is also obtained for the case of metallic foil screened cables. To derive the temperature values with respect to the modified SCETM, (3.9) and (3.10) are used, while a thickness of 0.2 mm is assumed in all cases. Although this parameter slightly varies in reality (not more than ±0.1 mm), its effect on accuracy is not significant if the same equations are applied. Following the same procedure as for SL-Type case, four X_{touch} values are examined, keeping t_{j_ar} = const. = 1.2 mm and varying D_j from 42 mm up to 78 mm. The relevant results can be seen in Table 3.7. Trends similar to Table 3.6 are noticed. Again, the existing SCETM appears to underestimate more the conductor temperature as larger cable sizes are considered. Although array cable designs of 132 kV may be not presently used, they are not unlikely to be so in the future, given the already high power capacity of each offshore wind turbine and the need for further loss reduction in large OWFs.

TABLE 3.7: Comparison of Results Obtained by FEA & Modified SCETM –Foil Screened Cables.

Array Cable Design	X_{touch} (t_{j_ar}/D_j)	Foil Material	FEA (°C)	Modified SCETM (°C)	Initial Difference (°C)	Final Difference (°C)
132 kV	0.016 (1.2/78)	Al	96.8	97.1	-6.8	0.3
		Cu	96.2	95.7	-6.2	-0.5
66 kV	0.019 (1.2/65)	Al	95.9	96.6	-5.9	0.7
		Cu	95.2	95.2	-5.2	0.0
33 kV	0.023 (1.2/53)	Al	95.6	95.4	-5.6	-0.2
		Cu	95.1	94.2	-5.1	-0.9
33 kV	0.029 (1.2/42)	Al	95.6	95.5	-5.6	-0.1
		Cu	94.9	93.5	-4.9	-1.4

3.5.3 Cables with Extruded (Profile) Fillers

Extruded (profile) fillers are very often used instead of solid ones in OWF cables to give the assembly of cores an effectively more round shape. Unlike the solid fillers made by PP ropes,

they typically comprise gaps to make the cable less stiff and at the same moment to enclose other composite elements, e.g. optical cable units. A detailed geometry, where the exact air gaps are included, is shown in Figure 3.11. Although the gaps are expected to be filled with water in the subsea sections of the cable route (thus resulting in a lower thermal resistance compared to the assumption of a fully solid filler), air-filled gaps can occur at the J-Tubes or the landfall sections where the cable interstices may not be saturated. Hence, the representation of these fillers by the existing SCETM is rather questionable.

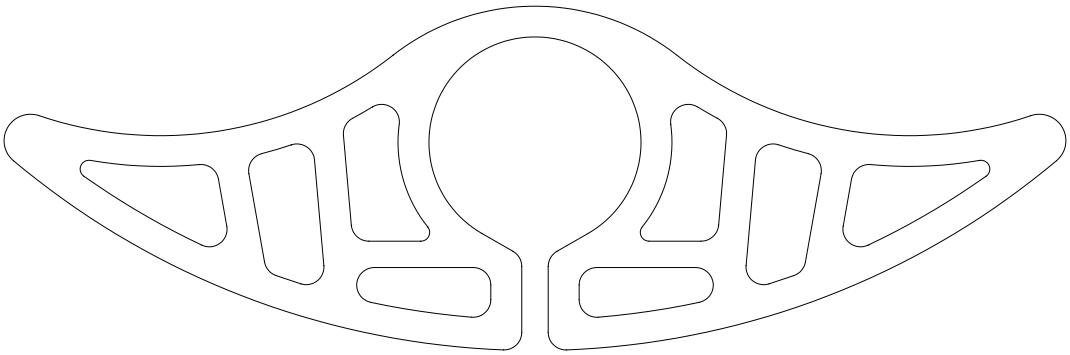

FIGURE 3.11: Detailed Geometry of an Extruded (Profile) Filler.

3.5.3.1 Air-filled Fillers

Owing to the poor thermal conductivity of air, very conservative results would occur if only conductive heat transfer were taken into account. On the other hand, convective heat transfer is likely to be negligible owing to the small size of the gaps and the low temperature gradient across them. To obtain an indication for the contribution of convective heat transfer, Nusselt numbers should be derived. However, it is not easy to calculate them in an analytical way for a geometry such as that of Figure 3.11. A Computational Fluid Dynamics (CFD) analysis implemented through FEM gives a good and relatively quick numerical estimation of how much realistic is to consider the air material as stagnant. Two test cases are examined for the geometry shown in Figure 3.11: one with the air section being treated as a solid material and another one with the air treated as a fluid. Natural convection is considered in the latter case. The air flow is treated as laminar: because of the limited space, air velocities not exceeding 0.1 m/s are expected. Considering typical, book values for the air thermophysical properties [32] and assuming as characteristic length the circumference of the largest hole of the filler (about 75 mm for that shown in Figure 3.11), the Reynolds number, *Re*, is approximately 460, thus justifying the assumption for laminar flow. The Boussinesq approximation is applied to model buoyancy effects inside the gaps. This approach is valid enough, due to the fairly small temperature drop, $\Delta\theta_f$ (K), expected across the filler [55], that is:

$$\beta \Delta\theta_f \ll 1 \tag{3.11}$$

where β is the thermal expansion coefficient (1/K) of the fluid. The temperature drop between jackets and armour, $\Delta\theta_{j\_ar}$, can be assumed around 10°C; taking β = 0.003 K^{-1} for air, $\beta\Delta\theta_{j\_ar}$ = 0.03, which is much lower than 1. By using (3.7), the thermal resistance of fillers and bedding is calculated for each case and the relevant results are presented in Table 3.8. It is verified that the omission of convective heat transfer mode and the consideration of stagnant air in the filler gaps is a reasonable assumption for the filler tested. It is noted that the maximum calculated velocity in the air gap eventually occurs lower than 0.012 m/s as shown in Figure 3.12, thus leading to *Re* equal to about 184: hence, the assumption for laminar flow is verified as fairly reasonable. Although $T_{2,FEA}$ is expected to vary depending on the filler geometry and size, no significantly different results concerning the contribution of natural convection are expected for different filler geometries, because the holes are always kept relatively small. As illustrated in Figure 3.12, a fairly weak velocity field occurs for the filler geometry shown in Figure 3.11, which, in combination with the poor thermal conductivity of air, prevents from any significant heat transfer that could justify convection mechanisms.

TABLE 3.8: Calculation of $T_{2,FEA}$ Assuming Conductive and Convective Heat Transfer (Air-filled Fillers).

Heat Transfer Mode inside Air Gaps	$T_{2,FEA}$ (Km/W)	Difference (%)
Conduction	0.097301	0.105
Convection (CFD analysis)	0.097199	

Although natural convection does not practically contribute to the total heat transfer, radiation from surface-to-surface inside the air gaps could have some considerable contribution in extruded fillers. The heat flow rate of radiation exchange between two surfaces *i*, *j* is given by (3.12) [34].

$$Q = \varepsilon\sigma_B A_{sr}\left(\theta_i^4 - \theta_j^4\right) \tag{3.12}$$

where ε is the emissivity of the surface, σ_B is the Stephan-Boltzmann constant ($5.67\cdot10^{-8}$ W/(m²K⁴)), A_{sr} is the effective radiation area (m²) and θ_i, θ_j is the temperature of the *i*-th and *j*-th surface, respectively (°C).

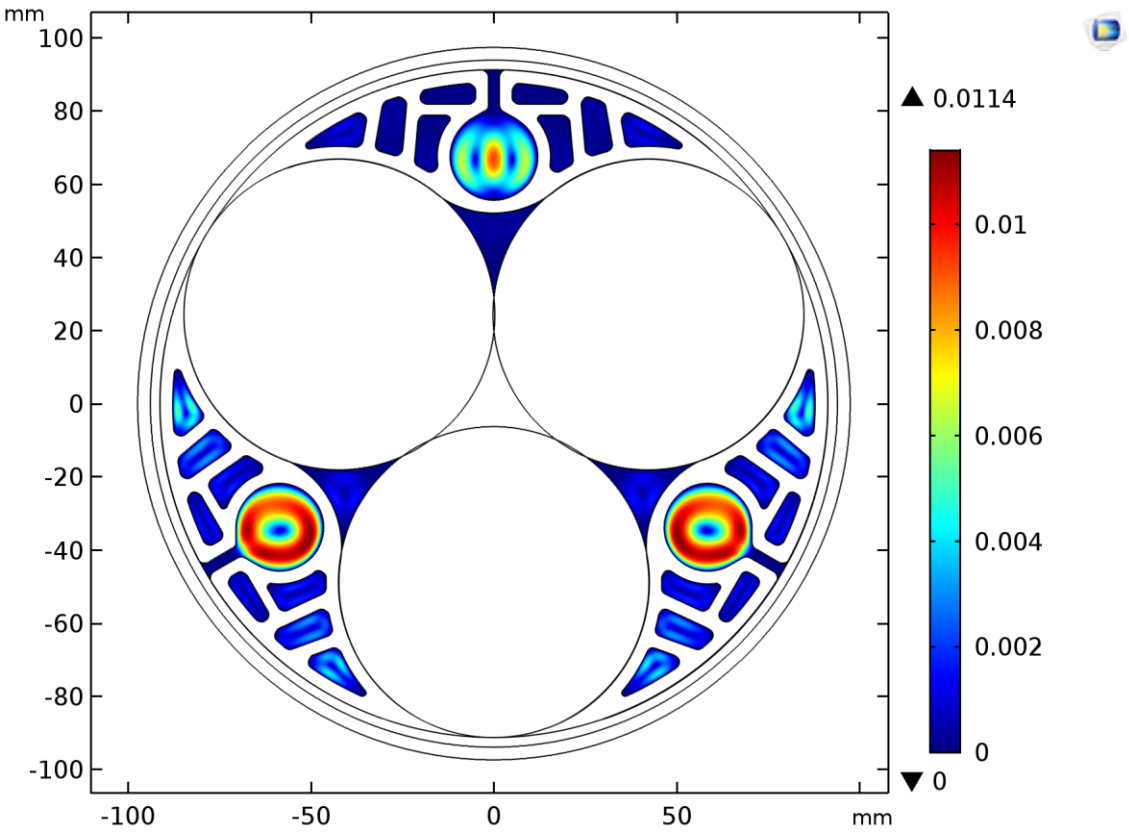

FIGURE 3.12: Fluid (Air) Velocity Magnitude (m/s) inside the Filler Gaps.

It is difficult to precisely define the surface emissivity, as it is strongly material dependent. Anders [34] refers to 0.9 for PVC and PE materials, which are often used for profile fillers, though without mentioning any variation around colour or finish. The same values are also cited by EPRI authors in [56]. The filler geometry is expected to affect the results obtained, since the contribution of each heat transfer mode, namely conduction and radiation, varies depending on the size of the gaps. Both parameters are herein examined and analysed through FEA.

The detailed filler geometry as that shown in Figure 3.11 is initially modelled: surface-to-surface radiation based on (3.12) must be considered within all gaps, so as to account for all the likely radiative heat paths. Although this approach is the most precise one, it is particularly time consuming: a very fine mesh (832392 elements) is required to model the complex geometry, thus rendering the solution computationally demanding. A simplified geometry is considered in the context of the present section (64420 elements) and illustrated in Figure 3.13, in comparison with the detailed one. It is noted that the same area ratio between the gap region and the solid material is kept. By using (3.7), $T_{2,\mathrm{FEA}}$ is estimated for both models, while varying emissivity ε. The relevant results are illustrated in Table 3.9, with the % relative difference in the last column implying the detailed geometry as a reference.

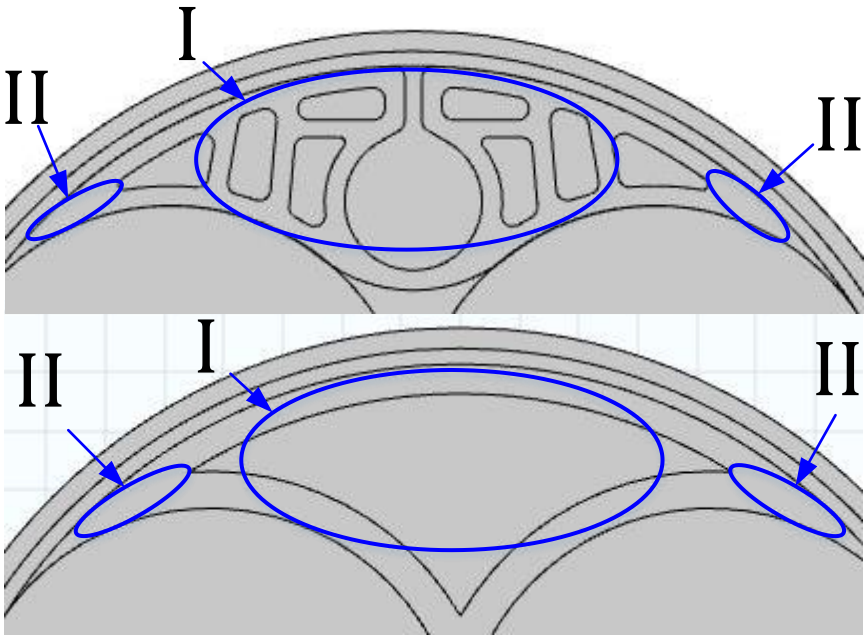

FIGURE 3.13: Detailed (above) and Simplified (below) Extruded (Profile) Filler Geometries.

TABLE 3.9: Thermal Comparison between Detailed and Simplified Filler Geometries.

Emissivity, ε	Filler geometry	$T_{2,FEA}$	% Difference
1	Detailed Geometry	0.097619	3.8
	Simplified Geometry	0.093906	
0.9	Detailed Geometry	0.098215	3.42
	Simplified Geometry	0.09486	
0.8	Detailed Geometry	0.098791	3.04
	Simplified Geometry	0.095789	
0.7	Detailed Geometry	0.099352	2.68
	Simplified Geometry	0.096693	
0.6	Detailed Geometry	0.099903	2.33
	Simplified Geometry	0.097574	
0.5	Detailed Geometry	0.10045	2.01
	Simplified Geometry	0.098434	
0.01	Detailed Geometry	0.1033	0.86
	Simplified Geometry	0.10241	

Fairly low % difference is seen for $T_{2,FEA}$ between detailed and simplified filler representations, especially for lower ε values. Although such a simplification in geometry is an approximation, it seems to work rather satisfactorily mainly because heat prefers more the shorter, conductive paths between the outer surface of the cores and the bedding (regions II in Figure 3.13) rather than the longer ones, i.e. through the main filler area (regions I in Figure 3.13); thus, the respective part of T_2, namely $T_{2,II}$, is much higher than $T_{2,I}$ and any approximation in geometry in that thicker area has minor effects in total T_2. In fact, although the conductive heat paths of $T_{2,I}$ are rearranged, their overall contribution remains essentially the same, since the area of the solid part is kept unchanged. Radiative heat paths are also rearranged, due to modification in geometry; however, the slightly stronger effect noticed for higher ε values implies that they are redistributed less effectively. It is noteworthy that the lowest % difference (below 0.9 %.) is noticed for the theoretical value ε = 0.01, i.e. a case that the radiative mechanism is intentionally kept almost deactivated.

In any case, the relative difference in terms of $T_{2,FEA}$ between detailed and simplified geometries occurs fairly low: a maximum of 3.8% is seen in Table 3.9 when varying emissivity ε. This is interpreted as maximum difference of 0.4 °C in conductor temperature when considering a cable in typical installation conditions (section 3.5.1). Hence, the simplified geometry may be considered accurate enough, while much easier to solve: a few seconds (5 – 7 s) are required, instead of about 4 min for the detailed geometry. Comsol Ver. 5,3a software is used for these calculations in a workstation with an Intel (R) i7-6700, 3.40 GHz CPU, 32 GB of RAM memory and a 500 GB solid-state drive for memory swapping. Although a solution time of 4 min does not look at first glance immense, it has to be pointed out that this relates to a Steady-State analysis, which is in general quite fast. However, Transient Analysis is likely to be required in order to deduce the current rating of the cable. For example, there are cases that yearly historical load data, which are generated from actual OWF operation, are given as an input, and the Dynamic response of the cable is requested. In such cases, significantly more computationally inefficient thermal models will occur if the detailed geometry is used, while the gain in accuracy will be small. For instance, if such a model needs in total 2 hours for the simplified fillers, it might need (4 min/6 s)·2 = 40·2 hours = 80 hours (more than 3 days) for the detailed ones. Thanks to this, computationally more efficient filler model, further analysis is subsequently done and useful conclusions are deduced with regard to the geometry of the filler.

Several geometries with the solid and non-solid part of the filler having thermal resistivity equal to ρ_{fb} and ρ_{air}, respectively, where ρ_{air} is the thermal resistivity of air (Km/W), are examined through FEA. The jackets are assumed isotherms to simplify the analysis. The non-solid part is considered filled with still air (no convection), while the emissivity varies from 0.5 to 1.0. Eq. (3.7) is used to calculate $T_{2,FEA}$. In addition, T_2 is analytically obtained from the

existing IEC 60287-2-1 Standard. In this latter case, the weighted average based on the volumetric proportions of the solid and non-solid parts is used to calculate the equivalent thermal conductivity of the fillers and bedding domain, $k_{\text{fb\_eqvl}}$ (W/(Km)):

$$k_{\text{fb\_eqvl}} = \left(\frac{1}{\rho_{\text{fb}}}\right) A + \left(\frac{1}{\rho_{\text{air}}}\right) B \tag{3.13}$$

where A and B is the volume fraction of the solid and the non-solid part, respectively, out of the total area of the filler and bedding domain. Obviously, $A + B = 1$. Four cases pertaining to A and B are examined, as per Figure 3.14. T_2 values calculated by (3.13) are noted as IEC_{eqvl}.

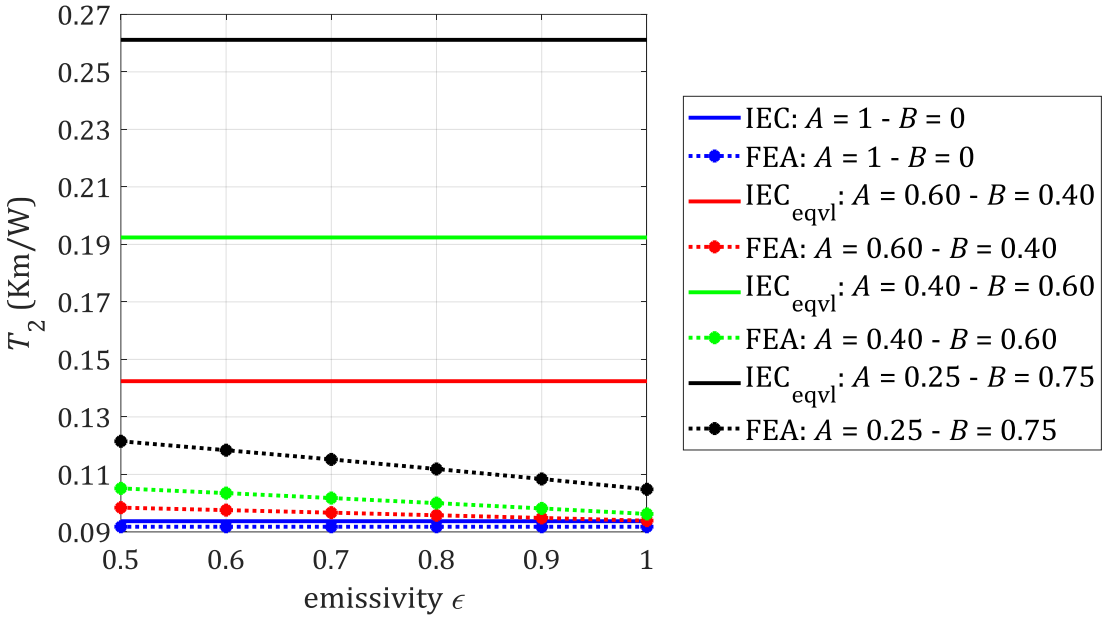

FIGURE 3.14: T_2 Results for Different Air-Filled Filler Geometries Considering Various Emissivity Values.

For entirely solid fillers (A = 1 and B = 0) $T_{2,\text{IEC}}$ and $T_{2,\text{FEA}}$ appear a fairly good agreement: the slight divergence of about 2% is attributed to the *geometrical error* cited in section 3.3.2. As A and B decreases and increases, respectively, a noticeable dependence on emissivity ε is seen in Figure 3.14: $T_{2,\text{FEA}}$ depends more on the emissivity of filler material and the heat transfer is dominated more by the conduction through the air gap. For higher emissivity values, the radiative heat transfer appears to compensate to some considerable extent for the poor air thermal conductivity. If the assumption of ε = 0.9 is considered, a relative difference of lower than 7% occurs between $T_{2,\text{FEA}}$ for a filler with A = 0.4 and B = 0.6 and $T_{2,\text{IEC}}$ for a totally solid filler (A = 1 and B = 0). This is translated to a difference of about 0.7°C in conductor temperature when typical installation conditions are considered (section 3.5.1). Therefore, filler geometry remains of minor importance when higher emissivity values are assumed. However, if more extreme assumptions are made, for instance that of ε = 0.5 in a filler with A = 0.25 and B = 0.75,

the difference in temperature may reach up to 3.4°C, thus making the geometry of higher importance.

The use of (3.13) in the existing IEC model leads to apparently more conservative $T_{2,IEC}$ values. This is expected, because k_{fb_eqvl} worsens not only $T_{2,I}$, which is indeed filled with air, but also $T_{2,II}$ (Figure 3.13), which in FEA still comprises solely solid material. Since $T_{2,II}$ contributes more to the total T_2, $T_{2,IEC}$ is eventually higher than $T_{2,FEA}$. Considering the most extreme scenario where A = 0.25 and B = 0.75, an overestimation of about 18°C occurs for ε = 0.9 regarding conductor temperature under typical installation conditions. This is interpreted in an ampacity which is 9% lower. However, assuming a more realistic geometry, such as that for A = 0.6 and B = 0.4 (this ratio holds true also in the case of the detailed filler geometry shown in Figure 3.11), the use of (3.13) leads to underestimating the ampacity by 3% only. Therefore, in most cases this practical method gives sensible results, standing on the safe side.

3.5.3.2 Water-filled Fillers

An analysis similar to that presented in section 3.5.3.1 is also made for water-filled fillers. Although the thermal conductivity of water is higher than that of air, the contribution of the convective heat transfer mode is expected to be low, because of the small size of the holes; indeed, the difference in $T_{2,FEA}$ when CFD analysis is employed and when only conductive heat transfer mode is assumed does not exceed 5%, as shown in Table 3.10. The maximum calculated velocity in the water gap occurs lower than 0.0014 m/s as shown in Figure 3.15.

TABLE 3.10: Calculation of $T_{2,FEA}$ Assuming Conductive and Convective Heat Transfer (Water-Filled Fillers).

Heat Transfer Mode inside Water Gaps	$T_{2,FEA}$ (Km/W)	Difference (%)
Conduction	0.081815	4.345
Convection (CFD analysis)	0.078408	

The consideration of the water section as a fluid appears to have a slightly stronger effect than the consideration of the air as a fluid, as demonstrated by comparing Table 3.8 and Table 3.10. Although the velocity field in the water occurs about one order of magnitude lower than air, which is expected because of the higher dynamic viscosity of water, the slightly lower $T_{2,FEA}$ shown for CFD in Table 3.10 is attributed to the better thermal conductivity of the water. Also the fact that a medium of higher thermal conductivity compared to the solid filler part is used enhances the contribution of $T_{2,I}$ to the total T_2 and renders the respective heat path more active; hence, even this slow motion of the fluid has a slightly more intense effect on $T_{2,FEA}$

compared to the air-filled filler. However, the contribution of convection may be considered negligible even in the case that the filler is filled with water without significant loss in accuracy.

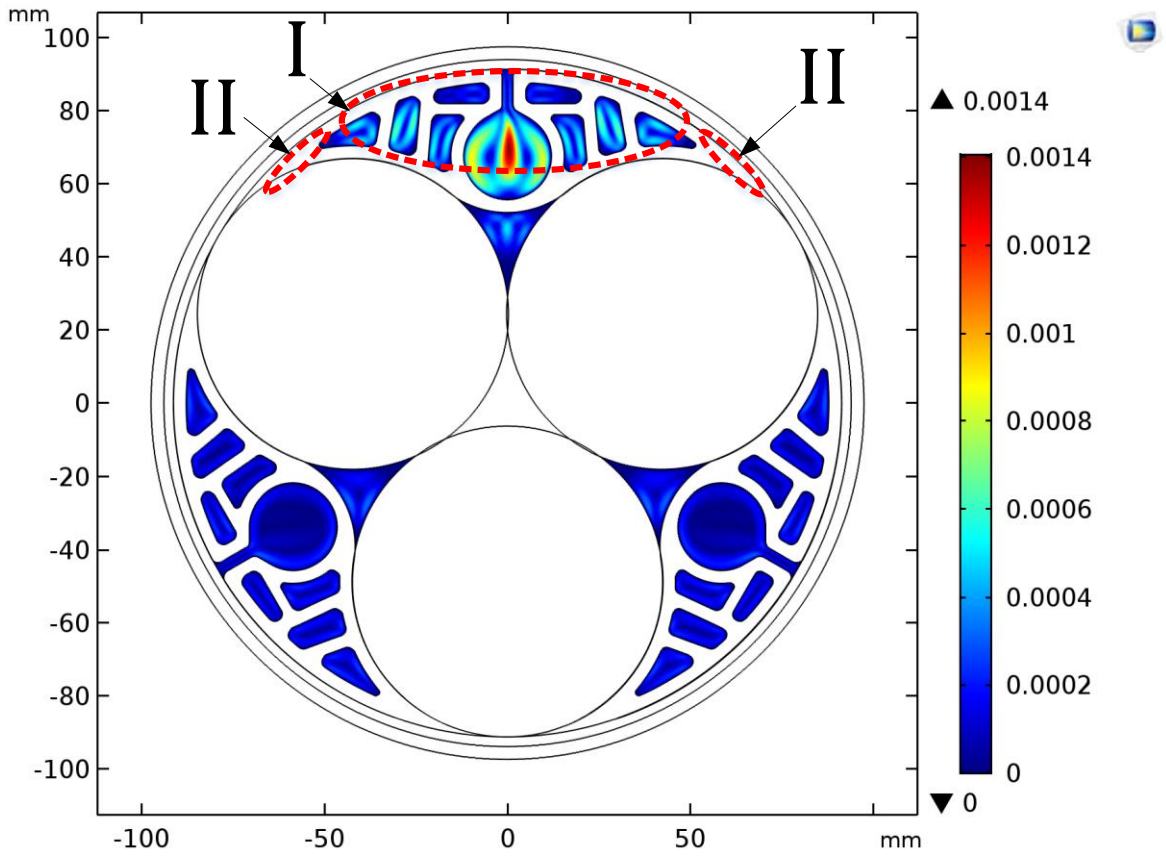

FIGURE 3.15: Fluid (Water) Velocity Magnitude (m/s) inside the Filler Gaps.

An analysis similar to that adopted in section 3.5.3.1 is also followed in this section: a more simplified geometry as that shown in Figure 3.13 is preferred. No radiative heat transfer is expected in this case, because the water is considered opaque. Geometries with A and B as those presented in Figure 3.14 are considered in this section, while (3.13) is used to calculate the T_2 based on the equivalent thermal conductivity. ρ_{water} is herein used instead of ρ_{air}. The relevant results are presented in Table 3.11.

Because of the better thermal conductivity of the water, the heat dissipation through the filler region I (Figure 3.15) is substantially better compared with the air-filled fillers. Increase in B results in improved $T_{2,FEA}$ values, as expected and shown in Table 3.11. In contrast with the results shown in Figure 3.14, the use of (3.13) leads to more optimistic $T_{2,IEC}$ results in Table 3.11 in comparison with $T_{2,FEA}$. Although the presence of the water affects T_2 in total, $T_{2,II}$ (Figure 3.15) still has dominant role to the total T_2. Since region II is occupied by the solid material in FE models, $T_{2,FEA}$ occurs now higher than $T_{2,IEC}$ values calculated based on (3.13). Considering an equivalent thermal conductivity which gives results not in the safe side would not be a good practice and the use of the solid material solely is recommended in this case. Considering the

most extreme scenario where A = 0.25 and B = 0.75, an ampacity which is by about 2% lower occurs, while the difference drops below 1% when dealing with more realistic A, B values, as for instance those of the detailed filler geometry shown in Figure 3.11 (A = 0.6 and B = 0.4 in that figure).

TABLE 3.11: T_2 Results for Different Water-Filled Filler Geometries.

Method	A, B values	T_2 (Km/W)
IEC	$A = 1 - B = 0$	0.09372
FEA		0.09179
IEC_{eqvl}	$A = 0.60 - B = 0.40$	0.04254
FEA		0.08419
IEC_{eqvl}	$A = 0.40 - B = 0.60$	0.03342
FEA		0.07619
IEC_{eqvl}	$A = 0.25 - B = 0.75$	0.02879
FEA		0.06472

3.6 Summary

This Chapter presents new analytical formulae which can be adopted by the existing SCETM presented in Chapter 2 and improve its accuracy. Comparisons are initially made between the existing analytical model and a quasi-1-D FE model and the results appear in a very good agreement. Subsequently, FE models are developed, by adopting gradually more realistic conditions compared to the existing SCETM. Focus is made on the thermal resistance between jackets and the armour, namely T_2. The current Standard method implies both the jackets and the filler are made of materials with identical thermal properties, while additionally it does not account for the thermal impact of different sheath materials. Most importantly, the 1-D thermal representation implied by the Standard appears in this chapter to be rather questionable. Relatively small divergences between the FE models developed and the existing SCETM are noticed when small core sizes are modelled. However, significant discrepancies are observed for larger core sizes, especially when the corresponding sheath thickness is small. This is particularly important for the forthcoming OWF projects which are expected to include increasingly larger cable sizes, as the results present here show that the SCETM model can underestimate the temperature by up to 8°C.

The key design factors, such as sheath thickness and material, as well as the core diameter, are then identified. FE models are used to implement an extensive sensitivity analysis by varying these factors. The new analytical formulae suggested regarding the geometric factor G are applicable to all modern OWF cable sizes. As shown, they improve the divergence between SCETM and FEA: from 8°C via the existing SCETM up to 1°C via the proposed formulae, additionally being on the safe side when tested for export cables laid under typical subsea installation conditions. Although the most accurate solution is obtained using the FE models, this would be unsuitable for quick current rating calculations, especially in the case that long transient thermal models are requested for the current rating of OWF cables. The derived analytical G formulae are easily adoptable by the present IEC 60287 version and can be used for Standardisation purposes, keeping at the same moment an acceptable degree of accuracy with respect to the FE models. Finally, useful modelling recommendations are given concerning the increasingly used extruded (profile) fillers, including both air- and water-filled fillers. The use of an equivalent thermal conductivity appears to give results on the safe side in the former case; however, the consideration of a solely solid material is recommended in the latter.

Focus has been so far given on the way cable losses are dissipated through the cable interior. Although this is of apparent importance, it is also valuable to examine in depth the way these losses are generated. As presented in Chapter 1, the electromagnetic model implied by the existing Standard needs to be reviewed, so as to derive more accurate current ratings. The next Chapter gives the necessary theoretical background for this purpose. A thorough literature review is made, investigating not only the origins of the existing analytical formulae, but also later modelling techniques already suggested by other researchers.

Chapter 4 Generation of Losses in 3C Submarine Cables: Existing Methods

The thermal model of the cable interior has been examined in Chapter 2 and Chapter 3. This implies a conductive heat transfer model, given the losses generated inside the cable. As mentioned in Chapter 1 (section 1.1.4), the second component of cable current rating is the estimation of these losses. The cost of a cable circuit is partly determined by the conductor size, and is often crucial for the economic viability of projects such as Offshore Wind Farms (OWFs). To optimise the cable size, an accurate calculation of losses is required. Besides the losses generated in the dielectric and the Joule loss in conductor, additional losses are induced in the remaining metallic parts of HVAC cables, i.e. sheaths and armour, because of the relevant AC phenomena.

This Chapter aims to review methods, already developed by other researchers, which are capable of simulating the AC phenomena occurring in power frequency, i.e. skin and proximity effects, in 3C SL-Type armoured cables. Firstly, the formulae currently adopted by the present IEC 60287-1-1 Standard version [16] are presented and their origins and assumptions are investigated. Emphasis is given to the extent these assumptions are likely to hold true for modern 3C submarine cables, while the gaps still existing are highlighted. Secondly, this Chapter presents more modern modelling approaches currently existing in the literature for loss calculation in SL-Type cables with magnetic armour: certain recently developed models which account for the twisting effect of the armour are discussed. Thirdly, other, existing models which are not so broadly applied for loss calculations, such as those used to calculate the frequency-dependent parameters of the cable through an impedance matrix, **Z**, are also examined. A numerical method which has an analytical background and considers the partitioning of the metallic components into smaller, filamentary current sources, is presented. Although this can be found via different names and versions in the literature (Subdivision of Conductors [20], Multiconductor Analysis [57], Filament Method [34], Partial Subconductor Equivalent Circuit [58]), all rely on the same principles. The term Filament Method is adopted in the present thesis. The various versions of the method are reviewed and their potential use for loss calculations in 3C Submarine Cables is discussed in the present Chapter.

4.1 Existing Analytical Formulae: IEC 60287

The formulae used by IEC 60287 [16] are presented in this section, and their origins are investigated. First, the loss generated in the phase conductors is presented; the losses induced in sheaths follow; finally, the losses generated in the armour are briefly shown.

4.1.1 Conductor Loss

The resistance of a conductor carrying an alternating current is higher than that of the conductor carrying a direct current due to skin and proximity effects. This resistance (Ω/m), already used in (2.1) to define W_C, is defined for all cable types except for pipe-type cables, as follows, according to IEC 60287-1-1 (§ 2.1) [16]:

$$R_{AC} = R_{DC}\left(1 + y_s + y_p\right) \tag{4.1}$$

where R_{DC} is the DC resistance of the conductor at operating temperature (Ω/m), y_s and y_p is the skin and proximity effect factor, respectively. When a conductor is isolated, it experiences the skin effect only (y_p = 0) and the current density increases towards its outer surface. Skin effect is a fundamental behaviour of a conductor in isolation. The following formulation is suggested by the IEC 60287-1-1 Standard (§ 2.1.2) [16]:

For $0 < x_s \leq 2.8$

$$y_s = \frac{x_s^4}{192 + 0.8x_s^4} \tag{4.2}$$

For $2.8 < x_s \leq 3.8$

$$y_s = -0.136 - 0.0177x_s + 0.0563x_s^2 \tag{4.3}$$

For $x_s > 3.8$

$$y_s = 0.354x_s - 0.733 \tag{4.4}$$

where

$$x_s^2 = \frac{8\pi f}{R_{DC}} 10^{-7} k_s \tag{4.5}$$

where f is the supply frequency (Hz) and k_s is an empirical coefficient introduced to take into account of the stranding and treatment of the conductor. k_s values between zero and unity are referred to Table 2 in [16], depending on the type of conductor and the insulation system.

The problem of an isolated solid conductor being at the centre of a tubular conductor (annulus) under single phase operation has a rigid analytical solution. One of the earliest and best known works is that by Russell, which dates back to 1909 and 1914 [59]. Russel adopts a different variable in place of x_s presented in (4.5). Assuming μ_r = 1, that is:

$$m_C^2 = \frac{2\pi f \mu_r \mu_0}{\rho_C} = \frac{8\pi^2 f 10^{-7}}{\rho_C} = \frac{8\pi^2 f\ 10^{-7}}{R_{DC}} \frac{1}{\pi r_C^2} \tag{4.6}$$

where ρ_C, μ_r and r_C is the electrical resistivity (Ω·m), the relative magnetic permeability and the radius (m) of conductor, respectively. For solid conductors it is $k_s = 1$, thus

$$x_s = m_C r_C \tag{4.7}$$

Russell considers the mathematical problem of an isolated coaxial cable, where the current density is the unknown spatial function. This is expressed in [59] by means of Bessel differential equations. Russell determines the R_{AC} to R_{DC} ratio as

$$\frac{R_{AC}}{R_{DC}} = \Re\left\{\frac{m_C r_C J_o(m_C r_C)}{2 J_1(m_C r_C)}\right\} = \frac{m_C r_C}{2}\left[\frac{ber\, m_C r_C\, bei' m_C r_C - bei\, m_C r_C\, ber' m_C r_C}{(ber' m_C r_C)^2 + (bei' m_C r_C)^2}\right] \tag{4.8}$$

where J_0 is a Bessel function of the first kind and zero order, J_1 is a Bessel function of the first kind and first order,

$$ber\, x = 1 + \sum_{k=1}^{\infty} \frac{(-1)^k}{[(2k)!]^2}\left(\frac{x}{2}\right)^{4k} \tag{4.9}$$

and

$$bei\, x = \sum_{k=0}^{\infty} \frac{(-1)^k}{[(2k+1)!]^2}\left(\frac{x}{2}\right)^{4k+2} \tag{4.10}$$

are Kelvin functions and *ber'* and *bei'* their derivatives with respect to variable *x*. Although Russell's formulae are strictly analytical and accurate, the computation of infinite series was a laborious task in 1914. For this reason, approximations for (4.8) were sought by many researchers. Arnold proposes in 1936 [60] the following approximations for (4.8) with an error lower than 0.6%:

For $0 < m_C r_C \leq 2.8$

$$\frac{R_{AC}}{R_{DC}} = 1 + \frac{(m_C r_C)^4}{192 + 0.8(m_C r_C)^4} \tag{4.11}$$

and, for $m_C r_C > 3.8$

$$\frac{R_{AC}}{R_{DC}} = 0.354(m_C r_C) + 0.267 \tag{4.12}$$

Assuming an isolated cable ($y_p = 0$), (4.1) gives

$$\frac{R_{AC}}{R_{DC}} = 1 + y_s \tag{4.13}$$

where it becomes apparent that the current IEC 60287-1-1 Standard version [16] relies on Arnold's work [60]. The $m_C r_C$ limits referred to the applicability of (4.11) and (4.12) may be interpreted to modest and by far larger conductors, respectively, at power frequency. Indeed, radii r_C up to about 18 mm and 23 mm in terms of copper and aluminium conductors, respectively, are covered by (4.11) at 50 Hz. These r_C values are equivalent to about 800 mm^2 Cu and 1200 mm^2 Al conductors, respectively. Radii r_C above 25 mm (corresponding to conductor sizes higher than 1800 mm^2) and 32 mm (corresponding to conductor sizes higher than 2500 mm^2) for copper and aluminium conductors, respectively, are covered by (4.12). To cover this gap for medium and large conductors, Goldenberg [61] adds in 1961 another approximation, i.e. that expressed by (4.3).

When two or more conductors are placed next to one another, their current distribution is further distorted, owing to the interaction of their magnetic fluxes and the eddy currents inevitably induced. In this case, besides the skin effect, also proximity effects take place. The following formulation is suggested by the IEC 60287-1-1 Standard (§ 2.1.4.1) [16] for 3C cables:

$$y_p = \frac{x_p^4}{192 + 0.8x_p^4}\left(\frac{d_c}{s}\right)^2\left[0.312\left(\frac{d_c}{s}\right)^2 + \frac{1.18}{\frac{x_p^4}{192 + 0.8x_p^4} + 0.27}\right] \tag{4.14}$$

where

$$x_p^2 = \frac{8\pi f}{R_{DC}} 10^{-7} k_p \tag{4.15}$$

where d_c is the diameter of conductor (m), s is the distance between conductor axes (m) and k_p is an empirical coefficient introduced to take into account of the stranding and treatment of the conductor. k_p values are referred to Table 2 in [16], depending on the type of conductor and the insulation system.

As with the skin effect factor, the exact expressions for the proximity factor require the solution of Bessel equations. Eqs. (4.14), (4.15) have their origins to Arnold's work [62] published in 1941. They also are approximations, which are demonstrated to be quite accurate: differences versus experimental data appear in [62] to be less than 0.8% for three phase solid conductors in triangular arrangement.

Similar formulae are considered by IEC 60287-1-1 for R_{AC} in pipe-type cables with magnetic pipe (§ 2.1.5 in [16]). However, in this case, (4.16) is used instead of (4.1), so as to account for the effect of the pipe on R_{AC}.

$$R_{AC} = R_{DC}\left(1 + 1.5\left(y_s + y_p\right)\right) \tag{4.16}$$

The 1.5 factor used in (4.16) is empirically derived and suggested by Silver [63]. Although the effect of the magnetic pipe on R_{AC} is taken into consideration for pipe-type cables, no such consideration is made in IEC 60287-1-1 for the corresponding effect in SL-Type cables with magnetic wire armour and the use of (4.1) is presently implied. The WG B1.56 constituted by Cigré Study Committee B1 [29] suggests the use of (4.16) even for SL-Type cables. However, the inclusion of factor 1.5 in (4.1) is believed to be a rather conservative approach for SL-Type cables with magnetic armour, as also noted in [29].

4.1.2 Sheath Eddy Loss

Losses induced in sheaths can be divided into two groups, depending on the type of bonding: losses mainly due to circulating currents flowing in sheaths if they are Solidly Bonded (SB), and those caused by eddy currents circulating radially and azimuthally for Single-Point Bonded (SPB) sheaths. As Anders points out in his book [34], eddy current loss occur irrespective of the bonding method, although it is often ignored in solidly bonded sheaths where it is assumed small in magnitude compared to circulating current loss.

Sheath eddy currents of 1st order occur as a result of the combined effect of the internal conductor current and the external currents in neighbouring cables. Eddies local to the sheath wall only (self-induced currents) are generated by the former, while currents circulating from wall to wall of the same sheath occur by the latter. Self-induced currents are in practice negligible. A 2nd order eddy current arises from the effect of the magnetic field of 1st order eddies in neighbouring sheaths and the process continues until the successive order eddies have negligible effect in the sheath considered [1].

The most precise analytical approach was provided by Jackson in 1975 [1]. He successfully extended Carter's earlier work [64] accounting for higher order eddy currents by means of formulae including infinite series. The 1st order loss factor in terms of external currents is shown in (4.17) assuming 1C cables in trefoil spaced formation with three-phase balanced currents.

$$\lambda''_{1\,1\mathrm{st}} = \frac{R_S}{R_{AC}} \sum_{n=1}^{\infty} \left[2 \left(\frac{d}{2s} \right)^{2n} \frac{m^2}{n^2 + m^2} \left(2 - cos \frac{n\pi}{3} \right) \right] \tag{4.17}$$

where R_S is the resistance of sheath per unit length (pul) of cable (Ω/m), d is the mean diameter of sheath (mm) and m is the frequency to resistance dimensionless ratio given by (4.18):

$$m = \frac{\omega}{R_S} 10^{-7} \tag{4.18}$$

where ω is the angular frequency (rad/s). Although (4.17) appears to be accurate enough for widely spaced cables or small m values, i.e. less conductive sheaths (e.g. Lead), considerable errors of up to 20% may occur for cables in close formation, or those with more conductive sheaths (e.g. Aluminium) if higher order eddy currents are excluded [1]. 2nd or higher order eddy current loss factors consist of multiple infinite series, and as shown by Jackson [1], the effect of 4th and higher order currents can usually be neglected.

The report published by ERA [65] suggests an empirical method based on the previous work published by Heyda [66], which comprises tabulated values. As reported in [65], these are in an excellent agreement with Jackson's method. Although Jackson's work is recognised as valuable and very accurate, the computation of infinite series was a laborious task in 1979. Hence, a simpler method suitable for hand calculation is proposed by [65]. ERA's method has been adopted by IEC 60287 (§ 2.3.6.1) and is currently used to calculate eddy current losses in single-point bonded sheaths. The relevant formulae are presented in the following equations for 1C cables in triangular formation:

$$\lambda''_{1,\mathrm{IEC}} = \frac{R_\mathrm{S}}{R_\mathrm{AC}}\left[g_\mathrm{S}\lambda_0(1+\Delta_1+\Delta_2)+\frac{(\beta_1 t_\mathrm{S})^4}{12\cdot 10^{12}}\right] \tag{4.19}$$

where t_S is the thickness of sheath (mm) and

$$g_\mathrm{S} = 1+\left(\frac{t_\mathrm{S}}{D_\mathrm{S}}\right)^{1.74}(\beta_1 D_\mathrm{S}10^{-3}-1.6) \tag{4.20}$$

$$\lambda_0 = 3\left(\frac{m^2}{1+m^2}\right)\left(\frac{d}{2s}\right)^2 \tag{4.21}$$

$$\Delta_1 = (1.14m^{2.45}+0.33)\left(\frac{d}{2s}\right)^{0.92m+1.66} \tag{4.22}$$

$$\beta_1 = \sqrt{\frac{4\pi\omega}{10^7\rho_\mathrm{S}}} \tag{4.23}$$

where D_S is the external diameter of cable sheath (mm), ρ_S is the electrical resistivity of sheath material (Ω·m) and $\Delta_2 = 0$ for 1C cables in trefoil formation. It is readily noticeable that the sum factor in (4.17) leads to (4.21) for $n = 1$. Term Δ_1 intends to approximate the infinite series derived by Jackson's paper [1].

4.1.3 Sheath Circulating Loss

When sheaths are solidly bonded and ungrounded, induced currents flow in one direction along one sheath, returning along another. If they are additionally grounded at both ends, as

are in practice in subsea links, a return current is allowed to flow through the earth and any other grounded metallic parts of the cable (armour, sheaths). Balanced currents are typically assumed in loss calculations. Additionally, a configuration which includes an SL-Type cable in isolation (no neighbouring cables or other metallic objects) may be considered as symmetrical. Under these two assumptions, the return current is considered null and the induced currents circulate from sheath to sheath. These assumptions are implied by the IEC 60287-1-1 Standard [16]. The formulae which is adopted by [16] regarding the sheath circulating loss factor date back to the work published by Arnold [67] and are presented in this section for three 1C cables in trefoil formation (§ 2.3.1 in [16]):

$$\lambda'_{1,\mathrm{IEC}} = \frac{R_\mathrm{S}}{R_\mathrm{AC}} \frac{1}{1 + \left(\frac{R_\mathrm{S}}{X_\mathrm{S}}\right)^2} \tag{4.24}$$

where X_S is the reactance pul of sheath (Ω/m), i.e.

$$X_\mathrm{S} = 2\omega 10^{-7} \ln\left(\frac{2s}{d}\right) \tag{4.25}$$

Total losses in the sheath consist of losses caused by circulating and eddy currents and the respective factor is [16]:

$$\lambda_{1,\mathrm{IEC}} = \lambda'_{1,\mathrm{IEC}} + \lambda''_{1,\mathrm{IEC}} \tag{4.26}$$

Although eddy current loss is important for single-point bonded sheaths, it becomes less significant when solidly bonded sheaths are considered, as already cited by Anders [34]. The IEC 60287-1-1 Standard has adopted this view, by neglecting $\lambda''_{1,\mathrm{IEC}}$ for solid bonding cases. However, $\lambda''_{1,\mathrm{IEC}}$ may become significant for cables laid in close proximity, whereas $\lambda'_{1,\mathrm{IEC}}$ is minimised for touching formation. Assuming, for instance, three power cores of outer diameter D_j with a Copper conductor of radius equal to 25 mm and an Lead sheath of t_S = 2.5 mm, $\lambda''_{1,\mathrm{IEC}}$ rises from about 0.02 to 0.13 when reducing the axial distance from $s = 3D_\mathrm{j}$ to $s = D_\mathrm{j}$ (touching) and at the same moment $\lambda'_{1,\mathrm{IEC}} = 0.46$ for $s = D_\mathrm{j}$. Therefore, $\lambda''_{1,\mathrm{IEC}}$ and $\lambda'_{1,\mathrm{IEC}}$ may not be so incomparable and the omission of eddy current loss appears to be questionable for cables in touching arrangement.

The analytical formulae presented in section 4.1.2 and in the present one for eddy and circulating losses in sheaths, respectively, assume three cores in trefoil formation with no armouring above them. Similar to section 4.1.1, the presence of magnetic armour is expected to alter the eddy and circulating current losses induced in the sheaths. It is of importance to note that the current IEC 60287-1-1 Standard version [16] considers this effect by amending circulating loss only, leaving unaltered the eddy current loss. This effect is expressed by multiplying (4.24) by 1.5 (§ 2.3.10 in [16]):

$$\lambda'_{1,\mathrm{IEC}} = \frac{R_S}{R_{AC}} \frac{1.5}{1 + \left(\frac{R_S}{X_S}\right)^2} \tag{4.27}$$

Factor 1.5, which had been initially 1.7, was added to comply with the measurements performed in the USA in 1980's for pipe-type cables [63]; thus, it is an empirically derived factor related to a cable geometry different than SL-Type with wire armour. The twisted armour wires are expected to behave in a rather different way compared to a pipe with respect to the distribution of magnetic flux in the armour. A pipe is a fairly simple, cylindrical geometry, where the circumferential (transversal to its thickness) magnetic flux has a dominant role; hence, 2-D analysis would be a rather easy and good approximation. On the other hand, in wire armoured cables some considerable amount of flux is expected to be longitudinally driven along the wire axis, due to its angle, φ (Figure 4.1), with reference to the power core axis; therefore, the total magnetic flux inevitably consists of a longitudinal and a transversal components, shown by $\overrightarrow{B_y}$ and $\overrightarrow{B_x}$, respectively, in Figure 4.1. This in principle requires 3-D analysis in order for the magnetic flux to be correctly considered. Therefore, the rather complex wire geometry is expected to affect not only the armour loss itself, but also the losses generated in sheaths and conductors, in a different way to that expected in pipe type cables, where no relative twisting exists and $\overrightarrow{B_y} = 0$.

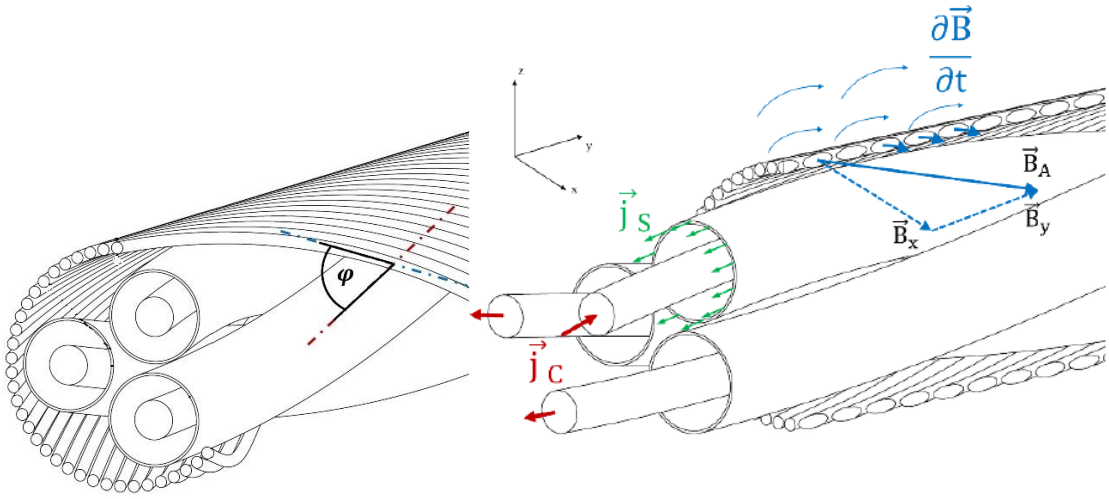

FIGURE 4.1: Illustration of the Angle φ between Power Cores and Armour Wires (on the Left) – Illustration of the Longitudinal and Transversal Components, i.e. $\overrightarrow{B_y}$ and $\overrightarrow{B_x}$, Respectively, of the Total Magnetic Flux, $\overrightarrow{B_A}$ [68] (on the Right).

4.1.4 Armour Loss

The current IEC 60287-1-1 Standard version [16] suggests the following formula for the armour loss factor when SL-Type cables are considered (§ 2.4.2.3.1 and § 2.4.2.5):

$$\lambda_{2,\mathrm{IEC}} = 1.23\frac{R_{\mathrm{A}}}{R_{\mathrm{AC}}}\left(\frac{2c}{d_{\mathrm{A}}}\right)^2 \frac{1}{\left(\frac{2.77R_A \cdot 10^6}{\omega}\right)^2 + 1}\left(1 - \frac{R_{\mathrm{AC}}}{R_{\mathrm{S}}}\lambda'_{1,\mathrm{IEC}}\right) \tag{4.28}$$

where R_{A} is the AC resistance of the armour (Ω/m) at operating temperature, c is the distance between the axis of a conductor and the cable centre (mm), d_{A} is the mean diameter of armour (mm). The last factor of (4.28) represents the so called "screening effect" caused by the currents circulating in sheaths and reduces the armour loss, according to [16]. The remaining factors of (4.28) are semi-empirically derived and their origins date back to the work published by Arnold [69] in 1939. Experimental results appear to be in agreement with the theoretically derived values in [69]. However, paper-insulated cables with a common sheath and an extra common layer of armour wires are implied, thus a geometry different than that of SL-Type armoured cables. Furthermore, the physical origin of armour losses is not clearly stated in the existing Standard version [16]. In Arnold's work [69] loss is implied to be generated by eddy currents induced in the armour. Eq. (4.28) seems rather similar to the first term of (4) in the work published by Whitehead [70], which also represents eddy current losses. Whitehead considers also the addition of a second term in (4) [70] to represent hysteresis loss. Although the significance of hysteresis loss is lessened in [70] compared to eddy loss, the formulation presented refers to multi-core cables, i.e. cables including unscreened power cores. In such a case, the overall magnetic field above cores is so high, that it might lead to increased eddy loss compared to hysteresis. However, in SL-Type cables significant mitigation of the overall field above cores is expected, because of the circulating currents flowing in sheaths. Hence, eddy current and hysteresis losses are expected to be comparable and the latter should not be omitted in loss calculations.

4.2 Improved Cable Loss Models Existing in Literature

It is today widely recognised in both the industry and scientific communities that the present IEC 60287-1-1 version overestimates the losses induced in the armour of SL-Type cables. Working Group B1.64 has been recently formed by Cigré Study Committee B1 with the aim to develop new analytical formulae that better capture the physical phenomena resulting in generation of losses in 3C armoured cables, thus recognising the gap of the existing analytical formulae not only with regard to armour loss itself, but also pertaining to the total cable losses. Many researchers have already dealt with the issue of calculating power losses for 3C armoured cables in more accurate and realistic ways compared with the existing Standard. The aim of this section is to review certain already published analytical and numerical methods which suggest more accurate cable losses compared with the existing Standard version. Focus

is made on the effect the presence of the armour has on the metallic components it encloses, i.e. the sheaths and conductors.

4.2.1 2.5-D Models

A Cigré paper published in 2010 by Bremnes [19] suggested that no circulating currents are expected to flow in the armour, because of the zero net induced voltage over one complete lay-length, on the condition that balanced currents are applied in the phase conductors and the armour wires are not in electrical contact one another. The so-called twisting or stranding effect is not considered by the current IEC 60287-1-1 version, i.e. (4.28), and the armour loss is apparently overestimated, since currents circulating in the armour are implied. Bremnes proposes a 2-D Finite Element (FE) model which connects in series, via an external circuit, all the armour wires: hence, identical currents are imposed to flow in each wire. The armour wires are also assumed to be solidly bonded, in a way that the in series circuit sees zero net voltage, while the wires are assumed not to be in electrical contact. Therefore, any net current flowing in the armour is prevented and only eddy currents are allowed. At the same time, the armour layer remains magnetically present, thus affecting somehow the losses induced in the metallic components enclosed, i.e. conductors and sheaths. Although this modelling approach is based on a 2-D analysis, it is called 2.5-D just because 3-D effects are partly considered.

In a similar way, Gustavsen considers the twisting effect in a model more recently published [71]. In that case, the combined Method of Moments-Surface Operator (MoM-SO) is used instead of FE Method (FEM), providing faster results of equally high accuracy. To prevent any net circulating current in the armour, the assumption of insulated wires, i.e. that there is no current jump from wire to wire, is also done in [71].

Although the methods referred to [19] and [71] are of apparent value, they do not account for the magnetic flux component parallel to the armour wires. As clearly discussed in [71], the longitudinal field component can appreciably affect cable impedance results. Additionally, a figure with equipotential lines inside and outside the cable geometry is shown in [19] for three values of relative magnetic permeability of the armour wires, μ_r, namely $\mu_r = 1$ (non-magnetic armour), 300 and 1000: a noticeable change is shown between $\mu_r = 1$ and $\mu_r = 300$, whereas negligible differences appear between $\mu_r = 300$ and $\mu_r = 1000$. Indeed, the flux distributions in the central and right cases illustrated in Figure 4.2 look identical one another. However, it seems rather unrealistic that the magnetic flux distribution is so weakly influenced by μ_r. This can be attributed to the vacuum magnetic permeability, μ_0, which is considered in the gaps between adjacent armour wires and dominates by keeping the overall magnetic reluctance of the armour high enough. For the same reason, negligible hysteresis loss occurs in [19].

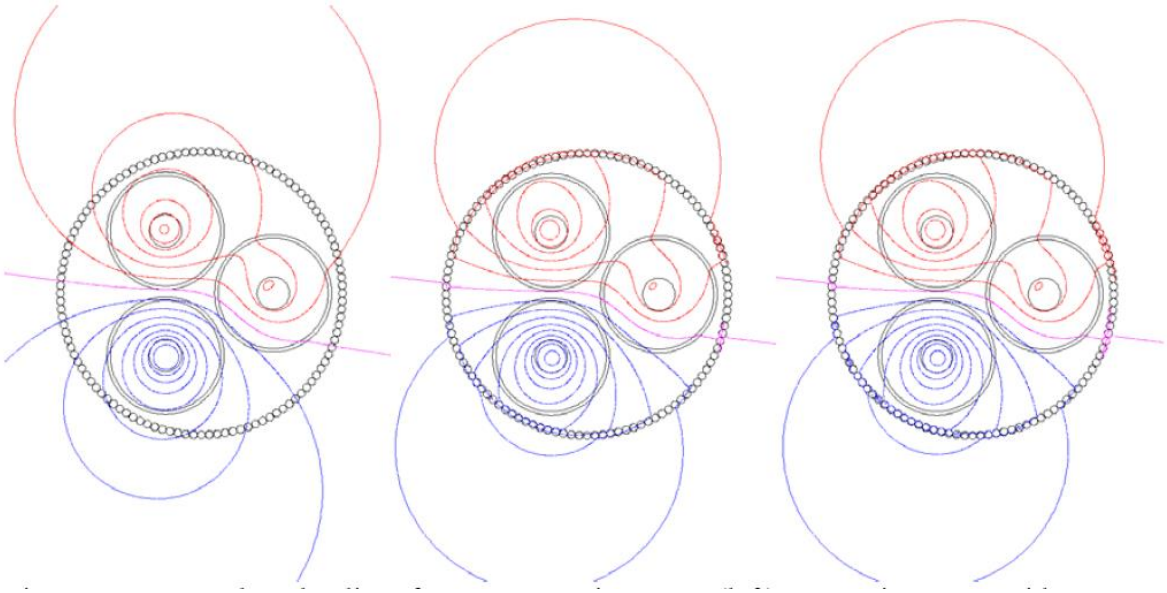

FIGURE 4.2: Flux lines for μ_r = 1 (centre), μ_r = 300 (centre) and μ_r = 1000 (right) in terms of armour [19].

4.2.2 Consideration of the Longitudinal Magnetic Flux

The weak points of 2.5-D modelling approach are identified by many researchers. Since 2.5-D approach relies on an essentially 2-D field analysis, only the magnetic flux perpendicular to the axis of an armour wire (transversal component) is considered. However, the magnetic flux which is induced longitudinally, in parallel with the axis of a wire, is expected to contribute considerably in armour loss generation: eddy currents circulating circumferentially around the axis are totally ignored in 2-D analysis. The respective current density, $\overrightarrow{J_{ec}}$, is seen in Figure 4.3.

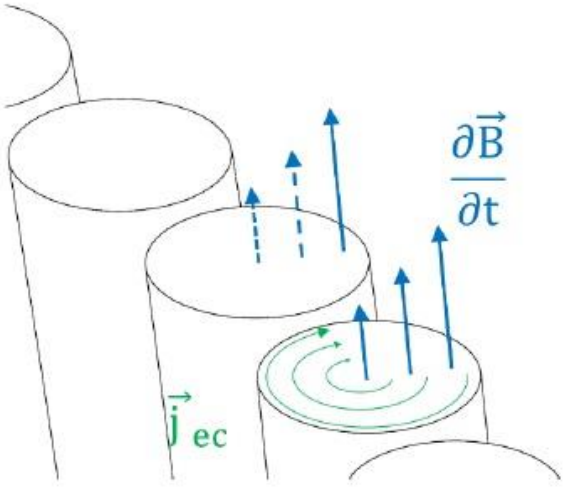

FIGURE 4.3: Eddy Current Density $\overrightarrow{J_{ec}}$ (A/m²) Circumferentially Circulating around Wire Axis due to the Alternating Longitudinal Flux Component $\vec{B}$ [68].

Considerable amounts of hysteresis losses are also expected, since the longitudinal flux component involves a continuous magnetic medium, not being interrupted by air gaps. Besides the influence in the armour loss itself, the longitudinal component is expected to affect also the losses induced in the metallic sheaths and phase conductors, which are enclosed by the armour layer: due to the angle, φ, between armour wires and power cores (Figure 4.1), the alternating flux driven along the wires causes extra eddy and circulating currents in phase conductor and metallic sheaths, which tend to induce such a flux, so as to cancel out the flux that created them, based on Lenz's Law. If armour wires were in absolute alignment with power cores (the relevant angle would be zero in such as case), as implied in 2.5-D models, induced currents would be only due to the circumferential (transversal) flux component; however, some considerable angle between wires and cores will always exist, mainly for mechanical purposes: submarine cables must be torsionally balanced.

The distinction between longitudinal and transverse magnetic flux components dates back to 1931 and 1976 in the early works published by Bosone [72] and Bianchi [73], respectively, who deal with loss calculation in 1C magnetically armoured cables. A complex magnetic permeability is introduced to account for eddy and hysteresis losses via its imaginary part. An improved model is later suggested by Barrett [74], who additionally accounts for the axial magnetic flux component induced by the armour circulating currents.

The situation becomes obviously more complicated in 3C armoured assemblies compared to 1C: proximity effects are present because of the physical proximity of power cores, which are further influenced by the presence of the magnetic armour. A more realistic representation of the armour is suggested by Hatlo [17], who considers both parallel and perpendicular armour inductance components. Hatlo suggests the solution of the actual partial differential equations in both parallel and perpendicular directions with respect to the wire axis, though adopting certain simplifying assumptions in his model: line currents are considered in phase conductors and the eddy current loss induced in metallic sheaths does not account for the presence of magnetic armour. In other words, magnetic coupling is considered only between the armour and sheath circulating losses, whereas conductor and sheath eddy losses are assumed unaffected.

Following a different analytical approach, Goddard suggests in [18] certain circuit models which also account for the longitudinal flux component along the armour wires. These circuit models are validated against FE models, where the armour is represented by a non-conductive, magnetic tubular geometry of proper thickness. In contrast with Hatlo's model, Goddard takes into consideration the magnetic effect of the armour on the induced eddy current loss in the metallic sheaths. In alignment with Hatlo, he also assumes line currents in the phase conductors, thus leaving the relevant losses unaffected by the presence of the armour.

4.2.3 3-D Models

3-D FE modelling is considered the most accurate computational approach, since the actual partial differential equations which represent the full electromagnetic problem are numerically solved in 3 dimensions. To obtain this high-level accuracy, one must pay the toll of time and resource consuming models, while care has to be given when posing the boundary conditions.

The already published works presenting results derived from 3-D analysis confirm, more or less, what is discussed in sections 4.2.1 and 4.2.2. Sturm shows in [75] that λ_1 can be underestimated by up to 31% and unreasonably high λ_2 occurs due to the circulating current induced in the armour when 2-D analysis is considered. What is also interesting in [75] is that conductor loss appears different not only between 3-D and 2-D analyses (up to 4.4% higher for 3-D), but also between 3-D models with armour of different magnetic permeability: W_C increases by 3% when changing μ_r from 50 to 300. Although the increase of 3% does not look so significant, this might be due to the specific cable geometry tested by Sturm. In general, the larger the angle φ, the higher the flux longitudinal component, $\overrightarrow{B_y}$ (Figure 4.1); therefore, the stronger the eddy currents expected to be induced in the phase conductors, thus enhancing the proximity effect and giving a higher R_{AC}. Unfortunately, pitch data for the relative twisting between power cores and armour wires are not provided by Sturm. Moreover, the transition of μ_r from 50 to 300 is not so dramatic: in both cases a magnetic armour of moderate μ_r is present. Measurements performed by Maioli [76] show an increase up to 29% in phase resistance when magnetic wires are applied above a 3C assembly in a 800 mm^2 typical OWF cable. The presence of the armour appears to affect R_{AC}, a fact which is not currently considered by the existing IEC 60287-1-1 version.

Similar trends from the qualitative point of view are also shown in the work recently published by del-Pino-López [27] when comparing 2-D and 2.5-D with 3-D simulations for several SL-Type cable geometries: λ_1 increases by up to 40% and 17%, respectively, thus demonstrating that both 2-D and 2.5-D models underestimate λ_1, though to a different extent. On the other side, λ_2 maximises in 2-D owing to the circulating currents allowed to flow. It is noted that λ_2 is still kept fairly low compared with IEC predictions even in these 2-D simulations: it does not exceed 67% of λ_2 calculated by IEC.

4.3 Noteworthy Points – Discussion on the Existing Models

The existing formulation suggested by IEC 60287-1-1 [16] for loss calculation in 3C SL-Type cables and presented in section 4.1 is certainly suitable for quick, hand calculations, which

were inevitable in the past, in the absence of more powerful computers. To be so, certain simplifying assumptions had to be made: although these may hold true in some cases, e.g. for smaller cables, they have to be re-examined when considering larger submarine cables, whose design needs to be additionally optimised. Furthermore, complex problems, such as that of 3C SL-Type cable with magnetic wire armour, are treated in a semi-empirical way by [16]. Equations whose origins date back to the middle of 20th century and are related to different cable types are used. More recent modelling approaches have already given enough evidence about the overestimation of λ_2 and remark on the weakness of the present Standard to provide higher accuracy in loss calculations. However, even these more accurate approaches rely on certain modelling assumptions which were necessary to simplify the analysis adopted. These assumptions are briefly presented and their potential impact on accuracy is discussed in the present section pertaining to modern submarine cables. The case of non-magnetic armouring, often met in practice when it is desirable to reduce the total cable losses (e.g. in route sections which are thermal bottlenecks, such as HDD), is considered first. The more typical case, i.e. that with magnetic armour, is subsequently discussed.

4.3.1 SL-Type Cables with Non-Magnetic Armour

There is, unfortunately, no reference in the IEC 60287-1-1 Standard [16] about the calculation of losses in 3C SL-Type cables with non-magnetic armour. However, in the Technical Brochure (TB) prepared by Cigré WG B1.56 [29], it is recommended to assume negligible armour loss, i.e. $\lambda_2 = 0$, although some eddy currents in the armour domain are expected. Measurements of the cable (effective) resistance for 1200 mm^2 Al conductor cables, both unarmoured and non-magnetically armoured, are performed by Stølan in [77]: a slight increase (2%) is reported, which is attributed by the author to small circulating currents in the armour, possibly due to incomplete lay lengths and/or not perfectly balanced phase currents. Negligible λ_2 occurs in the work recently published by del-Pino-López [27] for a cable having stainless (non-magnetic) steel armour: results derived from 3-D FE analysis appear to be in a very good agreement against experimental measurements presented in the same paper [27] in terms of λ_2 factor, which occurs nearly zero. Concerning the phase conductors and metallic sheaths in SL-Type cables with non-magnetic armour, three 1C cables in trefoil, touching formation are to be considered and the use of (4.1), (4.19) and (4.24) is implied. For solidly bonded sheaths, such as in the case of submarine cables, eddy current loss in sheaths is currently omitted by IEC 60287-1-1 [16]. However, in the TB prepared by Cigré WG B1.56 [29], this point is being reconsidered and the inclusion of sheath eddy loss is suggested.

Although the assumption for absolutely zero λ_2 may not be strictly true, it is clear from the above paragraph that the losses induced in the metallic sheaths become of higher importance rather than the armour loss itself in 3C SL-Type cables with non-magnetic armour. Hence, the

assumptions adopted by the present IEC 60287-1-1 formulation pertaining to sheath losses need to be carefully evaluated with respect to modern 3C submarine cables.

Starting from the eddy current loss, the assumption that the conductor current is concentrated along the longitudinal axis of the sheath is implied in both (4.17), (4.19). Although this is expected to be representative enough for either small or well-spaced conductors, it may not hold for larger conductors in trefoil, close arrangement. The external magnetic field produced by the three conductor currents is actually reduced by the crowding of the currents towards each other, as Arnold notes in his own work for sheath eddies [69]; hence, (4.17), (4.19) may become conservative for larger conductor sizes, as demonstrated later, in Chapter 5. Heyda considers the likely impact of the proximity effects in [66], but assumes them to be insignificant, owing to the possible use of Milliken conductors for higher power demands. Presently, Milliken conductors are rarely used for 3C subsea cables due to the practical difficulties in providing sufficient water blocking capability and the increase in cable size that complicates the installation stage. Ferkal implements in [78] an analytical method to compute eddy current loss in sheaths (called "proximity effect losses" in that paper), taking into account of the actual current distribution in the conductor instead of representing it via a single filament: "proximity effect losses" were found to be 16% lower than those calculated by methods neglecting the effect of the actual current distribution in the conductor when evaluating the sheath losses.

Continuing with circulating currents in sheaths, (4.24) accounts only for the sheath DC resistance, implying a uniformly distributed sheath current, I_S. Indeed, the skin effect in sheaths is not expected to be significant, since the thickness values typically met in practice (2.5-3.0 mm for Lead sheath) are lower than the corresponding skin depth (about 33 mm and 12 mm for Lead and Aluminium, respectively, at power frequency). However, the situation differs concerning proximity effects: as Arnold cites in [67], uneven distribution of I_S is expected in sheaths of neighbouring cables. The closer the cables are laid to one another, the greater the variation in the induced emf along the sheath circumference and the more uneven the distribution of I_S will be. More recently, Kovač [79] takes this into account via Filament Method when calculating sheath losses for solidly bonded cables laid in touching, flat formation. However, he neglects the uneven current distribution in conductors, assuming they could be sufficiently represented by a single filament.

4.3.2 SL-Type Cables with Magnetic Armour

Focus is made in this section on the effect the presence of the armour has on the metallic components it encloses, i.e. the sheaths and conductors. Starting the discussion again from eddy current loss in sheaths, the analytical formulae presented in section 4.1.2 assume three

cores in trefoil formation with no armouring above them. Although the presence of a non-magnetic armour is not expected to change considerably the distribution of the magnetic field beneath it, the situation will be different if a magnetic armour is applied. The work published by Goddard [18] shows an increase up to 56% in eddy current losses when magnetic armour is considered over the power cores. Although the present IEC 60287-1-1 [16] version includes formulae for 3 1C cables in trefoil formation (§ 2.3.6.1) in [16], these do not take into consideration of the effect of the magnetic armour.

As noted in section 4.1.3, the factor 1.5 in (4.27) is empirically introduced. The results published by certain researchers indicate that this works sufficiently well: Goddard suggests in his paper [18] an analytical model which appears to derive circulating losses in sheaths slightly lower (by 5-6%) than (4.27). Such a good agreement is also reported by Sturm, who implements 3-D FE simulations in order to investigate cable losses: sheath losses lower at worst by 8% are reported in [75]. However, some other researchers, also implementing 3-D FE models, report even lower sheath losses: Benato calculates in [80] figures 33% lower than IEC 60287-1-1. On the contrary, there are researchers presenting results of the opposite trend: Hatlo shows in his model [17] that λ_1 can be higher by 17% than IEC 60287-1-1. Different approaches and assumptions stand behind all these works and this may explain the extent of disagreement. Nevertheless, the fact that so different results regarding sheath circulating losses occur is a sufficient evidence that the empirical factor introduced in (4.27) can potentially lead to loss results of doubtful accuracy.

Since 2010 and the Cigré paper published by Bremnes [19] until today, certain remarkable changes in the early modelling approaches have occurred and improved loss models have been published, as presented in sections 4.2.1 - 4.2.3. Most researchers agree on the fact that no circulating currents in the armour are in reality expected and adopt assumptions of this kind in their models, such as that for non-conductive tubular geometry by Goddard [18]. However, certain unclear points still remain in these improved models:

- Although 2.5-D approaches, such as those by Bremnes [19] and Gustavsen [71], simulate quite effectively the twisting effect and the fact that no circulating currents are in reality expected in the armour, they do not take into consideration the longitudinal magnetic flux component along the armour wires, which is expected to affect not only armour loss itself, but also cable losses in total.

- Line currents are assumed by both Goddard [18] and Hatlo [17], being located in the centres of the phase conductors. In reality, the non-uniform current distribution in conductors is expected to affect the magnetic field induced, thus the losses generated

in sheaths and armour. This is already remarked by previous researchers, such as Arnold [69].

- As a continuation to the above point, the presence of the magnetic armour is expected to affect R_{AC}. Although a slight difference in R_{AC} appears in the 3-D models developed by Sturm [75], a higher effect is implied by the measurements carried out by Maioli [76]. This is currently not considered by [18] and [17].

- Hatlo [17] does not account for the effect of the magnetic armour on sheath eddy losses, thus implying they are calculated on the basis of an unarmoured 3C cable. The results presented by Goddard [18] show an increase up to 56% when magnetic armour is considered.

Although 3-D FE modelling could provide the necessary answers to both the above points and those referred to section 4.3.1, these would require computationally demanding and time consuming models. Measurements may give some valuable evidence; nevertheless, measuring cable losses in several samples is not an easy task: manufacturers give often priority to production testing needs and little room is in practice left for research purposes. Even under more ideal circumstances, the conclusions deduced from experimental works are not always clear, because of the inherent difficulties and limitations met when testing cable samples. For instance, the slight increase in the cable resistance of the non-magnetically armoured sample reported by Stølan in [77] is attributed to some small circulating currents: these currents are unlikely to be present in the largest part of the armour in a long cable actually installed, since the incomplete lay-lengths will be significantly shorter compared to the entire cable length.

Hence, alternative theoretical models, that would be capable of modelling AC phenomena and could address the issues discussed in sections 4.3.1 and 4.3.2, are sought. For studies of electromagnetic transients in power systems, it is common to apply EMTP-like software. These tools permit the calculation of the impedance matrix of the cable as a function of frequency, given the cable geometry and material properties. Although initially intended to solve time-domain problems, such as electromagnetic transients, their use in loss calculation under steady-state conditions is not ruled out, while the AC phenomena are obviously included by means of the frequency dependent impedance matrix. The use of these methods is examined in the next section, making focus on their potential applicability to calculating the losses in 3C SL-Type cables.

4.4 Cable Representation through Impedance Matrix

4.4.1 Existing Analytical Models

A general formulation of Impedance and Admittance of cables is proposed by Ametani [81], whose work intends to analyse wave propagation characteristics and transients. Ametani develops a full impedance matrix, **Z**, to represent both the cable interior and its surroundings. Focusing on buried cables, an internal impedance matrix, $\mathbf{Z_i}$, is separately built to represent 1C cables, accounting for all self and mutual impedances between cable components. $\mathbf{Z_i}$ ends at the cable outer surface, from where the external impedance (i.e. that representing the outer media), namely $\mathbf{Z_0}$, starts. Skin effect is taken into consideration by means of Bessel functions for both conductor and sheath. Although pipe-type cables are also examined, proximity effects are not considered in $\mathbf{Z_i}$. The effect of magnetic pipe on the derived cable impedance is considered via a constant, real relative magnetic permeability, μ_p. The consideration of constant μ_p is not strictly true in cases where ferromagnetic steels are used, but conductor currents are not typically expected so high that the pipe could reach in saturation region, as Ametani comments.

Barrett suggests a different way to define the impedance matrix, [Z], in [74] and develops a mathematical model to compute circulating and hysteresis losses in 1C armoured cables. What is important in [74] is the use of a complex magnetic permeability, $\boldsymbol{\mu_e}$, whose imaginary part, $\Im\{\boldsymbol{\mu_e}\}$, represents the hysteresis loss generated in the armour. Since $\boldsymbol{\mu_e}$ is part of the armour inductance, $\Im\{\boldsymbol{\mu_e}\}$ is eventually transferred to the real part of [Z] elements. In other words, the resistive part of [Z] describes not only Joule losses generated in the non-magnetic components, such as conductor and sheath, but also hysteresis loss generated in the magnetic armour. Although the representation of hysteresis loss in [Z] looks at first glance rather promising in terms of SL-Type cables with magnetic armour, Barrett's model assumes 1C cables being placed so spaced from one another that proximity effects can be considered negligible. This is not expected to introduce significant errors in 3 1C submarine cables, which in general are installed keeping considerable distances between phases. However, significant proximity effects occur in 3C cables, due to the close physical proximity between the power cores.

The inherent difficulty of representing proximity effects through a rigorous, analytical way leads one to look into some other alternative methods, which would be capable of accounting for a more realistic interaction between cable components, have an analytical background and be readily understandable. Filament Method is discussed in the next section.

4.4.2 Filament Method

Comellini introduced in 1972 a numerical method which suggests that each actual conductor is subdivided into a great number of elementary conductors of small, though finite, size [82]. The whole concept is based on the assumptions presented below. Comments related to the potential use of Comellini's method in SL-Type armoured cables also follow once presenting each assumption.

- The current flows only longitudinally in the subconductors.

In other words, any conductors are represented as solid entities. Although this is true for metallic sheaths, it is not so in reality for phase conductors, since stranded conductors are mostly used in practice, mainly for mechanical reasons (more flexible cables and easier installation process). However, stranded conductors are also compacted, a fact which leads to further reduction in the contact resistance between strands due to the high compressive forces applied. Hence, alternative current paths are afforded, besides the strand itself, and currents may jump from strand-to-strand, as also pointed out by Arnold [69]. Although different results in R_{AC} are in principle expected when comparing an actual stranded and compacted conductor against a solid one of the same DC resistance, it is believed that that difference won't be huge on the condition of good compaction between strands [83]. An extra indication for this is that the current IEC 60287-1-1 version treats stranded and solid Copper conductors the same in terms of k_p (k_p = 1 is assumed for both), while a slightly lower k_p is suggested for Aluminium stranded conductors (k_p =0.8) due to the higher corrosion rates expected in Al and, thus, the slight increase in contact resistance. Although a 3-D analysis would give further insight into this issue, this would be a very laborious and complex task.

- The current density is uniform in each subconductor.

Therefore, DC resistance is assumed to sufficiently represent every subconductor's resistance. Considering more subconductors of smaller size would give more accurate results, but increase the computational burden. An optimum compromise between the subconductors' size (and thus their total number) and the relevant effect in R_{AC} results becomes apparently inevitable in this sense. In any case, the whole bundle of subconductors must have the same DC resistance as the actual conductor.

- All subconductors are parallel and of infinite length, so that end effects can be disregarded.

In other words, the twisting of both the power cores and armour wires cannot be directly considered. In fact, such a direct consideration is feasible only when 3-D analysis is implemented. However, this assumption does not limit the indirect consideration of the 3-D

geometry, given that alternative approaches that transform the 3-D effects in 2-D models are presently used. Such approaches are already suggested by other researchers, as discussed in sections 4.2 and 4.3.

- The resistivity and magnetic permeability within each subconductor are uniform and independent of current. But they may differ from those of other subconductors.

A constant, flux independent magnetic permeability is a necessary assumption in order to keep the mathematical model linear and, thus, readily solvable. Such an assumption is obviously not an issue in SL-Type cables with non-magnetic armour; however, it is not strictly true when ferromagnetic materials are considered in the armour, because the *BH* curve is likely to reach close to the saturation region. The effect of a flux dependent permeability in the armour has not been widely examined in the literature so far. A $\mu = f(B)$ formula is suggested by Hatlo in [84] and [17], but there are no comparative results in terms of cable losses between constant and flux dependent μ. Some indication is provided by Sturm in [75], who concludes that no meaningful difference in factors λ_1, λ_2 occurs when applying a $\mu = f(B)$ for currents close to the expected current rating of the cables simulated.

Based on the 2nd bullet above, the resistance R_i (Ω/m) of subconductor (or filament) i is a function of the resistivity ρ_i (Ωm) and surface area (m^2). Assuming cylindrical subconductors of radius r_i (m):

$$R_i = \frac{\rho_i}{\pi r_i^2} \tag{4.29}$$

The self-inductance L_{ii} of a cylindrical subconductor i and the mutual inductance L_{ij} between cylindrical subconductors i and j in the presence of a cylindrical return path subconductor q are respectively defined as follows:

$$L_{ii} = \frac{\mu_0}{2\pi}\left[\ln\left(\frac{D_{iq}^2}{r_i r_q}\right) + \frac{\mu_i}{4} + \frac{\mu_q}{4}\right] \tag{4.30}$$

$$L_{ij} = \frac{\mu_0}{2\pi}\left[\ln\left(\frac{D_{iq}D_{jq}}{D_{ij}r_q}\right) + \frac{\mu_q}{4}\right] \tag{4.31}$$

where r_q is the radius of the return subconductor (m), D is the geometric mean distance between 2 cylindrical subconductors (for cylindrical subconductors this equals to their axial distance) and μ_i, μ_q is the relative magnetic permeability of subconductor i, q, respectively. As become apparent from the above equations, for the inductance calculation a return path must be designated, because inductances can only be defined for closed current paths. This becomes even clearer from (4.32), which essentially comes from the Second Kirchhoff's Law assuming in total n subconductors, and Figure 4.4 that describes it:

$$\Delta V_i = (R_i + R_q) I_i + \frac{d}{dt} \sum_{j=1}^{n} L_{ij} I_j \tag{4.32}$$

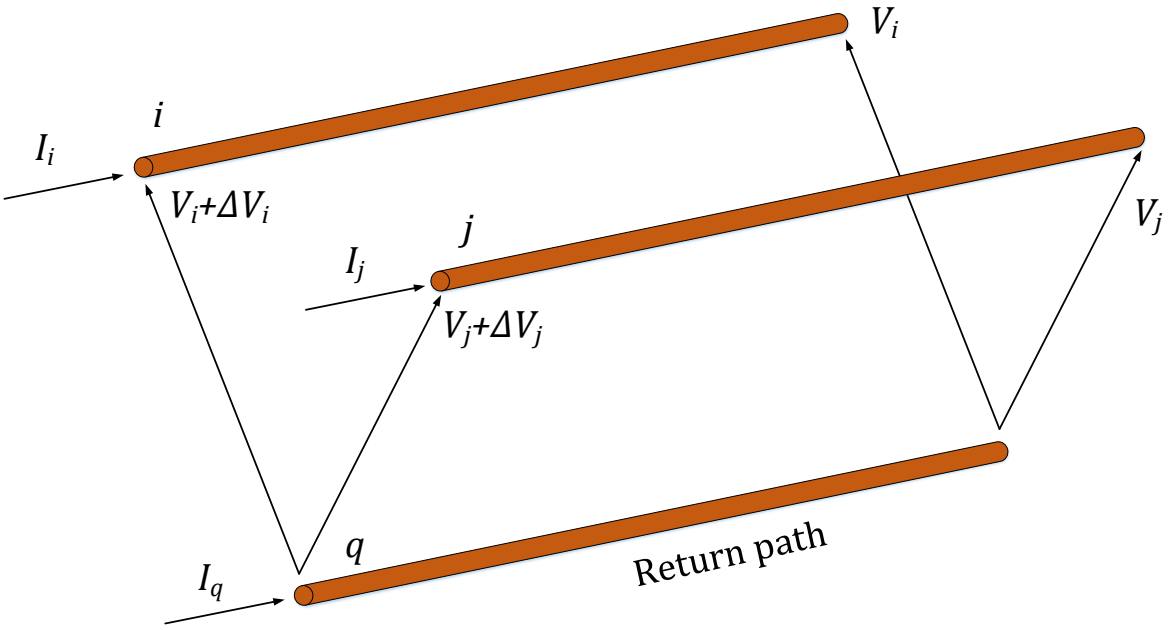

FIGURE 4.4: Loops Formed by Two Subconductors with a Common Return Path [20].

where R_q is the DC resistance of the subconductor representing the return path (Ω/m), I_i, I_j is the current in subconductor i, j, respectively (A) and ΔV_i is the voltage drop along subconductor i (V/m). Under steady-state conditions, $^{d}/_{dt}$ in (4.32) may be substituted by $j\omega$. Considering matrix notation the following n equations occur:

$$[\mathbf{V}] = ([\mathbf{R}] + j\omega[\mathbf{L}])[\mathbf{I}] = [\mathbf{Z}][\mathbf{I}] \tag{4.33}$$

Comellini validates his model by comparing it against Bessel functions for a cylindrical, isolated conductor. To implement it, the return path is assumed to be located sufficiently far from the actual conductor, so that the effect of the former's magnetic field can be disregarded.

De Arizon implements in [85] and [20] a similar formulation, examining in his work not only cylindrical filaments, but also other filament shapes. Concerning cylindrical filaments, the self-geometric mean distance defined in (4.34) is used (m) and (4.30), (4.31) turn into (4.35), (4.36) respectively:

$$D_{ii} = r_i e^{-0.25 \cdot \mu_i} \tag{4.34}$$

$$L_{ii} = \frac{\mu_0}{2\pi} \ln\left(\frac{D_{iq}^2}{D_{ii} D_{qq}}\right) \tag{4.35}$$

$$L_{ij} = \frac{\mu_0}{2\pi} \ln\left(\frac{D_{iq} D_{jq}}{D_{ij} D_{qq}}\right) \tag{4.36}$$

In contrast with Comellini, de Arizon treats the return path as another subconductor of the same shape which does not need to exist in reality. Thus, it is considered as a fictitious return path and its current is deliberately set equal to zero in order to cancel out its effect, irrespective of its position with respect to the main conductors. Although this assumption is valid when geometrically symmetrical and perfectly balanced phase systems are considered, it does not hold true for either non-symmetrical or imbalanced systems: a common mode current component is expected to flow through this path, thus inducing a different magnetic flux profile which correspondingly alters self and mutual inductances between filaments. The case of an isolated SL-Type cable examined in the present thesis is not such a case: it is an absolutely symmetrical geometry, while balanced conditions are to be assumed in loss calculations. However, the situation is likely to be different in some cases in practice, for instance when loss calculations are required when an SL-Type cable is installed next to existing cables of the same or different geometry (either different SL-Type or 1C cables).

Besides circular, also square and elemental shaped filaments are examined by de Arizon. This permits to optimise the computational algorithm and is rather useful when the skin depth becomes so thin, that an immense number of tiny filaments would be required to represent the actual current distribution. Frequencies of up to 0.1 GHz studied by de Arizon may not be unlikely in certain special transient conditions, yielding a skin depth of about 0.2 mm for Copper. However, skin depth values not lower than 8 mm are expected at power frequency when non-magnetic materials are considered. The situation may be different for someone attempting to simulate magnetic materials with Filament Method: assuming a μ_r = 400 according to IEC 60287 for 1C armoured cables a skin depth 0.4 mm occurs at 60 Hz. In such a case, a more efficient implementation of the method would be undoubtedly useful.

De Arizon also presents impedance results for pipe-type cables, assuming pipes of a constant magnetic permeability, μ_r, and implementing (4.35), (4.36). The assumption of constant μ_r is not unreasonable for low and modest current ratings, since the *BH* curve is not expected to reach the saturation region. Although the fact that de Arizon implements Filament Method to calculate impedances for pipe-type cables is encouraging for the potential use of the method for SL-Type cables with magnetic armour, it is not very clear from his work how he considers the effect of magnetic pipe on the other metallic components, i.e. the enclosed conductors and metallic sheaths. The consideration of magnetic properties in the self-geometric mean distance of pipe filaments, i.e. (4.34), is certainly necessary: the internal inductance of pipe filaments is corrected this way. However, filament currents of the other metallic components induce flux loops which are expected to link considerable parts in the pipe area: the contribution of this

flux linkage is significant and expected to affect inductance results. It is not clear how this flux linkage is considered by (4.35), (4.36). A similarly unclear approach of Filament Method implemented to calculate losses in SL-Type cables with wire armour (either magnetic or non-magnetic) is followed by Benato in [21]: a correction in the self-geometric mean distance only, (4.34), depending on μ_i is suggested, whereas the way the magnetic flux, induced by conductor and sheath filaments, links the armour layer is not shown in the inductance formulation presented (which is nearly identical to (4.35), (4.36)).

Equations similar to (4.35), (4.36) are also adopted by Rivas in [58]. Rivas treats the return path in a slightly different way than de Arizon: a circular shaped ring of radius a encloses the systems under study, as shown in Figure 4.5. Assuming this to be far enough from the enclosed conductors, $D_{iq} \simeq D_{jq} \simeq D_{qq} = a$ and (4.35), (4.36) become:

$$L_{ii} = \frac{\mu_0}{2\pi} \ln\left(\frac{a}{D_{ii}}\right) \tag{4.37}$$

$$L_{ij} = \frac{\mu_0}{2\pi} \ln\left(\frac{a}{D_{ij}}\right) \tag{4.38}$$

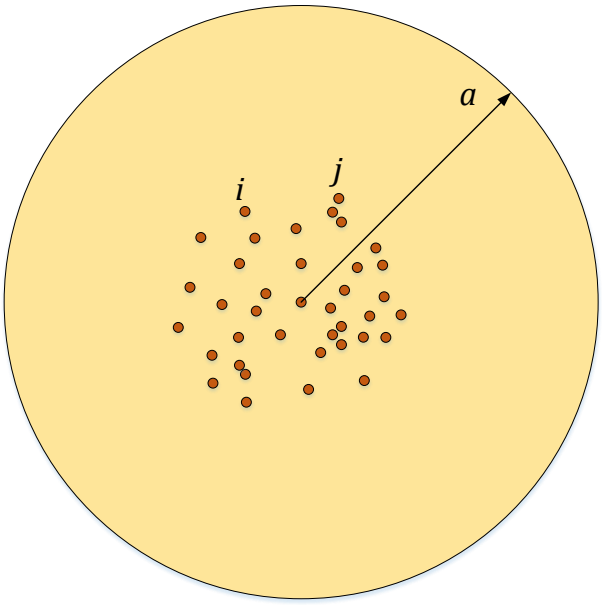

FIGURE 4.5: The Return Path Is Represented by a Ring of Radius a [58].

Both Rivas and de Arizon implement certain matrix manipulation techniques in order to reduce the equations to be solved for, thus improving the method's efficiency. By applying Kron's reduction, the initial equation system of order $n \times n$ turns into an $m \times m$ one, where m is the number of the actual metallic components, i.e. conductors, sheaths and armour. Although Rivas also assumes later in his paper this ring to be lossless and imposes zero-current conditions so as to eliminate it, the circular representation of return path does afford a remarkable advantage: it allows for Filament Method to be fully comparable against analytical EMTP

methods, such as that published by Ametani in [81]. Considering, for example, an 1C cable being composed of a conductor enclosed by a metallic sheath (m = 2 in such a case), it is possible to adjust the outer ring on the cable outer surface, thus making the internal impedance $\mathbf{Z_i}$ suggested by Ametani directly comparable to the 2 *x* 2 [**Z**] derived from this version of Filament Method.

A different formulation is employed by Moutassem who uses Filament Method to calculate losses in pipe-type cables [22]. The same formulation is also suggested by Anders, in his book [34]. Moutassem employs Filament Method assuming non-magnetic materials, whereas the Method of Images is used to account for the effect of the magnetic pipe. The latter is discussed more in Chapter 6, while focus is made on the former in the context of the present Chapter. Moutassem adopts a notation looking at first glance slightly different than (4.33) and is presented in (4.39).

$$[\mathbf{V}] = \left([\mathbf{R}] + j\frac{\omega\mu_0}{2\pi}[\mathbf{G}]\right)[\mathbf{I}] = [\mathbf{Z}][\mathbf{I}] \tag{4.39}$$

where

$$G_{ii} = \ln\left(\frac{1}{D_{ii}}\right) \tag{4.40}$$

$$G_{ij} = \ln\left(\frac{1}{D_{ij}}\right) \tag{4.41}$$

The argument in the logarithmic term of (4.40), (4.41) is apparently different than that of (4.37), (4.38). Let us assume 3 phase conductors being in trefoil arrangement for simplicity. It is easy to prove that starting from the formulation previously presented, Moutassem's equations may be derived, though making certain assumptions: first, that perfectly balanced phase currents, namely I_A, I_B, I_C, are applied in the phase conductors and, second, that, as implied in Rivas's work [58], a ring return of radius a, sufficiently large such that $D_{iq} \simeq D_{jq} \simeq D_{qq} = a$, is considered. If the phase conductors consist of $n = n_A + n_B + n_C$ filaments in total, where n_A, n_B, n_C is the number of filaments for each phase conductor, the following formulae may be derived from the First Kirchhoff's Law:

$$I_A = \sum_{i=1}^{n_A} I_i \tag{4.42}$$

$$I_B = \sum_{i=n_A+1}^{n_A+n_B} I_i \tag{4.43}$$

$$I_{\mathrm{C}} = \sum_{i=n_A+n_B+1}^{n} I_i \tag{4.44}$$

Putting all filament currents in a column vector, $\mathbf{I} = [I_1\, I_2 \ldots I_n]^T$ is obtained. Starting from (4.38), multiplying by $(2\pi/\mu_0)$ and assuming that G_{ij}' is the new inductance term, we have:

$$G_{ij}' = \ln\left(\frac{a}{D_{ij}}\right) = \ln\left(\frac{1}{D_{ij}}\right) + \ln(a) \tag{4.45}$$

Considering the matrix product [**G'**]·[**I**] we have:

$$[\mathbf{G}'][\mathbf{I}] = \begin{bmatrix} \ln\left(\frac{1}{D_{11}}\right) + \ln(a) & \cdots & \ln\left(\frac{1}{D_{1n}}\right) + \ln(a) \\ \vdots & \ddots & \vdots \\ \ln\left(\frac{1}{D_{n1}}\right) + \ln(a) & \cdots & \ln\left(\frac{1}{D_{nn}}\right) + \ln(a) \end{bmatrix} \begin{bmatrix} I_1 \\ \vdots \\ I_n \end{bmatrix} \tag{4.46}$$

After doing some rearrangements, (4.46) gives:

$$[\mathbf{G}'][\mathbf{I}] = \begin{bmatrix} \ln\left(\frac{1}{D_{11}}\right) & \cdots & \ln\left(\frac{1}{D_{1n}}\right) \\ \vdots & \ddots & \vdots \\ \ln\left(\frac{1}{D_{n1}}\right) & \cdots & \ln\left(\frac{1}{D_{nn}}\right) \end{bmatrix} \begin{bmatrix} I_1 \\ \vdots \\ I_n \end{bmatrix} + \begin{bmatrix} \sum_{i=1}^{n} I_i \\ \vdots \\ \sum_{i=1}^{n} I_i \end{bmatrix} \ln(a) \tag{4.47}$$

The matrix in the first term of (4.47) is apparently equal to [**G**]. Analysing further the column vector of the second term, we have:

$$\begin{bmatrix} \sum_{i=1}^{n} I_i \\ \vdots \\ \sum_{i=1}^{n} I_i \end{bmatrix} \ln(a) = \begin{bmatrix} \sum_{i=1}^{n_A} I_i + \sum_{i=n_A+1}^{n_A+n_B} I_i + \sum_{i=n_A+n_B+1}^{n} I_i \\ \vdots \\ \sum_{i=1}^{n_A} I_i + \sum_{i=n_A+1}^{n_A+n_B} I_i + \sum_{i=n_A+n_B+1}^{n} I_i \end{bmatrix} \ln(a) = \begin{bmatrix} I_{\mathrm{A}} + I_{\mathrm{B}} + I_{\mathrm{C}} \\ \vdots \\ I_{\mathrm{A}} + I_{\mathrm{B}} + I_{\mathrm{C}} \end{bmatrix} \ln(a) \tag{4.48}$$

However, due to the assumption for perfectly balanced phase currents, $I_{\mathrm{A}} + I_{\mathrm{B}} + I_{\mathrm{C}} = 0$. Hence, the column vector in (4.48) becomes equal to zero and, as a consequence, $G_{ij}' = G_{ij}$. The two necessary assumptions made for that, i.e. a sufficiently large a and the perfectly balanced currents, hold true when seeking to calculate cable losses under conventional system design assumptions. Even when solidly bonded sheaths are also included in the above analysis, balanced currents are expected to flow in these, provided that the entire geometry is kept symmetrical. However, a formulation employing (4.40), (4.41) is apparently less generic than (4.37), (4.38) and may not be correct for other, less symmetrical cases. For instance, when a trefoil cable arrangement is placed on the bottom of a magnetic pipe, a non-zero return current

is expected to flow in the pipe and/or the earth, because of the lack in symmetry. Another example is that of two or more submarine cables of same or different geometry placed next to one another. In such cases the geometrical non-symmetry will lead to a common mode component that must return through a return path. If this is ignored, the cable inductance and, thus, the entire impedance will be in principle erroneous, thus potentially leading to questionable cable losses.

Besides the aspect of non-symmetrical or imbalanced systems, two points have to be highlighted with regard to the use of (4.40), (4.41). First, the units of the logarithmic origin are not clearly meant: if geometric distances, D_{ii}, D_{ij} are in m, a = 1 m is implied. In this case, it is questionable whether such a ring is adequately large so as not to affect the cable impedance and the accuracy of impedance results become dependent on the cable size considered, thus less generic. Second, without considering a specific return path, as implied by the use of (4.40), (4.41), the comparability against other analytical tools, such as the EMTP model by Ametani [81], becomes ambiguous: Ametani provides the internal cable impedance for 1C cables, $\mathbf{Z_i}$, which implies that the return path lies on the cable outer surface. If no specific return path is assumed, then the validation of Filament Method against existing, analytical tools is not so obvious.

4.5 Summary

The existing analytical methods presently used for the calculation of losses in SL-Type, wire armoured cables according to the existing IEC 60287-1-1 Standard [16] are first reviewed in the present Chapter. Emphasis is given to the existing gaps which can potentially lead to inaccurate loss calculations when larger cables are utilised in the context of the larger OWFs currently operated or planned. Although many researchers deal with cables with magnetic armour, not so much focus has been so far made on cables with non-magnetic armour, that are likely to be preferred in the hotspots of the entire subsea route to reduce the total losses. In such a case, the importance of λ_1 factor increases, since λ_2 is negligible, as suggested by some researchers and the draft TB prepared by Cigré WG B1.56 [29].

Another interesting point also remarked in the draft TB [29] and differing from the presently adopted approach by IEC 60287-1-1 [16] is that eddy current losses should not be neglected and must always be calculated when cables with continuous sheaths are rated. In solid bonding cases the existing IEC 60287-1-1 Standard version suggests that eddy currents may be considered negligible, a suggestion which is judged as optimistic by the draft TB [29]. Therefore, attention must be paid not only to the eddy loss itself, but also to the total losses induced in the metallic sheaths when non-magnetic armour is employed. The losses due to eddy and circulating currents induced in the metallic sheaths are presently calculated based

on certain simplifying assumptions, such as the fact that line currents flow in conductors and only the DC resistance of sheaths being in close physical proximity is considered. Although these probably do not introduce significant errors for smaller cable sizes, they may not hold true when larger cables are considered, such as those expected in the case of the increasingly larger OWFs. When larger conductors are utilised, stronger proximity effect is expected; thus the current distribution will be even more non-uniform, with higher current values being located towards the cable centre. Hence, a different distribution of magnetic flux is expected in the region of sheaths and the assumption for line currents in phase conductors when calculating sheath losses does not seem consistent with reality. Furthermore, larger cables will also contain larger and, probably, thicker sheaths: the induced currents are expected to be quite non-uniform and the assumption of DC resistance presently used for λ_1' may not be accurate enough. These assumptions are in depth studied in Chapter 5, where the existing analytical methods are compared against modern, numerical approaches that take into account of proximity effects in both the phase conductors and the metallic sheaths.

Besides SL-Type cables with non-magnetic armour, the relevant loss formulae adopted by the IEC 60287-1-1 Standard for magnetic armour are also reviewed in the present Chapter. The vast majority of researchers agree that λ_2 is currently overestimated by the existing Standard formula, while the empirical factor 1.5 currently used in the existing Standard to account for the effect of the armouring on λ_1' yields contradicting results in many different works. The same factor is suggested by the draft TB [29] to correct R_{AC}, although judged as overly conservative for wire armoured, 3C cables. It is noted that certain more recently developed models, such as that by Hatlo [17] and Goddard [18], still assume line currents in the conductors, thus rendering the evaluation of a likely increase in R_{AC} impossible. Adopting unreasonably high losses can potentially lead to a considerable compromise in the economic viability of OWF projects. On the contrary, the existing Standard does not consider the effect of the magnetic armour on sheath eddy losses. Furthermore, certain recently published models, such as that by Hatlo [17], still assume eddy losses as though the armour was absent. It has become clear from the existing literature that the issue of loss calculations in SL-Type cables with wire armour does not only refer to the armour loss itself, but to an overall more realistic re-estimation of losses in the cable.

With regard to the above, 3-D FE analysis would provide more accurate results, though with the toll of significantly extra computational burden. Hence, alternative methods being capable of representing AC phenomena, such as skin and proximity effects, are investigated. Strictly analytical methods initially developed to study electromagnetic transients, such as EMTP-like software, do not account for proximity effects, although they effectively consider skin effect. Alternative methods, strictly numerical but with some analytical background, are examined as candidate key solutions to the cable loss problem in the present Chapter. The Filament Method

presented in section 4.4.2 appears in several versions in the existing literature. Although the main principles of the method are the same, certain points of divergence between the several approaches are identified and discussed in detail. Focus is made on the possibility for validating the method against existing analytical methods, such as that of Ametani [81]. Additionally, its potential use for SL-Type armoured cables is assessed. Although it is not clear in the existing literature how the effect of magnetic materials is represented in the basic inductance formulation, as pointed out in section 4.4.2 pertaining to de Arizon [20] and Benato [21] works, the fact that Filament Method is used to compute cable impedances and losses when magnetic materials are used looks, at least at first glance, encouraging. Further discussions on the consideration of magnetic materials through Filament Method are made later, in Chapter 6.

Chapter 5 Improved Sheath Loss Estimation in 3C Submarine Cables with Non-Magnetic Armour

The literature review presented in Chapter 4 demonstrates several gaps in the formulation presently adopted by the existing IEC 60287-1-1 Standard version [16], as well as the various analytical models used to calculate losses in 3C SL-Type armoured cables. Those cables involving non-magnetic material in the armour are of special interest for various reasons. First, they constitute a safe and economic choice when it is desirable to significantly reduce the cable losses in hotspot sections of the entire subsea route, such as the landfall. Indeed, in many cases the selection of stainless, austenitic steel grades proves to be more competitive rather than the increase in conductor size, especially in Copper conductor cables. Besides, austenitic steel grades are also preferred when reduced losses are wanted in combination with high mechanical performance. The higher the tensile strength, the higher the grade of the steel wire used [86]. Armouring of lower grades would be a high-risk solution for cables being installed in large sea depths, due to their poor tensile strength. No reference is made in the current IEC 60287-1-1 Standard version [16] concerning the armour loss factor, λ_2, for SL-Type cables with non-magnetic armour, while the draft Technical Brochure (TB) prepared by Cigré WG B1.56 [29] suggests that λ_2 can be considered negligible. In such a case, the losses generated by the currents induced in the sheaths become of higher importance for the thermal rating of the cable. The same draft TB [29] suggests that eddy current losses should be included irrespective of the bonding arrangement of the cable sheaths, although they are considered negligible in the existing IEC 60287-1-1 Standard version. Hence, the current rating of such cables is expected to be even more conservative, thus compromising the viability of submarine links and OWF projects.

The existing analytical formulae used to calculate the sheath loss factor, λ_1, are inevitably based on certain simplifying assumptions, such as the conductor currents being represented by line sources, and the DC resistance being used to represent sheath. Since the cable cores are in close physical proximity in SL-Type cables, proximity effects are expected, besides the skin effect always occurring in isolated cable cores. Filament Method (FM) is implemented in the present Chapter to model these AC phenomena, having adopted most of the strong points of the several versions already published. Then, a parametric analysis is performed, so as to identify the key design factors affecting the accuracy of the existing analytical methods in terms of λ_1. Although both FM and Finite Element Method (FEM) are capable of providing more accurate results, they are not suitable for Standardisation purposes, due to their inherent complexity. For this

purpose, approximating factors that can be combined with the existing IEC λ_1 factors and improve the accuracy of losses calculations are sought for. The material presented in this chapter is largely based on the paper "Impact of Proximity Effects on Sheath Losses in Trefoil Cable Arrangements" already published by the author in IEEE Transactions on Power Delivery [87].

5.1 Filament Method - Adopted Version

The FM version implemented is first briefly presented in this section. This is subsequently used and compared against EMTP-like software for a 3C assembly; since the consideration of SL-Type armoured cables is not feasible through EMTP, a pipe-type cable with non-magnetic pipe is chosen as a similar geometry. FM is assessed against not only EMTP tools, but also other, FE techniques which permit the extraction of **Z**-impedance matrix including proximity effects.

5.1.1 Formulation

The formulation presented in this section is not entirely new compared to the several versions being published in the existing literature and presented in section 4.4.2. As demonstrated, certain less generic forms of FM are published, which could potentially lead to erroneous results with regard to the **Z**-impedance matrix. In this context, it is intended to use an as generic formulation as possible, by adopting and combining any features from the existing formulations which are well-defined. Based on the review done, a formulation relied on the works published by de Arizon [20] and Rivas [58] is selected: the fundamental equations, i.e. the self and mutual inductances between filaments, come from the latter, whereas the whole matrix manipulation is the same in both [20] and [58]. The terms filament and composite conductor are used to describe each filamentary conductor (or subconductor) and metallic component (e.g. phase conductors, metallic sheaths or armour), respectively, in the context of the present Chapter. Additionally, cylindrical filaments are always implied.

The resistance R_i (Ω/m) of filament i is a function of its resistivity ρ_i (Ω·m) and surface area (m²). Assuming that the filaments are of radius r_i (m):

$$R_i = \frac{\rho_i}{\pi r_i^2} \tag{5.1}$$

The whole bundle of the filaments composing a composite conductor must have the same DC resistance as the latter. The use of the so called 'fill-factor', *ff*, which must be multiplied by R_i to obtain the corrected resistance, helps towards this direction:

$$ff_k = \frac{n_k \pi r_i^2}{S_k} \tag{5.2}$$

where n_k is the number of all the filaments the composite conductor k consists of and S_k is the cross-sectional area (m^2) of the actual composite conductor k. For instance, if the phase conductor in an SL-Type cable is of radius r_C, it is apparently $S_C = \pi r_C^2$. Since gaps will always exist between filaments irrespective of how small r_i is, ff_k will always be lower than unity and, thus, the product $ff_k R_i$ will be obviously reductive with reference to the initial R_i. The self-inductance L_{ii} of a filament i and the mutual inductance L_{ij} between filaments i and j in the presence of a cylindrical return path - ring of radius a (m) are respectively defined as follows:

$$L_{ii} = \frac{\mu_0}{2\pi} \ln\left(\frac{a}{D_{ii}}\right) \tag{5.3}$$

$$L_{ij} = \frac{\mu_0}{2\pi} \ln\left(\frac{a}{D_{ij}}\right) \tag{5.4}$$

where

$$D_{ii} = r_i e^{-0.25 \cdot \mu_i} \tag{5.5}$$

is the self-geometric mean distance (m), μ_i is the relative magnetic permeability of filament i, and D_{ij} is the geometric mean distance between 2 filaments, i.e. the axial distance between filaments i and j. Assuming in total n filaments, the following equations hold true:

$$\begin{bmatrix} V_1 \\ \vdots \\ V_n \end{bmatrix} = \left(\begin{bmatrix} R_1 & 0 & 0 \\ 0 & \ddots & 0 \\ 0 & 0 & R_n \end{bmatrix} + j\omega \begin{bmatrix} L_{11} & \cdots & L_{1n} \\ \vdots & \ddots & \vdots \\ L_{n1} & \cdots & L_{nn} \end{bmatrix} \right) \begin{bmatrix} I_1 \\ \vdots \\ I_n \end{bmatrix} \Rightarrow$$

$$\Rightarrow [\mathbf{V}_{\mathrm{FM}}] = ([\mathbf{R}_{\mathrm{FM}}] + j\omega[\mathbf{L}_{\mathrm{FM}}])[\mathbf{I}_{\mathrm{FM}}] = [\mathbf{Z}_{\mathrm{FM}}][\mathbf{I}_{\mathrm{FM}}] \tag{5.6}$$

where $\mathbf{V}_{\mathrm{FM}}$ and $\mathbf{I}_{\mathrm{FM}}$ are the voltage drop (V/m) and current (A) filament n x 1 vectors, respectively, $\mathbf{Z}_{\mathrm{FM}}$ is the detailed, n x n impedance matrix (Ω/m), $\mathbf{R}_{\mathrm{FM}}$ and $\mathbf{L}_{\mathrm{FM}}$ is the resistance (Ω/m) and inductance (H/m) matrix, respectively, and ω is the angular frequency (rad/s). The present notation does not include "FM" in the elements of matrices and column vectors for simplicity.

It must be noted that the representation of the return path as an annulus of radius a is necessary concerning the validation of FM models against EMTP-like software. The presence of a return path is inherent in the inductance definition: current loops are assumed between each filament and the return path. For this reason, the position of the return path must be always defined in EMTP-like software; to make FM comparable with EMTP, the return path must also be included. Moreover, its position (radius a if a ring return path is assumed) is expected to affect $\mathbf{Z}_{\mathrm{FM}}$, thus potentially affecting the losses. This is ignored in certain of the existing FM versions, such as de Arizon [20] and Moutassem [22] works. De Arizon suggests in [20] a simplified, reduced $\mathbf{Z}_{\mathrm{FM}}$ which implies a fictitious, lossless return path, where no current

flows. Although this assumption is reasonable for perfectly balanced systems, it is not so when either imbalanced conditions or non-symmetrical geometries are studied. In these cases a return current actually occurs. Moutassem considers in [22] that a = 1 m, implying that this is a sufficiently large ring radius that does not affect $\mathbf{Z}_{FM}$. Although this assumption is expected accurate enough when considering isolated, medium size cables, it may become questionable when for instance two or more neighbouring cables spaced apart at 0.5 m are to be considered. In conclusion, a formulation including the return path size is more generic and for this reason this is considered in the present Chapter.

As implied from (5.6), $\mathbf{Z}_{FM}$ is the detailed n x n impedance matrix and cannot be compared against Ametani formulation [81], which generates m x m matrices, where m is the number of composite conductors. Hence, $\mathbf{Z}_{FM}$ needs to be reduced to m-dimension to verify FM against EMTP-like software. The reduction process, which is largely based on de Arizon's work [85] and ends up to an m x m $\mathbf{Z}^{red}$-matrix, is presented in Appendix A for a 1C cable.

Power losses in each composite conductor are to be derived from the adopted FM version, so as to derive the respective λ_1' and λ_1" figures. This is later on employed, in section 5.2, where FM models are used as reference to validate the FE models with regard to the loss extracted. For this purpose, the case of 3 cable cores (3 conductors plus 3 sheaths, thus m = 6) being in trefoil touching arrangement is shown as an example in Appendix B; the same formulation can be extended for any number of composite conductors, since it is generic. It is noted that this part is largely based on the paper published by Moutassem [22], which can be also found in Anders's book [34]. However, the **Z** formulation described in the present section is used.

5.1.2 Verification of the FM model: 3C Assembly (Pipe-Type Cable)

Having derived the $\mathbf{Z}^{red}$ matrix based on Appendix A, FM can be compared against other analytical methods, such as the general formulation published by Ametani [81] which is employed by EMTP-like software. EMTP-like software is a group of programs capable of analysing electromagnetic transients in power systems using a variety of sophisticated models both in time- and frequency-domain. Making focus on cables under steady-state conditions, the starting points are the telegrapher's equations in frequency-domain:

$$-\frac{d\mathbf{I}}{dz} = \mathbf{YV} = (\mathbf{G} + j\omega\mathbf{C})\mathbf{V} \tag{5.7}$$

$$-\frac{d\mathbf{V}}{dz} = \mathbf{ZI} = (\mathbf{R} + j\omega\mathbf{L})\mathbf{I} \tag{5.8}$$

Where **I** and **V** is the m x 1 current (A) and voltage vector (V), respectively, while **Y** and **Z** are the per unit length (pul) m x m shunt admittance and series impedance matrices, respectively,

which consist of conductance **G** (S/m), capacitance **C** (F/m), resistance **R** (Ω/m) and inductance **L** (H/m) matrices. Eqs. (5.7) and (5.8) can be modelled by the *m*-element homogeneous transmission line with the assumption of plane-wave propagation along *z*-direction. In the present Chapter, the lumped PI equivalent model is employed, since it has been proven to be very accurate and stable under steady-state conditions [88]. In the context of the present Chapter any capacitive effects are omitted and only inductive effects are studied; hence, emphasis is given on (5.8). The use of **Y**-matrix would be needed if induced voltages were to be calculated: indeed, the coupling effect of both inductive and capacitive mechanisms is necessary to represent accurately the voltage raised. On the other hand, the capacitance **C** contributes to the charging current, while the conductance **G** is necessary for dielectric losses. However, these voltage-dependent losses are typically separately calculated in current rating calculations and the inclusion of **Y** would not change the current-dependent losses, which are the main object of the present work.

The impedance matrix for a 1C (coaxial) cable is given by [81]:

$$\mathbf{Z} = \mathbf{Z}_{\mathrm{i}} + \mathbf{Z}_{0} \tag{5.9}$$

where $\mathbf{Z}_{\mathrm{i}}$ is the cable internal impedance and $\mathbf{Z}_{0}$ is the earth-return impedance. For the purpose of loss calculation, the effect of $\mathbf{Z}_{0}$ is considered negligible. Such an evidence is given by Kovac in [89], where sheath losses for 3 1C cables in flat arrangement are studied: a difference of about 0.1% pertaining to total sheath losses is noticed between two different FM models, i.e. accounting and not accounting for the existence of the ground. The cable internal impedance, $\mathbf{Z}_{\mathrm{i}}$, is defined by (5.10) for a coaxial cable:

$$\mathbf{Z}_{\mathrm{i}} = \begin{bmatrix} Z_{\mathrm{CC}} & Z_{\mathrm{SC}} \\ Z_{\mathrm{SC}} & Z_{\mathrm{SS}} \end{bmatrix} \tag{5.10}$$

where Z_{CC} and Z_{SS} is the conductor and sheath self-impedances, respectively, Z_{CS} is the mutual impedance between the conductor and sheath (Ω/m). It is of importance to validate numerical methods, such as FM, versus rigorously analytical models, such as EMTP. This is certainly feasible in the case of coaxial cable where only skin effect occurs. The comparison of FM against EMTP in terms of 1C (coaxial) cables is more trivial and presented in Appendix C. However, SL-Type, armoured cables consist of three power cores which are in close physical proximity one another, where proximity effects are inevitable. Unfortunately, Ametani formulation [81] does not include any model for SL-Type, armoured cables.

One geometry similar to that of an SL-Type, armoured cable is a pipe-type cable enclosing three power cores, which are in trefoil touching formation and located at the centre of the pipe. In such a case, the impedance matrix **Z** is calculated as per (5.11) [81]:

$$\mathbf{Z} = \mathbf{Z}_{\mathrm{i}} + \mathbf{Z}_{\mathrm{p}} + \mathbf{Z}_{\mathrm{c}} + \mathbf{Z}_{0} \tag{5.11}$$

where $\mathbf{Z}_{\mathrm{p}}$ is the pipe internal impedance matrix, $\mathbf{Z}_{\mathrm{c}}$ is the connection impedance matrix between pipe inner and outer surfaces and $\mathbf{Z}_{\mathrm{i}}$ is the cable core impedance matrix, calculated as per (5.10). As becomes apparent, EMTP program calculates separately the impedances for each power core, $\mathbf{Z}_{\mathrm{i}}$, and the pipe itself, $\mathbf{Z}_{\mathrm{c}}$, while $\mathbf{Z}_{\mathrm{p}}$ is used to link the various impedances between the several composites inside the pipe with reference to the pipe inner surface. As for the coaxial cable case, the existence of the earth is decoupled and the pipe-type cable internal impedance matrix is calculated by the subtraction:

$$\mathbf{Z}_{\mathbf{i\_pt}} = \mathbf{Z} - \mathbf{Z}_{0} \tag{5.12}$$

A fictitious serving as thick as 1 m is assumed when constructing the cable geometry, thus considering that the return path lies on a fictitious ring of radius a = 1 m. Hence, $\mathbf{Z}_{\mathbf{i\_pt}}$ becomes directly comparable with $\mathbf{Z}^{\mathbf{red}}$ discussed in section 5.1.1 (the full derivation in a 1C cable is presented in Appendix A) for a number of composites m = 7: both $\mathbf{Z}_{\mathbf{i\_pt}}$ and $\mathbf{Z}^{\mathbf{red}}$ are obviously matrices of order 7 x 7 in the case of a pipe-type cable. Amongst other inputs, the relative magnetic, μ_r, is required for each composite conductor. Since SL-Type cables with non-magnetic armour are investigated in the present Chapter, a non-magnetic pipe, i.e. with μ_r = 1, is considered in all the methods used to calculate $\mathbf{Z}$.

It should be noted that the EMTP program becomes questionable in the case of power cores which are laid in close physical proximity, since it does not account for any proximity effects. For this reason, a method which is capable of accounting for both skin and proximity effects is sought for the validation of FM. The so called "Js-method" is used for this purpose [90]. This is based on a straight forward calculation of $\mathbf{Z}$ from the current density Js. A sinusoidal current excitation of arbitrary magnitude I_j is applied sequentially to each composite j, while the remaining composite $i \neq j$ (i, j = 1, 2, …, m) are forced to carry zero currents, i.e. to be open-circuited. At the same time, the corresponding voltages, V_i, are obtained. The mutual element Z_{ij} of matrix $\mathbf{Z}$ between conductive composites i and j can be defined as:

$$Z_{ij} = \frac{V_i}{I_j} \tag{5.13}$$

The self-impedance of a composite conductor may also be calculated from (5.13), by setting $i = j$. Thus, by using (5.13), the j^{th} column of $\mathbf{Z}$ is calculated. This procedure is repeated m times (m = 7 for the case of pipe-type cable) in order to calculate the m columns of $\mathbf{Z}$. Therefore, the problem is reduced to that of calculating the actual pul voltage drops, when a current excitation is applied on the conductors. Any method being capable of representing skin and proximity

effects could be applied and, in combination with the Js-method, eventually provide the requested **Z** elements.

Finite Element Method (FEM) can be used to numerically solve the electromagnetic field equations; assuming that the current density vector lies on *z*-direction, the problem becomes 2-D and confined on the *xy* plane, where the unknown magnetic vector potential, $\overrightarrow{A_z}$ (Wb/m), also lying in *z*-direction, is solved for. The linear electromagnetic diffusion equation is given [90]:

$$\frac{1}{\mu_0 \mu_r}\left(\frac{\partial^2 \overrightarrow{A_z}}{\partial x^2}+\frac{\partial^2 \overrightarrow{A_z}}{\partial y^2}\right)=-\left(\overrightarrow{J_{ez}}+\overrightarrow{J_{sz}}\right) \tag{5.14}$$

where

$$\overrightarrow{J_{ez}}=-j\omega\sigma\overrightarrow{A_z} \tag{5.15}$$

is the eddy current density (A/m^2), and

$$\overrightarrow{J_{sz}}=\sigma\vec{E}=-\sigma\nabla\Phi \tag{5.16}$$

is the source current density (A/m^2). σ is the electrical conductivity (S/m) and Φ is the unknown electric scalar potential (V). It is noted that the electric field $\vec{E}=-\nabla\Phi$ (V/m) has a *z*-component only and Φ is constant over the cross-section of each composite conductor in the problem. Hence, the FE solver doesn't have to solve for Φ at every node. Additionally, no displacement current, i.e. $j\omega\vec{D}$, where $\vec{D}$ is the electric displacement field (C/m^2), is included in (5.14), since it is considered negligible at power frequency. Therefore, the total current density, $\overrightarrow{J_z}$, is decomposed into the two component defined by (5.15) and (5.16), i.e.:

$$\overrightarrow{J_z}=\overrightarrow{J_{ez}}+\overrightarrow{J_{sz}} \tag{5.17}$$

For any problem described by partial differential equations, proper boundary conditions have to be considered. Two unknowns, i.e. $\overrightarrow{A_z}$ and Φ, are to be solved for. Besides (5.14), an externally imposed current, I_i, where i = 1, 2, …, m, is considered in each composite conductor such that:

$$\iint_{S_i}\overrightarrow{J_z}d\vec{S}=I_i \tag{5.18}$$

More details about the numerical solution of the above equations are given in [91]. A homogeneous Dirichlet boundary condition in terms of $\overrightarrow{A_z}$ is set at the boundary of a ring with a = 1 m, that is:

$$\vec{n}\times\overrightarrow{A_z}=0 \tag{5.19}$$

where $\vec{n}$ is the normal unit vector. Placing the boundary condition expressed by (5.19) in the FE model at a distance equal to the same location as the return path in FM is the key-technique in order to generate directly comparable results between the two methods. In fact, the so called 'Magnetic Insulation Boundary' affords a lossless current return path (it could be thought as representing a material with infinite conductivity along which current can flow unimpeded) which originates from the field approach. In other words, setting the Magnetic Insulation Boundary is another way to force the imposed current I_i to return through a lossless path that can be located at a specific distance from the cable. The Magnetic Insulation boundary condition is illustrated in Figure 5.1.

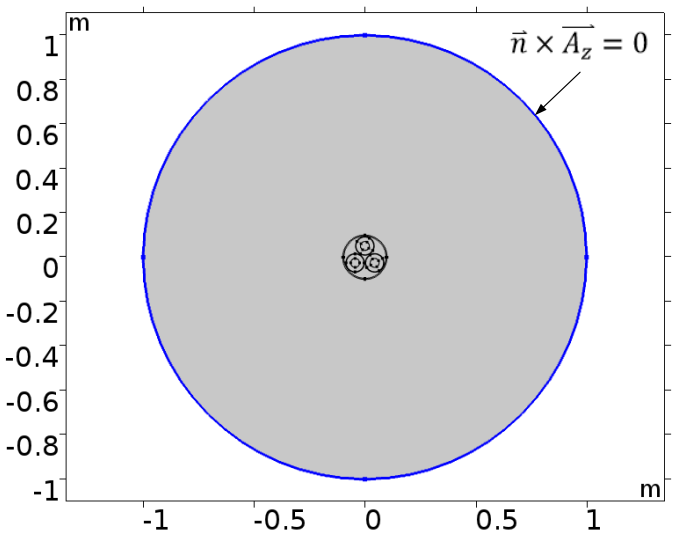

FIGURE 5.1: The So-Called 'Magnetic Insulation' Boundary Condition Placed at a Distance a = 1 m from the Cable Centre.

Values for $\overrightarrow{J_{sz}}$ on each composite conductor i of conductivity σ_i are then obtained and (5.13) takes the form

$$Z_{ij} = \frac{V_i}{I_j} = \frac{J_{sz_i}}{\sigma_i I_j} \tag{5.20}$$

The general notation including numbers is adopted in the present section, regardless of the method used to derive **Z**: 1, 3 and 5 correspond to phase conductors A, B and C, respectively, 2, 4 and 6 correspond to metallic sheaths of phases A, B and C, respectively, and 7 corresponds to the pipe. For instance, Z_{37} represents the mutual impedance between conductor B and the pipe. Due to symmetry, several mutual impedances are expected identical with others: mutual impedances between conductors, mutual impedances between sheaths and mutual impedances between conductors or sheaths and the pipe are such cases; additionally, the mutual impedances between conductors and the sheaths belonging to other phases than the former will be equal one another. In conclusion, Z_{11}, Z_{22}, Z_{77}, Z_{12}, Z_{13} and Z_{17} are enough to check the **Z** generated by any method.

Three cores, each one consisting of a Copper conductor with r_C = 20 mm and a Lead sheath with t_S = 2 mm and $r_{S,in}$ = 40 mm, are considered in trefoil with axial separation equal to $2r_{S,in} + 4t_S$. A non-magnetic pipe of inner radius and thickness $r_{P,in}$ = 95 mm and t_P = 5 mm, respectively, is also considered. The three models discussed in the present section are compared not only at power frequency (50 H), but also at 1000 Hz: a wider assessment of FM is permitted this way, which may be useful for transient applications where higher frequency components are present. In terms of FM, a modest "mesh" consisting of about 5000 filaments is assumed. The Js – FEM method is considered as a reference and the relative difference between EMTP or FM and Js – FEM, namely e_{EMTP} or e_{FM}, respectively, is obtained, with the respective values being presented in Table 5.1 for the **Z**-elements which are of interest.

TABLE 5.1: Comparison between EMTP, Js-FEM and FM for 50 Hz and 1000 Hz.

	50 Hz		1000 Hz	
Z - element	e_{EMTP} (%)	e_{FM} (%)	e_{EMTP} (%)	e_{FM} (%)
$\Re\{Z_{11}\}$	21.92	-0.07	54.35	2.28
$\Im\{Z_{11}\}$	2.05	0.00	-4.80	-0.06
$\Re\{Z_{22}\}$	1.48	-0.02	21.87	0.53
$\Im\{Z_{22}\}$	2.68	-0.05	-6.18	-0.07
$\Re\{Z_{77}\}$	0.00	0.00	0.00	1.23
$\Im\{Z_{77}\}$	-0.01	-0.02	0.00	-0.02
$\Im\{Z_{12}\}$	2.68	-0.02	-6.17	-0.03
$\Im\{Z_{13}\}$	-3.13	0.01	-4.76	-0.01
$\Im\{Z_{17}\}$	0.00	0.00	0.00	0.00

As expected, EMTP method generates **Z** results which diverge from Js – FEM method, particularly concerning $\Re\{Z_{11}\}$ and $\Re\{Z_{22}\}$: e_{EMTP} equals to 21.92% and 1.48% for 50 Hz, respectively, while becoming 54.35% and 21.87% for 1000 Hz, respectively. The increase in frequency apparently leads to more intense proximity effects, even for the higher resistivity Lead sheaths. EMTP stands considerably far from Js – FEM, since it does not take proximity effect into account. Significantly reduced divergence against FEM – Js method is obtained by FM, yielding e_{FM} lower than 0.1% for $\Re\{Z_{11}\}$ and $\Re\{Z_{22}\}$ at 50 Hz. e_{FM} appears slightly above 2% in terms of $\Re\{Z_{11}\}$ for 1000 Hz, implying that a finer "mesh" would provide even better results. A similar trend is seen for $\Re\{Z_{77}\}$, where e_{FM} appears higher than e_{EMTP} at 1000 Hz: in that case the analytical rigorousness of EMTP proves superior, whereas the modest "mesh" in

the pipe area is obviously not enough to represent at the same level the more intense skin effect. FM stands, in general, closer to Js – FEM method than EMTP does regarding also the imaginary parts of all **Z**-elements, as expected: cable inductances are in general affected by proximity effects, which are considered by both methods, in contrast with EMTP.

A FM model is developed in the present section, which is a combination of certain formulations reported in different works in the existing literature. The model is validated against EMTP-like software, which is a rigorously analytical model capable of representing skin effect. Provided that SL-Type cables consist of power cores being in close physical proximity, proximity effects are also expected in both conductors and sheaths. In this case EMTP gives less accurate results, while the Js method – FEM method is considered the most accurate method which is also capable of incorporating skin and proximity effects. The FM model seems to generate **Z**-results in a very good agreement with Js – FEM. FM is used in combination with FEM in the next section, making focus on the estimation of sheath losses in 3C SL-Type cables with non-magnetic armour.

5.2 Analysis of Sheath Losses in 3C SL-Type Cables

As discussed in Chapter 4, the losses induced in the metallic sheaths of SL-Type cables with non-magnetic armour are of great importance, since the armour loss itself, being generated from induced eddy currents, is expected very low and considered practically negligible. Based on the literature review, the existing analytical methods calculating the eddy current loss factor, λ_1", such as that suggested by Jackson [1] or that adopted by the IEC 60287-1-1 Standard [16], assume that line currents flow in the conductors. However, it is identified by Arnold in 1939 [69] that the total magnetic field produced by the three conductors is actually reduced, because of the crowding of the conductor currents towards each other; in other words, because of the proximity effects in conductors. In addition, the DC resistance still used by IEC 60287-1-1 [16] when calculating the circulating current loss factor, λ_1', is expected to be less accurate in the case of SL-Type cables, where the metallic sheaths are placed in close physical proximity one another. The two aforementioned assumptions regarding λ_1" and λ_1' become even more critical when larger submarine cables, such as those used in modern OWFs, are considered, since they often involve larger conductors and sheaths.

To evaluate the impact the proximity effects in both conductors and sheaths have on sheath losses, Finite Element Method (FEM) is employed. Thanks to the powerful capabilities which allows for an extended parametric analysis, the software implementing FEM offers a useful tool to identify the key-design factors affecting the sheath losses. On the other hand, FEM software are often considered as black-box approaches and their validation against other, analytical methods is sought. For this purpose, the FM model developed in section 5.1 is used: although

not strictly analytical, it is in its turn validated against other, analytical models, such as EMTP method, and, thus, is considered valid.

In the following sections, the effect of the non-magnetic armour on λ_1 and the overall modelling FE strategy are first discussed. Subsequently, the validation of FEM against the FM model in terms of losses is demonstrated, while certain experimental measurements of sheath losses carried out in a an actual 3C export, unarmoured cable sample add an extra indication which verifies the validity of the FE models used. Then, the main analysis starts by comparing FE and FM results against the existing analytical models; a parametric analysis is done and the key-design factors affecting sheath losses are identified. Although FE and FM models appear to provide more accurate results than the existing methods, they are not suitable for Standardisation purposes and the whole set-up and solution time is always a discouraging factor for their use. For this reason, approximating formulae, which are derived from the parametric analysis done, are finally suggested.

5.2.1 Finite Element Analysis (FEA): Modelling Strategy

The equations that are solved for the problem of losses calculation are the same as those presented in 5.1.2, where the Js – method is described (from (5.14) to (5.19)). In that case, it was desirable to confine the electromagnetic problem at some specific, finite cylindrical domain of radius *a* for the sake of comparison with the other methods (FM, EMTP). However, the calculation of losses in any cable is in principle an open-boundary problem: although the buried subsea cables are physically limited by the seafloor, they still are magnetically unbounded. On the other hand, the Magnetic Insulation condition, expressed by (5.19) and discussed in section 5.1.2, is placed at some specific distance *a* far from the cable and the variation of this distance is expected to have some impact on the obtained losses. A sensitivity analysis is useful in this case, so as to deduce about the proper *a* value.

In order to limit the extent of the FE model to a manageable region of interest with reasonable execution time, a coordinate scaling is adopted in the present Chapter to layers of virtual domains surrounding the physical region of interest. These virtual layers, often called as 'Infinite Domains', can be mathematically stretched out towards infinity, where (5.19) is applied. As a result, the model becomes computationally efficient, while the solution inside the region of interest is not affected by the artificial geometric boundaries. An indicative model comprising three power cores being in trefoil, closed formation, including the Infinite Domains, is illustrated in Figure 5.2. The same three-core cable as that studied in section 5.1.2 is also considered in the present section. Thanks to the use of Infinite Domains, the overall model size is kept quite small: hence, a very fine mesh in the domains of interest only can be made, so as to compare loss results against coarser meshes. However, the skin depth of Lead remains fairly

higher than sheath thickness at power frequency (about 33 mm at 50 Hz). Therefore, the mesh is not expected to have a huge impact on induced losses. Indeed, by increasing the mesh of each sheath from 124 to 6102 elements (or by almost $5 \cdot 10^3$ %), the change in sheath loss, namely W_S (W/m), is negligible (less than $4 \cdot 10^{-4}$ %).

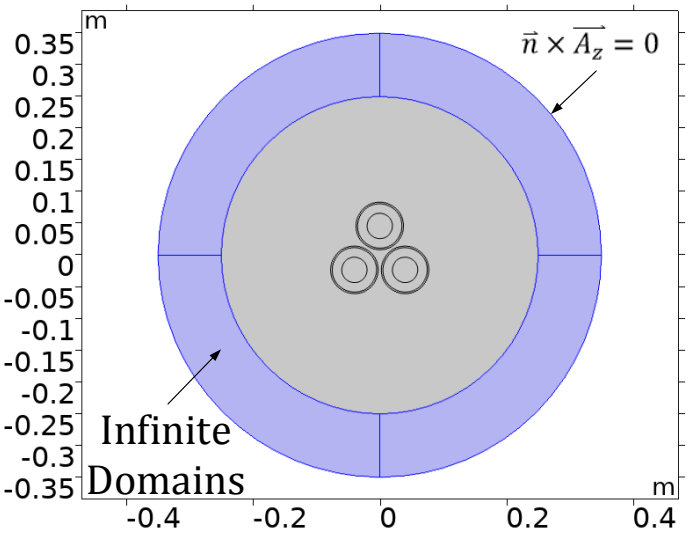

FIGURE 5.2: Indicative FE Model with Three Power Cores in Close Trefoil Formation Including the Infinite Domains.

Conductor loss, W_C, and W_S (W/m), are then compared (Figure 5.3) against the case the ring radius a increases until its value has no more effects on the losses obtained.

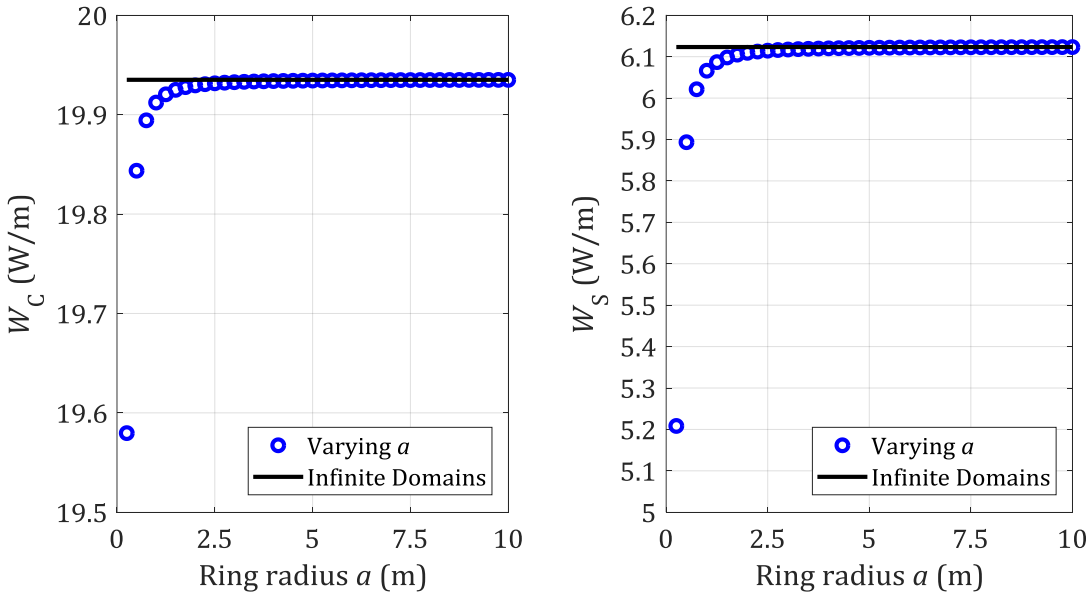

FIGURE 5.3: Comparison of Conductor and Sheath Losses when Varying Ring Radius a and Using the Infinite Domains, Respectively.

As shown in Figure 5.3, the W_C and W_S curves tend to the fixed values obtained from the use of Infinite Domains by increasing a. It is noted that W_C and W_S appear to be affected by a in

the region around a = 1 m, thus implying that such a ring wouldn't be large enough for the purpose of loss calculation.

As assumed for the FM models, three-phase balanced currents are also applied in the conductors in the FE models. Solid bonding and single-point bonding arrangements are examined in the next sections by using FE models. Although the former is typically applied in the sheaths of submarine cable links in order to avoid any excessive overvoltages, the latter is also of interest in order to study solely the eddy current loss. To simulate both bonding arrangements, the following technique is followed: external circuits which consist of a voltage source and a variable internal resistance, R_{Si_int} (Ω), where i equal to 1, 2 or 3, depending on sheath, are connected in parallel with sheaths, as illustrated in Figure 5.4. When linking each of these circuits with the corresponding sheath, the voltage source becomes equal to the electromotive force (emf) induced. By varying the R_{Si_int} from extremely small to extremely large values, solid and single-point bonding cases may be represented, respectively. A net induced current is noticed in the former, whereas practically no net current occurs in the latter case, where eddy currents only are allowed to circulate.

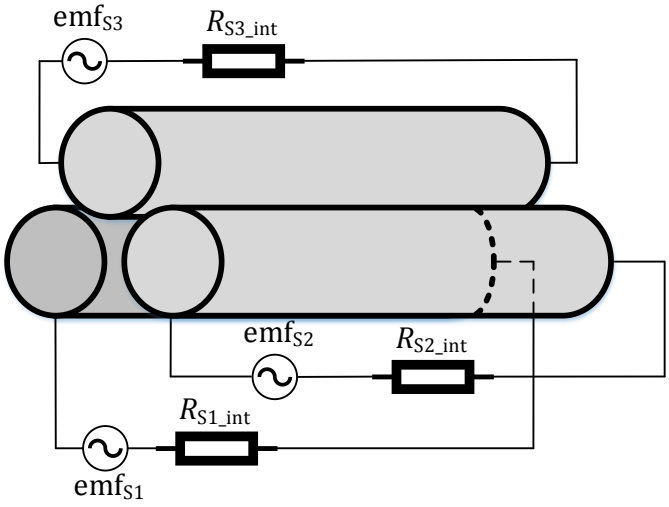

FIGURE 5.4: Use Of External Circuits to Simulate Single-Point and Solid Bonding Arrangements.

It should be noted that the three cores are assumed jacketed with a perfectly insulating material in the present Chapter. Jackets consist of some semiconductive polymer, which typically has a conductivity value about 5 orders of magnitude lower than Lead. Hence, no significant amounts of currents are expected to flow axially, along jackets' volume. Although their conductivity is so lower than Lead, they still exhibit some conductive behaviour, which allows for a good electrical contact in the radial direction. Thus, extra conductive paths through the jacket wall between cores develop, depending on their conductivity. This is not expected to cause any significant difference in the solid bonding case. However, in single-point bonding net currents may flow through jackets, along the sheaths, depending on the conductivity of the

jackets and the length simulated. Sturm cites in a recent work [92] a relative difference of about 30% in λ_1" for a jacket conductivity of 10 S/m, because of the current jumps between sheaths. However, the investigation of such an effect would require 3-D analysis, whereas the existing analytical methods are limited to 2-D analysis. Similar assumptions are made in the present Chapter, in order to derive comparable loss results. Moreover, single-point bonding is not expected in practice, since subsea links are typically so long that overly high induced voltages would occur in such a case.

The phase conductors are modelled as solid for the sake of simplicity. The same assumption is made for the FM model developed, as presented in section 4.4.2. This is an approximation, since stranded conductors are mostly used in practice, mainly for mechanical reasons. However, it is still an effective way of modelling SL-Type cables via FE software, particularly in the cases that focus is made on the losses induced in the sheaths and not the conductor themselves. However, the existence of various strand layers, being potentially twisted with different lay-lengths, is expected to have some impact on the proximity effect in conductors; hence, sheath losses may be affected. For this reason, the effect of stranded conductors is studied later, in section 5.2.6.

5.2.2 Finite Element Analysis: Effect of the Non-Magnetic Armour on λ_1

As remarked in Chapter 4, all researchers agree to the point that no circulating currents are expected to flow in armour wires, due to the twisting effect and the zero net induced voltage over a complete lay-length, on the condition that balanced currents are applied in the phase conductors and the armour wires are not in electrical contact one another. An effective way to represent this effect in 2-D models is suggested for the first time by Bremnes [19], where a 2.5-D model is established by connecting in series the armour wire domains. Although this approach is not expected to be realistic enough when considering a magnetic armour, as discussed in sections 4.2 and 4.3, the situation is different when non-magnetic armour is simulated: assuming a relative permeability μ_r = 1, the presence of the armour makes no difference to the amount of the flux induced by the power cores within the thickness of the armour. The presence of the armour would make a considerable difference to the total induced flux if net currents were allowed to flow in the armour wires. However, only eddy currents are expected in the armour, on the condition that a balanced three-phase current source is applied in conductors.

The same three-core cable as that studied in section 5.1.2 is also considered in the present section, though with a wire armour layer instead of a pipe. Three cases are modelled: one connecting the armour wires in parallel and considering three-phase balanced currents in the power cores, one connecting the armour wires in series and keeping three-phase balanced currents in the power cores and one connecting the armour wires in series and considering

three-phase imbalanced currents in the power cores. The current density $\overrightarrow{J_z}$ in the armour is plotted for each of the above cases and shown in Figure 5.5, Figure 5.6 and Figure 5.7, respectively. The plus and minus signs merely imply the direction of the vector $\overrightarrow{J_z}$: from the *xy*-plane to the reader and vice versa, respectively.

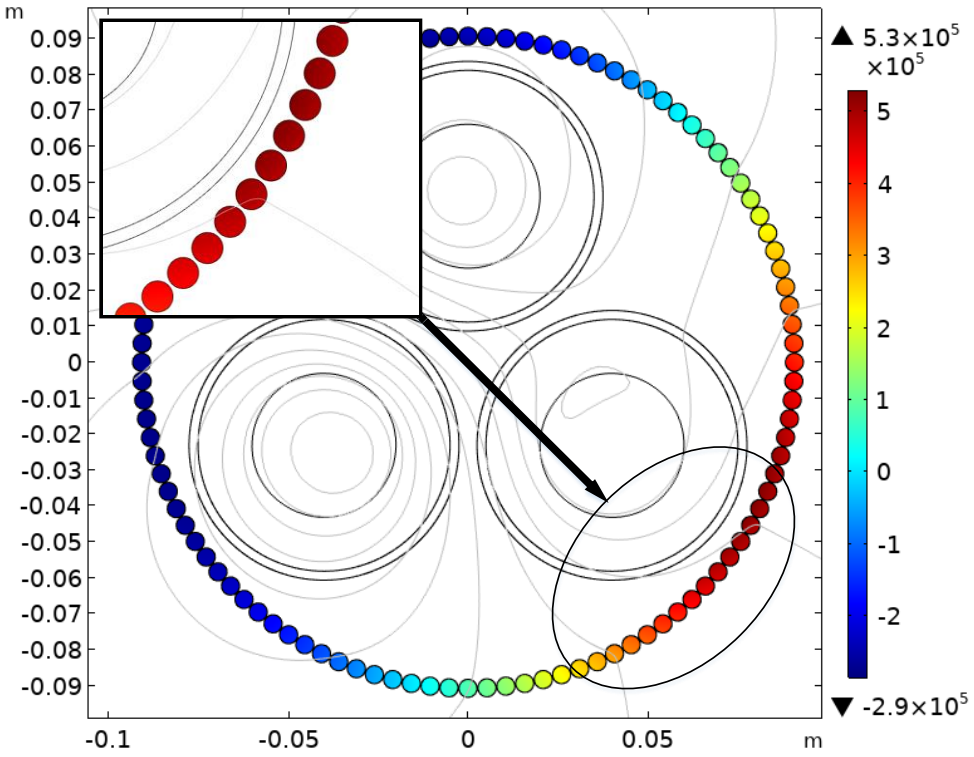

FIGURE 5.5: $\overrightarrow{J_z}$ (A/m^2) in the Armour for Connected Wires in Parallel and Balanced Phase Conductors.

In Figure 5.5 high net currents appear to flow in both directions (i.e. from the *xy*-plane to the reader and vice versa) along the armour wires, thus creating a less realistic flux distribution. A significantly lower $\overrightarrow{J_z}$ profile is shown in Figure 5.6: eddy currents only are noticed in each wire, which are represented by the plus and minus signs of J_z. The net current is zero in this case. A net current is clearly shown in Figure 5.7 (this is implied by the absence of negative J_z values), where in series connected wires are considered under imbalanced conditions.

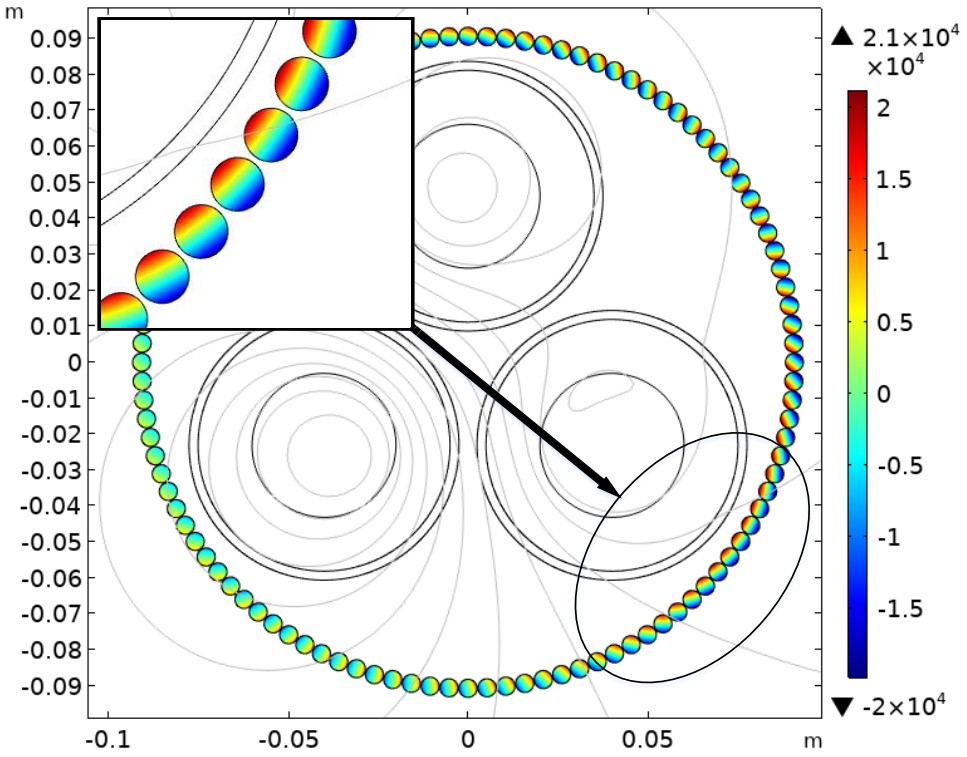

FIGURE 5.6: $\overrightarrow{J_z}(\mathrm{A/m^2})$ in the Armour for Connected Wires in Series and Balanced Phase Conductors.

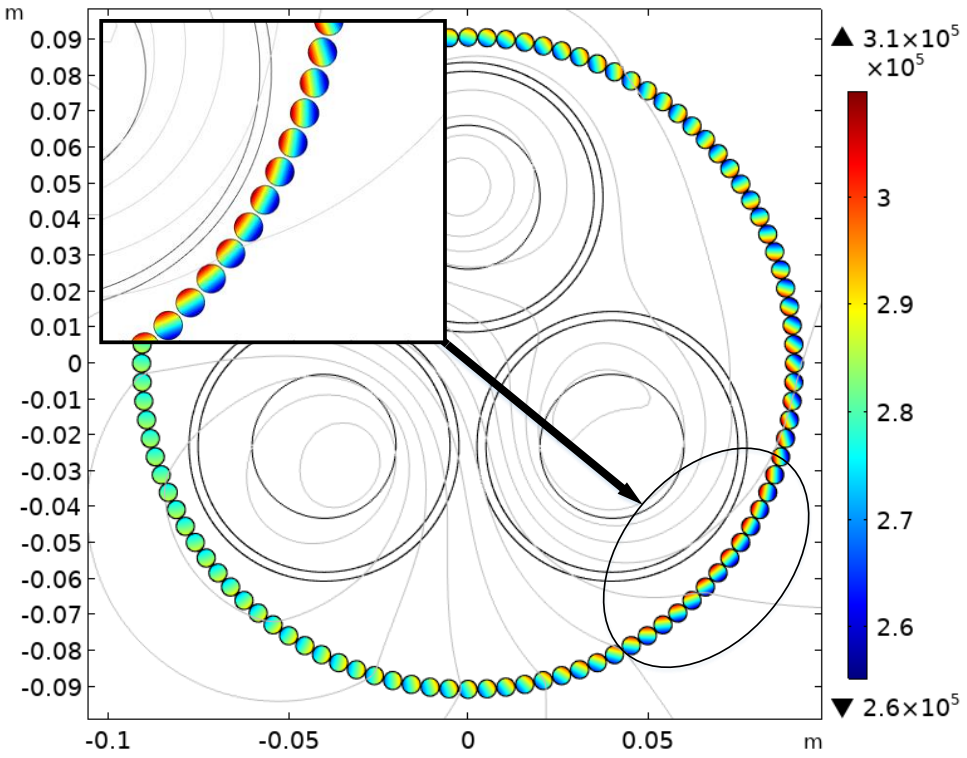

FIGURE 5.7: $\overrightarrow{J_z}(\mathrm{A/m^2})$ in the Armour for Connected Wires in Series and Imbalanced Phase Conductors.

The in-series wire connection is adopted and balanced currents in the conductors are assumed, while solidly bonded sheaths are considered in the present section. Three indicative cable sizes

of various geometrical parameters, i.e. with conductors of radius r_C, sheaths of inner radius $r_{S,in}$ and thickness t_S, as well as armour layers consisting of wires with diameter d_f, are considered. Simulations are conducted both with and without non-magnetic armour. The changes in sheath loss factor λ_1 are noticed at the 5^{th} – 6^{th} decimal digit and kept lower than 0.004%, as shown in Table 5.2. Thus, the presence of non-magnetic armour has almost no effect on the losses induced in sheaths. It should be noted that the essentially 2-D representation applied in this section does not include any eddy currents expected to circulate circumferentially, in the angular direction with reference to the wire axis: this is impossible in 2-D analyses. However, these extra eddy currents are not expected to change considerably the overall magnetic flux for most typical SL-Type cable designs, where the longitudinal flux driven along the wires is expected to be relatively low (because $\mu_r = 1$). Such an evidence is provided later, in Chapter 6, where 3-D FE analysis is performed assuming, amongst other grades, austenitic (stainless) steel armour. Various armour pitch values are considered and comparisons against the respective 2-D models are presented. The maximum relative difference noticed in terms of λ_1 factor does not exceed 2%. For the sake of simplicity, no armour is considered from now on in the following sections and focus is made on sheath losses.

TABLE 5.2: Comparison of λ_1 when Non-Magnetic and No Armour Is Considered over a 3C Cable.

r_C / r_{Sin} / t_S / d_f (mm)	λ_1 - with non-magnetic armour	λ_1 - with no armour	% difference
10.0 / 20.0 / 1.5 / 4.0	0.048884539	0.048885327	0.002
20.0 / 35.0 / 2.5 / 5.0	0.336404313	0.336416286	0.004
30.0 / 50.0 / 3.5 / 6.0	0.885863078	0.885884957	0.002

5.2.3 Validation of the Developed FE Model

In this section, the FE models developed based on the strategy referred to section 5.2.1 are first compared against the FM loss models developed in section 5.1.1. Infinite Domains are employed by the FE models, while a sufficiently large radius a is used to move the ring return path as far as possible (practically to infinity) regarding the FM models. Eqs. (B. 20)and (B. 21) shown in Appendix B are used to calculate conductor and sheath losses, respectively, via FM. Results are shown in Table 5.3 for Copper conductor, Lead sheathed cable cores, laid in trefoil, close formation, with conductor radius r_C, sheath inner radius $r_{S,in}$ and thickness t_S. Tests for both λ_1" and λ_1 cases are presented. As shown in the 3^{rd} and 4^{th} columns of Table 5.3, the % relative difference between FE and FM models, i.e. $e_{FE,FM}$, is kept fairly low for a relatively

modest number of filaments n, i.e. $660 \leq n \leq 760$. Better accuracy is obtained, as expected, for $2560 \leq n \leq 2950$, as shown in the 6th and 7th columns of Table 5.3.

TABLE 5.3: FM vs FE Models for Various Cable Sizes and Number of Filaments.

r_C / $r_{S,in}$ / t_S (mm)	n	$e_{FE,FM}$, λ_1" (%)	$e_{FE,FM}$, λ_1 (%)	n	$e_{FE,FM}$, λ_1", (%)	$e_{FE,FM}$, λ_1 (%)
10 / 20 / 1.0	663	0.03	0.19	2565	0.02	0.06
20 / 35 / 1.5	726	1.62	1.75	2817	0.54	0.59
30 / 50 / 2.0	759	4.19	4.25	2943	1.21	1.23

The validation of FE models against other, theoretical methods, such as FM, is very important and allows for a quick and wide assessment with regard to the cable cases tested. Although more time-consuming and more difficult to be carried out for many cable samples, the experimental verification of losses calculated by FE models adds an extra indication that the latter are valid. Loss measurements carried out in a 3 x 1000 mm² 155 kV cable with Copper conductors, solidly bonded Lead sheaths and no armour are briefly presented in this section. The experimental setup is briefly illustrated in the drawing of Figure 5.8.

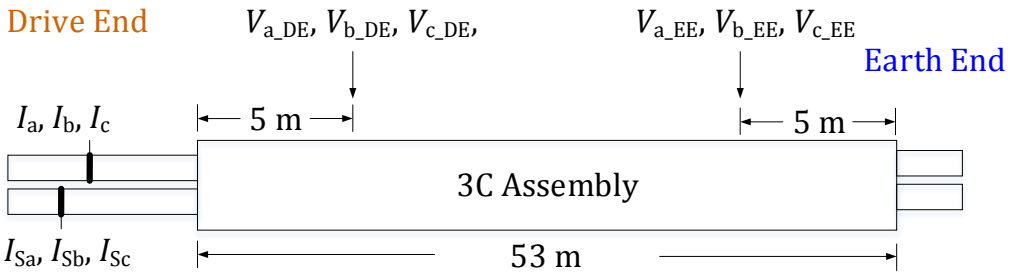

FIGURE 5.8: Experimental Setup Implemented in a 3x1000 mm² 155 kV Unarmoured Cable Sample.

Current measurements in the conductors and sheaths are taken by means of Rogowksi coils. To minimise gain errors, efforts are made to ensure that the measured currents are centrally located, as shown in Figure 5.9. It is important to test a fairly long cable sample, so as to avoid any end effects that in real installation would have no impact. On the other hand, testing an extremely long cable would require a very large space, while would need a high enough power input in order to reach the rated current. For the specific cable sample a good compromise is a cable sample as long as 53 m.

Current Transformers (CTs) driving the currents in the conductors are placed at the Drive End, where conductors and sheaths are connected together in a star point by means of Copper bars. The phase conductors and sheaths are also short-circuited by means of a Copper bar placed at the Earth End.

FIGURE 5.9: Measurements of Conductor (on the Left) and Sheath (on the Right) Currents via Rogowski Coils Placed as Centrally as Possible.

To minimise the connecting resistances, the Copper bars used are of a cross-sectional area not lower than that of conductors; concerning the sheath-sheath connections, double Copper braids of 250 mm^2 each are used, thus affording a total connecting resistance equivalent to 500 mm^2, which is close to the sheath area (about 600 mm^2). Measurements of the contact resistances at both Drive and Earth Ends are also carried out. The maximum connecting resistance (including both the Copper braid and the relevant contact resistances) is found between the Lead sheath of some phase and the bar at the Earth End and this does not exceed 280 μΩ. For the sample length tested, this is almost 60 times lower than the sheath resistance, thus affording a sufficiently good connection. Images showing the experimental configuration at Drive and Earth Ends are illustrated in Figure 5.10.

FIGURE 5.10: Drive End (on the Left) and Earth End (on the Right).

Voltage measurements at conductors are also taken by means of voltage taps. End effects are likely to occur, because of the change in geometry, i.e. the transition from the separated power cores in flat configuration (due to the use of CTs and bonding connections) to the 3C assembly. In order to avoid them, these taps are placed 5 m ahead and behind the Drive End (DE) and the

Earth End (EE), respectively, as shown in Figure 5.8. Thanks to these measurements the total complex power, S_{tot} (VA), related to the 3C assembly can be calculated:

$$S_{\text{tot}} = I_{\text{a}}\left(V_{\text{a\_DE}} - V_{\text{a\_EE}}\right) + I_{\text{b}}\left(V_{\text{b\_DE}} - V_{\text{b\_EE}}\right) + I_{\text{c}}\left(V_{\text{c\_DE}} - V_{\text{c\_EE}}\right) \tag{5.21}$$

where I_i is the phasor of the phase current measured (A), V_{i_DE} and V_{i_EE} is the phasor of the phase voltage measured (V) at the Drive and Earth End, respectively, and i is phase a, b or c. It is noted that line-to-line voltages are directly measured and the respective phase voltages are subsequently calculated in order to avoid any likely issues with ground reference. To consider the total pul active losses, P_{tot} (W/m), consumed in the cable, the real part of (5.21) is considered, by dividing S_{tot} by the sample length, i.e. 53 m, as shown in Figure 5.8.

The DC resistances of phase conductors and sheaths are also measured. The four-wire Kelvin measurement method is used for this purpose [93]. The temperature at the moment of measurement is also recorded in both conductors and sheaths; subsequently, the DC resistance is corrected based on the temperature coefficients referred to the IEC 60287-1-1 Standard [16]. Current levels from 500 A to 1300 A are injected in the conductors with a step current of 100 A. Between two successive tests, enough time is left in order for the temperature of the metallic parts to revert back to the ambient temperature, as possible. The circulating current in sheaths, I_{S}, is directly measured by means of the Rogowski coils placed; therefore, $\lambda'_{1,\text{test}}$ factor may be calculated via (5.22):

$$\lambda'_{1,\text{test}} = \frac{1}{3}\left(\frac{{I_{\text{Sa}}}^2 R_{\text{Sa}}}{{I_{\text{a}}}^2 R_{\text{AC}_\text{a}}} + \frac{{I_{\text{Sb}}}^2 R_{\text{Sb}}}{{I_{\text{b}}}^2 R_{\text{AC}_\text{b}}} + \frac{{I_{\text{Sc}}}^2 R_{\text{Sc}}}{{I_{\text{c}}}^2 R_{\text{AC}_\text{c}}}\right) \tag{5.22}$$

where I_{Si} is the sheath current measured (A), R_{Si} is the measured DC resistance of sheath (Ω/m), $R_{\text{AC\_i}}$ is the AC resistance of conductor (Ω/m). The AC resistance of conductors is calculated via IEC 60287-1-1 based on the DC resistance value measured, R_i. The results about λ'_1 factor are shown in Figure 5.11; the values measured present a deviation of less than 1% against FEA values, whereas the corresponding figure goes up to 9% when compared to the IEC ones.

Eddy current loss is difficult to directly measure. However, it can be indirectly measured by subtracting conductor and sheath circulating losses from total losses, as (5.23) implies:

$$\lambda''_{1,\text{test}} = \frac{1}{3}\left[P_{tot} - \left({I_{\text{a}}}^2 R_{\text{AC}_\text{a}} + {I_{\text{b}}}^2 R_{\text{AC}_\text{b}} + {I_{\text{c}}}^2 R_{\text{AC}_\text{c}}\right) - \left({I_{\text{Sa}}}^2 R_{\text{Sa}} + {I_{\text{Sb}}}^2 R_{\text{Sb}} + {I_{\text{Sc}}}^2 R_{\text{Sc}}\right)\right] \tag{5.23}$$

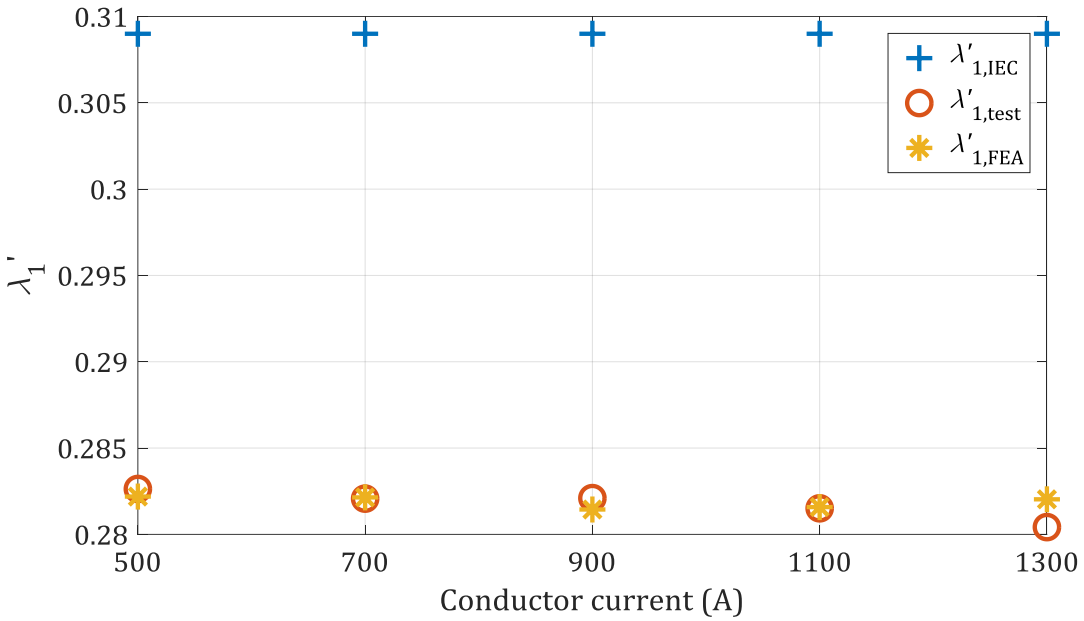

FIGURE 5.11: λ'_1 Factor Measured Data Against Those Calculated by IEC 60287-1-1 and FE Models.

The results about λ''_1 factor are shown in Figure 5.12. $\lambda''_{1,test}$ stands 5-7% higher than $\lambda''_{1,IEC}$ and even higher than $\lambda''_{1,FEA}$ which was not in theory expected. However, eddy current loss is in general a small quantity and the method used to determine it from the experimental data is prone to influence from measurement errors. Besides, the fact that the measured values occur within the same order of magnitude with those theoretically obtained is still of some value.

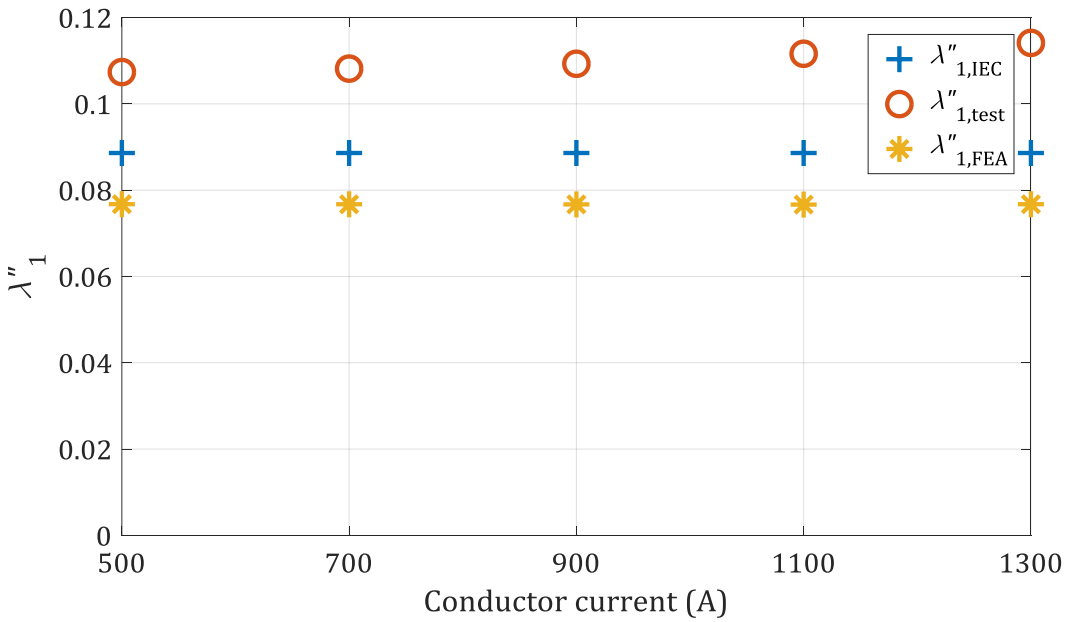

FIGURE 5.12: λ''_1 Factor Measured Data Against Those Calculated by IEC 60287-1-1 and FE Models.

Having validated the FE models pertaining to the 3C assembly, they can be used as a reference in the comparison against the existing analytical models. Two different assumptions are made in the following sections with regard to the current density J (A/m^2) in phase conductors regarding the FE models: uniform (no skin/ proximity effects) and non-uniform (skin/ proximity effects considered), namely J_u and J_{nu}, respectively. Although the former assumption is not realistic, it is still of interest, since it allows for a completely symmetrical current distribution to be considered; thus, the corresponding FE models are expected to generate induced losses closer to the analytical models suggested by Jackson in [1] and implied by the IEC 60287-1-1 Standard [16], which both imply line current in the conductors. This is, in other words, an alternative way of using the FE models to derive sheath loss values, though keeping artificially the assumptions made in the existing analytical methods.

Several geometrical parameters are considered to vary within representative ranges: conductor radius r_C from 10 to 30 mm, sheath inner radius $r_{S,in}$ from 25 to 60 mm and sheath thickness t_S from 1.0 to 4.0 mm. To check individually for the influence of the variation of each geometrical parameter, the rest remain unchanged and equal to a moderate value each time. Besides the solid bonding arrangement of sheaths, which is typically applied in subsea links employing export cables, comparisons are also made with single-point bonded sheaths: the eddy current loss itself can be examined this way. Results derived from FM, based on section 5.1.1, are also presented and, as expected, they stand very close to those calculated through FEA.

5.2.4 Single-Point Bonding Loss

This section presents the results derived from four different methods, i.e. those suggested by Jackson [1] and the IEC 60287-1-1 [16], as well as FE and FM models. The effect of eddy currents up to 3rd order is taken into consideration with respect to Jackson's method, since as reported in [1], the effect of 4th and higher order currents have usually negligible effects. The relevant formulation is briefly presented in this section for phase A assuming three cable cores, namely A, B and C, in trefoil configuration. Identical loss factors for the other two phases are obviously expected because of symmetry.

$$\lambda''_{1\text{Jack}} = \frac{R_S}{R_{AC}}\left[\frac{1}{2}\sum_{k=1}^{\infty}\left(\left|C_{A_k}\right|^2 + \left|C_{A_k}{}'\right|^2\right) + \frac{(\beta_1 t_S)^4}{12\cdot 10^{12}}\right] \tag{5.24}$$

where R_S is the resistance of sheath per unit length (pul) of cable (m), R_{AC} is the AC resistance of conductor pul (Ω/m), t_S is the sheath thickness (mm),

$$\beta_1 = \sqrt{\frac{4\pi\omega}{10^7 \rho_S}} \tag{5.25}$$

where ρ_S is the electrical resistivity of sheath material (Ω·m), and coefficients C_{A_k}, $C_{A_k}{}'$ are fully deployed in Appendix D.

The formula adopted by the IEC 60287-1-1 Standard [16] is briefly presented in the following equation for 1C cables in triangular formation:

$$\lambda''_{1,\mathrm{IEC}} = \frac{R_S}{R_{AC}}\left[g_S \lambda_0 (1 + \Delta_1 + \Delta_2) + \frac{(\beta_1 t_S)^4}{12 \cdot 10^{12}}\right] \tag{5.26}$$

where g_S, λ_0 factors and Δ_1 term are fully presented in Chapter 4, (4.20) - (4.22), and $\Delta_2 = 0$ for 1C cables in trefoil formation. Term Δ_1 is expected to approximate the first term of (5.24), which includes infinite series. The second terms of (5.24) and (5.26) are apparently identical: in both Jackson and IEC formulations the self-induced eddy currents (i.e. those generated by the internal conductor current) are similarly computed. It is noted that in the context of the present section the 'IEC model' refers to the formula presented above.

5.2.4.1 Lead Sheaths

Lead sheaths are routinely used for subsea, export cables where the water-tightness of insulation is of crucial importance. Figure 5.13 illustrates the effect of varying r_C on λ_1'' as calculated by four different methods. Since it is common to think of conductor cross-sectional areas (XSAs), the values r_C = 10, 20 and 30 mm correspond, approximately, to 300, 1000 and 2500 mm^2. The results derived by the methods of IEC 60287-1-1 [16] and Jackson [1] are in good agreement. This can be readily justified by the fact that the former, which is based on ERA's publication [65], successfully replaces the infinite series suggested by Jackson: the first term in (5.24) is replaced by term Δ_1 in (5.26). Similar agreement occurs when FEA is applied considering uniform current density, J_u, in phase conductors. However, once non-uniform density, J_{nu}, is considered, significant discrepancies appear. It is noticeable in Figure 5.13 that for decreasing r_C, J_{nu} values tend closer to J_u ones, with the relative difference shrinking from 60% to 1%. FM results follow very well those from FEA – J_{nu}, as expected, since both approaches accounts for the proximity effect in conductors when calculating sheath losses.

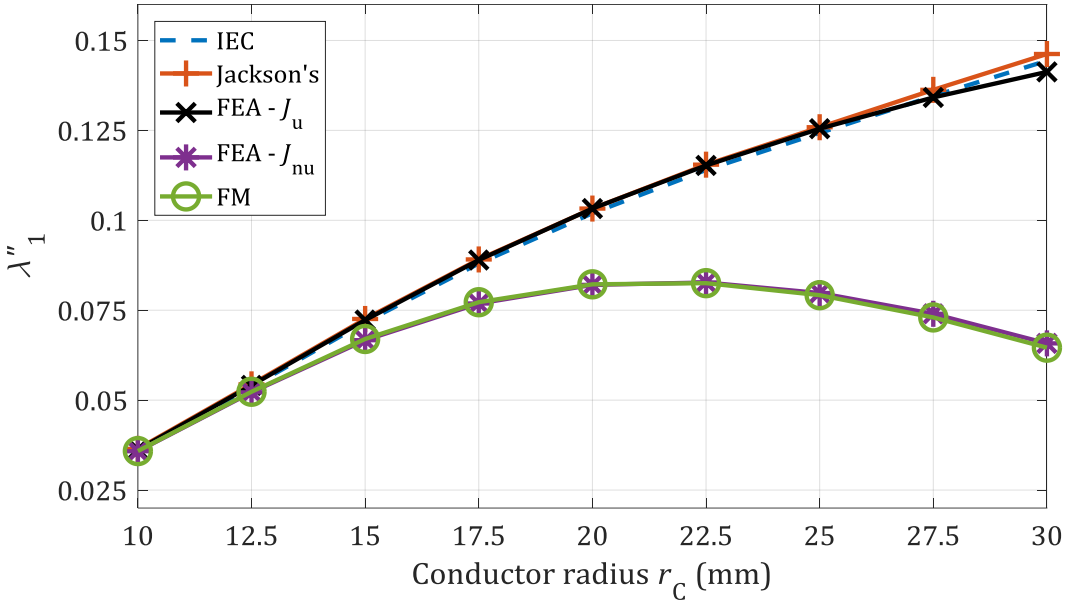

FIGURE 5.13: Dependence of λ_1" on r_C, $r_{S,in}$ = 40 mm, t_S = 2.5 mm – Lead Sheaths.

For increasing $r_{S,in}$ a similar trend is obtained; assuming a conductor with r_C = 20 mm, the difference between FEA – J_{nu} and the existing analytical methods drops from 43% down to 10%, as shown in Figure 5.14. The more remote the sheath is from the non-uniform current source, the less it is affected by it. In other words, the impact of the non-uniform conductor current is more significant with a thinner insulation. FE models with J_u appear a good agreement against Jackson's and the IEC models, while the curve from FM models almost coincides with that from FE models with J_{nu} assumption.

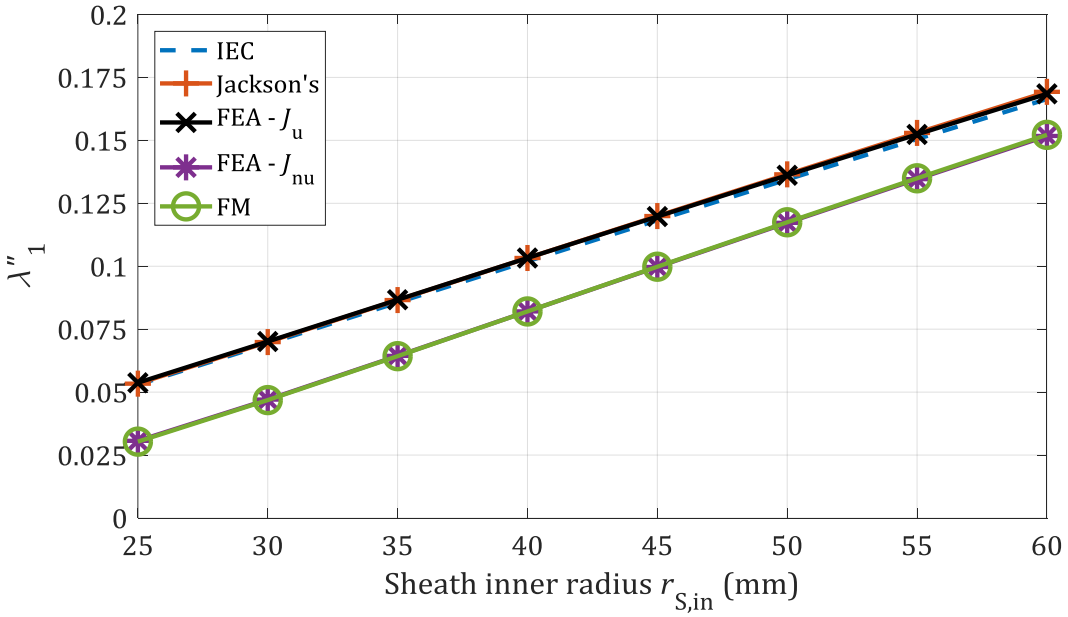

FIGURE 5.14: Dependence of λ_1" on $r_{S,in}$, r_C = 20 mm, t_S = 2.5 mm – Lead Sheaths.

The effect of varying t_S on the divergence between J_u and J_{nu} results is even weaker compared to r_C and $r_{S,in}$: indeed, a practically constant divergence of about 20% is depicted in Figure 5.15, whatever t_S is, for r_C = 20 mm and $r_{S,in}$ = 40 mm. Although not shown in Figure 5.15, by keeping $r_{S,in}$ constant and increasing r_C from 15 mm to 30 mm the relevant divergence also increases from about 7% up to 53%, thus implying that the divergence between J_{nu} and J_u demonstrated in Figure 5.15 is due to the relatively large conductor size.

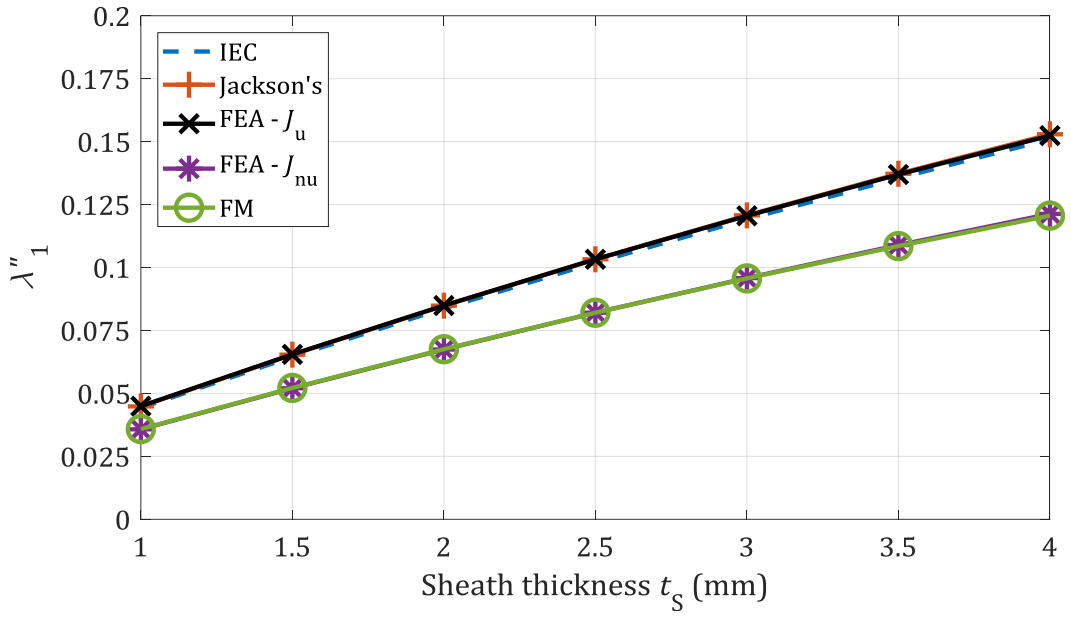

FIGURE 5.15: Dependence of λ_1" on t_S, r_C = 20 mm, $r_{S,in}$ = 40 mm – Lead Sheaths.

5.2.4.2 Variation VS Sheath Resistivity

Materials besides Lead are seldom used at present for sheaths of export cables. However, it is not impossible to see in the future export cables with sheaths of material other than Lead. It is thus worth noting the relative difference between J_{nu} results and the existing analytical methods when varying the electrical resistivity of sheath, ρ_S. As shown in Figure 5.16, this is kept nearly constant, about 28%, for ρ_S values in between Al and Lead materials [16] when a conductor of r_C = 22.5 mm (or 1400 mm²) is considered. Therefore, ρ_S appears not to affect the relation between FEA – J_{nu} and the existing analytical methods.

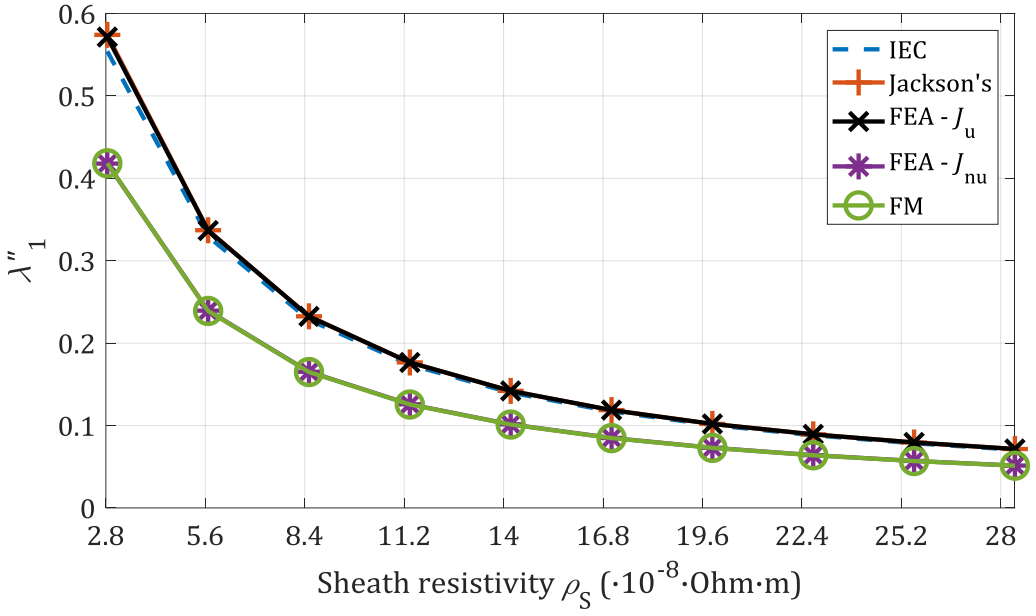

FIGURE 5.16: Dependence of λ_1" on ρ_S, r_C = 22.5 mm, $r_{S,in}$ = 40 mm, t_S = 2.0 mm.

5.2.4.3 Interpretation of Results - Effect of the Proximity Effects in Conductors

Smaller conductors will see less intense skin and proximity effects, and hence a more uniform distribution of current. Although the skin effect can be strong in large conductors, the non-uniform current remains fairly symmetrical for widely spaced conductors. However, proximity effect is expected to further distort the current distribution, affecting the magnetic flux induced and hence the induced losses. This is neglected in the present IEC 60287-1-1 Standard version [16], as well as Jackson's model [1]. To demonstrate the significance, the current distribution for 3 x 1000 mm² conductors is computed by means of FE models and illustrated in Figure 5.17. In particular, the phase average (average for a full cycle of 0.02 s, so from phase angle 0° to 360°) of current density J_C along the conductor diameter d_C is shown. The spatial average of J_C is shifted by about 40% from the centre (d_C = 20 mm) of the conductor and is located closer to the neighbouring conductor on the right, thus confirming the non-symmetry of current distribution.

Induced losses in sheaths depend on the magnetic flux along their circumference. Figure 5.18 shows magnetic flux levels at phase angle 0° along the circumference L when two extreme conductor sizes (150 mm² and 2000 mm²) are considered in FE models, both with J_{nu}. The maximum difference reaches 0.79 mT and the average is 0.38 mT, for matching current input I, axial separation s and sheath geometry. The influence of proximity effects in conductors on eddy current loss is considered by neither Jackson [1] nor Parr [65]. As implied in the former's formulation, linear currents are assumed as the field sources. This appears to be a quite

reasonable assumption for lower conductor sizes, but not so when higher sizes are considered, as illustrated in Figure 5.18.

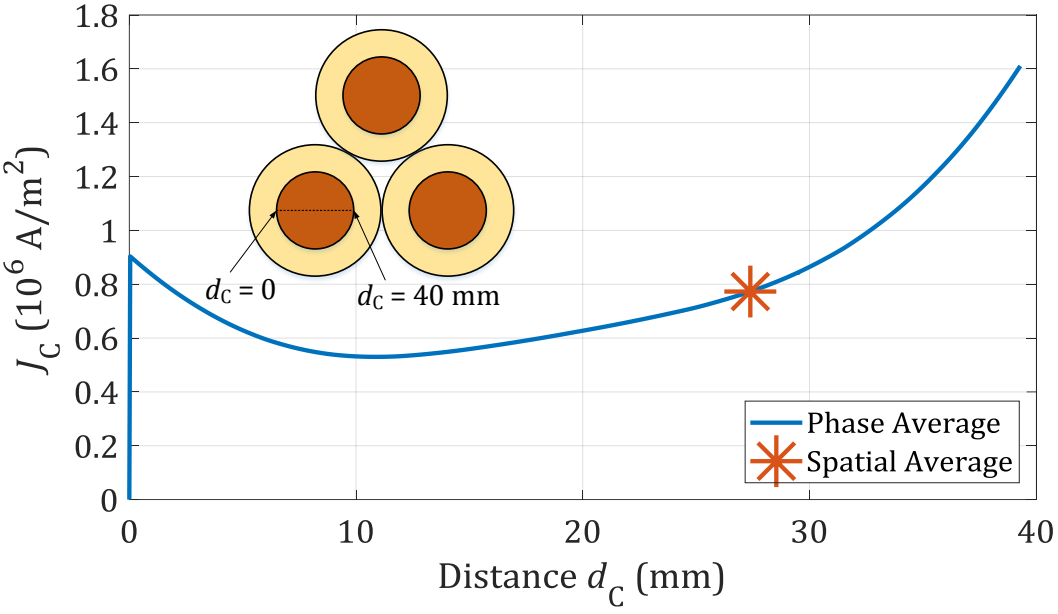

FIGURE 5.17: Current Density along d_C for 3 x 1000 mm² Conductors.

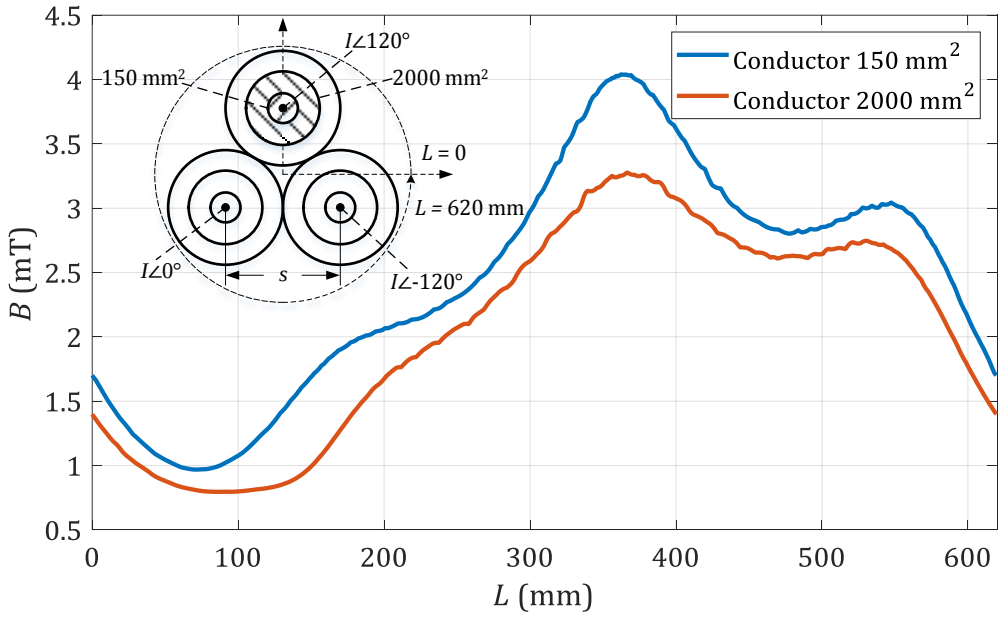

FIGURE 5.18: Distribution of Magnetic Flux along the Circumference above the 3 Cores for 150 mm² and 2000 mm² Conductors.

5.2.4.4 Approximating Formulae Suggested

As shown in section 5.2.4.1, r_C and $r_{S,in}$ appear to be the geometrical parameters mainly affecting the divergence between analytical and FE methods. Reductive Factors (RFs) for

single-point bonding losses are found for Lead sheaths, by minimising the square difference of λ_1" obtained with FEA and the corrected IEC method. The new value of λ_1" is shown in (5.27).

$$\lambda''_{1,\mathrm{New}} = RF_{\mathrm{SPB}}\,\lambda''_{1,\mathrm{IEC}} \tag{5.27}$$

where $RF_{\mathrm{SPB}} = \lambda''_{1,\mathrm{New}}/\lambda''_{1,\mathrm{IEC}}$ is the Reductive Factor (RF) for single-point bonding case. $\lambda''_{1,\mathrm{New}}$ should be in close agreement with $\lambda''_{1,\mathrm{FEA}}$ (ideally $\lambda''_{1,\mathrm{New}} = \lambda''_{1,\mathrm{FEA}}$). The ratio $\lambda''_{1,\mathrm{FEA}}/\lambda''_{1,\mathrm{IEC}}$ is illustrated in Figure 5.19 as a function of r_C and X_{sc}, where X_{sc} = $r_{S,in}$ – r_C. The $(r_C, X_{sc}, \lambda''_{1,\mathrm{FEA}}/\lambda''_{1,\mathrm{IEC}})$ points are linked via straight lines to show the corresponding trends. It is apparent from Figure 5.19 that by decreasing r_C or increasing X_{sc}, $\lambda''_{1,\mathrm{FEA}}$ tends to become equal to $\lambda''_{1,\mathrm{IEC}}$. The shapes of the curves suggest that the ratio could be approximated by polynomial functions of r_C and X_{sc}.

Since an accurate approximation against two variables, i.e. r_C and X_{sc}, is sought, surface fittings are selected: these employ a least square regression to find the optimum surface best fitting $(r_C, X_{sc}, \lambda''_{1,\mathrm{FEA}}/\lambda''_{1,\mathrm{IEC}})$ data. Results of both linear and polynomial of 3rd order are shown in Table 5.4, for certain indicative cable sizes. Better accuracy is obtained when the latter fitting is chosen, while sufficiently good correction is achieved with the former one, especially for larger cable sizes. *R*-square is also included for informative purposes.

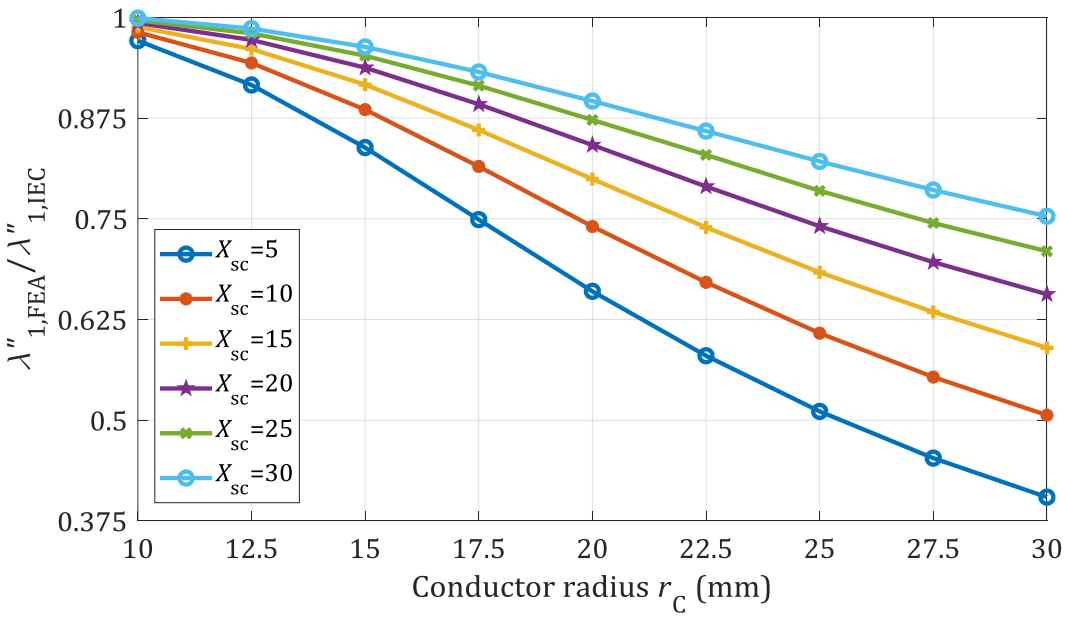

FIGURE 5.19: Parametric Curves Correlating FEA and IEC 60287-1-1 Values – SPB Losses.

TABLE 5.4: Relative Difference of the Corrected IEC, SPB Loss Factor ($\lambda''_{1,\mathrm{New}}$) VS FEA ($\lambda''_{1,\mathrm{FEA}}$).

r_C / $r_{S,in}$ / t_S [mm]	$\frac{\lambda''_{1,\mathrm{New}} - \lambda''_{1,\mathrm{FEA}}}{\lambda''_{1,\mathrm{FEA}}} 100\%$	
	Linear (R-square: 0.9239)	3rd polynomial (R-square: 0.9985)
10.0/ 20.0/ 1.0	-6.0%	-0.5%
20.0/ 35.0/ 1.5	-3.3%	-0.5%
30.0/ 50.0/ 2.0	-4.6%	-0.5%

The exact form of the *RF* formula derived is shown in (5.28) and (5.29) for linear and 3rd order polynomial approximation, respectively. The corresponding coefficients are shown in Table 5.5. Since r_C and $r_{S,in}$ appear to mainly affect the divergence between IEC and FEA results, other parameters, e.g. conductor resistivity, ρ_C, and t_S, are assumed to have a constant, moderate value in the parametric analysis done. The applicability of (5.28) and (5.29) for different ρ_C and t_S values is considered later, in section 5.2.6.

$$RF(r_C, X_{sc})_{lin} = p_{00} + p_{10}X_{sc} + p_{01}r_C \tag{5.28}$$

$$RF(r_C, X_{sc})_{3rd} = p_{00} + p_{10}X_{sc} + p_{01}r_C + p_{20}{X_{sc}}^2 + p_{11}X_{sc}r_C + p_{02}r_C^2 + \\ + p_{30}{X_{sc}}^3 + p_{21}{X_{sc}}^2 r_C + p_{12}X_{sc}r_C^2 + p_{03}r_C^3 \tag{5.29}$$

TABLE 5.5: Coefficients for RF Formulae Suggested for SPB Losses of Lead Sheathed Power Cores.

	Single-Point Bonding - $\lambda''_{1,\mathrm{New}}$	
Formula	(5.28)	(5.29)
p_{00}	1.037	1.083
p_{10}	8.125e-3	- 6.734e-3
p_{01}	-0.0191	1.112e-3
p_{20}	N/A	- 1.851e-4
p_{11}	N/A	1.585e-3
p_{02}	N/A	- 1.993e-3
p_{30}	N/A	4.253e-6
p_{21}	N/A	-1.239e-5
p_{12}	N/A	- 1.325e-5
p_{03}	N/A	3.489e-5

5.2.5 Solid Bonding Loss

This section presents results for solidly bonded sheaths derived from the IEC 60287-1-1 [16] Standard, FEA and FM calculations. Although there is no specific reference in [16] pertaining

to λ_1' factor in SL-Type cables with non-magnetic armour, this is implied to be the same as that for three 1C cables in trefoil formation:

$$\lambda'_{1,\mathrm{IEC}} = \frac{R_\mathrm{S}}{R_\mathrm{AC}} \frac{1}{1+\left(\frac{R_\mathrm{S}}{X_\mathrm{S}}\right)^2} \tag{5.30}$$

where X_S is the reactance pul of sheath (Ω/m), i.e.:

$$X_\mathrm{S} = 2\omega 10^{-7} \ln\left(\frac{2s}{d}\right) \tag{5.31}$$

where s and d is the axial distance between phase conductors (mm) and the mean diameter of sheath (mm), respectively. Total losses in the sheath consist of losses caused by circulating and eddy currents and the respective factor according to [16] is shown in (5.32). It is noted that in the context of the present section the 'IEC model' refers to the formula presented below.

$$\lambda_{1,\mathrm{IEC}} = \lambda'_{1,\mathrm{IEC}} + \lambda''_{1,\mathrm{IEC}} \tag{5.32}$$

In contrast with the IEC model, both FE and FM models do not distinguish circulating and eddy losses. In fact, it is not easy to separate the eddy loss from the total losses in solidly bonded sheaths, since the eddy currents are in reality affected to some slight extent by the existence of circulating currents. It is noted that the IEC 60287-1-1 Standard [16] suggests that a reductive factor F is multiplied by $\lambda''_{1,\mathrm{IEC}}$ when calculating $\lambda_{1,\mathrm{IEC}}$ to account for this effect. However, F refers to cables with Milliken conductors only in [16] and its value occurs in most cases pretty close to the unity. λ_1 results are presented for Lead sheaths in this section, while the effect of sheath conductivity is also studied.

5.2.5.1 Lead Sheaths

The trends seen for Lead sheaths are qualitatively similar to those seen for single-point bonding loss regarding r_C, $r_{\mathrm{S,in}}$ and t_S parameters. In all cases FM closely follows FEA – J_nu curves, as expected, since both models account for proximity effects in conductors and sheaths. r_C appears to be the geometric parameter mainly affecting loss results, as shown in Figure 5.20: a maximum difference of 37% between FEA – J_nu and IEC values is noticed. The assumption of centrally placed, line currents is made by (5.31) to calculate sheath reactance, X_S. However, as for single-point bonding, the proximity effect results in the crowding of the conductor currents towards the cable centre, thus affecting the actual sheath reactance and, thus, λ_1.

Increase in $r_{\mathrm{S,in}}$ from 25 mm to 60 mm leads to a slight –though noticeable- decrease of the divergence between FEA – J_nu and IEC from 25% to 10%, as shown in Figure 5.21. What is also worth noticing in this figure is that by further increasing $r_{\mathrm{S,in}}$ the FEA – J_u curve starts to diverge from the IEC line (reaching up to 4% for $r_{\mathrm{S,in}}$ = 60 mm), although remains closer to the latter

compared to FEA – J_{nu}. This slight divergence implies that factors other than the proximity effect in conductors affect λ_1. This is further discussed in sections 5.2.5.2 and 5.2.5.3.

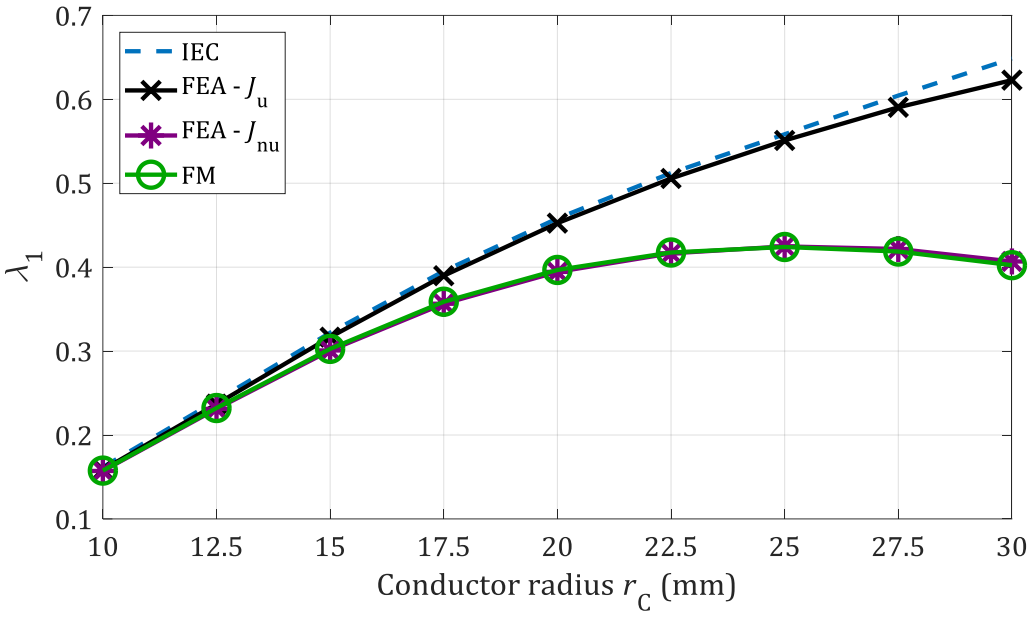

FIGURE 5.20: Dependence of λ_1 on r_C, $r_{S,in}$ = 40 mm, t_S = 2.5 mm – Lead Sheaths.

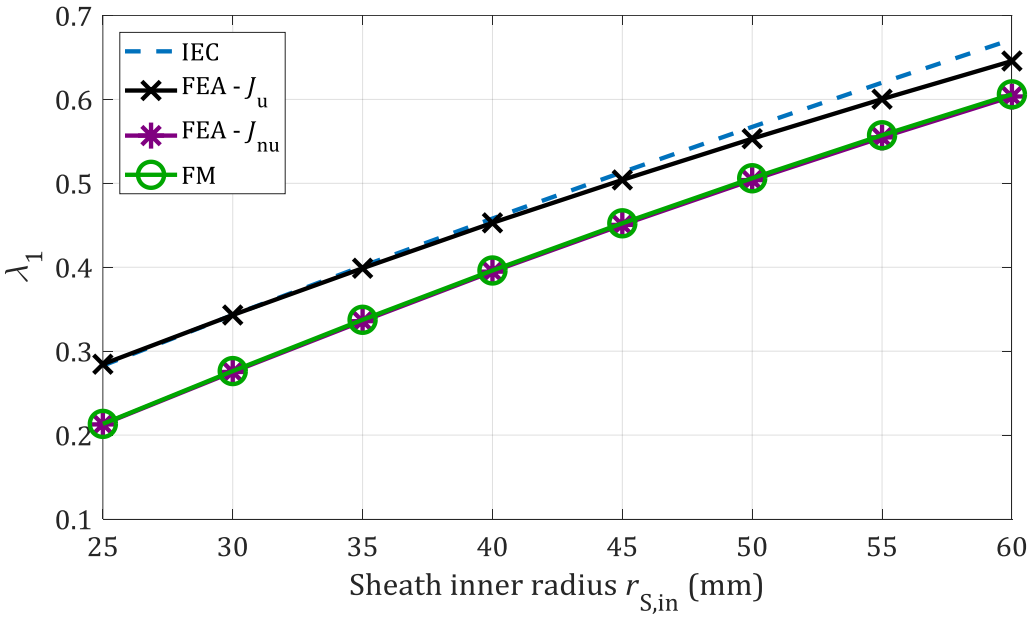

FIGURE 5.21: Dependence of λ_1 on $r_{S,in}$, r_C = 20 mm, t_S = 2.5 mm – Lead Sheaths.

Concerning t_S variation, a nearly constant divergence of about 14% is kept for r_C = 20 mm and $r_{S,in}$ = 40 mm, as shown in Figure 5.22, thus rendering t_S of minor effect compared to r_C and $r_{S,in}$. As for $r_{S,in}$, further increasing t_S leads to the appearance of a slight increase in the relation between FEA – J_u and the IEC model (reaching up to 4% for t_S = 4 mm).

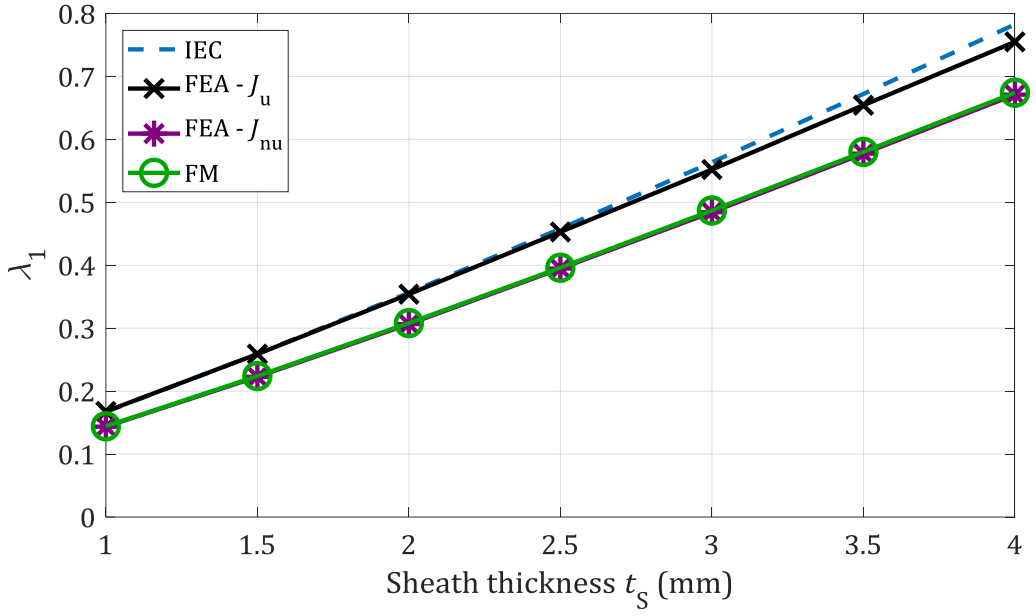

FIGURE 5.22: Dependence of λ_1 on t_S, r_C = 20 mm, $r_{S,in}$ = 40 mm – Lead Sheaths.

5.2.5.2 Variation VS Sheath Resistivity

Although the influence of variation in ρ_S does not derive surprising results for λ_1", as previously shown in Figure 5.16, more interesting is the dependence of λ_1 against ρ_S, as shown in Figure 5.23. For higher ρ_S values, the agreement between FEA – J_u values and IEC appears good enough. However, it becomes worse for lower ρ_S, implying that the proximity effect in conductors is not the only factor at play. This is further discussed in the next subsection.

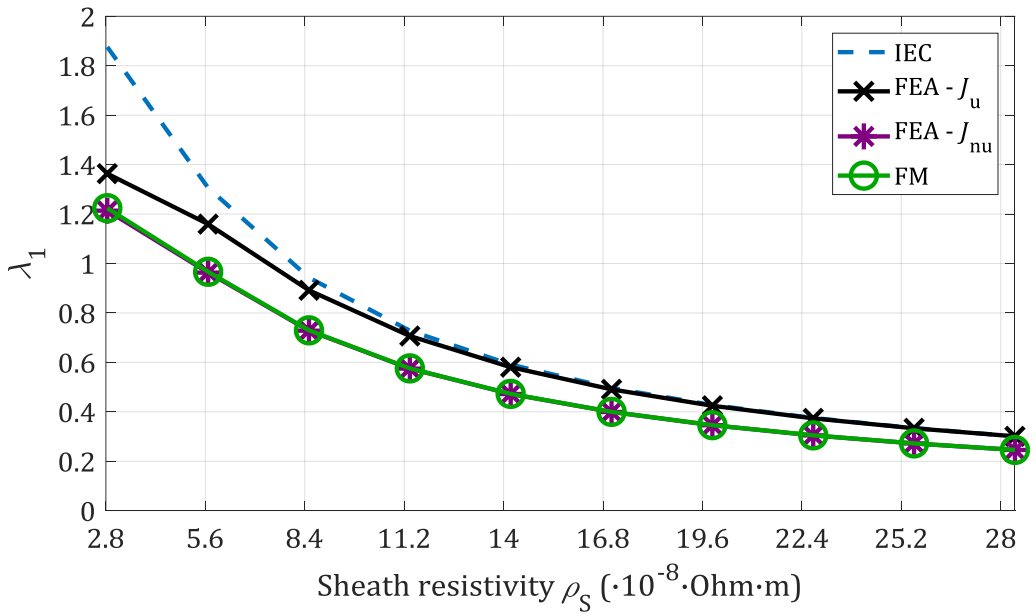

FIGURE 5.23: Dependence of λ_1 on ρ_S, r_C = 22.5 mm, $r_{S,in}$ = 40 mm, t_S = 2.0 mm.

5.2.5.3 Interpretation of Results – Effect of Cable Spacing

Besides the influence the proximity effect in conductors has on solid bonding losses, skin and proximity effects in sheaths themselves are modelled in FEA. Skin effect is fairly weak for the sheaths: calculated skin depths are about 33 mm (Lead) and 12 mm (Aluminium, Al) at power frequency, which are much larger than the range of t_S values involved. Two identical 3C cable geometries are examined to further investigate the effect of distance between cores, s, on sheath resistance and circulating current, I_S. Lead and Al sheaths of equal geometry are assumed to derive comparable results, while both J_u and J_{nu} are considered. Medium values for r_C and $r_{S,in}$ are also assumed (20 mm and 35 mm, respectively). Sheath resistance and current are extracted by FEA. Their ratios to the corresponding IEC values, namely R_{FEA}/R_{IEC} and I_{FEA}/I_{IEC}, respectively, are considered and shown in Table 5.6 and Table 5.7.

As shown in these tables, by reducing s, R_{FEA}/R_{IEC} increases and I_{FEA}/I_{IEC} decreases. IEC results are in a good agreement with FE ones for spaced cables, whereas the situation appears different for cores being in close proximity one another; the increase in R_{FEA}/R_{IEC} implies that I_S is not uniformly distributed around the sheath.

TABLE 5.6: Effect of Cable Spacing on Sheath Resistance and I_S – Lead Sheaths.

Cable Spacing s	$R_{FEA}/R_{IEC} - J_u$	$I_{FEA}/I_{IEC} - J_u$	$R_{FEA}/R_{IEC} - J_{nu}$	$I_{FEA}/I_{IEC} - J_{nu}$
d_{core} (touching formation)	1.32	0.87	1.28	0.80
1.5 x d_{core}	1.06	0.97	1.04	0.95
3 x d_{core}	1.01	1.00	1.00	0.99

TABLE 5.7: Effect of Cable Spacing s on Sheath Resistance and I_S – Al Sheaths.

Cable Spacing s	$R_{FEA}/R_{IEC} - J_u$	$I_{FEA}/I_{IEC} - J_u$	$R_{FEA}/R_{IEC} - J_{nu}$	$I_{FEA}/I_{IEC} - J_{nu}$
d_{core} (touching formation)	1.31	0.78	1.27	0.73
1.5 x d_{core}	1.05	0.93	1.04	0.92
3 x d_{core}	1.01	0.99	1.00	0.99

For Lead sheaths, FEA and IEC sheath losses appear alike each other when J_u is considered. The reduction of current ratio is compensated by the respective increase in resistance ratio, thus leading to nearly equal losses. Lower I_S values are obtained once J_{nu} is considered, because lower magnetic field is actually induced due to the proximity effect in conductors. Although higher R_S values are also seen in this case, the current dominates in the loss calculation ($W_S = I_S^2 R_S$), thus leading to lower losses.

The current distribution in conductors seems to affect the current ratio also for Al sheaths, leading to lower losses. However, the current ratio is significantly lower even for J_u assumption compared to Lead and the increase in resistance ratio is not capable of compensating the respective decrease in the current ratio. Due to the higher conductivity of Al, higher eddy currents occur, which cancel out locally the overall circulating current (I_S) to a greater extent, thus yielding a less uniform current distribution along sheaths' circumference and a stronger proximity effect.

5.2.5.4 Approximating Formulae Suggested

Similar analysis to section 5.2.4.4 is undertaken for solid bonding losses in Lead sheaths, with the same geometrical parameters being varied to obtain *RF*s. The new value of λ_1 is shown in (5.33).

$$\lambda_{1,\text{New}} = RF_{\text{SB}}\,\lambda_{1,\text{IEC}} \tag{5.33}$$

where $RF_{\text{SB}} = \lambda_{1,\text{New}}/\lambda_{1,\text{IEC}}$ is the Reductive Factor (RF) for solid bonding case. $\lambda_{1,\text{New}}$ should be in close agreement with $\lambda_{1,\text{FEA}}$ (ideally $\lambda_{1,\text{New}} = \lambda_{1,\text{FEA}}$). The ratio $\lambda_{1,\text{FEA}}/\lambda_{1,\text{IEC}}$ is illustrated in Figure 5.24 as a function of r_C and X_{sc}. The $(r_C, X_{sc}, \lambda_{1,\text{FEA}}/\lambda_{1,\text{IEC}})$ points are linked via straight lines to show the corresponding trends. It is apparent from Figure 5.24 that by decreasing r_C or by increasing $X_{sc,}$ $\lambda_{1,\text{FEA}}$ tends to become equal to $\lambda_{1,\text{IEC}}$. The shapes of the curves suggest that the ratio could be approximated by polynomial functions of r_C and X_{sc}.

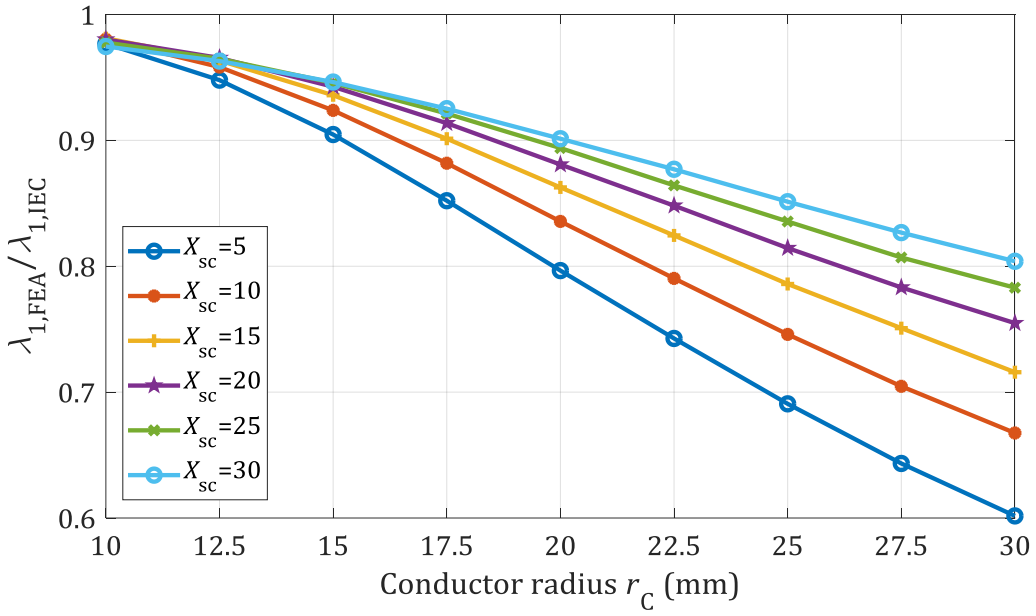

FIGURE 5.24: Parametric Curves Correlating FEA and IEC 60287-1-1 Values – SB Losses.

As in section 5.2.4.4, the optimum surface best fitting $(r_C, X_{sc}, \lambda_{1,\text{FEA}}/\lambda_{1,\text{IEC}})$ data is sought for. Results of both linear and polynomial of 3rd order are shown in Table 5.8, for certain indicative

cable sizes. Better accuracy is obtained when the latter fitting is chosen, while sufficiently good correction is achieved with the former one. The relevant formulae for linear and 3rd order polynomial have the same form as those presented in (5.28) and (5.29), respectively, with the relevant coefficients being presented in Table 5.9. As for SPB loss, the applicability of (5.28) and (5.29) for different ρ_C and t_S values is considered later, in section 5.2.6 also for SB losses.

TABLE 5.8: Relative Difference of the Corrected IEC, SB Loss Factor ($\lambda_{1,\mathrm{New}}$) VS FEA ($\lambda_{1,\mathrm{FEA}}$).

r_C/ $r_{S,in}$/ t_S (mm)	$\frac{\lambda_{1,\mathrm{New}} - \lambda_{1,\mathrm{FEA}}}{\lambda_{1,\mathrm{FEA}}} 100\%$	
	Linear (R-square: 0.9237)	3rd polynomial (R-square: 0.9991)
10.0/ 20.0/ 1.0	-3.3%	-0.5%
20.0/ 35.0/ 1.5	-1.9%	0.4%
30.0/ 50.0/ 2.0	-2.1%	0.1%

TABLE 5.9: Coefficients for RF Formulae Suggested for SB Losses of Lead Sheathed Power Cores.

	Solid Bonding - $\lambda_{1,\mathrm{New}}$	
Formula	(5.28)	(5.29)
p_{00}	1.041	1.02
p_{10}	0.00398	- 3.048e-3
p_{01}	- 0.0128	4.516e-3
p_{20}	N/A	- 1.133e-4
p_{11}	N/A	7.076e-4
p_{02}	N/A	- 1.258e-3
p_{30}	N/A	2.956e-6
p_{21}	N/A	- 8.957e-6
p_{12}	N/A	4.999e-8
p_{03}	N/A	1.828e-5

5.2.6 Review of the Assumptions Made

Solid conductors, which are assumed in the present Chapter, are less often used in practice, mainly due to mechanical reasons. Stranded conductors usually have uneven DC resistance throughout their cross-section, because of the different lay length applied between the various layers of strands during the twisting process. Therefore, proximity effect is expected to be slightly weaker compared with solid conductors.

The lay length of outer layers depends on the production process of each manufacturer. The assumption of 10% longer outer strands is made in this section. In addition, to avoid simulating

the conductor strand by strand, the electrical resistivity of the conductor is varied as a linear function of radius. The formula shown in (5.34) is employed:

$$\rho(r) = \left(\frac{0.1\rho_{\mathrm{Cu\_20°C}}}{r_{\mathrm{C}}}\right) r + \rho_{\mathrm{Cu_{20}°C}} \tag{5.34}$$

where r is the radial distance (m), $\rho_{\mathrm{Cu\_20°C}}$ is the electrical resistivity suggested by the IEC 60287-1-1 Standard (Ωm). A 2-D illustration of ρ(r) is shown in Figure 5.25. Considering r_{C} = 20 mm and t_{S} = 2.5 mm and by applying (5.34), eddy current loss appears 1% higher than the case where a uniform resistivity equal to $\rho_{\mathrm{Cu\_20°C}}$ is considered. At the same moment, eddy losses for J_{u} assumption occur by 26% higher than those for J_{nu} assumption. Therefore, the assumption for solid conductors appears to have a minor impact on the generated results and is adequately reasonable in terms of the effect on sheath loss. It is noted that overlength ratio values higher than 1.1 are not often met in practice.

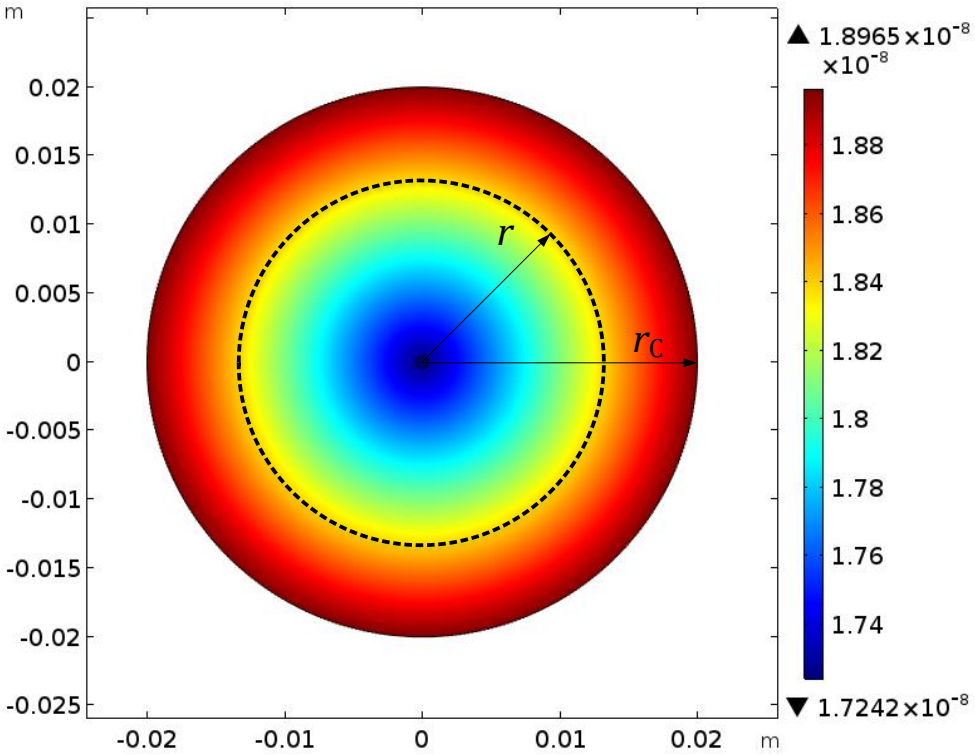

FIGURE 5.25: Depiction of the Resistivity (Ωm) Described by (5.34) in a Solid Conductor of R_{c} = 20 mm.

Certain assumptions are made for the derivation of both RF_{SPB} and RF_{SB} defined by (5.27) and (5.33), respectively, for the sake of simplicity. In particular, a constant, moderate value is considered for t_{S}, while the jacket over the sheath is supposed to be of thickness $t_{\mathrm{J}} = t_{\mathrm{S}}$. Hence, the applicability of (5.28) and (5.29), along with the corresponding coefficients presented in Table 5.5 and Table 5.9 must be checked for variable t_{S}, t_{J}, within reasonable margins. r_{C}, X_{sc} are varied for each pair of t_{S}, t_{J} values and the average of the relative differences

$(\lambda''_{1,\mathrm{New}} - \lambda''_{1,\mathrm{FEA}})/\lambda''_{1,\mathrm{FEA}}$ and $(\lambda_{1,\mathrm{New}} - \lambda_{1,\mathrm{FEA}})/\lambda_{1,\mathrm{FEA}}$, namely $e^{\mathrm{New}}_{\mathrm{AVG\_SPB}}$ and $e^{\mathrm{New}}_{\mathrm{AVG\_SB}}$, respectively, are considered in this section. Similarly, the relative differences between the existing IEC model and the FEA are $e^{\mathrm{IEC}}_{\mathrm{AVG\_SPB}}$ and $e^{\mathrm{IEC}}_{\mathrm{AVG\_SB}}$. Results are shown in Table 5.10 and Table 5.11. As noticed in Table 5.10, $e^{\mathrm{New}}_{\mathrm{AVG\_SPB}}$ appears to be consistent enough and not much affected by the variation in t_J, t_S. The 3rd polynomial approximating factor described by (5.29) gives more accurate results than the linear approach (5.28), as expected. In Table 5.11, $e^{\mathrm{New}}_{\mathrm{AVG\_SB}}$ seems to increase for higher t_S, t_J, while at the same time $e^{\mathrm{IEC}}_{\mathrm{AVG\_SB}}$ decreases. Although the RFs appear to work less effectively for some extreme cases in solid bonding case, cables with such thick sheaths and even thicker jackets are not possible in practice.

TABLE 5.10: Average Relative Difference $e_{\mathrm{AVG\_SPB}}$ for Various Geometries – SPB Loss.

	$e_{\mathrm{AVG\_SPB}}$ (%), $t_J = 2\ t_S$			$e_{\mathrm{AVG\_SPB}}$ (%), $t_J = 3\ t_S$		
t_S (mm)	IEC – FEA $e^{\mathrm{IEC}}_{\mathrm{AVG\_SPB}}$	(5.28)–FEA $e^{\mathrm{New}}_{\mathrm{AVG\_SPB}}$	(5.29)–FEA $e^{\mathrm{New}}_{\mathrm{AVG\_SPB}}$	IEC – FEA $e^{\mathrm{IEC}}_{\mathrm{AVG\_SPB}}$	(5.28)– FEA $e^{\mathrm{New}}_{\mathrm{AVG\_SPB}}$	(5.29)– FEA $e^{\mathrm{New}}_{\mathrm{AVG\_SPB}}$
1.0	36.4	4.2	1.4	36.6	4.6	2.1
2.0	36.8	4.1	1.7	37.6	4.2	2.3
3.0	36.7	4.0	1.7	37.7	4.1	2.4
4.0	36.3	3.8	1.6	37.3	4.0	2.2

TABLE 5.11: Average Relative Difference $e_{\mathrm{AVG\_SB}}$ for Various Geometries – SB Loss.

	$e_{\mathrm{AVG\_SB}}$ (%), $t_J = 2\ t_S$			$e_{\mathrm{AVG\_SB}}$ (%), $t_J = 3\ t_S$		
t_S (mm)	IEC – FEA $e^{\mathrm{IEC}}_{\mathrm{AVG\_SB}}$	(5.28)– FEA $e^{\mathrm{New}}_{\mathrm{AVG\_SB}}$	(5.29)– FEA $e^{\mathrm{New}}_{\mathrm{AVG\_SB}}$	IEC – FEA $e^{\mathrm{IEC}}_{\mathrm{AVG\_SB}}$	(5.28)– FEA $e^{\mathrm{New}}_{\mathrm{AVG\_SB}}$	(5.29)– FEA $e^{\mathrm{New}}_{\mathrm{AVG\_SB}}$
1.0	21.1	3.1	1.5	19.6	2.9	0.9
2.0	18.2	2.7	1.2	15.9	3.7	3.0
3.0	16.2	3.6	2.7	13.3	5.7	4.8
4.0	14.6	5.0	4.1	11.4	7.2	6.3

Besides the effect of t_S, t_J, that of conductor resistivity, ρ_C, is checked. ρ_C is selected equal to the average value between that of Copper conductors at 20°C, $\rho_{\mathrm{Cu\_20°}}$, and Aluminium at 90°C, $\rho_{\mathrm{Al\_90°}}$, (resistivity values as suggested by the IEC 60287-1-1 Standard [16]) during the derivation of the RFs. However, the higher ρ_C, the weaker the proximity effect of the conductor and vice versa; thus, this assumption is also worth reviewing. Results are shown in Table 5.12. Values for the mean of $\rho_{\mathrm{Cu\_20°}}$ and $\rho_{\mathrm{Al\_90°}}$ are also given as a reference. RFs give better results when tested for $\rho_{\mathrm{Cu\_20°}}$, since the proximity effect is more intense and e_{AVG} between IEC – FEA is higher. On the contrary, they give relatively worse results for $\rho_{\mathrm{Al\_90°}}$, since the proximity effect is less intense and e_{AVG} between IEC – FEA is lower. In any case, RFs provide results closer to FEA.

TABLE 5.12: Average Relative Difference for Various Conductor Resistivities.

Resistivity Selection	e_{AVG} (%), SPB Loss			e_{AVG} (%), SB Losses		
ρ_C	$e^{IEC}_{AVG\_SB}$	$e^{New}_{AVG\_SPB}$ (5.28)	$e^{New}_{AVG\_SPB}$ (5.29)	$e^{IEC}_{AVG\_SB}$	$e^{New}_{AVG\_SB}$ (5.28)	$e^{New}_{AVG\_SB}$ (5.29)
$\frac{\rho_{Cu\_20°C} + \rho_{Al\_90°C}}{2}$	33.2	5.3	0.7	19.4	3	0.3
$\rho_{Cu\_20°}$	42.0	7.6	5.6	23.1	3.8	3.0
$\rho_{Al\_90°}$	22.1	8.0	7.0	14.5	4.6	3.6

5.3 Effect on Thermal Rating

The results shown in the present Chapter suggest lower induced losses compared to the formulae provided by the IEC 60287-1-1 Standard for Lead sheathed cable cores laid in close trefoil arrangement and, based on the approach discussed in section 5.2.2, for SL-Type cable with non-magnetic armour. The thermal impact of this reduction is assessed in the present section, by considering three 1C Lead sheathed cores in close trefoil arrangement under "typical" subsea installation conditions, with solidly bonded sheaths.

Three indicative cable sizes are considered in this section. These may be considered as matching to actual export cable sizes at 66 kV, 150 kV and 220 kV, respectively, with larger sizes corresponding to higher voltage levels. Indeed, larger conductors and thicker insulations are in general expected in export cables of higher voltages, so as to transmit the increased power demands. For each cable size considered, sheath losses calculated by IEC 60287-1-1 and FE models are used, while conductor loss from FEA is imported in both cases. The cable is considered buried 1 m deep in a soil of thermal resistivity 0.7 Km/W at 15°C ambient temperature under steady-state conditions. Eddy current loss (λ_1" factor) is accounted for by the FE models, whereas two cases are considered for IEC calculations; those ignoring and including λ_1", respectively.

The cable ampacity is first considered as an input and the maximum conductor temperature is solved for. The ampacity derived from the FE models (90°C) is considered as a reference value: the same current magnitude is imported in both IEC method-cases (including and excluding λ_1"). The corresponding temperature results are illustrated in Table 5.13.

As shown in Table 5.13, $\Delta\theta_1$, which occurs from the subtraction between 3rd and 4th columns of Table 5.13, is low for small and medium cable sizes. However, FE results are about 7°C (or 8%) lower for larger cable sizes due to the IEC 60287-1-1 overestimating the losses. The FEA includes fully the eddy currents and resulting proximity effects, the extent of which is

outweighed by the reduction in circulating current loss. As seen by $\Delta\theta_2$ values, which occur from the subtraction between 3rd and 6th columns, IEC calculations can become overly conservative if including λ_1", particularly for larger cable sizes.

TABLE 5.13: Maximum Conductor Temperature: Sheath Losses Calculated by FEA and IEC for 3 1C Cables Laid in Trefoil Touching Arrangement.

Export Cable Design	r_C / $r_{S,in}$ / t_S (mm)	FE models (°C)	IEC (λ_1"= 0) (°C)	$\Delta\theta_1$ (°C)	IEC (λ_1"≠ 0) (°C)	$\Delta\theta_2$ (°C)
66 kV	10.0/ 20.0/ 1.5	90.0	89.7	0.3	90.4	-0.4
150 kV	20.0/ 35.0/ 2.5	90.0	91.4	-1.4	96.5	-6.5
220 kV	30.0/ 50.0/ 3.5	90.0	97.2	-7.2	109.2	-19.2

Although the temperature results presented in Table 5.13 give an impression of how much conservative the IEC method may become, it is rather useful to translate them in ampacity values (at 90°C) in order to assess the gain in the cable current rating. Instead of keeping the same current magnitude, the conductor temperature is subsequently considered as an input value (90°C) and the cable ampacity is solved for, for both FE and IEC models. The corresponding ampacity results are presented in Table 5.14.

Similarly to Table 5.13, ΔI_1, which is the relative difference between the 3rd and 4th columns of Table 5.14 (FE values as reference), is comparatively low for small and medium cable sizes. However, the cable ampacity may be underestimated by 4.4% for larger cable sizes due to the IEC 60287-1-1 overestimating the losses. This percentage may be translated to at least one standardised conductor size difference (e.g. from 1000 mm^2 to 1200 mm^2 of Copper) based on the DC resistance values suggested by the IEC 60228 Standard [94]. As seen by ΔI_2 values, which represent the relative difference between the 3rd and 6th columns (FE values as reference), the cable rating calculated by the IEC Standard can be overly underestimated if including λ_1", particularly for larger cable sizes (by about 11%). This latter percentage may be translated to a difference of at least four standardised conductor sizes (e.g. from 1000 mm^2 to 1800 mm^2 of Copper) based on the IEC 60228 Standard [94].

TABLE 5.14: Current Rating (90°C): Sheath Losses Calculated by FEA and IEC for 3 1C Cables Laid in Trefoil Touching Arrangement.

Export Cable Design	r_C / $r_{S,in}$ / t_S (mm)	FE models (A)	IEC (λ_1"= 0) (A)	ΔI_1 (%)	IEC (λ_1"≠ 0) (A)	ΔI_2 (%)
66 kV	10.0/ 20.0/ 1.5	878	880	0.2	876	-0.2
150 kV	20.0/ 35.0/ 2.5	1484	1470	-0.9	1425	-4.0
220 kV	30.0/ 50.0/ 3.5	1723	1647	-4.4	1538	-10.8

A threshold above which the RFs are significant may be identified from the present analysis; based on Figure 5.20, total solid bonding losses appear to be about 14% lower than IEC predicts for a conductor size of r_C = 20 mm or, approximately, 1000 mm^2. The ampacity difference for this case starts to become significant, as shown by ΔI_1 and ΔI_2 values of Table 5.14: these equal to about 1% and 4%, respectively. Although the value r_C = 30 mm or, approximately, 2500 mm^2 corresponds to the highest standardised conductor size [94], this is still used in practice. Milliken conductors are not easily manageable for large subsea projects, mainly because of the increased cable weight and the difficulty in making them watertight enough.

5.4 Summary

A robust and more generic formulation for Filament Method (FM) is employed in the present Chapter. Although its individual parts are not entirely new, the proposed formulation combines the features being well-defined in the existing formulations, such as the inclusion of the return path: this is demonstrated to be the key-parameter in order to achieve the theoretical validation of the developed FM model. Besides the validation against EMTP-like software, which represents skin effects only, the FM model is also validated against Js - FEM method, which captures the proximity effects inevitably occurring in SL-Type cables.

FM models are then used as reference to validate the FE models. Besides this theoretical validation, experimental measurements add an extra indication that the developed FE models generate sensible loss results. Having developed fairly accurate models, they are subsequently compared against the existing analytical methods presently used to calculate sheath losses in SL-Type cables with non-magnetic armour. The non-uniform current density in conductors appears to be the key-factor that makes the existing analytical methods overestimate sheath eddy losses, especially when larger conductors are considered. Much better agreement of both FM and FE models with the existing methods is achieved for smaller conductors, as expected, because of the less intense proximity effect in that case.

The current distribution in conductors affects also solid bonding losses, which is the bonding arrangement typically applied in the sheaths of submarine cables used in OWFs. The present IEC 60287-1-1 Standard version [16] suggests that λ_1" factor be ignored for solidly bonded sheaths; however, the draft Technical Brochure of Cigré WG B1.56 [29], which was recently issued, recommends that eddy current losses should always be included, irrespective of the bonding arrangement. Although this recommendation is in principle true, it is demonstrated in the present Chapter that the use of the existing IEC 60287-1-1 formulae can significantly overestimate the conductor temperature (or equally underestimate the cable ampacity) in the case of SL-Type cables, thus potentially oversizing them. This is particularly important for OWF

projects which employ non-magnetically armoured export cables, as the present Chapter demonstrates.

Although FM and FE models generate more accurate sheath losses compared to the existing analytical methods, they could hardly be used for Standardisation purposes, because of their inherent complexity. To give the possibility to the cable design engineer of using the current Standard version, though with improved accuracy, proper Reductive Factors (RFs), which account for either single-point or solid bonding losses, are suggested in the present Chapter.

Export cables with non-magnetic armour are preferred in certain cases, since they offer higher cable ratings, due to the lower induced losses. However, cables with magnetic armour are the most 'typical' solution, mainly because of the lower manufacture cost. Methods for calculating the cable losses for this, latter type of armour are investigated in the following Chapter.

Chapter 6 Modelling Aspects in 3C Submarine Cables with Magnetic Armour

Losses in 3C submarine cables with non-magnetic armour are investigated in Chapter 5. Higher grades of steel alloys (austenitic), which are non-magnetic, are mostly preferred in the hotspots of subsea routes due to the lower induced losses. They are also preferred in cases where high mechanical performance is required, such as in cables intended to be installed in large sea depths. However, lower steel grades are considerably cheaper. Since they are milder than austenitic alloys, they are easier to manage in the manufacturing process, thus leading to more efficient production schemes. For these reasons, they are typically used in the main, long section of the entire subsea link. The toll for the aforementioned advantages is the increased induced losses which inevitably occur as a result of the use of the ferromagnetic, lower-grade steels. To reach the requested ampacity, the cable designer has often to increase the conductor size, a fact that yields larger cable sizes and higher costs in total, including manufacture and installation. Therefore, the cost of offshore projects, such as OWFs, increases in total and their economic viability becomes questionable.

It is broadly known in both the scientific and industry communities that cable losses are currently overestimated by the IEC 60287-1-1 Standard [16] for SL-Type cables with magnetic armour. For this reason, the Cigré B1 Study Committee has recently constituted WG B1.64 which deals with this issue. Besides the overestimation in the armour loss, empirical factors are still employed by [16], such as the 1.5 in the case of sheath circulating losses, while eddy currents are recommended to be ignored. Furthermore, the effect of the magnetic armour is not at all considered when calculating the AC resistance of conductor. As discussed in Chapter 4, certain analytical models have been recently published ([17], [18]) and suggest more accurate cable losses. Although these models capture the 3-D effects concerning armour and, in some cases, sheath losses, they do not at all simulate the true distribution of conductor losses, since they imply line currents at the centres of conductors. The investigation of the cable losses underneath the armour, i.e. in sheaths and conductors, is the main topic of the present Chapter. First, the potential use of certain analytical methods, such as Filament Method (FM) and the Method of Images (MoI), is examined making focus on SL-Type cables. Then, 3-D Finite Element (FE) models are developed and compared against the existing analytical models. It should be noted that one of the latter is going to be suggested by the forthcoming Technical Brochure issued by WG B1.64; therefore, their evaluation against 3-D models is of importance in order to assess how effectively they represent cable losses. The influence of several design factors, such as the magnetic permeability of the armour, its pitch, as well as the diameter of wires, is also considered.

6.1 Filament Method: Consideration of the Existing Formulation

Filament Method (FM) is employed in Chapter 5 to represent losses for 3 cable cores in trefoil arrangement. It is important to note that a relative magnetic permeability, μ_r, equal to unity is implied everywhere around and in between the power cores in the formulation used. This is accurate enough when the metallic components of the cable are non-magnetic; however, it is not so when magnetic materials are involved, such as the ferromagnetic steel wires of the cable armour.

As pointed out in Chapter 4, de Arizon and Benato present in their works [20] and [21], respectively, the formulation used to construct **Z**-matrices including components with μ_r non-unity. The self-inductance L_{ii} of a filament i and the mutual inductance L_{ij} between filaments i and j in the presence of a cylindrical return path - ring of radius a (m) are respectively defined as follows (Chapter 5):

$$L_{ii} = \frac{\mu_0}{2\pi} \ln\left(\frac{a}{D_{ii}}\right) \tag{6.1}$$

$$L_{ij} = \frac{\mu_0}{2\pi} \ln\left(\frac{a}{D_{ij}}\right) \tag{6.2}$$

where

$$D_{ii} = r_i e^{-0.25 \cdot \mu_i} \tag{6.3}$$

is the self-geometric mean distance (m), μ_i is the relative magnetic permeability of filament i, and D_{ij} is the geometric mean distance between 2 filaments, i.e. the axial distance between filaments i and j. The consideration of μ_i in the self-geometric mean distance of the filaments belonging to the magnetic component involved (either pipe for [20] or armour for [21]) is certainly necessary: this accounts for the internal flux linkage, i.e. the flux which is induced by the filament itself and links the current flowing in the interior of the filament. However, it is not enough to account only for the right internal inductance of the magnetic filaments. The external inductance of the filaments enclosed by the magnetic entity should also account for the correct flux linkage: the flux induced by these filaments crosses partly a geometrical domain with μ_r equal to unity and partly geometrical entities (i.e. either the pipe or the armour) having μ_r different from unity. Unfortunately, (6.1) and (6.2), adopted by de Arizon and Benato, imply that the entire region around any filament has μ_r equal to unity.

The potential extension of FM in order to include magnetic components is investigated in the following sections. The simpler case of a 1C cable consisting of a conductor and a magnetic

sheath is first considered. Subsequently, the more complicated case of an SL-Type cable with tubular, magnetic armour is examined.

6.1.1 1C (Coaxial) Cable with Magnetic Sheath

The 1C cable presented in this section comprises a conductor, consisting of a single filament of radius r_C, and a sheath of inner and outer radius $r_{S,in}$ and $r_{S,out}$, respectively, which remains as it is, i.e. with no individual filaments. The conductor filament has a variable position with respect to the centre of the sheath: it is initially concentrically placed; then, it is displaced by a distance d_{ecc} such that it approaches close to the magnetic sheath, as shown in Figure 6.1. The sheath has a magnetic permeability $\mu_S = \mu_{r,S}\mu_0$ which is in general different than μ_0. A ring return of radius a is also illustrated in Figure 6.1. To be consistent with FM assumptions, dc conditions are considered, i.e. the DC resistance of the conductor filament and the sheath is only considered.

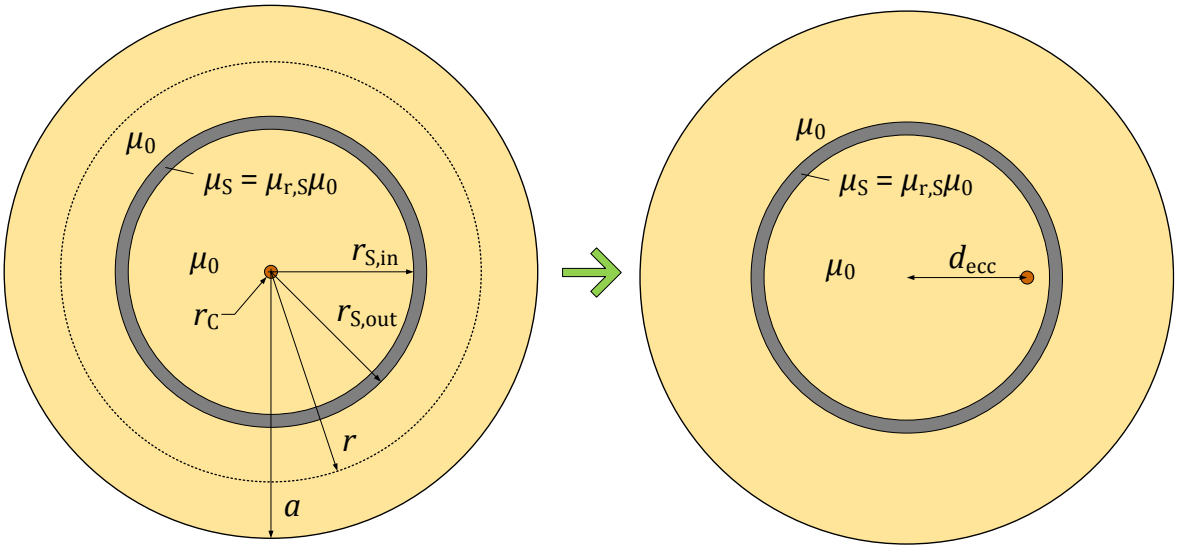

FIGURE 6.1: Concentrically (on the Left) and Eccentrically (on the Right) Placed Conductor Filament.

Barrett deals in [74] with 1C cables with magnetic, lossy wire armour and suggests an impedance matrix based on which cable losses may be extracted. Taking advantage of the cylindrical geometry of the cable core, conductor and sheath inductances are calculated based on the respective flux linkages. Because of the inherent complexity in the armour geometry, Barrett adopts a field approach instead of flux linkages to deduce the armour inductance. However, the flux linkage concept may be applied even in the simpler case of a 1C, unarmoured cable with magnetic sheath. Assuming that the total current I (A) is concentrated at the conductor surface, the external conductor inductance, $L_{11,ext}$ (H/m), may be derived from the external conductor flux linkage pul, $\lambda_{1,ext}$ (Wb/m):

$$\lambda_{1,\text{ext}} = \int_{r_\text{C}}^{a} d\lambda = \int_{r_\text{C}}^{r_\text{S,in}} d\lambda + \int_{r_\text{S,in}}^{r_\text{S,out}} d\lambda + \int_{r_\text{S,out}}^{a} d\lambda = \int_{r_\text{C}}^{r_\text{S,in}} \frac{\mu_0 I}{2\pi r} dr + \int_{r_\text{S,in}}^{r_\text{S,out}} \frac{\mu_0 \mu_{\text{r,S}} I}{2\pi r} dr + \int_{r_\text{S,out}}^{a} \frac{\mu_0 I}{2\pi r} dr \Rightarrow$$

$$\Rightarrow L_{11,\text{ext}} = \frac{\lambda_{1,\text{ext}}}{I} = \frac{\mu_0}{2\pi} \ln\left(\frac{r_\text{S,in}}{r_\text{C}}\right) + \frac{\mu_0 \mu_{\text{r,S}}}{2\pi} \ln\left(\frac{r_\text{S,out}}{r_\text{S,in}}\right) + \frac{\mu_0}{2\pi} \ln\left(\frac{a}{r_\text{S,out}}\right) \tag{6.4}$$

Since the total current I is not actually concentrated at the conductor surface at power frequency, the internal inductance of the conductor, $L_{11,\text{int}}$ (H/m), is also to be considered and added to (6.4), so as to calculate the total self-inductance of the conductor. For hollow conductors, the following formula may be in general used [74]:

$$L_{11,\text{int}} = \frac{\mu_0}{2\pi} \frac{0.25 - \gamma^2 + \gamma^4 (0.75 - \ln \gamma)}{(1 - \gamma^2)^2} \tag{6.5}$$

where γ is the ratio of inner to outer radius of a generic hollow conductor. γ is apparently equal to zero for solid conductors. Thus, the total self-inductance of the conductor, L_{11} (H/m), is:

$$L_{11} = L_{11,\text{int}} + L_{11,\text{ext}} \tag{6.6}$$

It may be noticed that, starting from (6.6) and using (6.4) and (6.5), one can readily obtain (6.1) just by applying basic logarithm properties and provided that $\mu_{\text{r,S}} = 1$.

The sheath is literally a hollow conductor: thus, (6.5) can be used also for the internal inductance of the sheath, $L_{22,\text{int}}$ (H/m), by considering γ equal to $r_{\text{S,in}}/r_{\text{S,out}}$. The external sheath inductance, $L_{22,\text{ext}}$ (H/m), may be obtained from the flux linkage over the sheath, as follows:

$$\lambda_{2,\text{ext}} = \int_{r_\text{S,out}}^{a} \frac{\mu_0 I}{2\pi r} dr \Rightarrow L_{22,\text{ext}} = \frac{\lambda_{2,\text{ext}}}{I} = \frac{\mu_0}{2\pi} \ln\left(\frac{a}{r_\text{S,out}}\right) \tag{6.7}$$

Similar to L_{11} and (6.6), the total sheath self-inductance, L_{22} (H/m), occurs by adding $L_{22,\text{int}}$ with $L_{22,\text{ext}}$. Concerning the mutual inductances, the internal conductor – sheath inductance, $L_{12,\text{int}}$ (H/m), also involves the magnetic sheath. Eq. (33) from Barrett's paper [74] is reproduced considering $\mu_{\text{r,S}}$ instead of unity:

$$L_{12,\text{int}} = \frac{\mu_0 \mu_{\text{r,S}}}{2\pi} \int_{r_\text{S,in}}^{r_\text{S,out}} \frac{1}{r} \frac{r^2 - {r_\text{S,in}}^2}{2 r_\text{S} t_\text{S}} dr = \cdots = \frac{\mu_0 \mu_{\text{r,S}}}{4\pi} \left[1 - \frac{{r_\text{S,in}}^2}{r_\text{S} t_\text{S}} \ln\left(\frac{r_\text{S,out}}{r_\text{S,in}}\right)\right] \tag{6.8}$$

where r_S and t_S is the mean sheath radius and sheath thickness, respectively (m). The external conductor - sheath inductance, which equals to the sheath external inductance, i.e. (6.7), is to be added in (6.8), so as to deduce the total conductor – sheath inductance, L_{12}. L_{21} equals to L_{12} due to symmetry. By implementing the above formulation, all the inductances of the 1C cable

are defined. Assuming R_1 and R_2 are the DC resistance (Ω/m) of the conductor and sheath, respectively, the impedance matrix of order 2 x 2 may be derived, as follows:

$$\mathbf{Z} = \begin{bmatrix} Z_{11} & Z_{12} \\ Z_{21} & Z_{22} \end{bmatrix} = \begin{bmatrix} R_1 + j\omega L_{11} & j\omega L_{12} \\ j\omega L_{21} & R_2 + j\omega L_{22} \end{bmatrix} \tag{6.9}$$

where ω is the angular frequency (rad/s). The following points should be remarked upon:

- Eq. (6.4) - (6.8) assume uniform current distributions in the conductor and the sheath. The non-uniform current distributions expected in reality under AC conditions influence the actual current loops and, thus, the cable inductances. Non-uniform current density is in general expected in a 1C cable due to skin and proximity effects. However, no significant influence on cable inductances is expected in the concentric model, where proximity effects are minimal: although the current is non-uniform, it still remains radially symmetrical. The inductance of radially distributed current loops in generically hollow, concentric conductors is not expected to change if compared to absolutely uniform current distributions.
- Eq. (6.4) - (6.8) imply that the conductor current is symmetrically placed with reference to sheath. In other words, they are not in theory expected to work for non-symmetrical cases, such as that of the eccentric cable or the SL-Type cable. Unfortunately, there are currently no FM versions accounting for this effect.

The impact of using the existing formulation in non-symmetrical geometries with magnetic materials is studied in the present section. To be consistent with the assumptions behind the analytical formulation, quasi-DC conditions are assumed by considering frequency equal to 0.1 Hz. An indicative 1C cable with r_C, $r_{S,in}$, t_S and a equal to 1 mm, 30 mm, 2 mm and 1 m respectively, is considered. Two values are examined with regard to $\mu_{r,S}$: 1 and 300. $\mathbf{Z}$ derived from (6.9) is compared with the corresponding impedance matrix occurring from Js-FEM method, which is presented in Chapter 5 and considered here as a reference. Results with a four-digit accuracy are shown in Table 6.1 and Table 6.2 for concentric and eccentric cases. The real part of $\mathbf{Z}$ occurs identical in both Js-FEM and analytical methods, as expected, since skin and proximity effects are very weak at 0.1 Hz. For this reason $\Re\{\mathbf{Z}\}$ is not shown.

By comparing the concentric with the eccentric case in Table 6.1, it can be seen that the analytical formulation described by (6.4) - (6.9) gives sufficiently consistent results for $\mu_{r,S}$ equal to unity (non-magnetic sheath), whatever the geometry is, i.e. either concentric or eccentric. By comparing the same cases in Table 6.2, $\Im\{Z_{11}\}$ derived from the analytical model is 4% lower than by the Js-FEM method.

TABLE 6.1: **Z**-Results for $\mu_{r,S}$ = 1 – 1C Cable.

Case	Js-FEM method		Analytical (6.9)		Relative Difference ε [%]	
	$\Im\{Z_{11}\}$	$\Im\{Z_{12}\}$	$\Im\{Z_{11}\}$	$\Im\{Z_{12}\}$	$\Im\{Z_{11}\}$	$\Im\{Z_{12}\}$
Concentric	8.9947e-07	4.3650e-07	8.9947e-07	4.3650e-07	0	0
Eccentric	8.9939e-07	4.3650e-07	8.9947e-07	4.3650e-07	0.009	0
	$\Im\{Z_{21}\}$	$\Im\{Z_{22}\}$	$\Im\{Z_{21}\}$	$\Im\{Z_{22}\}$	$\Im\{Z_{21}\}$	$\Im\{Z_{22}\}$
Concentric	4.3650e-07	4.3515e-07	4.3650e-07	4.3515e-07	0	0
Eccentric	4.3650e-07	4.3515e-07	4.3650e-07	4.3515e-07	0	0

TABLE 6.2: **Z**-Results for $\mu_{r,S}$ = 300 – 1C Cable.

	Js-FEM method		Analytical (6.9)		Relative Difference ε [%]	
	$\Im\{Z_{11}\}$	$\Im\{Z_{12}\}$	$\Im\{Z_{11}\}$	$\Im\{Z_{12}\}$	$\Im\{Z_{11}\}$	$\Im\{Z_{12}\}$
Concentric	3.3244e-06	1.6229e-06	3.3244e-06	1.6229e-06	0	0
Eccentric	3.4629e-06	1.6229e-06	3.3244e-06	1.6229e-06	-3.9995	0
	$\Im\{Z_{21}\}$	$\Im\{Z_{22}\}$	$\Im\{Z_{21}\}$	$\Im\{Z_{22}\}$	$\Im\{Z_{21}\}$	$\Im\{Z_{22}\}$
Concentric	1.6229e-06	1.2176e-06	1.6229e-06	1.2176e-06	0	0
Eccentric	1.6229e-06	1.2176e-06	1.6229e-06	1.2176e-06	0	0

The difference noticed in $\Im\{Z_{11}\}$ in Table 6.2 reflects the fact that a non-symmetrical magnetic field is induced in the eccentric case, because of the physical proximity of the conductor filament to the magnetic sheath. This uneven magnetic field potentially means a different flux linkage, thus a different inductance. The external flux linkage of the conductor at radius r (shown in Figure 6.1) may be computed by means of the following formula in the FEM model:

$$\lambda_{1,\text{ext}}(r) = \iint d\lambda = \iint \vec{B} \cdot d\vec{S} = \int_{r_C}^{r} \vec{B} \cdot \hat{n} \cdot l dr \tag{6.10}$$

where $\vec{B}$ is the magnetic flux density (T) computed by FEM, $\hat{n}$ is the unit vector normal to the infinitesimal surface, $d\vec{S}$ (m²), which in its turn has length equal to l (m), (l is in parallel with the cable axis), and width equal to the infinitesimal radius dr (m). The flux linkage at the sheath domain only, $\lambda_{1,S}$ (Wb/m), is first calculated: this is done by changing r_C and r with $r_{S,in}$ and $r_{S,out}$, respectively, in (6.10), and assuming an indicative current of 5 A. Subsequently, the total external flux linkage of the conductor, $\lambda_{1,ext}$ (Wb/m), is calculated, by integrating from r_C up to

$r = a$ and assuming the same indicative current. Results for both concentric and eccentric cases are compared in Table 6.3, with concentric being considered as a reference. It should be noted that the magnetic field in the eccentric case is circumferentially uneven, as expected, and so does the flux linkage. For this reason the spatial average $\int_0^{2\pi} \lambda_{1,\text{ext}} d\varphi / 2\pi$ is actually presented in Table 6.3 for both $\lambda_{1,S}$ and $\lambda_{1,\text{ext}}$. The relative difference between eccentric - concentric is apparently higher in the sheath domain, because of the increased $\mu_{r,S}$. It is noteworthy that the relative difference regarding the total external flux linkage is almost the same as that noticed in Table 6.2 for $\Im\{Z_{11}\}$.

TABLE 6.3: Flux Linkage FEM Results for Both Concentric and Eccentric Models.

	Eccentric	Concentric	ε [%]
$\lambda_{1,S}^{\text{avg}}$ (Wb/m)	2.0479E-05	1.9362e-05	-5.7714
$\lambda_{1,\text{ext}}^{\text{avg}}$ (Wb/m)	2.7288E-05	2.6205E-05	-3.9699

6.1.2 SL-Type Cable with Magnetic, Tubular Armour

To evaluate the potential use of FM for SL-Type armoured cables, three power cores are considered to be enclosed by a tubular armour, as illustrated in Figure 6.2. Each core consists of a conductor, with a single filament, and a non-magnetic sheath, which is composed of a single layer of filaments. As with the sheath in section 6.1.1, the armour is treated as a hollow conductor in the present section, having a magnetic relative permeability $\mu_{r,A}$ which is in general different than unity. Quasi-DC conditions are also considered in the present section. The numbering adopted to construct the **Z**-matrix of order 163 x 163 is also shown in Figure 6.2. The analytical formulation used to describe all self-inductances and the mutual inductances between the filaments and the armour is similar to that presented in section 6.1.1. Concerning the mutual inductances between the filaments, (6.2) is used, though being modified such that the armour, which generally has different magnetic properties than the conductors and sheaths, is considered:

$$L_{ij} = \frac{\mu_0}{2\pi} \ln\left(\frac{r_{\text{A,in}}}{D_{ij}}\right) + \frac{\mu_0 \mu_{\text{r,A}}}{2\pi} \ln\left(\frac{r_{\text{A,out}}}{r_{\text{A,in}}}\right) + \frac{\mu_0}{2\pi} \ln\left(\frac{a}{r_{\text{A,out}}}\right) \tag{6.11}$$

where $r_{\text{A,in}}$ and $r_{\text{A,out}}$ (m) is the inner and outer radius, respectively, of the armour. The analytical model is compared against the Js – FEM method and inductance values for specific filaments are selected and shown in Table 6.4 and Table 6.5 for $\mu_{r,A} = 1$ and $\mu_{r,A} = 300$, respectively. Sheath filaments are located at the inner and the outer part of the core circumference, so as to investigate the effect of the eccentricity on the derived results. The relative difference between the two methods is lower than 0.1% for most filaments of the non-magnetic case. An exception

is noticed with regard to the most eccentric filament, number 33 (Figure 6.2), with the difference being slightly higher than 0.1%. On the contrary, higher ε % values are seen when magnetic armour is considered: the 33rd filament has a self-inductance which is by almost 8% lower when calculated by the analytical formulation in comparison with the Js – FEM method. Similar trends for the rest of the filaments are noticed, depending on their position with reference to the centre of the tubular armour.

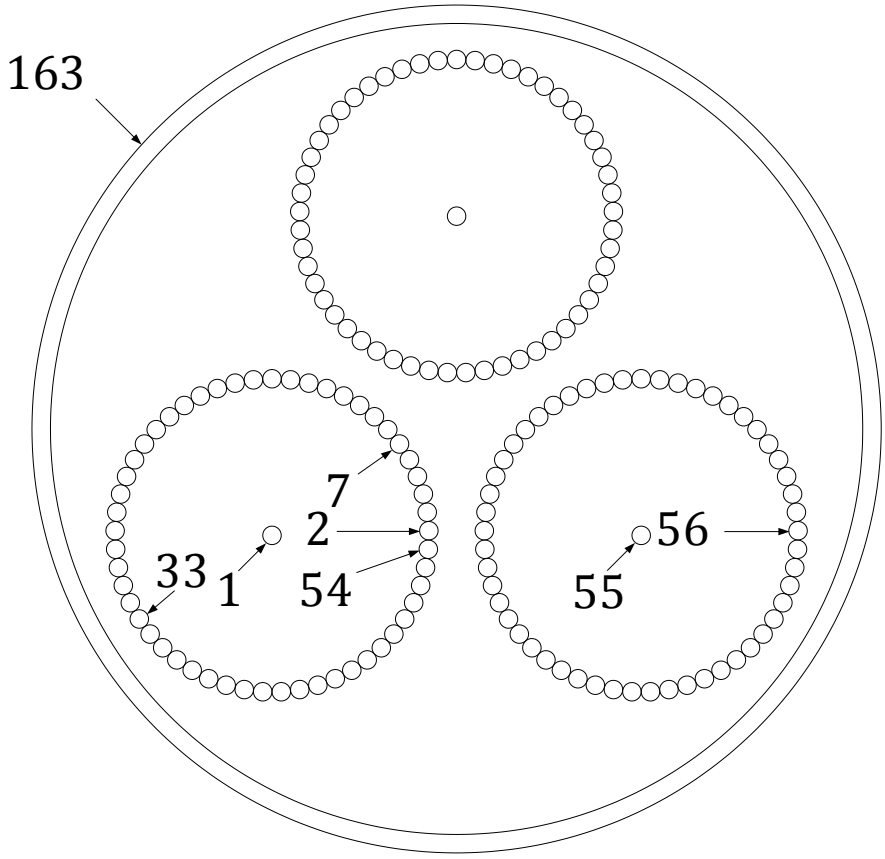

FIGURE 6.2: Filamentary Conductors and Sheaths in an SL-Type Cable. The Numbering Adopted to Construct the **Z**-Matrix of Order 163 x 163 Is Depicted.

TABLE 6.4: **Z**-Results for $\mu_{r,A}$ = 1 – SL-Type Cable with Magnetic, Tubular Armour.

	$\Im\{Z_{1,1}\}$	$\Im\{Z_{7,7}\}$	$\Im\{Z_{33,33}\}$	$\Im\{Z_{7,33}\}$	$\Im\{Z_{7,163}\}$	$\Im\{Z_{33,163}\}$
Js-FEM method	7.8391e-07	7.8432e-07	7.8308e-07	3.0964e-07	2.7454e-07	2.7454e-07
Analytical	7.8433e-07	7.8433e-07	7.8433e-07	3.0983e-07	2.7454e-07	2.7454e-07
ε [%]	0.054	0.001	0.159	0.062	0	0

TABLE 6.5: **Z**-Results for $\mu_{r,A}$ = 300 – SL-Type Cable with Magnetic, Tubular Armour.

	$\Im\{Z_{1,1}\}$	$\Im\{Z_{7,7}\}$	$\Im\{Z_{33,33}\}$	$\Im\{Z_{7,33}\}$	$\Im\{Z_{7,163}\}$	$\Im\{Z_{33,163}\}$
Js-FEM method	2.4901e-06	2.4568e-06	2.6583e-06	1.9949e-06	1.0973e-06	1.0973e-06
Analytical	2.4545e-06	2.4545e-06	2.4545e-06	1.9800e-06	1.0973e-06	1.0973e-06
ε [%]	-1.428	-0.091	-7.665	-0.743	0.001	0.001

At power frequency, more filaments are needed in both conductors and sheaths, in order to represent the skin and proximity effects. Therefore, the discrepancy noticed in the inductive parts of filament inductances (due to eccentricity) is going to have an impact on the derived filament current vector (which is to be extracted in a similar manner as that for the three power cores in Appendix B); thus, the finally obtained losses will be influenced. Moreover, the reduced 7x7 $\mathbf{Z}^{\mathbf{red}}$ matrix (extracted in a similar manner as that for 2x2 matrix shown in Appendix A) will also be affected: in that case, the discrepancies presented in the inductive part of **Z** are going to be transferred, to some extent, to the resistive part, due to matrix manipulations: this may be readily understood just by realising that the multiplication of two imaginary numbers leads to a real one; hence, the discrepancies initially noticed in the imaginary part of **Z** will be eventually transferred to the real part of $\mathbf{Z}^{\mathbf{red}}$.

It should be remarked that the problem regarding the existing formulation of FM is not closely related to the different magnetic properties of the armour. Instead, breaking the logarithm in the inductance formulae as shown in (6.11) is equivalent to transferring the return part of the inductance loop much closer to the non-eccentric filaments, i.e. at a distance equal to $r_{A,in}$. This becomes clear if noticing in Table 6.4 the higher divergence in the 33rd filament even in the non-magnetic case. A return ring equal to 1 m is considered in all these cases. However, if a ring return significantly closer to the inner, eccentric filaments was considered, **Z** values would be worse, even for $\mu_{r,A}$ = 1. In other words, there is a fundamental problem concerning the eccentricity in the existing formulation, which merely vanishes when all the components involved are non-magnetic, just because the return is placed sufficiently far away. The idea of using a conformal transformation is suggested by Schinzinger in [95] to account for the eccentricity in the internal impedance formulation for pipe-type cables; however, Schinzinger deals mainly with high-frequency phenomena and the method described in [95] has a limited range of eccentric locations. Moreover, the magnetic field is assumed in [95] to be restricted at the inner surface of the pipe, i.e. the pipe is assumed to provide a complete magnetic shielding effect. Although magnetic shielding is expected to some extent in SL-Type, wire armoured cables, this is certainly weaker than in pipe-type cables, due to the gaps existing between the

wires. Proposals on how this issue may be treated with respect to the existing FM formulation are further discussed in Chapter 7.

Besides the eccentricity, the representation of the magnetic, wire armour is a challenging issue to address. In problems where 2-D analysis is sufficient, such as in pipe-type cables, certain researchers avoid using FM for the magnetic pipe itself, such as Moutassem: as pointed out in his work [22], a very large number of filaments would be required for the pipe domain, owing to the very small skin depth compared to its thickness. Instead, Moutassem employs the Method of Images (MoI) to replace the magnetic pipe with fictitious filaments carrying such currents that generate an equivalent magnetic field in the pipe interior. In parallel, Moutassem uses FM to represent the actual current distributions in the pipe interior, by applying the Principle of Superposition for both physical and fictitious filaments.

However, in SL-Type cables with wire armour the situation becomes more complicated: the magnetic flux longitudinally driven in the wires is expected to influence the magnetic field in the armour interior and should be considered in the analysis; hence, this 3-D aspect must be translated, in a way, in 2-D, so as to use FM. The tubular representation is certainly convenient for this purpose. An idea that takes into account the longitudinal magnetic flux and represents the wire armour by means of an annulus is given by Goddard in [18]: in that paper, the 3-D effects are considered by setting special material properties and thickness in the 'equivalent tube'. The potential use of MoI for this equivalent tube is investigated in the following section.

6.2 Method of Images for SL-Type Cables in 2-D

The Method of Images (MoI) is used for loss calculation in pipe-type cables by Mekjian in [96], while the detailed mathematical formulation is presented in EPRI report [97]. One of the main assumptions of the method is that the skin depth, δ_P (mm), of the pipe is much smaller than its actual thickness, t_P (mm). It is:

$$\delta_P = \sqrt{\frac{2}{\mu_0 \mu_{r,P} \sigma_P \omega}} \tag{6.12}$$

where $\mu_{r,P}$ and σ_P is the relative permeability and the conductivity (S/m) of the pipe, respectively. δ_P is indeed significantly lower than t_P for most magnetic pipes used in practice, due to their high $\mu_{r,P}$. Based on this assumption, the physical system can be approximated by stretching the outer diameter of the pipe up to infinity. In other words, a full magnetic shielding may be assumed due to $\delta_P << t_P$ and the space outside the pipe can be treated as having identical electromagnetic properties with the pipe. This is a fundamental assumption of the MoI, which is necessary in order for the Principle of Superposition (PoS) to be applicable. Although this is

not true regarding the pipe exterior, it may be quite accurate regarding the fields induced inside the pipe and, thus, the induced currents in any metallic components enclosed by the pipe. In parallel, it affords a convenient way to simplify the mathematical solution of the problem under investigation by limiting its outer boundary at the interface between the pipe interior and the pipe itself. The level of accuracy at power frequency depends on pipe properties, i.e. $\mu_{r,P}$ and σ_P. To obtain a strictly accurate solution, one of the following two theoretical conditions must hold true [97]:

- Super Magnetic and Non-Conductive (SM & NC) pipe, i.e. $\mu_{r,P} \to \infty$ and $\sigma_P \to 0$
- Non-Magnetic and Super Conductive (NM & SC) pipe, i.e. $\mu_{r,P} \to 1$ and $\sigma_P \to \infty$

In the SM & NC case, the pipe can be replaced by fictitious (or image) filaments being laid at a specific distance and carrying currents equal in magnitude and phase with the physical filaments inside the pipe. In the NM & SC case the image filaments carry currents equal in magnitude but with a 180° phase difference. According to Mekjian [96], the image currents are located at:

$$d_{f,i} = \frac{{r_{P,in}}^2}{d_{ph,i}}, \qquad \varphi_{f,i} = \varphi_{ph,i} \tag{6.13}$$

where $(d_{f,i}, \varphi_{f,i})$ and $(d_{ph,i}, \varphi_{ph,i})$ are the cylindrical coordinates of the fictitious and physical filaments, respectively, with respect to the pipe centre, and $r_{P,in}$ is the pipe inner radius (m).

The interface between the pipe interior and the pipe itself is a critical boundary, at which the conditions must be such that an equivalent field distribution occur in the pipe interior, in the absence of the pipe. It is useful to visualise, by means of FEM, the derived flux lines, making focus at that boundary. An indicative pipe-type cable with the power cores being in trefoil, touching arrangement, located at the centre of the pipe is considered for this purpose. As shown in Figure 6.3, the flux lines occur entirely normal to the critical boundary when a SM & NC pipe is assumed (a very large number and zero is given in terms of $\mu_{r,P}$ and σ_P, respectively). In other words, the tangential to the boundary field component, B_{tang} (T), occurs 5 order of magnitude lower than the normal component, B_{norm} (T), thus being practically zero.

On the other hand, the flux lines occur entirely tangential to the critical boundary when a NM & SC pipe is assumed (unity and a very large number is given in terms of $\mu_{r,P}$ and σ_P, respectively), as shown in Figure 6.4. It should be noted that for both cases the situation in terms of the critical boundary (thus, for the pipe interior) will not change if someone extends the pipe thickness to infinity, thus verifying the fundamental assumption discussed in the beginning of this section.

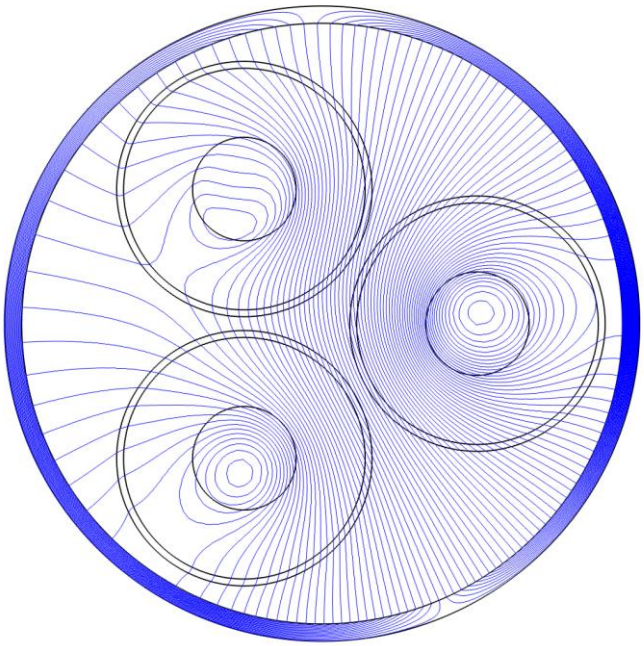

FIGURE 6.3: Flux Lines for a SM & NC Pipe ($\mu_{r,P} \to \infty$ and $\sigma_P \to 0$).

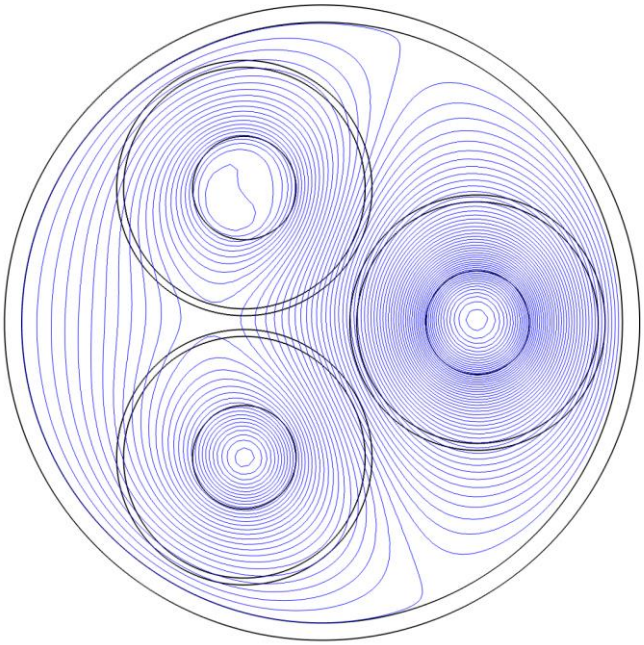

FIGURE 6.4: Flux Lines for a NM & SC Pipe ($\mu_{r,P} \to 1$ and $\sigma_P \to \infty$).

Moutassem manages in [22] to extend the use of the MoI for more realistic pipes, i.e. with high $\mu_{r,P}$ and high σ_P, simultaneously: an approximation is employed for this purpose and a special current, analytically calculated, is given in the fictitious filaments. Although this is not a generic solution, it seems from the results presented in [22] that works sufficiently for the pipe properties considered.

Indeed, if $\mu_{r,P}$ = 1500 and σ_P = 7.413·10⁶ S/m, which are used in [22], the flux lines occur as in Figure 6.5: although not absolutely normal to the critical boundary, they seem to be close to the SM & NC case, presented by Figure 6.3. In numbers, B_{tang} appears to be one order of magnitude lower than B_{norm} for Figure 6.5. The increase in σ_P, keeping at the same time a fairly high $\mu_{r,P}$, seems to have a minor impact, which can be addressed by applying the special currents suggested in [22] by Moutassem. It is noted that the distribution of flux lines will not change if someone extends the pipe thickness up to infinity, even for this, more realistic pipe.

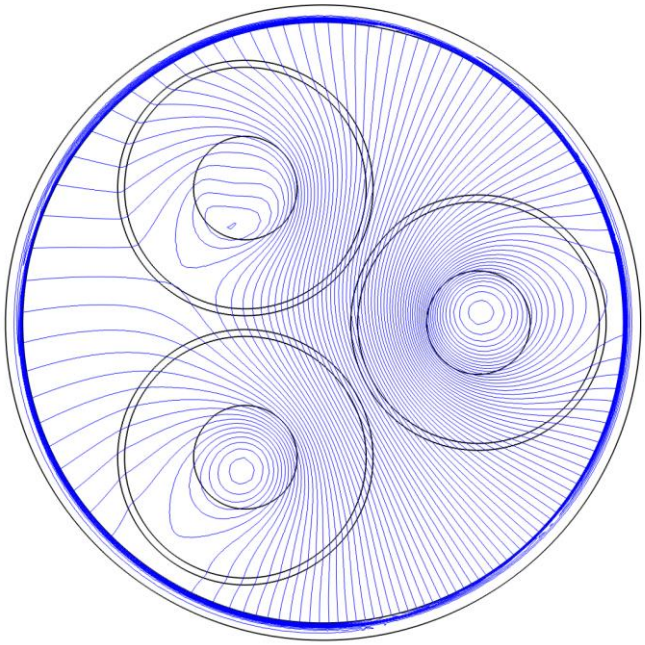

FIGURE 6.5: Flux Lines for a More Realistic Pipe ($\mu_{r,P} = 1500$ and $\sigma_P = 7.143 \cdot 10^6$ S/m, [22]).

The equivalent tube suggested by Goddard in [18] must have a special, complex magnetic permeability, $\boldsymbol{\mu}_{\mathbf{r,A\_eqvl}}$, and thickness, t_{A_eqvl} (m). Additionally, zero conductivity, σ_{A_eqvl} (S/m), is set, so as to prevent the likely generation of any circulating currents in the armour. The eddy current loss is included in the imaginary part of $\boldsymbol{\mu}_{\mathbf{r,A\_eqvl}}$. The latter is calculated as follows:

$$\boldsymbol{\mu}_{\mathbf{r,A\_eqvl}} = 1 + \frac{\dfrac{\boldsymbol{\mu}_{\mathbf{T}}(\cos\beta)^2 + \boldsymbol{\mu}_{\mathbf{L}}(\sin\beta)^2}{\cos\left[\tan^{-1}\left(\dfrac{2\pi r_A}{p_C}\right)\right]}}{t_{A\_eqvl}} \tag{6.14}$$

where $\boldsymbol{\mu}_{\mathbf{T}}$ and $\boldsymbol{\mu}_{\mathbf{L}}$ is the complex tranverse and longitudinal relative permeability, respectively, translated to the tubular geometry, and

$$\beta_{CA} = \tan^{-1}\left(\frac{2\pi r_A}{p_A}\right) - \tan^{-1}\left(\frac{2\pi r_A}{p_C}\right) \tag{6.15}$$

is the angle considered, so as to allow for a shorter helical path through the armour, where p_C and p_A is the pitch of the power cores and the armour, respectively (m).

By considering several SL-Type pitch designs, the corresponding $|\boldsymbol{\mu}_{\mathbf{r,A\_eqvl}}|$ values calculated as per (6.14) are shown in Table 6.6. It seems that a value as low as 15 is not impossible to occur for $|\boldsymbol{\mu}_{\mathbf{r,A\_eqvl}}|$, whereas $\sigma_{A\_eqvl} = 0$. By assuming this $|\boldsymbol{\mu}_{\mathbf{r,A\_eqvl}}|$, σ_{A_eqvl} combination, the flux lines occur as illustrated per Figure 6.6.

TABLE 6.6: Relative Permeability Values to Be Assigned in the Equivalent Tube [18] for Several Pitch Designs.

SL-Type Cable	630 mm² – 132 kV		1000 mm² – 150 kV		2500 mm² – 220 kV	
Pitch Design	p_C = 4.0 m, p_A = -2.0 m	p_C = 4.0 m, p_A = 2.0 m	p_C = 2.84 m p_A = -1.45 m	p_C = 2.84 m, p_A = 1.45 m	p_C = 4.5 m, p_A = -1.5 m	p_C = 4.5 m, p_A = 1.5 m
$\|\boldsymbol{\mu}_{\mathbf{r,A\_eqvl}}\|$	65.6	11.5	119	17.8	136.9	35.4

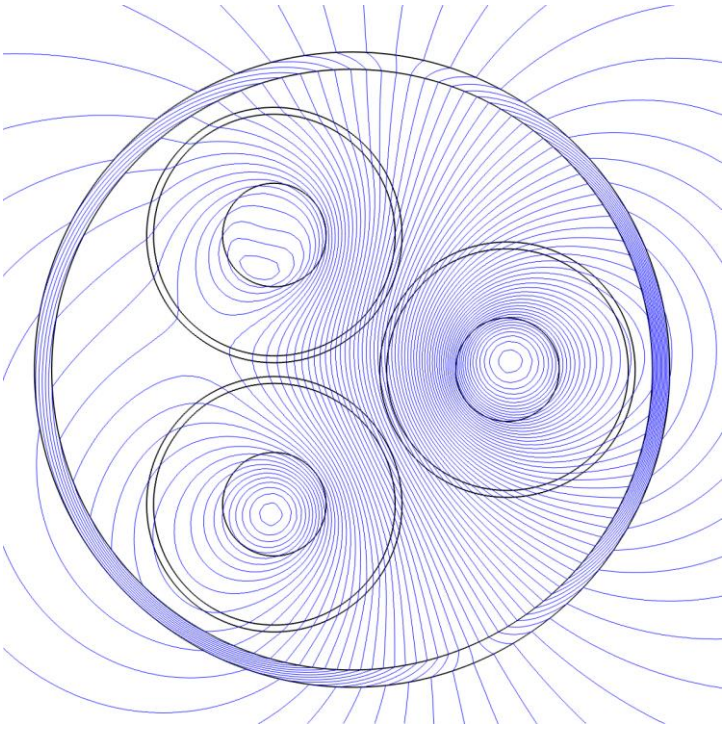

FIGURE 6.6: Flux Lines for the Equivalent Tube ($|\mu_{r,A\_eqvl}| = 15$ and $\sigma_{A\_eqvl} = 0$ S/m).

It can be noticed from Figure 6.6 that the flux lines are incident to the critical boundary with angles in general different from either 90 or 0°. In other words, both B_{tang} and B_{norm} are present at the interface between the tube interior and the tube itself: for the specific case shown in Figure 6.6, B_{tang} maximum equals to about 60% times B_{norm}. Furthermore, the situation changes substantially if the tube thickness is extended up to infinity: B_{norm} increases significantly

against B_{tang}, which decreases by one order of magnitude. Since zero $\sigma_{A,eqvl}$ is combined with a relatively low μ_{r,A_eqvl}, one of the fundamental assumptions of the MoI is violated: the tube exterior cannot be assumed to have identical electromagnetic properties with the tube itself or, in other words, the armour does not provide full magnetic shielding because of the $\sigma_{A,eqvl}$, $\boldsymbol{\mu_{r,A\_eqvl}}$ values expected in an SL-Type cable. Hence, the PoS is not applicable and any likely replacement of the equivalent tube by fictitious currents will not be, in principle, equivalent with reference to the critical boundary condition and, thus, the armour interior.

The existing formulation of FM and the MoI appear to be insufficient to represent the actually induced magnetic fields in the cable interior. Hence, alternative approaches are to be investigated in order to obtain a more accurate estimation of the cable losses. 3-D Finite Element Analysis (FEA) is considered in the following section for this purpose.

6.3 3-D Finite Element Analysis

The problem of calculating the power losses in SL-Type, wire armoured cables requires, in fact, 3-D analysis. Due to the complexity in geometry, a rigorous analytical solution is difficult; for this reason, certain researchers, such as Goddard [18] and Hatlo [17], try to simplify the analysis by adopting several assumptions, as already discussed in Chapter 4. The undoubted advantage of such approaches is that they provide quick results with sufficient accuracy, given the assumptions adopted.

However, the models suggested by Goddard [18] and Hatlo [17] cannot be used to estimate the effect of the magnetic armour on the conductor AC resistance, R_{AC}. The current IEC 60287-1-1 Standard [16] version does not consider any armour effect on R_{AC}, whereas the draft TB prepared by Cigré WG B1.56 [29] recommends that the skin and proximity effect factors, y_s and y_p, respectively, be multiplied by 1.5, as suggested by the IEC 60287-1-1 Standard for pipe-type cables. Such an increase in R_{AC} might result in about 5% decrease in the current rating of a 2500 mm^2 Copper conductor, 220 kV cable. Given that armour loss is believed to be significantly overestimated by the existing current IEC 60287-1-1 version, a further increase in conductor loss should be carefully considered, so as to avoid even more excessive cable losses. In addition, the present IEC calculation method, as well as the analytical model suggested by Hatlo [17], do not account for the effect of the magnetic armour on the eddy currents induced in the sheaths. It is of importance to quantify this effect.

3-D Finite Element Analysis (FEA) is employed in the present Chapter in order to evaluate cable losses, making focus on the impact the magnetic armour has on the losses induced in the metallic components underneath it, i.e. conductors and sheaths. For this purpose, a reference model is initially developed and the strategy followed is presented. Subsequently, the effect of

several design factors is investigated, such as the armour pitch, p_A, and the wire diameter, d_f. Various magnetic permeability values are also examined. All 3-D models are implemented in a workstation composed of two Intel Xeon E5-2667 v4, 3.20 GHz CPUs with 128 GB of RAM memory and a 2 TB hard disk drive for memory swapping. The results extracted from the 3-D analysis are compared with those derived from the analytical models developed by Goddard [18] and Hatlo [17], while the losses calculated by the IEC 60287-1-1 Standard are also shown.

6.3.1 Reference Cable: 3 x 630 mm² 150 kV

A cable with conductor radius r_C, sheath inner and outer radius $r_{S,in}$ and $r_{S,out}$, respectively, core outer radius $r_{J,out}$, armour mean radius r_A, number and diameter of wires n_A and d_f, respectively, core and armour pitch p_C and p_A, respectively, is considered. The relevant dimensional data are shown in Table 6.7 (mm). These represent a 3 x 630 mm² Copper conductor, 150 kV export cable. The minus sign in p_A implies the opposite direction of laying with reference to p_C. It is noted that pitches with opposite directions (contra-lay) are typically applied in export cables, so as to achieve torsional stability, which is necessary during cable installation. Pitches of the same direction (uni-lay) are more likely in array cables, which are in general of lower weight; hence, lower tensile forces are developed during installation, while the cables become coilable, thus enabling their easier handling and transportation. The present analysis focuses on export, contra-lay cables. The number of wires, n_A, shown in Table 6.7 may be relatively small for a 3 x 630 mm² 150 kV cable. Various p_A values are examined in section 6.3.5. To derive comparable loss results, the same number of wires must be kept when varying p_A: for lower p_A, n_A has to be small enough to avoid physical overlapping of the wires. Magnetic wires with $\boldsymbol{\mu_{r,A}}$ equal to 600-*j*350 are initially considered in this reference cable.

TABLE 6.7: Reference Cable, 3 x 630 mm² 150 kV – Dimensional Data (mm).

r_C	$r_{S,in}$	$r_{S,out}$	$r_{J,out}$	r_A	n_A x d_f	p_C	p_A
15	35	37.5	41	98	70 x 6.0	2800	-1400

6.3.2 Modelling Strategy and Boundary Conditions

As pointed out in Chapter 4, at least one full periodicity needs to be completed, so as to ensure no circulating currents in the armour. When two helices are combined, a full periodicity is expressed by the Least Common Multiple (LCM) of p_A and p_C. In actual cable installations, at least one full periodicity certainly occurs, due to the large length of the cable link in comparison with p_C and p_A. Any incomplete periodicities may lead to certain circulating currents close to the ends of the cable, but these are not expected to be significant, due to the large length of the link. Therefore, the proper cable length that has to be considered is a modelling challenge: p_C

and p_A are in reality so large, that their LCM occurs tens or, sometimes, even hundreds of metres.

A relevant work, recently published by del-Pino-López [27], suggests that a sensitivity study with various lengths in non-periodic models has to be considered to reduce the computational burden. The crossing-pitch (CP) length is identified as a critical value, affording some sort of shorter periodicity: each armour wire crosses the same power core every CP. A length equal to 1.25 times CP appears to give results with relative difference lower than 5% compared with fully periodic models. However, the number 1.25 is empirically derived and refers to the specific cables examined in [27]. An interesting approach is adopted by del-Pino-López at this point: properly rotated, periodic boundary conditions are applied at the vertical boundaries of a model with length equal to CP. Promising results are cited in [27] (relative difference lower than 0.5% compared to fully periodic models); however, this approach is not straightforwardly implementable and requires high set-up times; also, an in depth expertise on the specific FEM software used in [27] appears necessary.

A full periodicity is completed at $l = p_C$ for the reference cable described by Table 6.7. This is assumed to be laid at the axis of an external cylinder representing the surrounding medium, as shown in Figure 6.7.

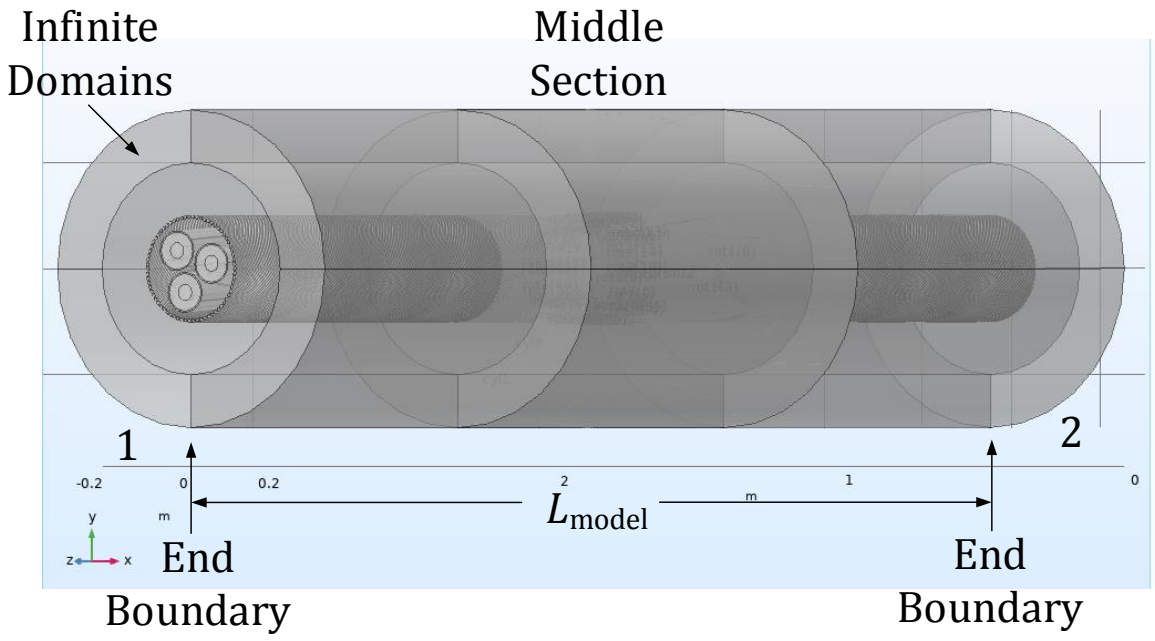

FIGURE 6.7: Considered Geometry for the Reference Cable Model.

It must be noted that the cable is in reality installed under or on the seafloor; thus, surrounding media with different electromagnetic properties coexist. However, the soil and the water have electrical resistivity values several order of magnitude higher than those of the cable metallic components. Moreover, 3-phase balanced conditions are assumed for loss calculation. Hence,

any likely return path is considered lossless due to phase symmetry and, thus, no significant impact on the cable losses is expected [89].

It should also be noted that the cores are assumed unjacketed in the context of the present Chapter. In reality, however, the jackets consist of some semiconductive polymeric compound, which has a resistivity in the range of 0.1 – 10 Ω·m [98]. Although these values stand at least 6 order of magnitude above conductors, sheaths and armour, they create distributed conductive paths for the induced currents and, thus, might influence induced losses, especially for unbonded sheaths. A work recently published by Sturm [92] demonstrates that unreasonably high circulating currents may occur when three jacketed power cores in trefoil, touching arrangement are considered, depending on the model length, as well as the conductivity assumed for the jacket. However, no significant impact on losses is expected, as also pointed out by Sturm, when solidly bonded sheaths are considered.

As for the 2-D models presented in Chapter 5, a coordinate scaling is adopted to layers of virtual domains surrounding the physical region of interest. These virtual layers, often called as 'Infinite Domains' (Figure 6.7), can be mathematically stretched out towards infinity, where a homogeneous Dirichlet boundary condition in terms of the magnetic vector potential, $\vec{A}$ (Wb/m), is set, such that:

$$\hat{n} \times \vec{A} = 0 \tag{6.16}$$

where $\hat{n}$ is the unit vector normal to the surface. As a result, the extent of the FEM model can be limited to a manageable region of interest with respect to the radial direction. A relative difference not exceeding 0.1% in terms of losses is noticed when compared such a model with one having a surrounding cylinder of radius equal to 1 m, with no Infinite Domains (just (6.16) directly applied). However, this difference may become higher when, for instance, a larger cable or cables spaced apart have to be considered.

The boundary conditions (BCs) applied on the end boundaries, perpendicular to the cable axis, are of great importance. The model illustrated in Figure 6.7 is a periodic model: thus, proper periodic BCs that guarantee this periodicity besides ends 1 and 2 must be considered. These are expressed by the following:

$$\hat{n} \times \left(\vec{H}_1 - \vec{H}_2\right) = 0 \tag{6.17}$$

where $\vec{H}_1$ and $\vec{H}_2$ is the magnetic field intensity (A/m) at end boundary 1 and 2, respectively. By applying (6.17), field continuity is guaranteed between circular bases 1 and 2, i.e.:

$$H_{1,x} = H_{2,x} \text{ and } H_{1,y} = H_{2,y} \tag{6.18}$$

while H_z is left undefined. Due to the periodic symmetry of the model, H_z occurs eventually identical at end boundaries 1 and 2. An alternative option may be the use of (6.16) instead of (6.17): in this case, A_x and A_y are forced to be zero and only A_z remains non-zero. In other words, the analysis at the end boundaries becomes essentially 2-D, since any likely fields induced by currents having non-zero I_x and I_y components are nullified and only fields induced by I_z are actually considered. Since both the power cores and the armour wires are incident at boundaries 1, 2 with an angle different than 90°, I_x and I_y components are physically non-zero. Hence, end effects are expected in such a case and their influence on the losses calculated must be investigated. For this purpose, three cases are examined: first, the use of (6.17) is considered in Case A; then, (6.16) is applied in Case B; finally, a model as long as twice the initial one is considered in Case C, applying (6.16). In this latter case, two full periodicities are actually simulated, thus enabling, in theory, one full periodicity unaffected by the effects occurring at the ends. In all cases, sheaths and the armour are solidly bonded. Conductor, sheath, armour and total losses, W_C, W_S, W_A and W_{tot}, respectively, are computed in the middle section (Figure 6.7) and depicted in Table 6.8 for each case. Certain simulation data, such as the number of elements and degrees of freedom (DsOF), are also shown for informative purposes. It is noted that the same mesh density is kept in Case C, so as to obtain comparable results. The relative difference ε (%) is additionally shown, considering as a reference Case A.

TABLE 6.8: Assessment of the Three Possible Cases in Terms of the Applied BCs at 1, 2.

Case	A (6.17)-Periodic	B (6.16)	B VS A ε (%)	C (6.16) – 2x	C VS A ε (%)
Elements	1579326	1579326	0	2962420	87.6
DsOF	12174267	12174267	0	22681581	86.3
Solution time (h)	30.53556	1.531389	-95	11.25611	-63
W_C (W/m)	15.015	15.019	0.03	15.010	-0.03
W_S (W/m)	6.5093	6.4221	-1.34	6.5512	0.64
W_A (W/m)	6.3704	6.3757	0.08	6.4517	1.28
W_{tot} (W/m)	70.943	70.699	-0.34	71.135	0.27

The use of (6.16) introduces certain noticeable end effects in case B, especially concerning W_S: magnetic field intensity, H, is mitigated close to the end boundaries, because H_z is forced to be zero. This mitigation leads to some decrease in the current circulating in sheaths, I_S, thus decreasing W_S by 1.3%. Having lower I_S, the total magnetic field above the power cores is less

cancelled and, thus, higher W_A is expected in Case B. However, the end effects influence also the eddy and hysteresis losses induced in the armour wires: hence W_A appears less increased in Case B in comparison with W_S. The results derived from Case C seem to be in general closer to Case A: ε is smaller in terms of W_S and W_{tot}. An unexpectedly higher W_A may be seen. Considering the same mesh density in Case C may be not necessarily an equivalent approach, as initially believed: in smaller models the distance from the boundaries is in general shorter and, thus, a relatively finer mesh might be needed to obtain the same level of accuracy. In any case, ε values are kept sufficiently low in both Cases B, C. As seen in Table 6.8, the solution time in Case B occurs significantly lower than Cases A, C.

To further evaluate the impact of the end effects on the losses obtained in Case B, they are compared with losses obtained at various points of the model. Cable losses (W) are initially obtained in the middle volume section of the model, as this is shown in Figure 6.7. They are subsequently divided by $L_{model}/3$ to obtain loss pul of the cable (W/m). In parallel, cable losses (W/m) are taken in ten 2-D successive slices along the cable. As shown in Figure 6.8, W_{tot} computed at the middle volume section is less than 0.5% different than the corresponding values taken in the 2-D slices close to the midpoint of L_{model}. Therefore, the middle volume section appears to be an adequately representative region of the model to calculate the losses. The modelling approach developed for Case B is adopted in the following sections of the present Chapter, since this appears to be accurate enough and substantially more time-efficient.

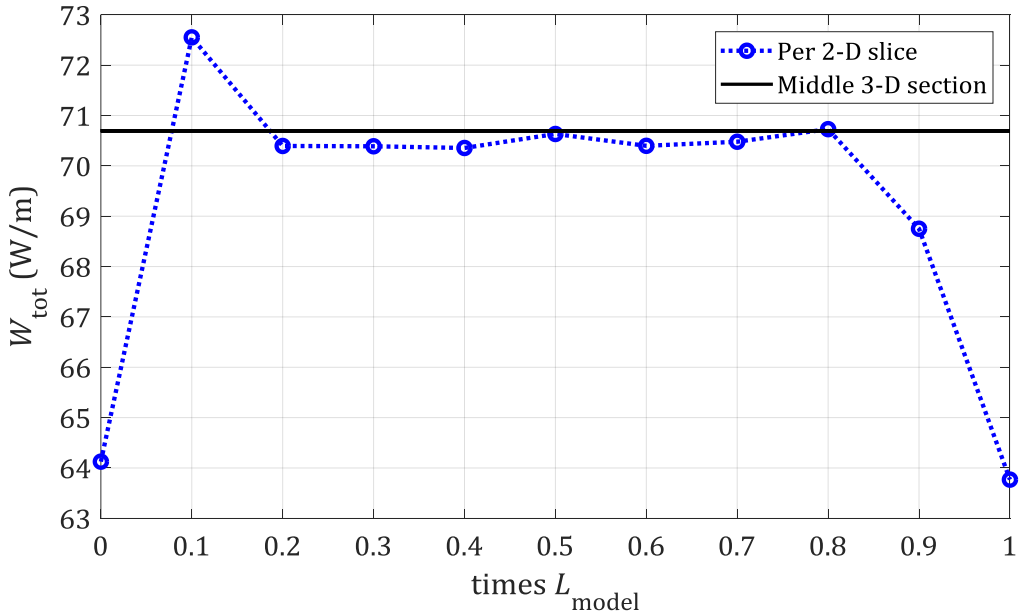

FIGURE 6.8: W_{tot} Computed in the Middle Section and in 2-D Successive Slices along the Cable.

6.3.3 Mesh Study

In FE studies the mesh strategy followed is a rather critical part of the entire analysis: this becomes even more crucial when developing 3-D models, since the compromise between accuracy and computational burden is inevitable. A convenient way of controlling the mesh is by imposing mesh controls along the helical path of the power cores and the armour wires, as depicted in Figure 6.9. The validity of this approach relies on the fact that the gradients of the magnetic vector potential in the longitudinal direction of the helix are not expected to be significant, particularly if compared with those expected in the radial direction.

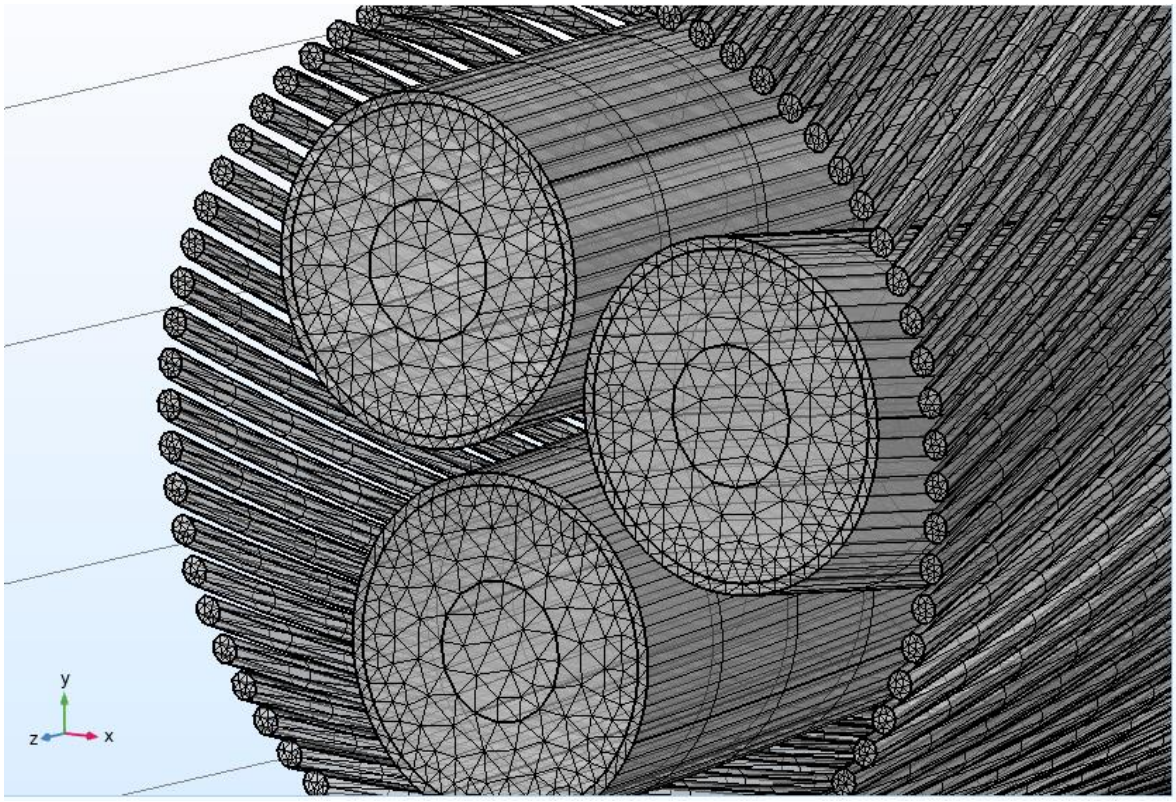

FIGURE 6.9: Cable Mesh with Mesh Controls along the Power Cores and the Armour Wires – Reference Model.

To investigate the effect of this mesh strategy, two models are developed and compared against the reference model, results of which have already been presented in Table 6.8: one involving denser mesh in the sheaths and another one with denser mesh in the armour. In each case the rest of the mesh remains unchanged, i.e. as it is in the reference model. The coarser and finer mesh considered for the armour wires may be seen in Figure 6.10. In this, case it is necessary to increase the mesh not only in the longitudinal direction, but additionally in the radial direction, such that the 2-D cross-section of each wire be finer: for a wire with $\boldsymbol{\mu}_{r,A}$ equal to 600-j350 the skin depth can be in the order of 1 mm for Steel at power frequency. Hence, a wire with d_f equal to 6.0 mm is likely to experience a quite intense skin effect, that might affect the

armour loss. The corresponding results along with the relevant informative data are presented in Table 6.9 - Table 6.11.

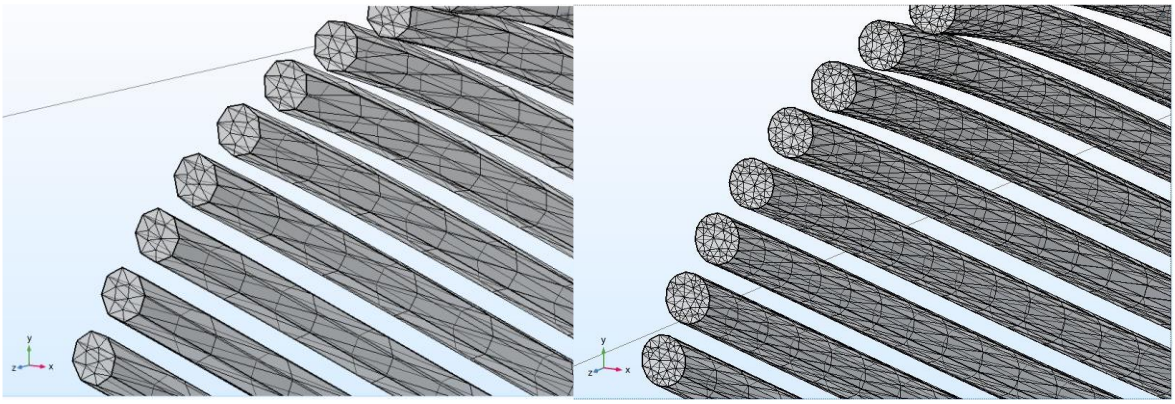

FIGURE 6.10: Coarser (on the Left) and Finer (on the Right) Wire Meshing.

TABLE 6.9: Loss Results for the Reference Model.

Elements	Sheath Elements	Armour Elements	DsOF	Solution Time (h)	W_C (W/m)	W_S (W/m)	W_A (W/m)	W_{tot} (W/m)
1579326	29160	563436	12174267	1.531389	15.019	6.4221	6.3757	70.699

TABLE 6.10: Loss Results – Finer Mesh in the Sheaths.

Elements	Sheath Elements	Armour Elements	DsOF	Solution Time (h)	W_C (W/m)	W_S (W/m)	W_A (W/m)	W_{tot} (W/m)
3132446	523800	563436	23574527	82.23806	15.012	6.4250	6.3722	70.683

TABLE 6.11: Loss Results – Finer Mesh in the Armour.

Elements	Sheath Elements	Armour Elements	DsOF	Solution Time (h)	W_C (W/m)	W_S (W/m)	W_A (W/m)	W_{tot} (W/m)
5343272	29160	2694792	44525213	255.2667	15.023	6.4361	6.3205	70.698

By comparing Table 6.10 with Table 6.9, a relative change of lower than 0.05% is noticed when making the mesh of the sheaths denser by about 1696%. Considering a mesh by 378% finer for the armour and an, in total, much heavier model, a relative difference lower than 0.2% may be noticed from Table 6.11 with reference to Table 6.9.

6.3.4 Comparison against 2-D Models

The use of 2-D analysis in SL-Type cables with magnetic armour imposes several limitations, as already discussed in the present Chapter and Chapter 4: this is because the longitudinal magnetic flux, which is expected significant due to high $\mu_{r,A}$, is not accounted for. However, the

situation may be not so severe in cables with non-magnetic armour. As pointed out in Chapter 5, the presence of non-magnetic armour is not expected to have significant impact on sheath losses: zero net induced currents circulate in the armour, thus the amount of the flux induced by the power cores does not change significantly within the thickness of the armour.

A 2-D analysis, though, does not allow to take into consideration of any eddy currents circulating circumferentially, in the angular direction with respect to the wire axis, because all the cable components are assumed in a straight configuration. In this section, this effect is accounted for, by comparing losses derived from 2-D and 3-D analyses for the reference cable, assuming the latter has $\mu_{r,A}$ equal to unity. Four cases regarding p_A are examined for this purpose, keeping p_C constant (2.8 m), as shown in Table 6.12: the selection of p_A is such that the LCM of p_A and p_C occurs fairly low and facilitate the analysis. Conductor AC resistance, R_{AC}, λ_1 and λ_2 values are presented in Table 6.12. A relative change lower than 1% and 2% for R_{AC} and λ_1, respectively, may be noticed, considering as reference the 3-D values. Armour loss occurs quite low in all cases, thus implying that any comparison between them is meaningless.

TABLE 6.12: Loss Results for Non-Magnetic Armour – 2-D against 3-D Models.

Case #	p_A (m)	LCM (p_A, p_C)	R_{AC} (Ω/km)	λ_1	λ_2
1 – 3-D	5.6	5.6	0.028922	0.26296	0.00020
1 – 2-D			0.028696	0.26724	0.00018
2 – 3-D	2.8	2.8	0.028872	0.27282	0.00033
2 – 2-D			0.028696	0.26724	0.00017
3 – 3-D	1.4	2.8	0.028866	0.27269	0.00036
3 – 2-D			0.028696	0.26724	0.00016
4 – 3-D	0.7	2.8	0.028868	0.27269	0.00020
4 – 2-D			0.028696	0.26724	0.00013

Two useful points must be noted from the above analysis. First, the 2.5-D approach (in series connection of the armour wire domains) adopted in Chapter 5 to represent losses in cables with non-magnetic armour appears to be accurate enough concerning the λ_1 values obtained. Further analysis, involving different cable sizes, would certainly provide even safer evidence towards this direction. This is further discussed in Chapter 7. Second, the 3-D model presented in the present Chapter is, to some extent, validated against 2-D models: these in their turn are validated against other analytical or numerical methods, such as Ametani formulation [81] and Filament Method (FM), as presented in Chapter 5. This sort of validation is, unfortunately,

limited to cables with non-magnetic armour. In order to evaluate better the losses obtained from 3-D analysis involving magnetic wires, a comparative study follows in the next section, where 3-D results are compared against existing analytical methods.

6.3.5 Parametric Analysis

The effect of the magnetic armour on the losses generated in conductors and sheaths is the key-objective of the present Chapter, as already discussed in the introduction (before section 6.1). For this purpose, loss results derived from 3-D FE simulations are presented in this section considering magnetic wires in the armour. These are compared against the analytical models developed by Goddard [18] and Hatlo [17], which both account for the longitudinal magnetic flux driven along the wires. Since these analytical models assume line currents in the conductors and do not account for the effect of the armour on conductor AC resistance, R_{AC}, this is obtained from the IEC 60287-1-1 Standard [16]. Three $\boldsymbol{\mu}_{\mathbf{r,A}}$ values are examined: 600-j350, 150-j50 and 1, representing lower, higher and austenitic (stainless) steel grades, respectively [77]. Hysteresis loss is represented by $\Im\{\boldsymbol{\mu}_{\mathbf{r,A}}\}$. It should be noted that $\boldsymbol{\mu}_{\mathbf{r,A}}$ is considered constant in the present study, based on the assumption that the magnetic field in an SL-Type, armoured cable is kept so low, that the hysteresis loop does not reach at the saturation region. In reality, $\boldsymbol{\mu}_{\mathbf{r,A}}$ is a field dependent material property, a fact that is further discussed later, in Chapter 7. Resistivity values for all the metallic components are as suggested by the IEC 60287-1-1 Standard [16], which will be referred to as merely IEC in the context of the present section. The resistivity of Steel is considered constant to $13.8 \cdot 10^{-8}$ Ωm, irrespective of the steel grade. Finally, all resistivity values are assumed constant at 20°C, since only electromagnetic analysis is considered, decoupled from any thermal effects.

6.3.5.1 Variation in Armour Pitch

The pitch of the armour, p_A, is varied in the present section and the effect on cable losses is considered. Cases 1, 2, 3 and 4 represent p_A values equal to 5.6 m, 2.8 m, 1.4 m and 0.7 m, respectively, while p_C is constant, equal to 2.8 m and in opposite direction than p_A. The above p_A values are theoretical and such that the LCM of p_A and p_C (thus the model length) occurs fairly low. In practice, p_A is often slightly higher than p_C in export cables, so as to achieve minimal torsional stresses and minimise the tensile load undertaken by the phase conductors [11]. However, by reducing p_A lower than p_C, the trend concerning the effect of the pitch can still be studied, while computationally efficient 3-D models occur. The sheaths are initially considered solidly bonded: thus, total losses, i.e. circulating plus eddy current, are obtained in sheaths, as in actual subsea projects. Then, the eddy current loss is solely examined, assuming single-point bonding.

The AC resistance of conductor, R_{AC}, is depicted in Figure 6.11, as computed by FEM, IEC 60287-1-1 and IEC with the recommendation made by Cigré WG B1.56. The formula related to the latter two methods is as per (6.19):

$$R_{AC} = R_{DC}\left(1 + \left(y_s + y_p\right)\right) \tag{6.19}$$

where R_{DC} is the DC resistance of the conductor at operating temperature (Ω/m), y_s and y_p is the skin and proximity effect factor, respectively. y_s and y_p factors must be multiplied by 1.5, according to the Cigré recommendation when magnetic armour is considered.

The effect of magnetic, lower-grade armouring is clearly shown in Figure 6.11: the lower p_A, the stronger the effect. This is expected, because by decreasing p_A the amount of longitudinal magnetic flux driven along the wires also increases. Hence, the magnetic field underneath the armour intensifies and the phase conductors experience stronger proximity effects. However, the Cigré recommendation turns out to be conservative for all p_A values compared with FEM: it starts to look reasonable for quite low p_A, where it overestimates R_{AC} less than IEC 60287-1-1 underestimates it. For higher p_A values, it overestimates R_{AC} by up to 5%, while the IEC method underestimates it by 2%, with reference to FEM. As expected, the empirically derived 1.5 factor suggested by IEC 60287-1-1 for pipe-type cables is not capable of capturing accurately the magnetic effect in wire armoured cables, where other factors, such as the armour pitch, are at play. It is worth noting that the empirical factor initially used by the cable designers had been 1.7 instead of 1.5 for pipe-type cables [26].

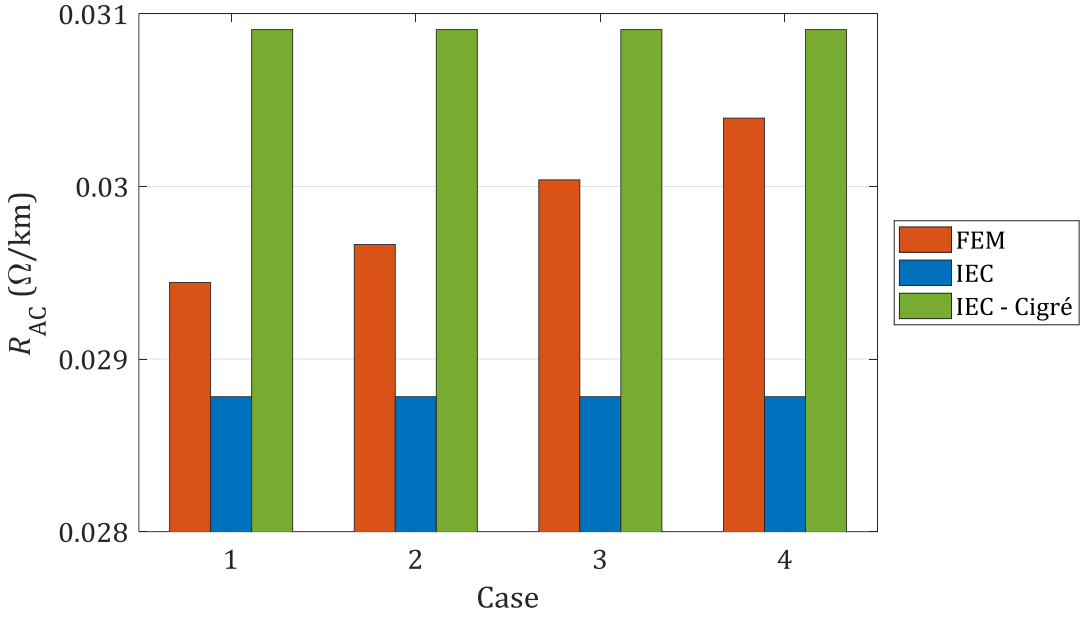

FIGURE 6.11: Conductor AC Resistance obtained from FEM, IEC Method & IEC with the Recommendation by Cigré WG B1.56 Draft TB [29] – $\boldsymbol{\mu_{r,A}}$ = 600-J350.

The effect of the armour on R_{AC} becomes weaker when higher grade steel is used, as shown in Figure 6.12. In this case, the Cigré recommendation is clearly overestimating for higher p_A values. The existing IEC method underestimates R_{AC} by about 2% for higher p_A: this may be interpreted to an overestimation less than 1% in current rating assuming 'typical' installation conditions (1 m depth, 0.7 Km/W soil, 15°C). When stainless steel is considered, the relative difference between IEC and FEM falls down to lower than 0.5%, as seen in Figure 6.13, thus verifying that the IEC method provides sufficient accuracy in cables with non-magnetic armour.

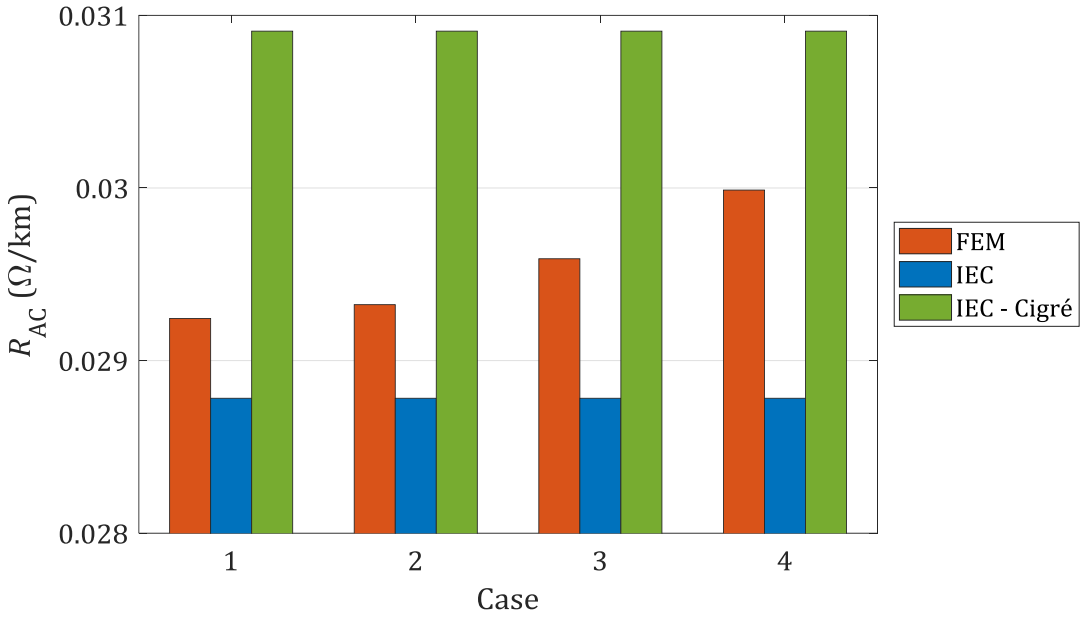

FIGURE 6.12: Conductor AC Resistance obtained from FEM, IEC Method & IEC with the Recommendation by Cigré WG B1.56 Draft TB [29] – $\boldsymbol{\mu_{r,A}}$ = 150-j50.

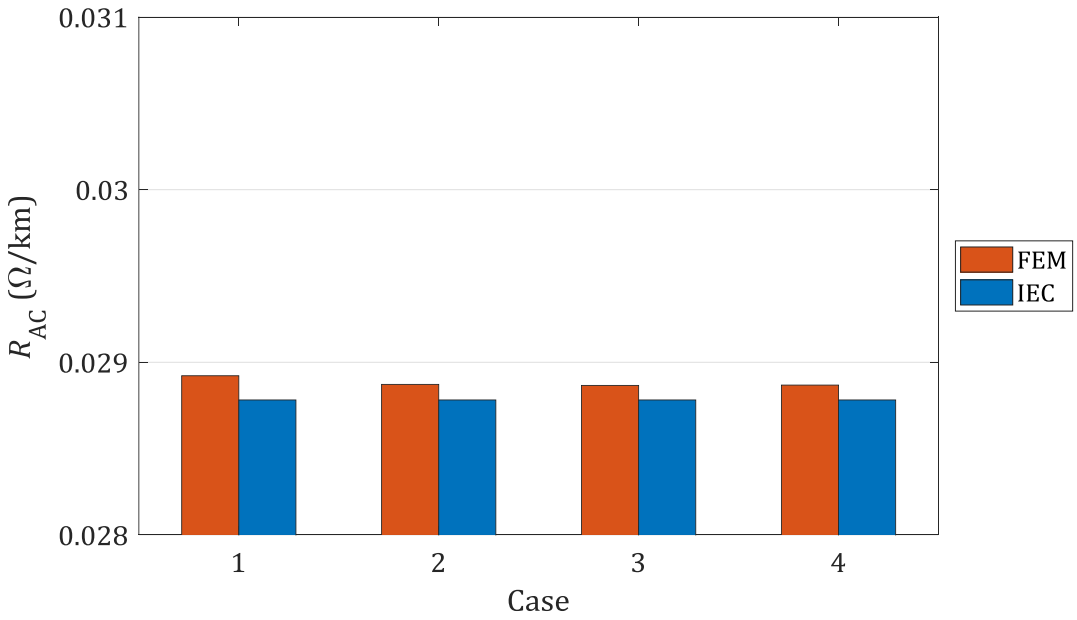

FIGURE 6.13: Conductor AC Resistance obtained from FEM, IEC Method – $\mu_{r,A}$ = 1.

Total losses in sheaths, i.e. circulating and eddy current, are subsequently considered. The IEC 60287-1-1 formula for the circulating loss factor is:

$$\lambda'_{1,\mathrm{IEC}} = \frac{R_\mathrm{S}}{R_\mathrm{AC}} \frac{1.5}{1+\left(\frac{R_\mathrm{S}}{X_\mathrm{S}}\right)^2} \tag{6.20}$$

where R_S is the resistance of sheath per unit length (pul) of cable (Ω/m), and X_S is the reactance pul of sheath (Ω/m), i.e.:

$$X_\mathrm{S} = 2\omega 10^{-7} \ln\left(\frac{2s}{d}\right) \tag{6.21}$$

where d is the mean diameter of sheath (mm) and s is the distance between conductor axes (mm). When non-magnetic armour is studied, the 1.5 factor in (6.20) turns into 1.0. Eddy current loss factor, $\lambda''_{1,\mathrm{IEC}}$ as calculated by (4.19) is to be added to (6.20) to obtain the total sheath loss factor, $\lambda_{1,\mathrm{IEC}}$.

Although $\lambda''_{1,\mathrm{IEC}}$ does not account for the effect of the magnetic armour, $\lambda_{1,\mathrm{IEC}}$ appears to be conservative by up to 24% with reference to FEM for higher p_A, as demonstrated in Figure 6.14. Since the 1.5 factor employed by (6.20) is empirically derived, as discussed in Chapter 4, $\lambda_{1,\mathrm{IEC}}$ remains unchanged whatever p_A or $\mu_{\mathrm{r,A}}$ are, whereas $\lambda_{1,\mathrm{FEM}}$ may increase by about 40% when reducing p_A from 5.6 to 0.7 m for both lower and higher Steel grades (Figure 6.15). As for R_AC, the smaller p_A, the higher the flux linkage induced in the armour wires and, thus, the driving and eddy currents in sheaths are also expected to increase.

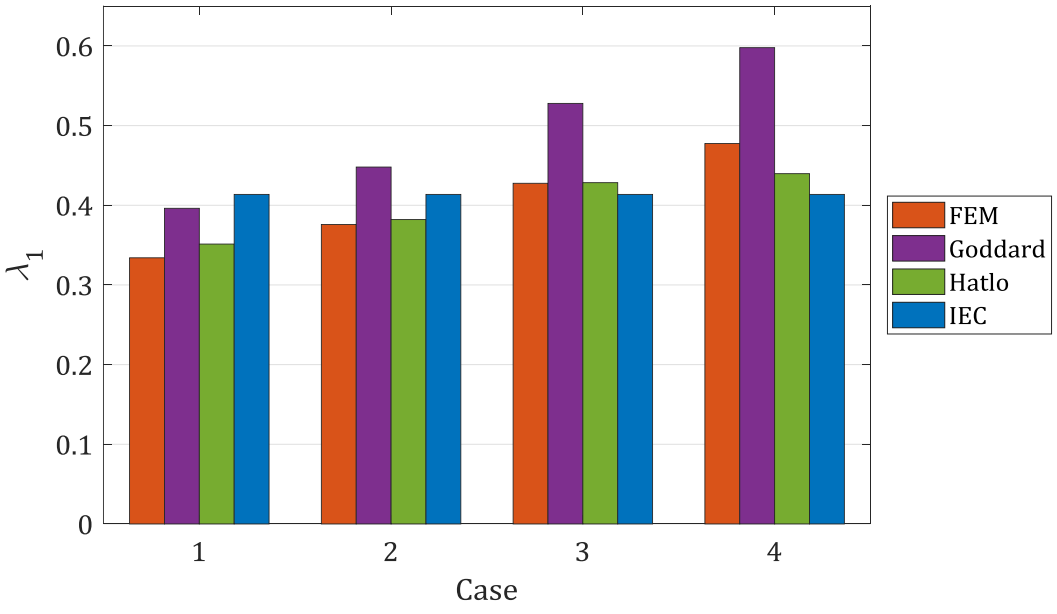

FIGURE 6.14: Sheath Total Loss Factor λ_1 obtained from FEM, Goddard [18], Hatlo [17] and IEC Method - $\boldsymbol{\mu_{r,A}}$ = 600-j350.

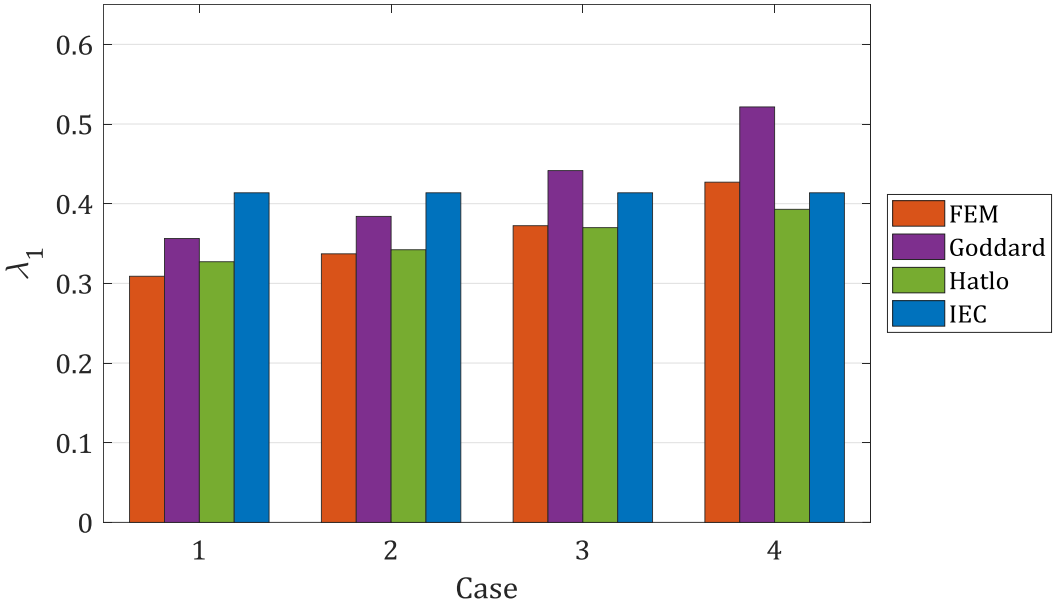

FIGURE 6.15: Sheath Total Loss Factor λ_1 obtained from FEM, Goddard [18], Hatlo [17] and IEC Method - $\boldsymbol{\mu}_{r,A}$ = 150-j50.

The model suggested by Goddard [18] appears to follow, in general, the FEM trend, although it stands always above it and overestimates λ_1 by up to 25% for lower p_A. It is noted that such an increase would lead to a less than 2% decrease in the thermal rating of the cable for 'typical' installation conditions. The model developed by Hatlo [17] presents better agreement with FEM for Cases 1, 2 and 3, although underestimates λ_1 by 8% for the smallest p_A value (Case 4). This may be attributed to the fact that Hatlo does not account in his model for the effect of the magnetic armour on the eddy currents induced in sheaths. For austenitic grades, λ_1 values present a totally better agreement, as expected (Figure 6.16): $\lambda_{1,FEM}$ appears lower by about 7% than the other three methods. Proximity effects in the conductors and sheaths are considered by the FE analysis when computing sheath loss and can lead to decreased λ_1, as discussed in Chapter 5. However, Goddard [18] and Hatlo [17] assume line currents located at the centres of conductors, thus ignoring any reductive effects on λ_1 occurring from the crowding of conductor currents towards the cable centre.

Although emphasis is given on the effect of the armour on sheath and conductor losses in the context of the present Chapter, λ_2 results are also presented in this section for the sake of completeness. As shown in Figure 6.17, the existing IEC 60287-1-1 method overestimates λ_2 by a factor of 3.5 for higher p_A and lower grade Steel wires compared to FEM. This factor increases up to 9 for higher grades, as shown in Figure 6.18. Assuming FEM losses, an increase by 6% and 8% in the thermal rating of the cable occurs for lower and higher Steel grades, respectively. It is worth noting that by using a conductor of 500 mm^2 instead of 630 mm^2 [94], the requested ampacity would be met for this specific case.

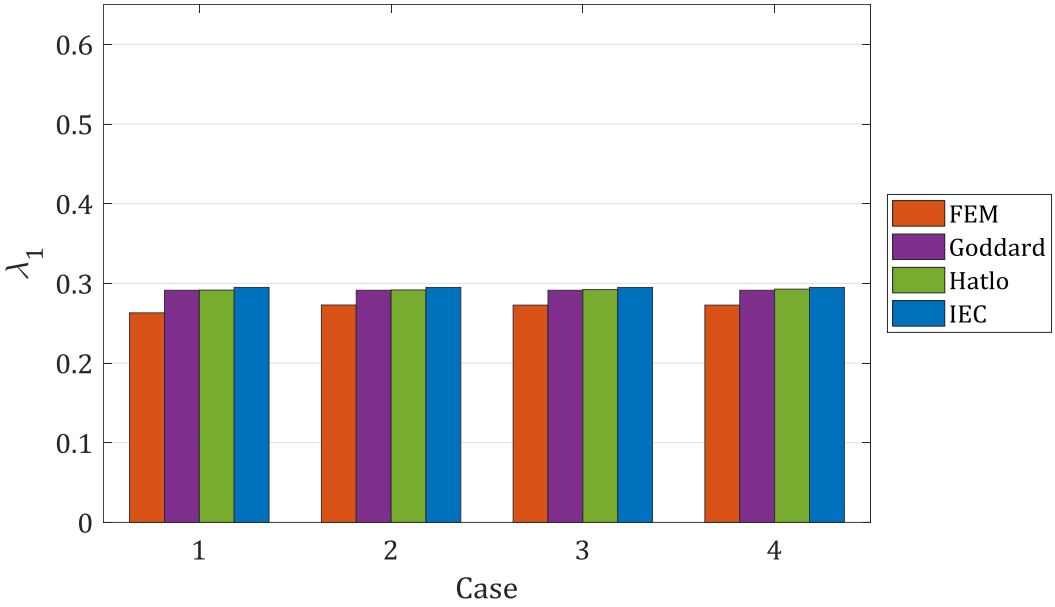

FIGURE 6.16: Sheath Total Loss Factor λ_1 obtained from FEM, Goddard [18], Hatlo [17] and IEC Method - $\mu_{r,A}$ = 1.

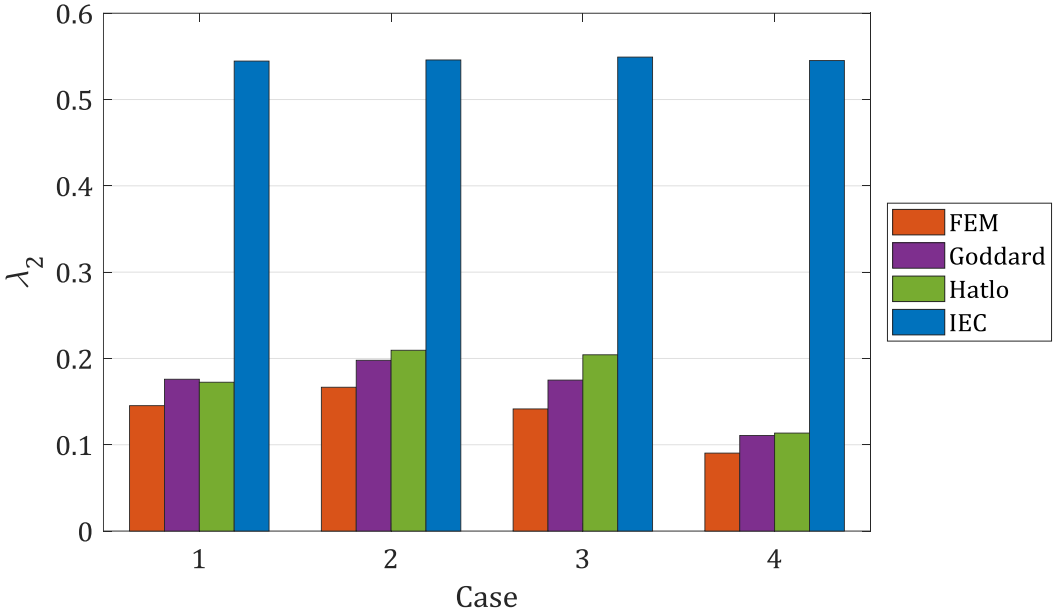

FIGURE 6.17: Armour Loss Factor λ_2 obtained from FEM, Goddard [18], Hatlo [17] and IEC Method - $\boldsymbol{\mu_{r,A}}$ = 600-j350.

Although certain discrepancies between the analytical methods suggested by Goddard and Hatlo may be noticed if compared to FEM results, both seem to be in a substantially better agreement with FEM than IEC is, particularly for higher grades (Figure 6.18) where the IEC method becomes overly conservative. Armour loss for austenitic grades occurs extremely low for FEM and both analytical methods, as expected: λ_2 values lower than $4 \cdot 10^{-4}$ are calculated,

thus implying that the recommendation given by the Cigré WG B1.56 draft TB [29] for negligible λ_2 is reasonable.

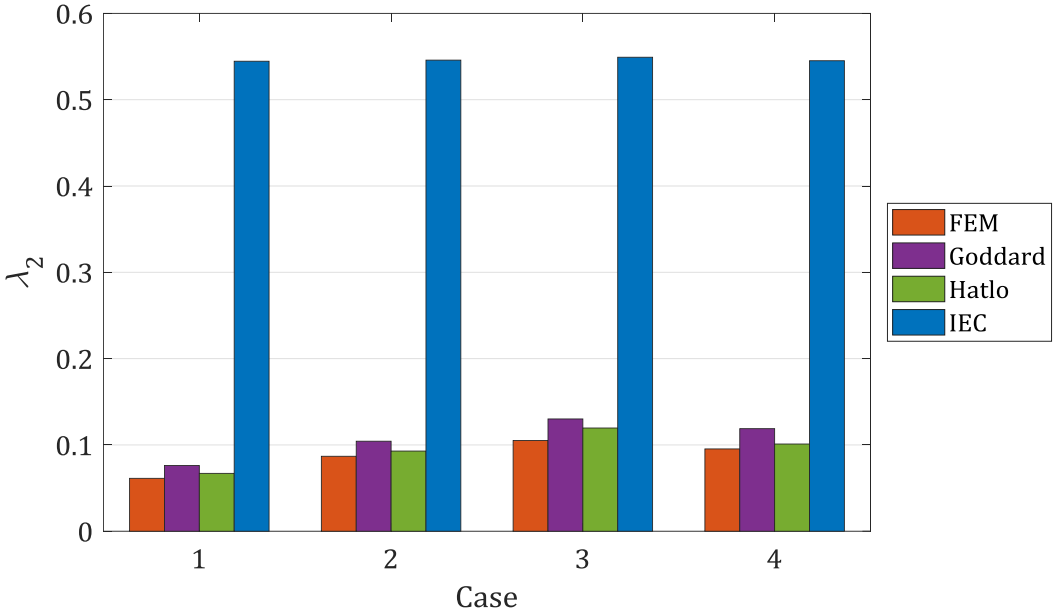

FIGURE 6.18: Armour Loss Factor λ_2 obtained from FEM, Goddard [18], Hatlo [17] and IEC Method - $\boldsymbol{\mu_{r,A}}$ = 150-j50.

Single-point bonding (SPB) in sheaths is not really possible in submarine cable projects: subsea links are in general as long as tens of km and excessive overvoltages would be generated if the metallic sheaths were left unbonded. However, it is worth investigating losses in SPB sheaths, since the analysis regarding eddy current loss in sheaths is enabled this way.

As shown in Figure 6.19 and Figure 6.20, the effect of the armour on λ_1'' is significant: an increase of about 35% is seen in higher p_A by comparing FEM with IEC, while this figure goes up to 50% for even lower p_A with regard to lower steel grades; a 24% increase is noticed for higher steel grade (higher p_A). Goddard's model appears to follow substantially better the FEM results than Hatlo's, although becomes slightly conservative for extremely low p_A. This was expected, since Hatlo's method does not account for the presence of the armour when calculating sheath eddy losses. Finally, all methods appear to be in a good agreement one another when non-magnetic armour is considered, as illustrated in Figure 6.21.

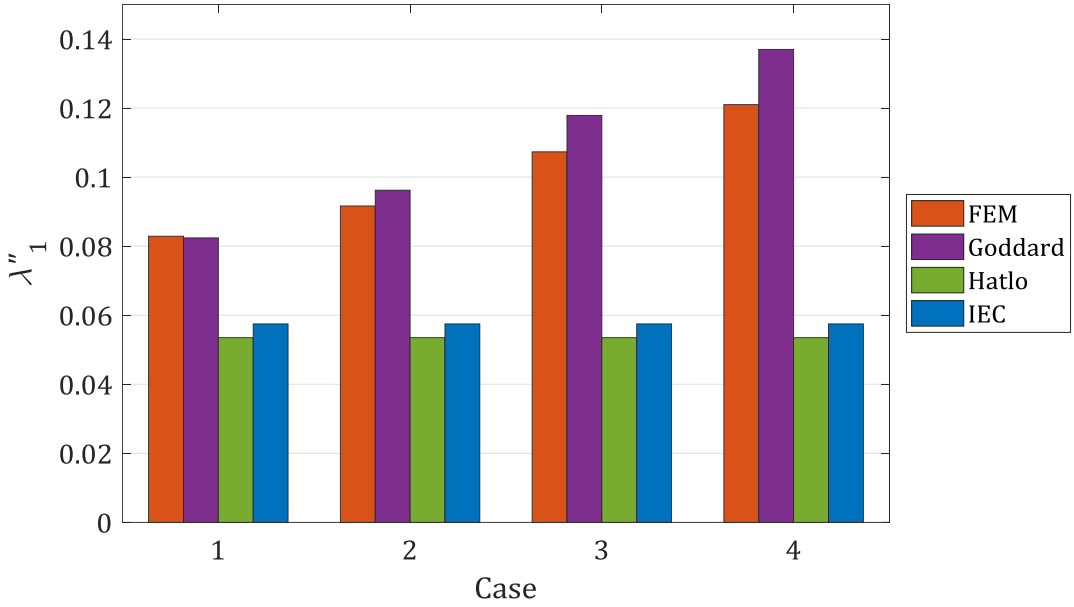

FIGURE 6.19: Sheath Eddy Loss Factor λ_1'' obtained from FEM, Goddard [18], Hatlo [17] and IEC Method - $\boldsymbol{\mu_{r,A}}$ = 600-j350.

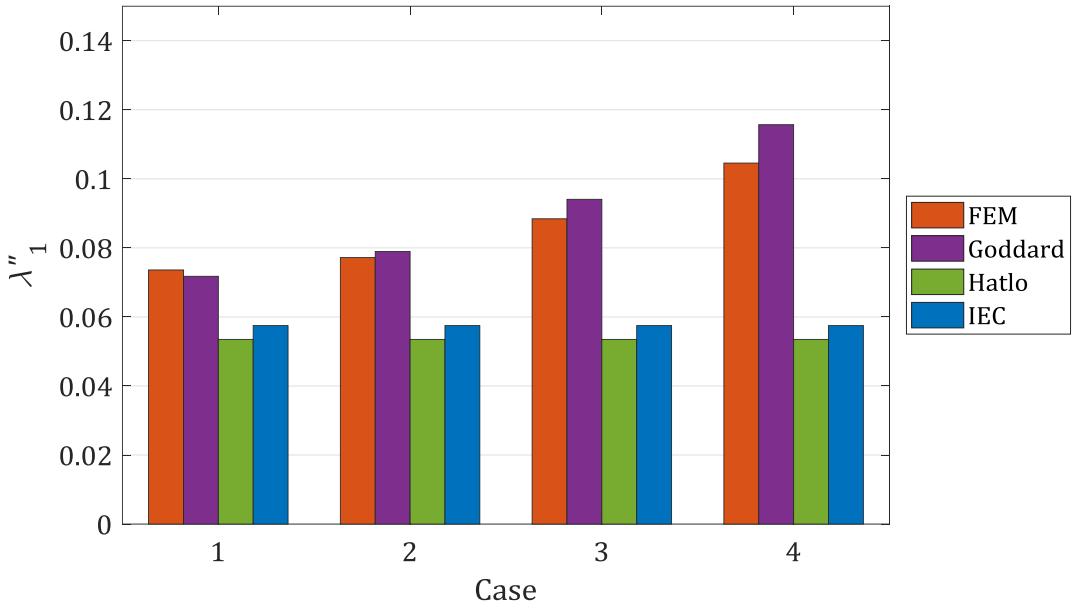

FIGURE 6.20: Sheath Eddy Loss Factor λ_1'' obtained from FEM, Goddard [18], Hatlo [17] and IEC Method - $\boldsymbol{\mu_{r,A}}$ = 150-j50.

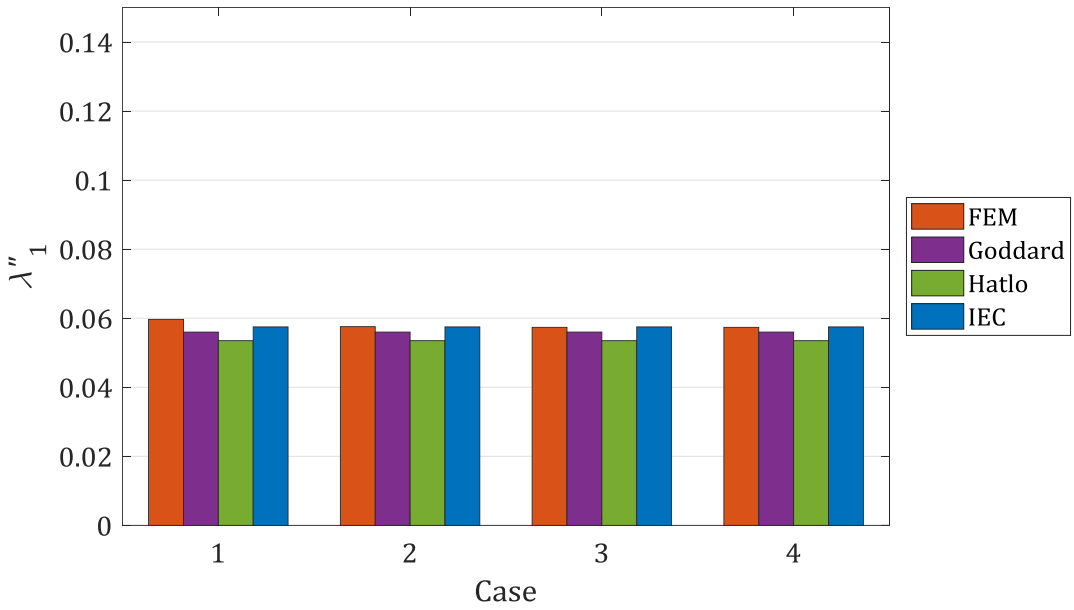

FIGURE 6.21: Sheath Eddy Loss Factor λ_1'' obtained from FEM, Goddard [18], Hatlo [17] and IEC Method - $\mu_{r,A}$ = 1.

6.3.5.2 Variation in Wire Diameter

Besides the lay-length of the armour wires, the wire diameter, d_f (mm), is a design parameter often varying amongst cables. Larger cables have in general higher d_f: as the cable size increases, so does the cable weight and, thus, more wires are required so as to achieve the same mechanical performance. To avoid armouring with excessive numbers of wires, d_f gets higher, thus facilitating the production process. The variation of d_f is considered in the present section, keeping the cross-sectional area of the armour constant and considering the cores assembly of the reference cable (section 6.3.1). Hence, the DC resistance of the armour remains unchanged, while the several variations studied are also considered mechanically equivalent. Case 3 (p_A = 1.4) with $\boldsymbol{\mu_{r,A}}$ = 600-j350 is considered, assuming n_A x d_f equal to 45 x 7.5, 70 x 6.0 (reference cable) and 101 x 5.0.

Results for R_{AC}, λ_1 and λ_2 are shown in Figure 6.22 - Figure 6.24: R_{AC} remains nearly unchanged, as shown in Figure 6.22; $\lambda_{1,FEM}$ increases by about 7% when decreasing d_f, a trend also followed by Goddard's and Hatlo's model, from the qualitative viewpoint. This increase in λ_1 reflects the higher flux linkage in the armour, occurring from the denser armouring: by decreasing and increasing d_f and n_A, respectively, the wire coverage turns from 55% into 82%, thus reducing the gaps between the wires. Although the IEC 60287-1-1 method does not account for d_f when calculating sheath losses, the impact of varying d_f on λ_1 seems to be in general weak. It is noted that d_f values besides the range [5.0, 7.5] mm are seldom used in typical export cables.

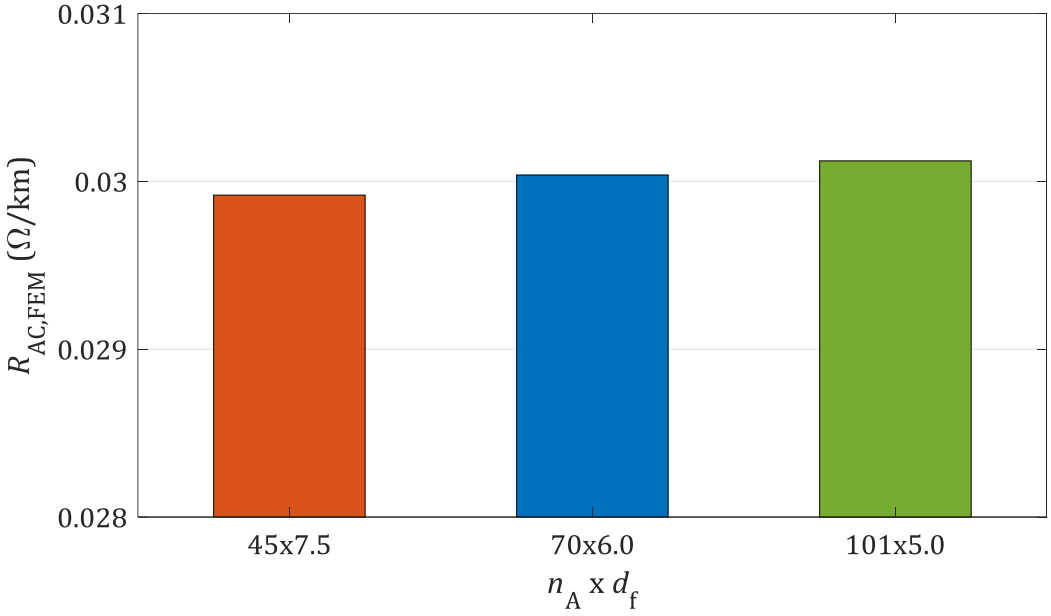

FIGURE 6.22: Conductor AC Resistance for Various Wire Diameter Values - $\boldsymbol{\mu_{r,A}}$ = 600-j350.

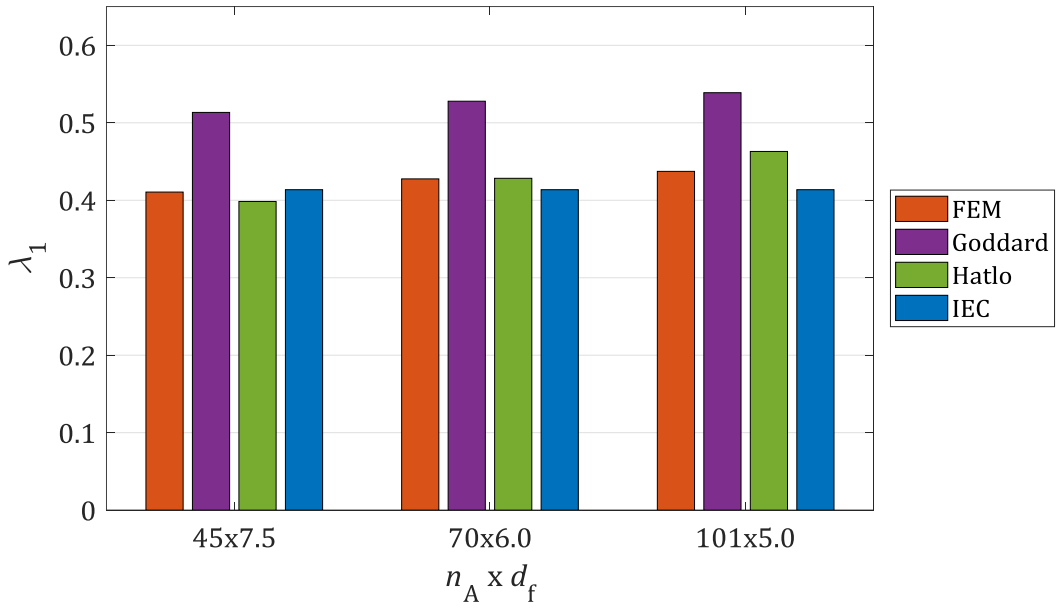

FIGURE 6.23: Sheath Total Loss Factor λ_1 obtained from FEM, Goddard [18], Hatlo [17] and IEC Method for Various Wire Diameter Values - $\boldsymbol{\mu_{r,A}}$ = 600-j350.

Armour loss factor, λ_2, follows the opposite trend than λ_1 when decreasing and increasing d_f and n_A, respectively, as shown in Figure 6.24 for FEM and Goddard results. This is to some extent expected, since the armour is magnetically coupled with the sheaths: thus, when higher currents are induced in sheaths, the total magnetic field above the cores is cancelled out to a greater extent and, as a result, weakens at the armour region.

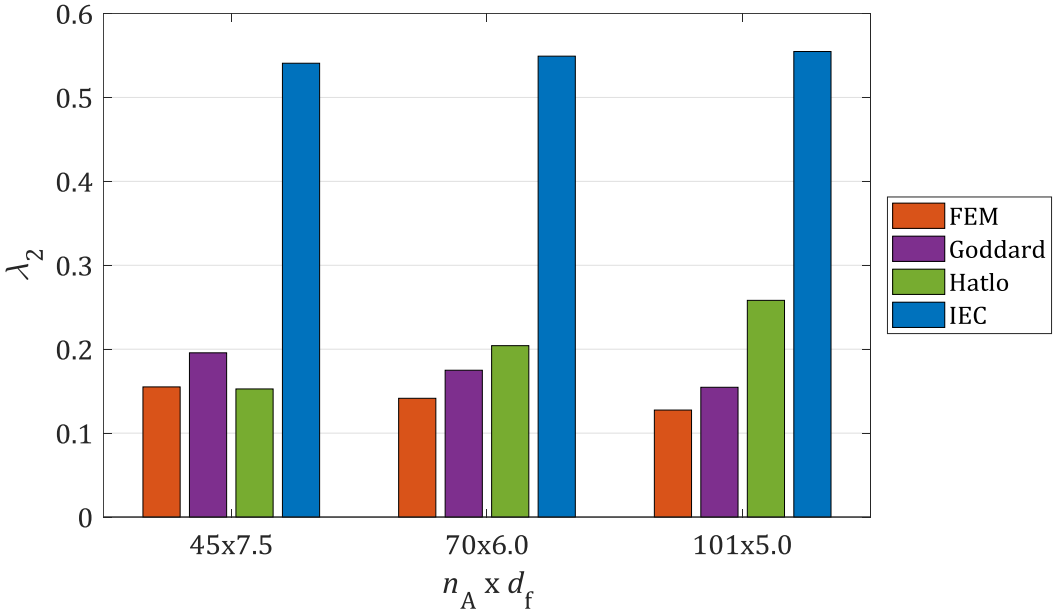

FIGURE 6.24: Armour Loss Factor λ_2 obtained from FEM, Goddard [18], Hatlo [17] and IEC Method for Various Wire Diameter Values - $\boldsymbol{\mu}_{r,A}$ = 600-j350.

6.4 Summary

The investigation of several modelling approaches concerning losses in 3C submarine cables with magnetic wire armour is the topic of the present Chapter. The potential use of existing analytical methods, effectively used for similar problems, is first investigated. The present formulation of Filament Method (FM) proves to be doubtful when geometries with a magnetic relative permeability different than unity come into play. Although certain available publications present impedance results derived from a FM version which appears to involve magnetic domains, such as de Arizon for pipe-type [85] and Benato for SL-Type armoured cables [21], it is not clear how this issue is addressed in these works. The existing FM version relies on 2-D analysis and, thus, is in principle incapable of capturing the 3-D effects in reality present in SL-Type, wire armoured cables. The potential use of the Method of Images (MoI) is investigated in the present Chapter, in combination with an effective 2-D transformation of the armour, suggested by Goddard in [18]. Relatively low magnetic relative permeability values occur in this case, which make the use of the MoI rather questionable.

Having demonstrated that it is not possible to approach the loss problem via a simple extension of the existing analytical methods, 3-D FE models are developed in the present Chapter. Although certain effective 3-D techniques are already available, such as the recently published work by Del-Pino-López [27], the present Chapter is confined to study certain fundamental principles around 3-D modelling, such as the selection of the proper boundary conditions and the followed mesh strategy.

The outcomes obtained from the 3-D analysis developed give an indicative picture of how accurate the existing IEC 60287-1-1 method is. As pointed out in Chapter 7, more cable geometries should be considered in order to deduce more general and safe conclusions. For realistic (higher) armour pitch values, the AC resistance of conductor, R_{AC}, and the losses induced in sheaths appear to be in a reasonable alignment with FEM results for the cable modelled. The recommendation of introducing the 1.5 factor in the R_{AC} formula seems to be rather conservative, especially for higher grade Steel wires. Although the eddy current loss factor, $\lambda_{1,IEC}$", does not account for the presence of the magnetic armour, sheath total loss factor, $\lambda_{1,FEM}$, occurs lower for most cases, possibly because the empirically derived factor 1.5 is to some extent conservative. The armour loss factor, $\lambda_{2,IEC}$, looks to be very conservative, even for lower Steel grade wires. Significant margins for design optimisation are expected to occur by adopting a more accurate calculation model.

The results obtained from the developed 3-D models are compared against the analytical models developed by Goddard [18] and Hatlo [17]. It is noted that these models are currently investigated by the WG B1.64, recently constituted by Cigré B1 Study Committee, as candidate suggestions for the forthcoming Technical Brochure. For the specific cable studied, Hatlo's model appears more consistent with FEM with regard to sheath loss factor, λ_1, although does not account for the effect of the armour on eddy loss factor, λ_1". This may be justified by the fact that eddy current losses are generally lower than circulating current losses when sheaths of lower conductivity, such as Lead, are examined. However, it might result in higher discrepancies for sheaths of higher conductivity, such as Aluminium. Although Lead sheathed cables are the typical technical solution for export cables today, Aluminium sheathed cables are not excluded in the future for weight and cost reduction purposes. Finally, both Goddard's and Hatlo's methods appear in a significantly better agreement with FEM in terms of the armour loss factor, λ_2, in comparison with the IEC 60287-1-1 Standard [16].

Chapter 7 Conclusions – Future Works

This thesis presents a series of new current rating methods which are applicable to present and future 3C HVAC submarine cable designs, used to interconnect Offshore Windfarms (OWFs) to the mainland. First, the existing calculation methods are thoroughly considered to investigate their potential applicability to larger cable sizes presently installed or planned to be so: as demonstrated in Chapter 3 and Chapter 5, these are mostly semi-empirical or analytical methods which provide sufficient accuracy only for smaller cable sizes due to inherent simplifying assumptions. For this reason, numerical models based on Finite Element Method (FEM) and Filament Method (FM) are developed and demonstrated to be applicable. These models are used to examine various cable sizes and provide improving formulae readily adoptable by the existing IEC 60287 Standard. The present Chapter summarises the contribution made by this work, underlines the key results along with the value added to the cable designing process and, finally, recommends topics for further research.

7.1 Research Contribution

The research conducted in this thesis forms a significant contribution to the literature in the field of current rating calculations for 3C HVAC submarine cables. First, the thermal model presently adopted by the IEC 60287-2-1 Standard is reviewed and compared with the FE models developed in Chapter 3. The 1-D heat transfer implied by the existing formulation proves to be inaccurate when export cables with larger sheaths are considered. The physical proximity of the power cores renders the Principle of Superposition inapplicable and the 2-D effects, being inevitably present, have to be considered. The thermal resistance between jackets and the armour, T_2, is found to be in general higher when calculated by the developed FE models, thus implying that the current IEC method underestimates the cable temperature given the ampacity. A new formulation for T_2 is proposed, which may be used in analytical calculations and improves the accuracy of the present Standard version. Furthermore, recommendations around the modelling of extruded (profile) fillers, increasingly used in modern cables, are given. The methodology followed along with the improved thermal model is published in [48].

An additional contribution to the state of the art is made by developing new methods used to calculate the losses generated in submarine cables with non-magnetic armour. These cables are becoming increasingly common due to the need to achieve higher ratings at lower losses. The existing analytical methods are considered for potential use in larger cables, while they are evaluated against FE and FM models in Chapter 5. The assumption for uniform, symmetrical conductor currents, which is unavoidably made by the analytical methods, is

demonstrated to result in higher sheath losses. The numerical models used in the present thesis, capable of capturing proximity effects in conductors and sheaths, are validated both theoretically and experimentally. The key design factors affecting sheath losses are identified and a parametric analysis is deployed based on the models developed. Reductive factors, which may be readily adopted by the present IEC 60287-1-1 Standard version and improve its accuracy significantly, are proposed in Chapter 5. The entire methodology followed along with the relevant results are published in [87].

The final aim of the present research is to investigate the effect of the magnetic armour on the induced losses in conductors and sheaths. For this purpose, the potential use of certain theoretical methods for submarine cables with magnetic armour is initially considered in Chapter 6. The weak points of the existing formulation of Filament Method are identified: the introduction of magnetic components and its impact on the total inductance of each filament should be more carefully considered. Additionally, the Method of Images (MoI) appears doubtfully applicable, due to inherent, theoretical constraints. Subsequently, 3-D FE models are developed in order to study the effect of several design factors and material properties on the induced losses in export cables. Emphasis is given on the proper preparation of the model, including careful selection of the boundary conditions and the optimum mesh. The present IEC 60287-1-1 Standard seems to provide sufficiently accurate results with regard to the AC resistance of conductor and the sheath losses when realistic design assumptions are made. Certain existing analytical models, presently discussed in the Cigré Working Group B1.64, are evaluated against the 3-D FE models developed. Although some discrepancies between the various models with respect to sheath losses are noticed, all agree that the existing IEC 60287-1-1 method is overly conservative with respect to armour loss. Taken together, this thesis and its associated work is summarised in 3 peer reviewed papers. A list of conference and journal publications may be found in Appendix E.

7.2 Benefits Gained for Cable Designers

Amongst other interested individuals, cable designers are the main beneficiaries from the research conducted in the present thesis. By using the thermal model currently suggested by the IEC 60287-2-1 Standard, lower conductor temperature values are obtained or, conversely, higher current ratings occur. This is due to the fact that the metallic sheaths are presently treated as isotherms, which in reality does not hold true, because the power cores are in close physical proximity. The circumferential heat transfer, expected along the sheath periphery, is the key-mechanism that changes the total heat dissipation inside the cable. By adopting the improved T_2 formulation suggested in Chapter 3, temperature results significantly closer to those derived by FEM are obtained. Besides the typical export cable design, consisting of Lead

sheaths for water-tightness purposes, improved T_2 formulation for array-cable designs is also available in Chapter 3. This takes into account for the different sheath material, often used in array-cables, i.e. Copper or Aluminium. In addition, larger array-cable sizes are covered, so as to account for the increased power demands expected in the future, stemming from the increasingly larger offshore wind turbines used. Finally, useful recommendations about how the extruded (profile) fillers should be treated in current rating calculations are provided. It is demonstrated that by assuming an equivalent thermal conductivity based on the weighted average between the air-gap and the plastic filler sections gives sensible results, standing on the safe side, for most realistic filler designs. However, the assumption for totally plastic fillers when water-filled gaps are considered appears to be a safer practice, as comparisons against FE models indicate.

The existing formulation implied by the IEC 60287-1-1 Standard for export cables, armoured with austenitic (stainless) grade steel wires seems to be fairly accurate when smaller cable sizes are considered. Indeed, the assumption for line (uniform) currents in conductors, implied also by other analytical, more precise methods, is reasonable for lower cross-sectional areas. However, increasing the conductor size results in more non-symmetrical current distributions and the total magnetic field induced above the power cores occurs eventually lower, because of the conductor current crowding towards the cable centre. The FE and FM models developed in Chapter 5 are capable of representing the proximity effects expected in both conductors and sheaths. It is found that lower losses are induced in the metallic sheaths, with a considerable thermal impact, especially for conductor sizes above 1000 mm^2. Although the main subsea cable section is typically installed under favourable, water conditions, particularly adverse conditions are encountered in hotspots, where the laying depth increases considerably, such as the landfall section. In these cases export cables with stainless steel armour are often preferred, due to lower induced losses. The cable designer is often confined between costly alternative solutions, such as the increase in conductor size. By using the reductive factors suggested in Chapter 5 along with the existing IEC 60287-1-1 Standard formulae, design optimisation becomes feasible, which is necessary and sometimes critical in hotspots.

It is widely recognised in both the scientific and the industry communities that cable losses are presently overestimated by the IEC 60287-1-1 Standard for export cables with magnetic armour. The WG B1.64 recently constituted by Cigré Study Committee B1 deals with this issue, considering both analytical and 3-D FE models. Although Filament Method appears to be used in the present literature for similar or identical to SL- cable types, it is not very clear how the existing formulation accounts for the magnetic components involved. Discussions on the critical points that should be considered with care are presented in Chapter 6, advising researchers and engineers accordingly. Additionally, 3-D FE models are developed and emphasis is given on the proper preparation of such models. 3-D FE modelling is an effective

approach to verify other loss estimation methods, such as analytical approaches or experimental measurements. Powerful workstations are today available for a reasonable cost, thus enabling more time-efficient solutions than used to be in the past. Cable engineers have often to carry out 3-D FE computations in order to account for the 3-D effects being inevitably present in 3C submarine cables. Therefore, the advice and guidance provided in Chapter 6 offers valuable time savings, especially for those having no previous relevant experience.

Overall, cable designers benefit particularly from the research conducted in the present thesis. Taking together the key-contributions obtained from Chapter 3 and Chapter 5, optimisation in cable design becomes feasible for 3C submarine cables with stainless steel armour, since the main two components of current rating, i.e. heat dissipation and loss generation models, are considered and improved. Taking the recommendations given in Chapter 6 for 3-D FE modelling, benefits are gained also for 3C submarine cables employing lower grade steel wires.

7.3 Recommendations for Future Work

Despite the contribution made by this thesis, a number of areas, which merit further work, are identified. Concerning the thermal representation of the cable, it should be noted that thermal resistance T_2 is assumed in Chapter 3 (sections 3.2 and 3.3) to include a uniform material pertaining the fillers and bedding section, as also the IEC 60287-2-1 does. Fillers are in general made of different material than the armour bedding. Although an approach similar to that implemented to calculate the equivalent thermal conductivity of extruded fillers (section 3.5.3, formula (3.13)) might give sensible T_2 values for several cable sizes, the applicability of such an approach needs to be evaluated for a variety of filler and bedding designs. Taking advantage of the cylindrical geometry of the bedding, this could be easily represented assuming 1-D heat transfer, as for T_1 and T_3 (cable insulation and armour serving, respectively). However, the inner surface of the bedding is actually subject to 2-D effects, which are inevitable in SL-Type cables, and is most likely expected to be non-isothermal: the heat dissipation will be considerably higher in the sections just above the power cores rather than the section in between them.

Besides the likely improvements concerning the work presented in Chapter 3, the topic representing the greatest challenge relates to the modelling of losses in export cable with magnetic armour. The eccentricity issue is identified in Chapter 6, section 6.1 as the main drawback of the existing Filament Method version. The problem stems from the fact that a filament enclosed in a magnetic tube is in general eccentrically placed: thus, the existing inductance formula, which implies concentrically placed flux loops around each filament, should be modified such that multiple distances from the filament centre to the inner surface of the tube be taken into consideration. By discretising the inner surface into several circular

domains, the contribution of each one may be accounted for. Then, by considering a numerical integration of the flux linked in each such domain, a more representative external inductance might be obtained for each filament.

Concerning the 3-D modelling approach presented in Chapter 6, section 6.3, an indicative, modest cable size (3 x 630 mm^2 150 kV) with Copper conductor and Lead sheaths is only considered. Export cables with Aluminium sheaths are not used today, but they are not unlikely to be considered in the future for cost and weight reduction purposes. Moreover, Aluminium foils are presently used in array cables: thus, cables with different sheath material are to be studied. It is also important to evaluate cable losses in even larger cable sizes, which are increasingly required to cover the higher power demand. A rather critical point is the validation of these 3-D models: the comparisons presented in Chapter 6, section 6.3.5 against certain existing analytical models is indicative, but not sufficient, because these models come from some specific theoretical approaches that adopt several simplifying assumptions. Given the complexity of the cable geometry, experimental measurements of the losses generated in real cable samples are recommended for this purpose. Finally, some of the assumptions adopted in the 3-D modelling approach presented in Chapter 6, section 6.3.5 must be reviewed in future works. In particular, the magnetic permeability of the armour wires is actually a function of the magnetic field rather than a constant material parameter, making the mathematical problem non-linear. Measurements of the magnetic permeability performed in steel wires, which are actually used in cable armouring, are necessary to estimate this dependency. Fortunately, non-linear solvers are available in most FEM commercially available software and, thus, this can be incorporated in the physical model.

Appendix A Filament Method: Reduction of $\mathbf{Z_{FM}}$

This appendix is a supplement to section 5.1.1 and presents the process of reducing the full n x n $\mathbf{Z}_{\text{FM}}$-matrix to an m x m $\mathbf{Z}^{\text{red}}$-matrix, where m is the number of composite conductors. This is largely based on the work done by de Arizon [85] and is necessary in order for someone to validate the FM model against other, analytical methods that generate m x m matrices and are considered fairly accurate, such as the formulation provided by Ametani [81] and used in EMTP-like software. To make this simpler and easier understandable, the case of m = 2 is herein considered: this may correspond to a coaxial cable consisting of a conductor and a metallic sheath enclosing it. The basic formula, (5.6), is repeated here for ease:

$$\begin{bmatrix} V_1 \\ \vdots \\ V_n \end{bmatrix} = \left(\begin{bmatrix} R_1 & 0 & 0 \\ 0 & \ddots & 0 \\ 0 & 0 & R_n \end{bmatrix} + j\omega \begin{bmatrix} L_{11} & \cdots & L_{1n} \\ \vdots & \ddots & \vdots \\ L_{n1} & \cdots & L_{nn} \end{bmatrix} \right) \begin{bmatrix} I_1 \\ \vdots \\ I_n \end{bmatrix} \Rightarrow$$

$$\Rightarrow [\mathbf{V}_{\text{FM}}] = ([\mathbf{R}_{\text{FM}}] + j\omega[\mathbf{L}_{\text{FM}}])[\mathbf{I}_{\text{FM}}] = [\mathbf{Z}_{\text{FM}}][\mathbf{I}_{\text{FM}}] \quad \text{(A. 1)}$$

Let's assume the conductor and sheath consisting of n_{C} and n_{S} filaments, respectively. The notation of $\mathbf{Z}_{\text{FM}}$-elements implied in (A. 1) is extended to 4 indices instead of 2, so as to include the reference to composite conductors: the 1st and 3rd indices refer to composite conductors (in this case 1 for conductor and 2 for sheath), while the 2nd and 4th indices to the filament of the corresponding composite conductor. For instance, Z_{1i2j} refers to the i-filament of the conductor and j-filament of the sheath. Following the same concept for $\mathbf{V}_{\text{FM}}$ and $\mathbf{I}_{\text{FM}}$ vectors, their elements involve 2 indices instead of 1 implied in (A. 1), with the 1st and 2nd digit referring to composite conductors and filaments, respectively. In that case, $\mathbf{V}_{\text{FM}}$- and $\mathbf{I}_{\text{FM}}$-elements containing one index only refer to the voltage drop and current in the composite conductor. The aim of reducing the full, n x n $\mathbf{Z}_{\text{FM}}$-matrix into a 2 x 2 $\mathbf{Z}^{\text{red}}$ is to express the voltage of composite conductors 1 and 2 (conductor and sheath, respectively) as a function of the corresponding composite currents only.

Two conditions are necessary before proceeding with the reduction of $\mathbf{Z}_{\text{FM}}$:

- The voltage drops along filaments forming the same composite conductor are equal:

  $$V_{11} = \cdots = V_{1n_C} = V_1 \quad \text{(A. 2)}$$

  and

  $$V_{21} = \cdots = V_{2n_S} = V_2 \quad \text{(A. 3)}$$

- The current in any composite conductor is equal to the sum of the currents in the filaments into which it is divided:

$$I_1 = I_{11} + \cdots + I_{1n_C} \tag{A. 4}$$

and

$$I_2 = I_{21} + \cdots + I_{2n_S} \tag{A. 5}$$

Substituting (A. 2) and (A. 3) into the left hand of (A. 1), one obtains the following system of equations:

$$\begin{bmatrix} V_{11} \\ \vdots \\ V_{1n_C} \\ V_{21} \\ \vdots \\ V_{2n_S} \end{bmatrix} = \begin{bmatrix} V_1 \\ \vdots \\ V_1 \\ V_2 \\ \vdots \\ V_2 \end{bmatrix} = \begin{bmatrix} Z_{1111} & \cdots & Z_{111n_C} & Z_{1121} & \cdots & Z_{112n_S} \\ \vdots & \ddots & \vdots & \vdots & \ddots & \vdots \\ Z_{1n_C11} & \cdots & Z_{1n_C1n_C} & Z_{1n_C21} & \cdots & Z_{1n_C2n_S} \\ Z_{2111} & \cdots & Z_{211n_C} & Z_{2121} & \cdots & Z_{212n_S} \\ \vdots & \ddots & \vdots & \vdots & \ddots & \vdots \\ Z_{2n_S11} & \cdots & Z_{2n_S1n_C} & Z_{2n_S21} & \cdots & Z_{2n_S2n_S} \end{bmatrix} \begin{bmatrix} I_{11} \\ \vdots \\ I_{1n_C} \\ I_{21} \\ \vdots \\ I_{2n_S} \end{bmatrix} \tag{A. 6}$$

Then, the first equation of each composite conductor is subtracted from the subsequent equations of the same conductor. This leaves the left-hand side of the other equations equal to zero. By substituting the first filament current in each composite conductor on the right-hand side of (A. 6) with those occurring from (A. 4) and (A. 5), and by properly rearranging rows and columns, the following set of linear equations expressing the voltage on the composite conductors in terms of the total current in these conductors is generated:

$$\begin{bmatrix} V_1 \\ 0 \\ \vdots \\ 0 \\ V_2 \\ 0 \\ \vdots \\ 0 \end{bmatrix} = \begin{bmatrix} Z_{1111} & \cdots & \zeta_{111n_C} & Z_{1121} & \cdots & \zeta_{112n_S} \\ \zeta_{1211} & \cdots & \zeta_{121n_C} & \zeta_{1221} & \cdots & \zeta_{122n_S} \\ \vdots & \ddots & \vdots & \vdots & \ddots & \vdots \\ \zeta_{1n_C11} & \cdots & \zeta_{1n_C1n_C} & \zeta_{1n_C21} & \cdots & \zeta_{1n_C2n_S} \\ Z_{2111} & \cdots & \zeta_{211n_C} & Z_{2121} & \cdots & \zeta_{212n_S} \\ \zeta_{2211} & \cdots & \zeta_{221n_C} & \zeta_{2221} & \cdots & \zeta_{222n_S} \\ \vdots & \ddots & \vdots & \vdots & \ddots & \vdots \\ \zeta_{2n_S11} & \cdots & \zeta_{2n_S1n_C} & \zeta_{2n_S21} & \cdots & \zeta_{2n_S2n_S} \end{bmatrix} \begin{bmatrix} I_1 \\ I_{12} \\ \vdots \\ I_{1n_C} \\ I_2 \\ I_{22} \\ \vdots \\ I_{2n_S} \end{bmatrix} \tag{A. 7}$$

where for any k, q composite conductors (k, q may be either 1 or 2 for the coaxial cable)

$$\zeta_{kiqj} = Z_{kiqj} - Z_{k1qj} - Z_{kiq1} + Z_{k1q1} \text{ for } i, j \neq 1 \tag{A. 8}$$

$$\zeta_{k1qj} = Z_{k1qj} - Z_{k1q1} \text{ for } i \neq 1 \text{ and } j = 1 \tag{A. 9}$$

$$\zeta_{kiq1} = Z_{kiq1} - Z_{k1q1} \text{ for } i = 1 \text{ and } j \neq 1 \tag{A. 10}$$

The equations are rearranged for the reduction process by interchanging rows and columns, so that the final matrix has the form

$$\begin{bmatrix} 0 \\ \vdots \\ 0 \\ V_1 \\ V_2 \end{bmatrix} = \begin{bmatrix} \cdots & \cdots & \cdots & \cdots & \cdots & \cdots \\ \vdots & \ddots & \vdots & \vdots & \ddots & \vdots \\ \cdots & \cdots & \cdots & \cdots & \cdots & \cdots \\ \vdots & \ddots & \vdots & Z_{1111} & \cdots & Z_{1121} \\ \cdots & \cdots & \cdots & Z_{2111} & \cdots & Z_{2121} \end{bmatrix} \begin{bmatrix} \vdots \\ \vdots \\ I_1 \\ I_2 \end{bmatrix} \tag{A. 11}$$

or in abbreviated form

$$\begin{bmatrix} 0 \\ \mathbf{V}^c \end{bmatrix} = \begin{bmatrix} \mathbf{A}^{\mathbf{int}} & \mathbf{B}^{\mathbf{int}} \\ \mathbf{C}^{\mathbf{int}} & \mathbf{Z}^{\mathbf{int}} \end{bmatrix} \begin{bmatrix} \mathrm{i} \\ \mathbf{I}^c \end{bmatrix} \tag{A. 12}$$

where

$$\mathbf{V}^{\mathbf{c}} = \begin{bmatrix} V_1 \\ V_2 \end{bmatrix} \tag{A. 13}$$

$$\mathbf{I}^{\mathbf{c}} = \begin{bmatrix} I_1 \\ I_2 \end{bmatrix} \tag{A. 14}$$

the voltage drop (V/m) and current (A) vectors in terms of the composite conductors, and

$$\mathbf{Z}^{\mathbf{int}} = \begin{bmatrix} Z_{1111} & \cdots & Z_{1121} \\ Z_{2111} & \cdots & Z_{2121} \end{bmatrix} \tag{A. 15}$$

Applying Kron's reduction [99], (A. 12) gives

$$\mathbf{V}^c = \left(-\mathbf{C}^{\mathbf{int}}\mathbf{A}^{\mathbf{int}^{-1}}\mathbf{B}^{\mathbf{int}} + \mathbf{Z}^{\mathbf{int}}\right)\mathbf{I}^c = \mathbf{Z}^{\mathbf{red}}\mathbf{I}^c \Rightarrow \begin{bmatrix} V_1 \\ V_2 \end{bmatrix} = \begin{bmatrix} Z_{11}^{\mathrm{red}} & Z_{12}^{\mathrm{red}} \\ Z_{21}^{\mathrm{red}} & Z_{22}^{\mathrm{red}} \end{bmatrix} \begin{bmatrix} I_1 \\ I_2 \end{bmatrix} \tag{A. 16}$$

where $\mathbf{Z}^{\mathbf{red}}$ (Ω/m) is an m x m matrix (2 x 2 in the case of a coaxial cable). It is noted that the elements of $\mathbf{Z}^{\mathbf{red}}$ take into account of any skin and proximity effects (skin effects only in the case of coaxial cable). In a similar manner, $\mathbf{Z}^{\mathbf{red}}$ may occur for any m, for instance in the case of an SL-Type and armoured cable m = 7 and $\mathbf{Z}^{\mathbf{red}}$ will be 7 x 7, assuming the armour is represented by a single composite conductor. It should be noted that several typographical errors identified in de Arizon's thesis [85] are presented in this section corrected.

Appendix B Filament Method: Calculation of Losses

This appendix is a supplement to section 5.1.1 and presents the formulation used to derive the power losses in each composite conductor. It is employed in section 5.2, where FM models are used as reference to validate the FE models with regard to the loss extracted. For this purpose, the case of 3 cable cores (3 conductors plus 3 sheaths, thus m = 6) being in trefoil touching arrangement is shown as an example in the present section; however, the same formulation can be extended for any number of composite conductors, since it is generic. It is noted that this formulation is largely based on the paper published by Moutassem [22], which can be also found in Anders's book [34]. However, the **Z** formulation (use of (5.3), (5.4)) described in section 5.1.1 is used in the present section.

To derive the power losses, the filament currents, which are unknown, have to be expressed as a function of the composite currents, which are in advance known. Indeed, 3-phase balanced currents are typically assumed in the phase conductors in loss calculations. Therefore, both $\mathbf{V}^{\mathbf{c}}$ and $\mathbf{V}_{\mathrm{FM}}$ must be eliminated. Let's assume that each phase conductor and metallic sheath in the case of 3 cores consists of n_{C} and n_{S} filaments, respectively. Thus, the total number of filaments is $n = 3n_{\mathrm{C}} + 3n_{\mathrm{S}}$. A connection matrix m x n (m = 6 in the present case) **M** is defined, i.e.

$$\mathbf{M} = \begin{bmatrix} 1 & \cdots & 10 & \cdots & 00 & \cdots & 00 & \cdots & 00 & \cdots & 00 & \cdots & 0 \\ 0 & \cdots & 01 & \cdots & 10 & \ldots & 00 & \ldots & 00 & \ldots & 00 & \ldots & 0 \\ 0 & \cdots & 00 & \cdots & 01 & \cdots & 10 & \cdots & 00 & \cdots & 00 & \cdots & 0 \\ 0 & \cdots & 00 & \cdots & 00 & \cdots & 01 & \cdots & 10 & \cdots & 00 & \cdots & 0 \\ 0 & \cdots & 00 & \cdots & 00 & \cdots & 00 & \cdots & 01 & \cdots & 10 & \cdots & 0 \\ 0 & \cdots & 00 & \cdots & 00 & \cdots & 00 & \cdots & 00 & \cdots & 01 & \cdots & 1 \end{bmatrix} \quad \begin{matrix} \underbrace{\quad} \\ n_{\mathrm{C}} \end{matrix} \quad \begin{matrix} \underbrace{\quad} \\ n_{\mathrm{S}} \end{matrix} \quad \begin{matrix} \underbrace{\quad} \\ n_{\mathrm{C}} \end{matrix} \quad \begin{matrix} \underbrace{\quad} \\ n_{\mathrm{S}} \end{matrix} \quad \begin{matrix} \underbrace{\quad} \\ n_{\mathrm{C}} \end{matrix} \quad \begin{matrix} \underbrace{\quad} \\ n_{\mathrm{S}} \end{matrix} \tag{B. 1}$$

such that the current in any composite conductor be the sum of the currents in the filaments into which it is divided, i.e.

$$\begin{bmatrix} I_1 \\ \vdots \\ I_6 \end{bmatrix} = \mathbf{M}[I_{11} \quad \ldots \quad I_{1n_{\mathrm{C}}} I_{21} \quad \ldots \quad I_{2n_{\mathrm{S}}} I_{31} \quad \ldots \quad I_{3n_{\mathrm{C}}} I_{41} \quad \ldots \quad I_{4n_{\mathrm{S}}} I_{51} \quad \ldots \quad I_{5n_{\mathrm{C}}} I_{61} \quad \ldots \quad I_{6n_{\mathrm{S}}}]^T \Rightarrow$$

$$\Longrightarrow \mathbf{I}^{\mathbf{C}} = \mathbf{M}\mathbf{I}_{\mathrm{FM}} \tag{B. 2}$$

and the voltage drops along filaments forming the same composite conductor are equal, i.e.

Appendix B

$$[V_{11} \quad \dots \quad V_{1n_C} V_{21} \quad \dots \quad V_{2n_S} V_{31} \quad \dots \quad V_{3n_C} V_{41} \quad \dots \quad V_{4n_S} V_{51} \quad \dots \quad V_{5n_C} V_{61} \quad \dots \quad V_{6n_S}]^T = \\ = \mathbf{M}^T \begin{bmatrix} V_1 \\ \vdots \\ V_6 \end{bmatrix} \Rightarrow \mathbf{V}_{\mathrm{FM}} = \mathbf{M}^T \mathbf{V}^{\mathbf{c}} \tag{B. 3}$$

Substituting (B. 3) into (A. 1), $\mathbf{V}_{\mathrm{FM}}$ is eliminated, i.e.:

$$\mathbf{M}^T \mathbf{V}^{\mathbf{c}} = \mathbf{Z}_{\mathrm{FM}} \mathbf{I}_{\mathrm{FM}} \Rightarrow \mathbf{I}_{\mathrm{FM}} = {\mathbf{Z}_{\mathrm{FM}}}^{-1} \mathbf{M}^T \mathbf{V}^{\mathbf{c}} \tag{B. 4}$$

and by multiplying both sides of (B. 4) with $\mathbf{M}$ leads to (B. 5).

$$\mathbf{M} \mathbf{I}_{\mathrm{FM}} = \mathbf{M} {\mathbf{Z}_{\mathrm{FM}}}^{-1} \mathbf{M}^T \mathbf{V}^{\mathbf{c}} \Rightarrow \mathbf{I}^{\mathbf{c}} = \mathbf{M} {\mathbf{Z}_{\mathrm{FM}}}^{-1} \mathbf{M}^T \mathbf{V}^{\mathbf{c}} \Rightarrow \mathbf{V}^{\mathbf{c}} = \left[\mathbf{M} {\mathbf{Z}_{\mathrm{FM}}}^{-1} \mathbf{M}^T\right]^{-1} \mathbf{I}^{\mathbf{c}} \tag{B. 5}$$

By multiplying (B. 5) with $\mathbf{M}^T$, $\mathbf{V}^{\mathbf{c}}$ is eventually also eliminated:

$$\text{(B. 5)} \overset{\cdot \mathbf{M}^T}{\Longrightarrow} \mathbf{M}^T \mathbf{V}^{\mathbf{c}} = \mathbf{M}^T \left[\mathbf{M} {\mathbf{Z}_{\mathrm{FM}}}^{-1} \mathbf{M}^T\right]^{-1} \mathbf{I}^{\mathbf{c}} \overset{\text{(B.4)}}{\Longrightarrow} \mathbf{I}_{\mathrm{FM}} = {\mathbf{Z}_{\mathrm{FM}}}^{-1} \mathbf{M}^T \left[\mathbf{M} {\mathbf{Z}_{\mathrm{FM}}}^{-1} \mathbf{M}^T\right]^{-1} \mathbf{I}^{\mathbf{c}} \tag{B. 6}$$

Thus, the unknown filament currents can be derived from (B. 6), given the composite current vector, $\mathbf{I}^{\mathbf{c}}$. In the case of single-point bonding systems, $\mathbf{I}^{\mathbf{c}}$ is fully defined in advance: the sheaths are open-circuited, thus no net circulating current is expected to flow through them. This is achieved by imposing zero currents in the corresponding elements of $\mathbf{I}^{\mathbf{c}}$, i.e.:

$$\mathbf{I}^{c} = \begin{bmatrix} I_1 \\ 0 \\ I_3 \\ 0 \\ I_5 \\ 0 \end{bmatrix} \tag{B. 7}$$

However, in the case of solid bonding systems, the circulating currents I_2, I_4 and I_6 are non-zero and must be separately computed. To achieve that, certain extra matrix conditions have to be imposed. In the general case, the sheaths are solidly bonded and grounded at both ends by means of grounding resistances R_{g1} and R_{g2}, as shown in Figure B. 1. Since R_{g1} and R_{g2} in general have non-zero, finite values, a floating voltage V_0 is expected to rise: hence, the longitudinal voltage drop along the bonded sheaths equals to V_0, as dictated by Kirchhoff's Second Law (B. 8) and shown in Figure B. 1. Additionally, the sum of all currents shall be equal to the current returning from the ground, I_{g}: this condition is mathematically expressed by Kirchhoff's First Law, as per (B. 9). In this case, the floating voltage V_0 may be calculated from (B. 10).

$$V_2 = V_4 = V_6 = V_0 \tag{B. 8}$$

$$I_2 + I_4 + I_6 = I_{\mathrm{g}} \tag{B. 9}$$

$$I_{\mathrm{g}} \left(R_{\mathrm{g1}} + R_{\mathrm{g2}}\right) = V_0 \tag{B. 10}$$

To simplify the problem, the sheaths are considered bonded and ungrounded or, in other words, R_{g2} is assumed infinite. In this case, I_g equals to zero and, thus, is eliminated. Assuming also balanced phase currents in the conductors, (B. 11) holds true. Eqs. (B. 9) and (B. 11) may now be combined together in a single equation, i.e. (B. 12):

$$I_1 + I_3 + I_5 = 0 \tag{B. 11}$$

$$I_1 + I_2 + I_3 + I_4 + I_5 + I_6 = 0 \tag{B. 12}$$

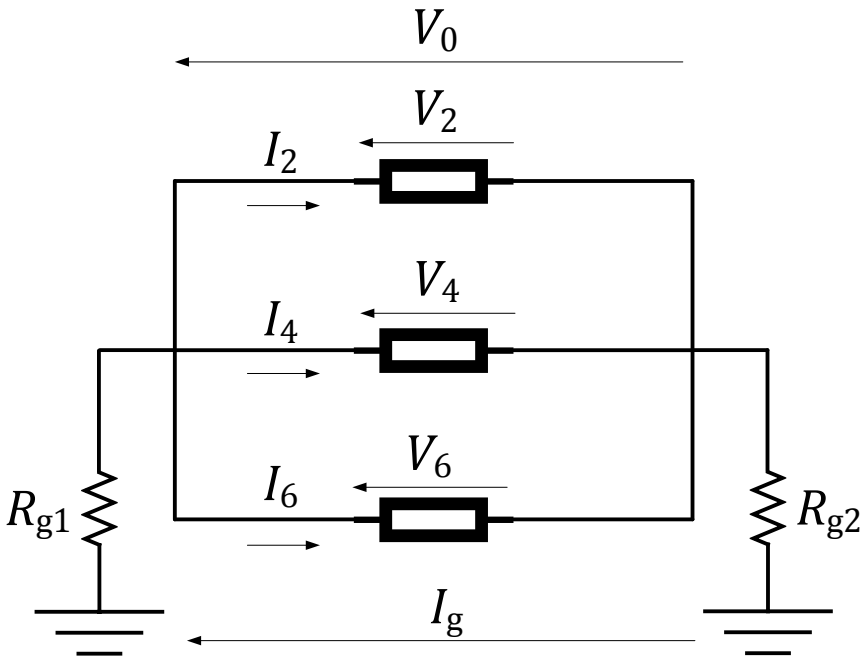

FIGURE B. 1: Electrical Network Representing the Generic Case of Solidly Bonded and Grounded Metallic Sheaths of a 3C Submarine Cable.

Combining (B. 5), (B. 8) and (B. 12) and letting

$$\mathbf{F} = \left[\mathbf{M}\mathbf{Z}_{\mathrm{FM}}{}^{-1}\mathbf{M}^{T}\right]^{-1} \tag{B. 13}$$

one obtains:

$$\begin{bmatrix} V_1 \\ V_0 \\ V_3 \\ V_0 \\ V_5 \\ V_0 \\ 0 \end{bmatrix} = \begin{bmatrix} F_{11} & \cdots & F_{16} \\ \vdots & \ddots & \vdots \\ F_{61} & \cdots & F_{66} \\ 1 & \cdots & 1 \end{bmatrix} \begin{bmatrix} I_1 \\ I_2 \\ I_3 \\ I_4 \\ I_5 \\ I_6 \end{bmatrix} \tag{B. 14}$$

I_1, I_3 and I_5 are known, while V_1, V_3, V_5, V_0, I_2, I_4 and I_6 are unknowns in the column vectors of (B. 14). After rearranging the variables in order to include all the unknowns in the same column vector, the following equation system occurs:

$$\begin{bmatrix} F_{11} & F_{13} & F_{15} \\ \vdots & \vdots & \vdots \\ F_{61} & F_{63} & F_{65} \\ 1 & 1 & 1 \end{bmatrix} \begin{bmatrix} I_1 \\ I_3 \\ I_5 \end{bmatrix} = \begin{bmatrix} 0 & 1 & 0 & 0 & -F_{12} & -F_{14} & -F_{16} \\ 1 & 0 & 0 & 0 & -F_{22} & -F_{24} & -F_{26} \\ 0 & 0 & 1 & 0 & -F_{32} & -F_{34} & -F_{36} \\ 1 & 0 & 0 & 0 & -F_{42} & -F_{44} & -F_{46} \\ 0 & 0 & 0 & 1 & -F_{52} & -F_{54} & -F_{56} \\ 1 & 0 & 0 & 0 & -F_{62} & -F_{64} & F_{66} \\ 0 & 0 & 0 & 0 & -1 & -1 & -1 \end{bmatrix} \begin{bmatrix} V_0 \\ V_1 \\ V_2 \\ V_3 \\ I_2 \\ I_4 \\ I_6 \end{bmatrix} \tag{B. 15}$$

By defining

$$\mathbf{F}' = \begin{bmatrix} F_{11} & F_{13} & F_{15} \\ \vdots & \vdots & \vdots \\ F_{61} & F_{63} & F_{65} \\ 1 & 1 & 1 \end{bmatrix} \tag{B. 16}$$

$$\mathbf{F}'' = \begin{bmatrix} 0 & 1 & 0 & 0 & -F_{12} & -F_{14} & -F_{16} \\ 1 & 0 & 0 & 0 & -F_{22} & -F_{24} & -F_{26} \\ 0 & 0 & 1 & 0 & -F_{32} & -F_{34} & -F_{36} \\ 1 & 0 & 0 & 0 & -F_{42} & -F_{44} & -F_{46} \\ 0 & 0 & 0 & 1 & -F_{52} & -F_{54} & -F_{56} \\ 1 & 0 & 0 & 0 & -F_{62} & -F_{64} & F_{66} \\ 0 & 0 & 0 & 0 & -1 & -1 & -1 \end{bmatrix} \tag{B. 17}$$

and the unknown column vector

$$\mathbf{U} = \begin{bmatrix} V_0 \\ V_1 \\ V_2 \\ V_3 \\ I_2 \\ I_4 \\ I_6 \end{bmatrix} \tag{B. 18}$$

one obtains the requested unknown currents from the 5th, 6th and 7th elements of **U** once inversing **F"**, i.e.

$$\mathbf{U} = \mathbf{F}''^{-1}\mathbf{F}' \begin{bmatrix} I_1 \\ I_3 \\ I_5 \end{bmatrix} \tag{B. 19}$$

Having obtained from (B. 6) the filament currents for both single-point and solid bonding cases, the joule losses can be then calculated for any of these two arrangements. Although solid bonding is typically applied in practice in submarine cable links, single-point bonding is still useful from the theoretical standpoint, since it allows to evaluate the eddy current loss itself. Considering the case of 3 cable cores in trefoil touching arrangement, the corresponding conductor and sheath losses in terms of phase A are calculated as per (B. 20) and (B. 21), respectively. Similar formulae are used for the other two phases.

$$W_{\mathrm{CA}} = \sum_{i=1}^{n_{\mathrm{C}}} I_{1i}^2 R_{1i} f f_1 \tag{B. 20}$$

$$W_{\mathrm{SA}} = \sum_{j=1}^{n_{\mathrm{S}}} I_{2j}^2 R_{2j} f f_2 \tag{B. 21}$$

The formulation presented in this section is adopted to calculate the cable losses in Chapter 5. Although this is a less generic version and ignores the actual grounding scheme, eliminating the return current, I_{g}, losses are expected identical even in the more generic case, provided that balanced three-phase currents flow in the conductors and the physical system is fully symmetrical. Balanced currents are typically assumed for loss calculation purposes. When the losses are calculated for an SL-Type cable, this may be considered as a fully symmetrical case, since it is implied to be sufficiently far away from other cables; however, attention must be paid when losses are requested in a system lacking in symmetry: for instance, when two or more SL-Type cables are of different size and laid in physical proximity one another. In such cases, the present formulation may be inaccurate.

Appendix C Filament Method: Verification against EMTP-like Software for 1C (Coaxial) Cable

This appendix is a supplement to section 5.1.2 and presents the validation of the FM model developed in section 5.1.1 and Appendix A against EMTP-like software for a 1C (coaxial) cable. The impedance matrix for such a cable is given by [81]:

$$\mathbf{Z} = \mathbf{Z}_\mathrm{i} + \mathbf{Z}_0 \tag{C. 1}$$

where $\mathbf{Z}_\mathrm{i}$ is the cable internal impedance and $\mathbf{Z}_0$ is the earth-return impedance. For the purpose of loss calculation, the effect of $\mathbf{Z}_0$ is considered negligible and thus excluded from the present appendix. The cable internal impedance, $\mathbf{Z}_\mathrm{i}$, is defined by (C. 2) for a coaxial cable:

$$\mathbf{Z}_\mathrm{i} = \begin{bmatrix} Z_\mathrm{CC} & Z_\mathrm{SC} \\ Z_\mathrm{SC} & Z_\mathrm{SS} \end{bmatrix} \tag{C. 2}$$

where Z_CC and Z_SS is the conductor and sheath self-impedances, respectively, Z_CS is the mutual impedance between the conductor and sheath (Ω/m). Eq. (C. 2) is calculated by evaluating the appropriate Bessel functions for each element [81]. A fictitious oversheath as thick as 1 m is assumed when constructing the cable geometry in $\mathbf{Z}_\mathrm{i}$. This way, the return path lies on a ring of radius a = 1 m. It is noted that Z_CC, Z_SS and Z_CS correspond to Z_{11}^{red}, Z_{22}^{red} and Z_{12}^{red}, respectively, as derived in (A. 16). They are in general noted as Z_{11}, Z_{22} and Z_{12} in the context of the present appendix, regardless of the method used to calculate them.

The same assumption of a = 1 m for the return ring is made for the FM model, too. Values pertaining to $\mathbf{Z}_\mathrm{i}$ derived from (C. 2) and $\mathbf{Z}^{\mathbf{red}}$ derived from (A. 16) are directly comparable. Frequencies of 50 Hz and 1000 Hz are tested and the relevant results are shown in Figure C. 1 - Figure C. 3 for increasing number of filaments. The coaxial cable tested consists of a Copper conductor of radius r_C = 20 mm and a Lead sheath of thickness t_S = 2.0 mm and inner radius $r_\mathrm{S,in}$ = 40 mm. The self-impedances for the conductor and the sheath, i.e. Z_{11} and Z_{22}, are first shown. Concerning the mutual impedance between conductor and sheath, Z_{12}, $\Im\{Z_{12}\}$ is only presented, since $\Re\{Z_{12}\}$ has no physical meaning. Additionally, $Z_{21} = Z_{12}$ for both EMTP and FM models, as expected, and for this reason Z_{21} is not included in the figures.

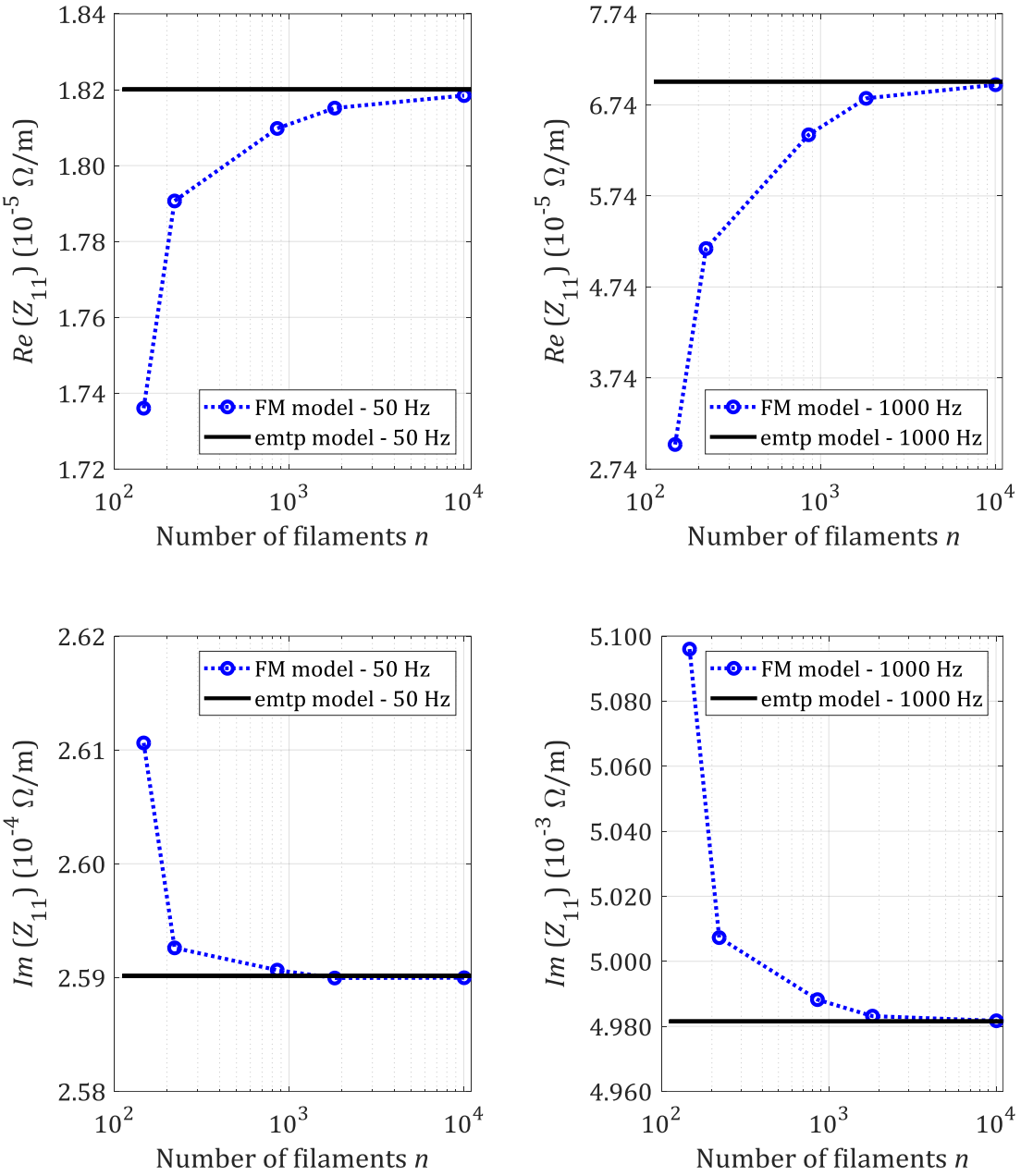

FIGURE C. 1: Comparison in terms of Z_{11} between EMTP and FM models – 1C Cable at 50 Hz and 1000 Hz.

It becomes apparent from Figure C. 1 that the $\Re\{Z_{11}\}$ computed by FM tends fairly fast to that by EMTP by increasing the number of filaments. The relative difference (assuming the EMTP model as a reference) starts from 4.6% and 57.0% for 50 Hz and 1000 Hz, respectively, and drops down to 0.09% and 0.5% for 50 Hz and 1000 Hz, respectively, when the maximum number of filaments is considered. Although $\Im\{Z_{11}\}$ does not present the same variation as $\Re\{Z_{11}\}$ in relation to the number of filaments, that computed by FM also tends fairly fast to that by EMTP: the relative difference drops from 0.79% and 2.30% down to 0.006% and 0.004% for 50 Hz and 1000 Hz, respectively. As was expected, higher divergence in Z_{11} is noticed for FM models of "coarser mesh", especially in higher frequencies that involve significantly lower

skin depth: from about 9 mm at 50 Hz the skin depth becomes 2 mm at 1000 Hz for Copper, requiring a higher number of filaments to achieve the same level of accuracy in the conductor (r_C = 20 mm).

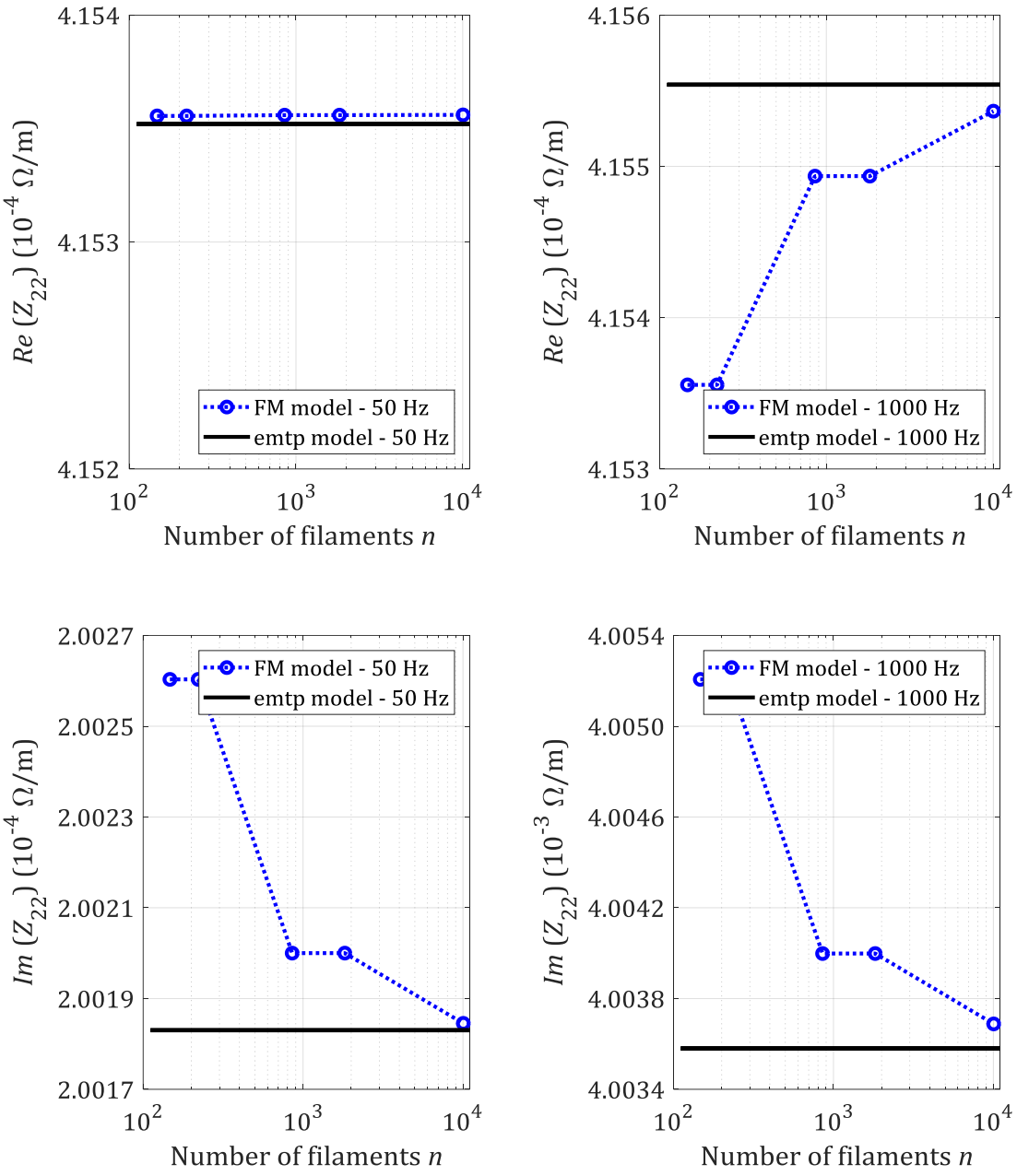

Figure C. 2: Comparison in terms of Z_{22} between EMTP and FM models – 1C Cable at 50 Hz and 1000 Hz.

Similar behaviour, though generally less intense, is noticed for Z_{22}. Due to the higher electrical resistivity of Lead ($21.4 \cdot 10^{-8}$ Ω·m according to IEC 60287-1-1 [16]), its skin depth equals to about 7 mm at 1000 Hz, which remains higher than t_S. For this reason, a nearly constant variation of 0.001% is noticed in Figure C. 2 at 50 Hz concerning $\Re\{Z_{22}\}$, while this appears to decrease when getting from 50 Hz to 1000 Hz concerning $\Im\{Z_{22}\}$, i.e. from 0.05% to 0.004%,

respectively. Low variation (0.003% maximum) is also noticed regarding $\Im\{Z_{12}\}$, as illustrated in Figure C. 3.

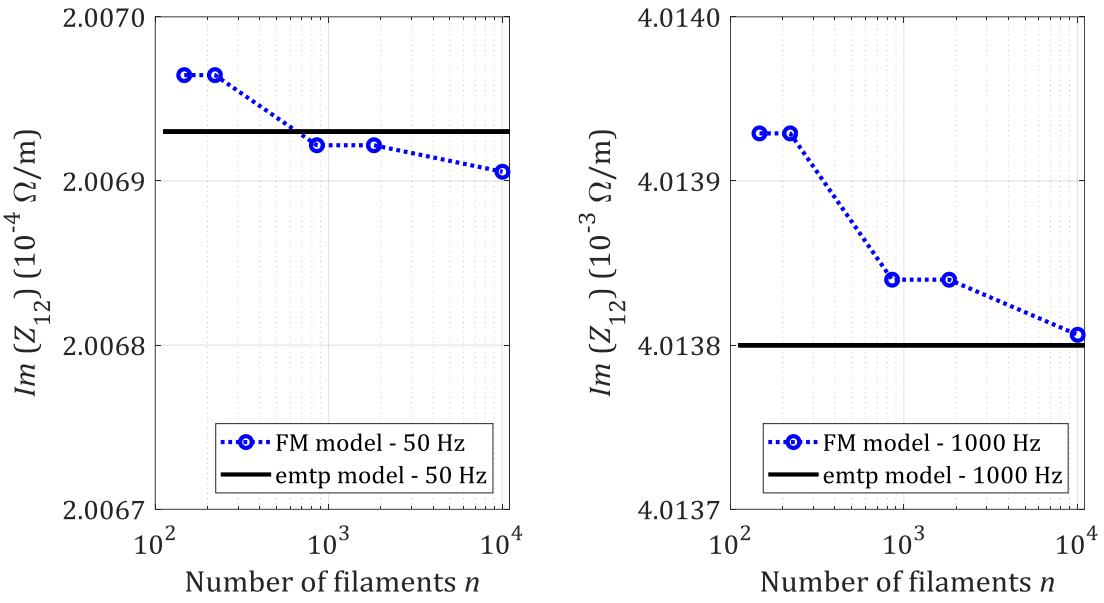

FIGURE C. 3: Comparison in terms of Z_{12} between EMTP and FM models – 1C Cable at 50 Hz and 1000 Hz.

Appendix D Jackson's Formulation: Eddy Current Loss in Unbonded Sheaths for Trefoil Configurations

This appendix is a supplement to section 5.2.4 and presents the formulation used to calculate the eddy current loss in single-point bonded sheaths for 3 1C cables laid in trefoil arrangement. This is based on the paper published by Jackson [1]. The effect of eddy currents up to 3rd order is taken into consideration, since as reported in [1], the effect of 4th and higher order currents have usually negligible effects. The relevant formulation is presented in this section for phase A assuming three cable cores, namely A, B and C, in trefoil configuration. Identical loss factors for the other two phases are obviously expected because of symmetry.

$$\lambda''_{1_J} = \frac{R_S}{R_{AC}}\left[\frac{1}{2}\sum_{k=1}^{\infty}\left(\left|C_{A_k}\right|^2 + \left|C_{A_k}{}'\right|^2\right) + \frac{(\beta_1 t_S)^4}{12\cdot 10^{12}}\right] \tag{D. 1}$$

where R_S is the resistance of sheath per unit length (pul) of cable (Ω/m), R_{AC} is the AC resistance of conductor pul (Ω/m),

$$\beta_1 = \sqrt{\frac{4\pi\omega}{10^7\rho_S}} \tag{D. 2}$$

where ω is the angular frequency (rad/s), ρ_S is sheath resistivity (Ω·m),

$$C_{A_k} = F_{A_k} + G_{A_k} + H_{A_k} \tag{D. 3}$$

and

$$C_{A_k}{}' = F_{A_k}{}' + G_{A_k}{}' + H_{A_k}{}' \tag{D. 4}$$

where the first terms of (D. 3) and (D. 4) are:

$$F_{A_k} = F_k\left(\frac{e^{j\frac{2\pi}{3}}}{s^k} + \frac{\cos\left(\frac{k\pi}{3}\right)e^{j\frac{4\pi}{3}}}{s^k}\right) \tag{D. 5}$$

where s is the distance between conductor axes (m), and

$$F_{A_k}{}' = F_k\left(\frac{\sin\left(\frac{k\pi}{3}\right)e^{j\frac{4\pi}{3}}}{s^k}\right) \tag{D. 6}$$

where

$$F_k = 2\left(\frac{d}{2}\right)^k \frac{jm}{k+jm} \tag{D. 7}$$

where d is the mean diameter of sheath (m) and

$$m = \frac{\omega}{R_S} 10^{-7} \tag{D. 8}$$

where ω is the angular frequency (rad/s).

The second terms of (D. 3) and (D. 4) are:

$$G_{A_k} = \frac{F_k}{2} \sum_{l=1}^{\infty} \left(\frac{d}{2}\right)^k \frac{(k+l-1)!}{(k-1)!\,l!} (-1)^{l+1} \left(\frac{F_{B_l}}{s^{k+l}} + \frac{F_{C_l} \cos\left(\frac{(k+l)\pi}{3}\right)}{s^{k+l}} + \frac{F_{C_l}{}' \sin\left(\frac{(k+l)\pi}{3}\right)}{s^{k+l}} \right) \tag{D. 9}$$

where

$$F_{B_l} = F_l \left(\frac{(-1)^l}{s^l} + \frac{\cos\left(\frac{l\pi}{3}\right) e^{j\frac{4\pi}{3}}}{s^l} \right) \tag{D. 10}$$

$$F_{C_l} = F_l \left((-1)^l \frac{\cos\left(\frac{l\pi}{3}\right)}{s^l} + (-1)^l \frac{\cos\left(\frac{l \cdot 2\pi}{3}\right) e^{j\frac{2\pi}{3}}}{s^l} \right) \tag{D. 11}$$

$$F_{C_l}{}' = F_l \left((-1)^l \frac{\sin\left(\frac{l\pi}{3}\right)}{s^l} + (-1)^l \frac{\sin\left(\frac{l \cdot 2\pi}{3}\right) e^{j\frac{2\pi}{3}}}{s^l} \right) \tag{D. 12}$$

and

$$G_{A_k}{}' = \frac{F_k}{2} \sum_{l=1}^{\infty} \left(\frac{d}{2}\right)^k \frac{(k+l-1)!}{(k-1)!\,l!} (-1)^{l+1} \left(-\frac{F_{B_l}{}'}{s^{k+l}} + \frac{F_{C_l} \sin\left(\frac{(k+l)\pi}{3}\right)}{s^{k+l}} - \frac{F_{C_l}{}' \cos\left(\frac{(k+l)\pi}{3}\right)}{s^{k+l}} \right) \tag{D. 13}$$

The third terms of (D. 3) and (D. 4) are:

$$H_{A_k} = \frac{F_k}{2} \sum_{l=1}^{\infty} \left(\frac{d}{2}\right)^k \frac{(k+l-1)!}{(k-1)!\,l!} (-1)^{l+1} \left(\frac{G_{B_l}}{s^{k+l}} + \frac{G_{C_l} \cos\left(\frac{(k+l)\pi}{3}\right)}{s^{k+l}} + \frac{G_{C_l}{}' \sin\left(\frac{(k+l)\pi}{3}\right)}{s^{k+l}} \right) \tag{D. 14}$$

where

Appendix D

$$G_{B_k} = \frac{F_k}{2}\sum_{l=1}^{\infty}\left(\frac{d}{2}\right)^l \frac{(k+l-1)!}{(k-1)!\,l!}(-1)^{l+1}\left((-1)^{k+l}\frac{F_{A_l}}{s^{k+l}} + \right.$$

$$\left. + \frac{F_{C_l}\cos\left(\frac{(k+l)\cdot 2\pi}{3}\right)}{s^{k+l}} + \frac{{F_{C_l}}'\sin\left(\frac{(k+l)\cdot 2\pi}{3}\right)}{s^{k+l}}\right) \qquad \text{(D. 15)}$$

$$G_{C_k} = \frac{F_k}{2}\sum_{l=1}^{\infty}\left(\frac{d}{2}\right)^l \frac{(k+l-1)!}{(k-1)!\,l!}(-1)^{l+1}\left((-1)^{k+l}\frac{F_{A_l}\cos\left(\frac{(k+l)\pi}{3}\right)}{s^{k+l}} + (-1)^{k+l}\frac{{F_{A_l}}'\sin\left(\frac{(k+l)\pi}{3}\right)}{s^{k+l}} + \right.$$

$$\left. + (-1)^{k+l}\frac{F_{B_l}\cos\left(\frac{(k+l)\cdot 2\pi}{3}\right)}{s^{k+l}} + (-1)^{k+l}\frac{{F_{B_l}}'\sin\left(\frac{(k+l)\cdot 2\pi}{3}\right)}{s^{k+l}}\right) \qquad \text{(D. 16)}$$

$${G_{C_k}}' = \frac{F_k}{2}\sum_{l=1}^{\infty}\left(\frac{d}{2}\right)^l \frac{(k+l-1)!}{(k-1)!\,l!}(-1)^{l+1}\left((-1)^{k+l}\frac{F_{A_l}\sin\left(\frac{(k+l)\pi}{3}\right)}{s^{k+l}} - (-1)^{k+l}\frac{{F_{A_l}}'\cos\left(\frac{(k+l)\pi}{3}\right)}{s^{k+l}} + \right.$$

$$\left. + (-1)^{k+l}\frac{F_{B_l}\sin\left(\frac{(k+l)\cdot 2\pi}{3}\right)}{s^{k+l}} - (-1)^{k+l}\frac{{F_{B_l}}'\cos\left(\frac{(k+l)\cdot 2\pi}{3}\right)}{s^{k+l}}\right) \qquad \text{(D. 17)}$$

and

$${H_{A_k}}' = \frac{F_k}{2}\sum_{l=1}^{\infty}\left(\frac{d}{2}\right)^l \frac{(k+l-1)!}{(k-1)!\,l!}(-1)^{l+1}\left(-\frac{{G_{B_l}}'}{s^{k+l}} + \frac{G_{C_l}\sin\left(\frac{(k+l)\pi}{3}\right)}{s^{k+l}} - \frac{{G_{C_l}}'\cos\left(\frac{(k+l)\pi}{3}\right)}{s^{k+l}}\right) \text{(D. 18)}$$

where

$${G_{B_l}}' = \frac{F_k}{2}\sum_{l=1}^{\infty}\left(\frac{d}{2}\right)^l \frac{(k+l-1)!}{(k-1)!\,l!}(-1)^{l+1}\left(-(-1)^{k+l}\frac{F_{A_l}}{s^{k+l}} + \right.$$

$$\left. + \frac{F_{C_l}\sin\left(\frac{(k+l)\cdot 2\pi}{3}\right)}{s^{k+l}} - \frac{{F_{C_l}}'\cos\left(\frac{(k+l)\cdot 2\pi}{3}\right)}{s^{k+l}}\right) \qquad \text{(D. 19)}$$

Appendix E List of Published Papers

E.1 Refereed Conference Papers

The following paper has been presented at an International Conference and has been subject to peer review.

Chatzipetros, D., Pilgrim, J.A. (2018) "Induced Losses in Non-Magnetically Armoured HVAC Windfarm Export Cables" IEEE International Conference on High Voltage Engineering and Application, 10-13 September 2018, Athens, Greece.

E.2 Peer Reviewed Journal Papers

The following paper has been published in a peer reviewed academic journal.

Chatzipetros, D., Pilgrim, J.A. (2018) "Review of the Accuracy of Single Core Equivalent Thermal Model for Offshore Wind Farm Cables" IEEE Transactions on Power Delivery, vol. 33, no. 4, pp 1913-1921.

The following paper has been accepted for publication in a future issue of a peer reviewed academic journal.

Chatzipetros, D., Pilgrim, J.A. (2019) "Impact of Proximity Effects on Sheath Losses in Trefoil Cable Arrangements" IEEE Transactions on Power Delivery, Early Access.

List of References

[1] R. L. Jackson, “Eddy-current losses in unbonded tubes,” *Proc. Inst. Electr. Eng.*, vol. 122, no. 5, pp. 551–557, 1975.

[2] IPCC WG, “Climate Change 2014 Synthesis Report Summary Chapter for Policymakers,” *Intergovernmental Panel on Climate Change (IPCC)*, 2014. [Online]. Available: https://www.ipcc.ch/site/assets/uploads/2018/02/AR5_SYR_FINAL_SPM.pdf.

[3] L. L. Grigsby, *Electric Power Engineering Handbook*, 2nd ed. California: The Electrical Engineering Handbook Series, CRC Press, 2001.

[4] T. H. Nguyen, A. Prinz, T. Friisø, and R. Nossum, “Smart grid for offshore wind farms: Towards an information model based on the IEC 61400-25 standard,” in *2012 IEEE PES Innovative Smart Grid Technologies, ISGT 2012*, 2012, pp. 1–6.

[5] LEANWIND, “Driving Cost Reductions in Offshore Wind,” *The LEANWIND Project Final Publication*, 2017. [Online]. Available: https://windeurope.org/wp-content/uploads/files/about-wind/reports/LEANWIND-Driving-cost-reductions-in-offshore.pdf.

[6] I. Komusanac, D. Fraile, and G. Brindley, “Wind energy in Europe in 2018 - Trends and statistics,” 2018. [Online]. Available: https://windeurope.org/wp-content/uploads/files/about-wind/statistics/WindEurope-Annual-Statistics-2018.pdf.

[7] A. Nghiem and I. Pineda, “Wind energy in Europe: Scenarios for 2030,” *Wind Europe*, 2017. [Online]. Available: https://windeurope.org/wp-content/uploads/files/about-wind/reports/Wind-energy-in-Europe-Scenarios-for-2030.pdf.

[8] M. I. Blanco, “The economics of wind energy,” *Renew. Sustain. Energy Rev.*, vol. 13, no. 6–7, pp. 1372–1382, 2009.

[9] K&L Gates, LLP, and S.-L. A. Business, “US Offshore Wind Handbook,” *Joint Publication*, 2018. [Online]. Available: http://www.klgates.com/files/Upload/2018-08_OG_Offshore-Wind-brochure.pdf.

[10] OWPB, “Transmission Costs for Offshore Wind Final Report April 2016,” *Offshore Wind Program Board (OWPB) Report*, 2016. [Online]. Available:

https://ore.catapult.org.uk/app/uploads/2018/02/Transmission-Costs-for-Offshore-Wind.pdf.

[11] T. Worzyk, *Submarine Power Cables*. Springer, 2009.

[12] S. Belli, G. Perego, A. Bareggi, L. Caimi, F. Donazzi, and E. Zaccone, "P-Laser: Breakthrough in power cable systems," in *Conference Record of IEEE International Symposium on Electrical Insulation*, 2010, pp. 1–5.

[13] Cigré Working Group B1.40, "Technical Brochure 610: Offshore Generation Cable Connections," Cigré, 2015.

[14] Cigré Working Group B1.35, "Technical Brochure 640: A guide for rating calculations of insulated power cables," Cigré, 2015.

[15] J. A. Pilgrim, "Circuit Rating Methods for High Temperature Cables," University of Southampton, 2011.

[16] IEC 60287-1-1, "Electric cables – Calculation of the current rating – Part 1-1: Current rating equations (100 % load factor) and calculation of losses – General," 2014.

[17] M. Hatlo, E. Olsen, R. Stølan, and N. As, "Accurate analytic formula for calculation of losses in three-core submarine cables," in *9th International Conference on Insulated Power Cables, Jicable 2015*, 2015, pp. 1–6.

[18] K. F. Goddard, J. A. Pilgrim, R. Chippendale, and P. L. Lewin, "Induced losses in three-core SL-type high-voltage cables," *IEEE Trans. Power Deliv.*, vol. 30, no. 3, pp. 1505–1513, 2015.

[19] J. J. Bremnes, G. Evenset, and R. Stølan, "Power loss and inductance of steel armoured multi-core cables: comparison of IEC values with '2,5D' FEA results and measurements," in *Cigré 2010 Session*, 2010, vol. B1-116.

[20] P. De Arizon and H. W. Dommel, "Computation of Cable Impedances Based on Subdivision of Conductors," *IEEE Trans. Power Deliv.*, vol. 2, no. 1, pp. 22–27, 1987.

[21] R. Benato and S. D. Sessa, "A New Multiconductor Cell Three-Dimension Matrix-Based Analysis Applied to a Three-Core Armoured Cable," *IEEE Trans. Power Deliv.*, vol. 33, no. 4, pp. 1636–1646, 2018.

[22] W. Moutassem and G. J. Anders, "Calculation of the eddy current and hysteresis losses in sheathed cables inside a steel pipe," *IEEE Trans. Power Deliv.*, vol. 25, no. 4, pp.

2054–2063, 2010.

[23] G. Forbes, “On the relation which ought to subsist between the strength of an electric current and the diameter of conductors , to prevent overheating.,” *J. Soc. Telegr. Eng.*, vol. 13, no. 52, pp. 232–262, 1884.

[24] A. E. Kennelly, “Heating conductors by electric currents,” *Electr. World*, vol. XIV, no. 21, p. 336,355,372,386, 1891.

[25] A. E. Kennelly, “On the carrying capacity of electric cables, submerged, buried or suspended in air,” in *Proc. Minutes 9th Annu. Meeting Association Edison Illuminating Companies*, 1893, pp. 79–93.

[26] J. H. Neher and M. H. McGrath, “The Calculation of the Temperature Rise and Load Capability of Cable Systems,” *Trans. Am. Inst. Electr. Eng. Part III Power Appar. Syst.*, vol. 76, no. 3, pp. 752–764, 1957.

[27] J. C. Del-Pino-López, M. Hatlo, and P. Cruz-Romero, “On simplified 3D finite element simulations of three-core armored power cables,” *Energies*, vol. 11, no. 11, 2018.

[28] G. Anders and G. Georgallis, “Transient analysis of 3-core SL-type submarine cables with jacket around each core,” in *9th International Conference on Insulated Power Cables, Jicable 2015*, 2015.

[29] Cigré Working Group B1.56, “Draft Technical Brochure: Power Cable Rating Examples for Calculation Tool Verification,” Cigré, 2018.

[30] F. De Wild *et al.*, “Overview of Cigre WG B1.56 Regarding the Verification of Cable Current Ratings,” in *10th International Conference on Insulated Power Cables, Jicable 2019*, 2019, pp. 1–6.

[31] L. D. Ramirez, W. Kamara, and G. J. Anders, “Thermal Analysis of 3-Core SL-type Cables with Jacket Around Each Core using the IEC Standard,” in *10th International Conference on Insulated Power Cables, Jicable 2019*, 2019, no. 3, pp. 23–27.

[32] F. P. Incropera, D. P. DeWitt, T. L. Bergman, and A. S. Lavine, *Fundamentals of heat and mass transfer*, Sixth. John Wiley & Sons, 2007.

[33] IEC 60287-2-1, “Electric cables – Calculation of the current rating – Part 2-1: Thermal resistance - Calculation of thermal resistance,” 2015.

[34] G. J. Anders, *Rating of electric power cables: ampacity computations for transmission,*

distribution, and industrial applications, vol. 35, no. 02. IEEE Press, 1997.

[35] G. Mie, "Über die Warmeleitung in einem verseilten Kable," *Electrotech. Zeitschrift*, pp. 137-, 1905.

[36] D. M. Simons, "Cable Geometry and the Calculation of Current-Carrying Capacity," *Trans. Am. Inst. Electr. Eng.*, vol. 42, no. 2, pp. 600–620, 1923.

[37] A. Russel, "Alternating Currents." Cambridge Physical Series, p. 187, 1914.

[38] R. W. Atkinson, "The Dielectric Field in an Electric Power Cable," *Trans. Am. Inst. Electr. Eng.*, pp. 971–1036, 1919.

[39] G. J. Anders, A. K. T. Napieralski, and W. Zamojski, "Calculation of the internal thermal resistance and ampacity of three-core unscreened cables with fillers," *IEEE Power Eng. Rev.*, vol. 17, no. 9, p. 31, 1997.

[40] G. J. Anders, A. Napieralski, and Z. Kulesza, "Calculation of the internal thermal resistance and ampacity of 3-core screened cables with fillers," *IEEE Trans. Power Deliv.*, vol. 14, no. 3, pp. 729–733, 1999.

[41] S. W. Melsom, "Permissible current loading of British standard impregnated paper insulated electric cables, second report on the research on the heating of buried cables,Appendix IV: "Calculation of the thermal resistance of three-core cables and examination of Russell"," *J. Inst. Electr. Eng.*, vol. 61, no. 318, pp. 568–570, 1923.

[42] D. J. Swaffield, P. L. Lewin, and S. . Sutton, "Methods for rating directly buried high voltage cable circuits," *IET Gener. Transm. Distrib.*, vol. 2, no. 3, pp. 393–401, 2008.

[43] V. S. Arpaci, A. Selamet, and S.-H. Kao, *Introduction to Heat Transfer*. Portland, ME, USA: Pearson, 2000.

[44] V. T. Morgan and P. Slaninka, "The external thermal resistance of power cables in a group buried in non-uniform soil," *Electr. Power Syst. Res.*, vol. 29, no. 1, pp. 35–42, 1994.

[45] P. Slaninka and V. T. Morgan, "External thermal resistance of power cable in nonuniform soil," *Proc. Inst. Electr. Eng.*, vol. 139, no. 3, pp. 117–124, 1992.

[46] G. Luoni, A. Morello, and H. W. Holdup, "Calculation of the external thermal resistance of buried cables through conformal transformation," *Proc. Inst. Electr. Eng.*, vol. 120, no. 10, p. 1260, 2010.

[47] Cigré Working Group 02, “The calculation of the effective external resistance of cables laid in materials having different thermal resistivities,” *Electra*, vol. 98, pp. 19–42, 1985.

[48] D. Chatzipetros and J. A. Pilgrim, “Review of the Accuracy of Single Core Equivalent Thermal Model for Offshore Wind Farm Cables,” *IEEE Trans. Power Deliv.*, vol. 33, no. 4, pp. 1913–1921, 2018.

[49] R. M. Eichhorn, “A critical comparison of XLPE and EPR for use as electrical insulation on underground power cables,” *IEEE Trans. Electr. Insul.*, vol. EI-16, no. 6, pp. 469–482, 1981.

[50] IEC TR 62095, “Electric cables — Calculation of current rating — Cable current rating calculations using finite element method,” 2003.

[51] I. Kocar and A. Ertas, “Thermal analysis for determination of current carrying capacity of PE and XLPE insulated power cables using finite element method,” in *IEEE Melecon*, 2004, pp. 905-908 Vol.3.

[52] S. Catmull, R. D. Chippendale, J. A. Pilgrim, G. Hutton, and P. Cangy, “Cyclic Load Profiles for Offshore Wind Farm Cable Rating,” *IEEE Trans. Power Deliv.*, vol. 31, no. 3, pp. 1242–1250, 2016.

[53] Natural Environ. and B. G. S. Res. Council, GeoReports, “Temperature and thermal properties (detailed),” Nottingham, UK, 2011.

[54] P. L. Lewin, J. E. Theed, A. E. Davies, and S. T. Larsen, “Method for rating power cables buried in surface troughs,” *IEE Proc. - Gener. Transm. Distrib.*, vol. 146, no. 4, p. 360, 2002.

[55] C. Long, *Essential Heat Transfer*. Harlow, UK, 1999: Pearson Education, 1999.

[56] S. Eckroad, *EPRI Underground Transmission Systems Reference Book*. Palo Alto, US: Electric Power Research Institute, 2006.

[57] R. Benato, “Multiconductor analysis of underground power transmission systems: EHV AC cables,” *Electr. Power Syst. Res.*, vol. 79, no. 1, pp. 27–38, 2009.

[58] R. A. Rivas and J. R. Marti, “Calculation of Frequency-Dependent Parameters of Power Cables: Matrix Partitioning Techniques,” *IEEE Trans. Power Deliv.*, vol. 17, no. 4, p. 64, 2002.

[59] A. Russell, *A Treatise On The Theory Of Alternating Currents*, 2nd ed., vol. 1. Cambridge University Press, 1914.

[60] A. H. M. Arnold, "The alternating-current resistance of tubular conductors," *J. Inst. Electr. Eng.*, vol. 78, no. 473, pp. 580–596, 1936.

[61] H. Goldenberg, "Some approximations to Arnold's formulas for skin and proximity effect factors for circular and shaped conductors," 1961.

[62] A. H. M. Arnold, "Proximity effect in solid and hollow round conductors," *J. Inst. Electr. Eng. - Part II Power Eng.*, vol. 88, no. 4, pp. 349–359, 1941.

[63] D. A. Silver and G. W. Seman, "Investigation of AC/DC Resistance Ratios of Various Designs of Pipe-Type Cable Systems," *IEEE Trans. Power Appar. Syst.*, vol. PAS-101, no. 9, pp. 3481–3492, 1982.

[64] F. W. Carter, "Note on Losses in Cable Sheaths," *Math. Proc. Cambridge Philos. Soc.*, vol. 23, no. 01, pp. 65–73, 1927.

[65] R. G. Parr, "Formulae For Eddy-Current Loss Factors In Single-Point Or Cross Bonded Cable Sheaths," UK, 1979.

[66] P. G. Heyda, G. E. Kitchie, and J. E. Taylor, "Computation of eddy-current losses in cable sheaths and busbar enclosures," *Proc. Inst. Electr. Eng.*, vol. 120, no. 4, pp. 447–452, 1973.

[67] A. H. M. Arnold, "The theory of sheath losses in single-conductor lead-covered cables," *J. Inst. Electr. Eng.*, vol. 67, no. 384, pp. 69–89, 1928.

[68] S. Sturm, J. Paulus, and F. Berger, "Studies on Parameters Influencing the Armour and Shield Losses of Submarine Power Cables," in *The 20th International Symposium on High Voltage Engineering*, 2017, pp. 1–6.

[69] A. H. M. Arnold, "Eddy Current Losses in Multi-Core Paper-Insulated Lead-Covered Cables, Armoured and Unarmoured, Carrying Balanced Three-Phase Current," 1939.

[70] S. Whitehead and E. E. Hutchings, "Current rating of cables for transmission and distribution," *J. Inst. Electr. Eng.*, vol. 83, no. 502, pp. 517–557, 1938.

[71] B. Gustavsen, M. Hoyer-Hansen, P. Triverio, and U. R. Patel, "Inclusion of Wire Twisting Effects in Cable Impedance Calculations," *IEEE Trans. Power Deliv.*, vol. 31, no. 6, pp. 2520–2529, 2016.

[72] L. Bosone, “Contributo allo studio delle perdite e dell’ autoiduzione dei cavi unipolari,” *L’ Elettrotec.*, pp. 2–8, 1931.

[73] G. Bianchi and G. Luoni, “Induced currents and losses in single-core submarine cables,” *IEEE Trans. Power Appar. Syst.*, vol. 95, no. 1, pp. 49–58, 1976.

[74] J. S. Barrett and G. J. Anders, “Circulating current and hysteresis losses in screens, sheaths and armour of electric power cables — mathematical models and comparison with IEC Standard 287,” *IEE Proc. - Sci. Meas. Technol.*, vol. 144, no. 3, pp. 101–110, 1997.

[75] S. Sturm and J. Paulus, “Estimating the losses in three-core submarine power cables using 2D and 3D FEA simulations,” *9th Int. Conf. Insul. Power Cables*, pp. 21–25, 2015.

[76] P. Maioli, M. Bechis, and G. Dell’Anna, “AC Resistance of Submarine Cables,” in *9th International Conference on Insulated Power Cables*, 2015, no. 1, pp. 1–6.

[77] R. Stølan and M. M. Hatlo, “Armour Loss in Three Core Submarine Cables – Measurements of Cable Impedance and Armour Wire Permeability,” in *Cigré 2018 Session*, 2018, vol. B1-306, pp. 1–9.

[78] K. Ferkal, M. Poloujadoff, and E. Dorison, “Proximity effect and eddy current losses in insulated cables,” *IEEE Trans. Power Deliv. Power Deliv.*, vol. 11, no. 3, pp. 1171–1178, 1996.

[79] N. Kovač, G. Anders, and T. Kilić, “Sheath loss factors taking into account the proximity effect for a cable line in a touching flat formation,” *IEEE Trans. Power Deliv.*, vol. 30, no. 3, pp. 1363–1371, 2015.

[80] R. Benato, S. Dambone Sessa, M. Forzan, M. Marelli, and D. Pietribiasi, “Core laying pitch-long 3D finite element model of an AC three-core armoured submarine cable with a length of 3 metres,” *Electr. Power Syst. Res.*, vol. 150, pp. 137–143, 2017.

[81] A. Ametani, “A general formulation of impedance and admittance of cables,” *IEEE Trans. Power Appar. Syst.*, vol. PAS-99, no. 3, pp. 902–910, 1980.

[82] E. Comellini, A. Invernizzi, and G. Manzoni, “A computer program for determining electrical resistance and reactance of any transmission line,” *IEEE Trans. Power Appar. Syst.*, vol. PAS-92, no. 1, pp. 308–314, 1973.

[83] V. T. Morgan, “The current distribution, resistance and internal inductance of linear power system conductors-a review of explicit equations,” *IEEE Trans. Power Deliv.*, vol.

28, no. 3, pp. 1252–1262, 2013.

[84] M. M. Hatlo and J. J. Bremnes, “Current dependent armour loss in three-core cables: comparison of FEA results and measurements,” in *Cigré 2014 Session*, 2014, no. B1-306.

[85] P. De Arizon, “A Comparison Of Numerical Algorithms For Determining Electrical Resistance And Reactance Using Subdivision Of The Cable Conductors,” The University Of British Columbia, 1984.

[86] BS EN 10257-2, “Zinc or zinc alloy coated non-alloy steel wire for armouring either power cables or telecommunication cables - Part 2 : Submarine cables,” 2011.

[87] D. Chatzipetros and J. Pilgrim, “Impact of Proximity Effects on Sheath Losses in Trefoil Cable Arrangements,” *IEEE Trans. Power Deliv.*, vol. PP, no. c, pp. 1–1, 2019.

[88] H. W. Dommel, *EMTP Theory Book*. Portland, OR, US, 1986.

[89] N. Kovac, N. Grulovic-Pavljanic, and A. Kukavica, “Generated heat within power cable sheaths per unit time and volume,” *Appl. Therm. Eng.*, vol. 52, no. 1, pp. 90–96, 2013.

[90] G. K. Papagiannis, D. G. Triantafyllidis, and D. P. Labridis, “A one-step finite element formulation for the modeling of single and double-circuit transmission lines,” *IEEE Trans. Power Syst.*, vol. 15, no. 1, pp. 33–38, 2000.

[91] J. Weiss and Z. J. Csendes, “A one-step finite element method for multiconductor skin effect problems,” *IEEE Trans. Power Appar. Syst.*, vol. PAS-101, no. 10, pp. 3796–3803, 1982.

[92] S. Sturm, J. Paulus, and F. Berger, “FEM analysis on influence of semiconductors in 3-core submarine power cables regarding cable losses,” in *Jicable’19*, 2019, pp. 1–6.

[93] Cropico, “A Guide to Low Resistance Measurement Contents,” Peterlee, UK, 2007.

[94] BS IEC 60228, “Conductors of insulated cables,” 2005.

[95] R. Schinzinger and A. Ametani, “Surge propagation characteristics of pipe enclosed underground cables,” *IEEE Trans. Power Appar. Syst.*, vol. PAS-97, no. 5, pp. 1680–1688, 1978.

[96] A. Mekjian, M. Sosnowski, and C. Katz, “A New Method for Calculating Alternating Current Losses in Pipe-Type Cable Systems,” *IEEE Trans. Power Appar. Syst.*, vol. 7, pp. 1850–1858, 1982.

[97] M. Sosnowski, G. Bahder, and A. Mekjiian, “Calculating AC/DC Resistance Ratios for High-Pressure Oil-Filled Cable Designs, Volume 2: Details of Mathematical Derivations,” New Brunswick, New Jersey, 1985.

[98] B. Gustavsen, J. A. Martinez, and D. Durbak, “Parameter determination for modeling system transients - Part II: Insulated Cables,” *IEEE Trans. Power Deliv.*, vol. 20, no. 3, pp. 2045–2050, 2005.

[99] S. Y. Caliskan and P. Tabuada, “Towards Kron reduction of generalized electrical networks,” *Automatica*, vol. 50, no. 10, pp. 2586–2590, 2014.

[100] IEC 60502-2, “Power cables with extruded insulation and their accessories for rated voltages from 1 kV (Um = 1,2 kV) up to 30 kV (Um = 36 kV) – Part 2: Cables for rated voltages from 6 kV (Um = 7,2 kV) up to 30 kV (Um = 36 kV),” 2014.